Transition Path Theory for Markov Processes

Application to molecular dynamics

Betreuer: Prof. Dr. Christof Schütte
Freie Universität Berlin
Fachbereich Mathematik und Informatik
Arnimallee 6
14195 Berlin

Gutachter: Prof. Dr. Christof Schütte
Prof. Dr. Eric Vanden-Eijnden (New York, USA)

Contents

Contents

1. Introduction

Transition events in complex systems between long lived states are a key feature of many systems arising in physics, chemistry, biology, etc. It was early recognized that transition processes are characterized by rare but important events, i.e., transition processes are phenomena that take place on a long time scale compared to the time scale characterizing the states of local stability, also called *metastable* states. For example, the timescale for folding of a small protein, i.e. the transition from an unfolded in a folded state is in the range of microseconds to milliseconds, whereas that for small-amplitude motions of amino acid side chains and water solvent is 1 femtosecond.

The first step towards an understanding of rare events was to realize that escape from a metastable state can only happen via noise-assisted hopping events where the amplitude of the noise reflects the finite temperature at which the process takes place. In other words, the dynamics of the process is subject to random perturbations. If we relate the fluctuation induced by the noise to an appropriate energy scale E_{noise}, escape from a metastable state will be rare whenever the condition $E_{barrier}/E_{noise} \gg 1$ holds, where $E_{barrier}$ denotes the energy barrier height which separates the metastable state.

Under physical assumptions on the governing dynamics of the process, the time scale of escape from a metastable state depends exponentially on the ratio $E_{barrier}/E_{noise}$. This means that one has to wait exponentially long to observe a single transition. On the other hand, the impact of the motion on the fastest time scale on the global behavior of the process is not negligible. Consequently, any direct numerical simulation of the dynamics in order to get a sufficient statistics on transition events would fail. Hence, alternative and effective strategies are required and had been developed such as Transition State Theory, Transition Path Sampling, and more recently Transition Path Theory.

In the present work we give a unified presentation of Transition Path Theory (TPT) for time-continuous Markov processes and we elucidate its range of applicability on the example of conformational dynamics of bio-molecules.

We consider the most interesting results to include the following:

- Illustration of TPT on several low dimensional examples for Smoluchowski and Langevin dynamics arising from the stochastic modeling of molecular dynamics.

- Derivation of a stable finite discretization scheme of the committor function equation associated with the hypoelliptic Langevin dynamics.

- Adaptation of TPT to the class of time-continuous Markov processes with discrete state space (Markov jump processes).

- Development of efficient graph algorithms for identifying transition pathways for Markov jump processes and in Markov chains.

- Presentation, improvement and comparison of methods to estimate an infinitesimal generator of a Markov jump process if only an incomplete observation of the process is available.

- Derivation of an Metropolis Monte Carlo Markov chain method to investigate the error propagation in the discrete committor function computation for Markov chains.

Rare Events in Molecular Dynamics   In the classical description of molecular processes the dynamics of the molecule's microscopic configurations (position and momenta) are mathematically modeled in terms of ordinary differential equation, resulting from formulations of Lagrange and Hamilton. Within these models, the physical interactions of atoms are encoded in the interaction *potential* which is composed of sums of contributions of different physical origin as the bond structure of the molecule and electrostatic interactions. But most biomolecular processes can only be understood within a thermodynamical context; instead of a single molecular system as a solution of the classical equations, one is interested in statistical ensembles, since only such ensembles can be object of experimental investigation. Throughout this thesis we will focus on that ensemble view.

Functions of bio-molecules depend on their dynamical properties, and especially on their ability to undergo transitions between long-living states, called *conformations*. A conformation of a molecule is understood as a mean geometric structure of the molecule which is conserved on a large time scale compared to the fastest molecular motions where the system may well rotate, oscillate or fluctuate. From the dynamical point of view, a conformation typically persists for a long time (again compared to the fastest molecular motions) such that the associated subset of microscopic configurations is almost invariant or *metastable* [82] with respect to the dynamics. Hence transitions between different conformations of a molecule are rare events compared to the fluctuations within each conformation.

A very popular model to describe molecular systems including thermal noise is the stochastic Langevin dynamics or Smoluchowski dynamics. A Langevin system can be regarded as a mechanical system with additional noise and friction where the noise can be thought of modeling the influence of a heat bath surrounding the molecule and the friction is chosen such as to counterbalance the energy fluctuations due to the noise [45]. The Smoluchowski dynamics [87] is a Brownian motion which results from the Langevin dynamics in the high friction limit and acts only on the position space.

Mathematically, the Langevin and Smoluchowski dynamics are time-continuous Markov diffusion processes on a continuous state space. Under weak conditions both admit a unique stationary (equilibrium) distribution in configuration space which corresponds to the stationary (canonical) ensemble in experiments under constant volume and temperature, respectively.

As mentioned above, the problem of identifying conformations amounts to the identification of metastable sets in configuration space. The characterization of metastability within the canonical ensemble hence requires the mathematical description of the propagation of sub-ensembles. This is accomplished by the *transfer operator approach* [80]; if we define a transition probability from a sub-ensemble C into another sub-ensemble B in time τ, denoted by $p(\tau, C, B)$ then C will be called

metastable on a time slice τ if the fraction of the systems in that sub-ensemble which stays in C after time τ is almost one, i.e. $p(\tau, C, C) \approx 1$ [51]. Finally, the algorithmic strategy to decompose the state space into metastable states is based on spectral properties of the *transfer operator* [24].

Transition State Theory   Since the 1930s transition state theory (TST) and evolutions thereof based on the reactive flux formalism have provided the main theoretical framework for the description of rare events [37, 95, 97, 7, 15]. Originally, TST was derived in the context of analyzing the rate of chemical reactions $R \to P$, where R denotes the reactant and P the product. The idea behind TST is to approximate the reaction rate k by the mean crossing frequency k^{TST} of transitions from R to P through a *transition state*, the dynamical bottleneck for the reaction. Generally, the transition state can be any dividing surface separating the reactant state R from the product state P. Then the TST rate, k^{TST}, is proportional to the total flux of *reactive trajectories*, i.e., trajectories from the reactant to the product side of the dividing surface, and can be expressed in terms of thermodynamical quantities.

The TST rate is always an upper bound of the true reaction rate because reactive trajectories can recross the transition state many times during one reaction. Therefore, the true rate is given by

$$k = \kappa k^{TST},$$

where κ, the *transition coefficient*, is a correcting factor accounting for these recrossings. Due to this overestimation, several strategies have been proposed to improve the TST rate. For example, the earliest one is called *variational* TST [50] and amounts to choose the dividing surface which minimizes the TST rate constant (see also [91, 94]).

Performing the computation in practice, however, may prove very challenging, and this difficulty is related to a deficiency of the theory. TST is based on partitioning the system into two, leaving the reactant state on one side of a dividing surface and the product state on the other, and the theory only tells how this surface is crossed during the reaction. As a result, TST provides very little information about the mechanism of the transition, which has bad consequences e.g. if this mechanism is totally unknown *a priori*. In this case, it is difficult to choose a suitable dividing surface and a bad choice will lead to a very poor estimate of the rate by TST (too many spurious crossings of the surface that do not correspond to actual reactive events). The TST estimate is then extremely difficult to correct. The situation is even worse when the reaction is of diffusive type, since in this case all surfaces are crossed many times during a single reactive event and there is simply no good TST dividing surface that exists.

Transition Path Sampling   How to go beyond TST and describe rare events whose mechanism is unknown *a priori* is an active area of research and several new techniques have been developed to tackle these situations. Most notable among these techniques are the transition path sampling (TPS) technique of Bolhuis, Chandler, Dellago, and Geissler [72, 21] and the action method of Elber [35, 36] which allow to sample directly the ensemble of reactive trajectories, i.e. the trajectories by which the reaction occurs.

1. Introduction

The basic idea behind TPS is a generalization of standard Monte Carlo Markov Chain (MCMC) [39, 56] procedures on the trajectory space of the considered dynamics. Generally, an MCMC procedure performs a biased random walk on the configuration space such that the number of visits of a configuration x is proportional to its probability $p(x)$. In TPS a configuration $X(\mathcal{T}) = (x_0, x_{\Delta t} \ldots, x_{\mathcal{T}})$ is a sequence of states representing a time-discretization of a true dynamical trajectory of fixed length $\mathcal{T}$ rather than individual states of the dynamics itself. The statistical weight $p(X(\mathcal{T}))$ depends on the initial conditions and on the underlying dynamics. Since one is only interested in reactive trajectories connecting A and B, TPS finally performs a random walk on the *transition path ensemble* with respect to the *reactive path probability*

$$p_{AB}(X(\mathcal{T})) = Z_{AB}^{-1}(\mathcal{T})\mathbb{1}_A(x_0)p(X(\mathcal{T}))\mathbb{1}_B(x_{\mathcal{T}}),$$

where Z_{AB} normalizes the distribution of the transition path ensemble and the characteristic $\mathbb{1}_A(x)$ is equal one if $x \in A$ and 0 otherwise ($\mathbb{1}_B(x)$ is defined analogously).

Following [72]:

> *Metaphorically, TPS is akin to "throwing ropes over rough mountains passes, in the dark" where "throwing ropes" stands for shooting trajectories, attempting to reach one metastable state from another and "in the dark" because high-dimensional systems are so complex that it is generally impossible to make any prediction on the relevant energy surfaces.*

We want to emphasize that reactive trajectories in the transition path ensemble are true dynamical trajectories, free of any bias by non-physical forces, constraints or assumptions on the reaction mechanism. The mechanism of the reaction and possibly its rate can then be obtained *a posteriori* by analyzing the ensemble of reactive trajectories. However, these operations are far from trivial. TPS or the action method *per se* do not tell how this analysis must be done and simple inspection of the reactive trajectories may not be sufficient to understand the mechanism of the reaction. This may sound paradoxical at first, but the problem is that the reactive trajectories may be very complicated objects from which it is difficult to extract the quantities of real interest such as the probability density that a reactive trajectory be at a given location in state-space, the probability current of these reactive trajectories, or their rate of appearance. In a way, this difficulty is the same that one would encounter having generated a long trajectory from the law of classical mechanics but ignoring all about statistical mechanics: how to interpret this trajectory would then be unclear. Similarly, the statistical framework to interpret the reactive trajectories is not given by the trajectories themselves, and further analysis beyond TPS or the action method is necessary (for an attempt in this direction, see [52]).

Transition Path Theory Recently, a theoretical framework to describe the statistical properties of the reactive trajectories in the context of Markov diffusion processes has been introduced [34, 92]. This framework, termed transition path theory (TPT), goes beyond standard equilibrium statistical mechanics and accounts for the nontrivial bias that the very definition of the reactive trajectories imply – they must be involved in a reaction.

TPT allows to understand the statistical properties of the ensemble of all reactive trajectories (not only reactive trajectories with respect to a fixed length as in TPS) by giving precise answers to the following questions:

- What is the probability to encounter a reactive trajectory in a given state, i.e. what is the *probability density function of reactive trajectories*?

- What is the net amount of reactive trajectories going through a given state, i.e. what is the *probability current of reactive trajectories*?

- What is the mean frequency of transitions between two sets, say A and B, i.e. what is the *rate of reaction*?

- What are the mechanisms of transitions, i.e. what are the *transition tubes* or *transition pathways*?

The key ingredient in the main objects provided by TPT is the *committor function* $q_{AB}(x) \equiv q(x)$ which is the probability to go rather to the set B than to the set A conditional on the process has started in the state x. The committor function $q(x)$ can be seen as an abstract reaction coordinate, because under appropriate conditions on the dynamics the levels sets of the committor function foliate the state space in sets of equal probability to rather end up in B than A, i.e. it describes the progress of reaction from A to B in terms of probabilities.

For Markov diffusion processes, the committor function satisfies a boundary value problem where the involved partial differential operator is the generator of the diffusion process under consideration. Solving the committor equation numerically in high dimensions is infeasible and, hence, TPT is impractical for the analysis of high dimensional complex processes.

As a remedy to avoid the "curse of dimension" we will follow a two-step procedure. Instead of considering the system in all its degrees of freedom, we will choose appropriate low-dimensional observables which allow to describe the effective dynamics of the system. In the second step the dynamics in these observables is considered on a coarse grained level, e.g. on a discretization of the image space of the observables, and modeled as a Markov jump process. As a result the essential dynamics of the complex system is captured in a discrete transition network (see Figure 1).

For discrete representatives of the sets A and B, discrete TPT [66] allows to analyze the statistical properties of the associated reactive trajectories, i.e. these trajectories by which the walkers transit on the discrete state space from A to B driven by the underlying Markov jump process. Discrete TPT provides discrete analogs of the probability density, the transition rate and the probability current of reaction trajectories. Again, these objects depend on a discrete committor function which satisfies a linear system of equations involving the infinitesimal generator of the considered jump process. Within this discrete setting, then it is easy to compute transition rates and, moreover, to identify transition pathways by utilizing Graph algorithms.

Finally, it is worth to point out that TPT is the theoretical background beyond the string method [30, 31, 32, 33, 75, 60], which is a numerical technique to compute the statistical properties of the reactive trajectories directly (that is, without having to identify these trajectories themselves beforehand as in TPS or the action method) in complicated systems with many degrees of freedom.
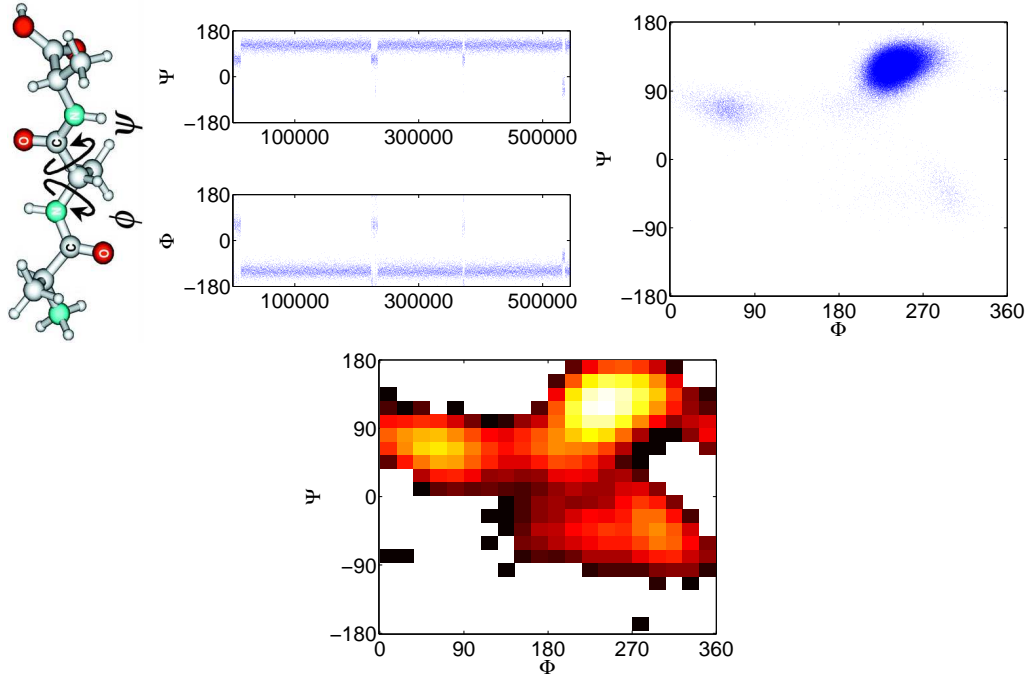
Figure 1.1.: In this figure we exemplify our strategy to capture the essential dynamics of a bio-molecule in a coarse grained model. The top left panel shows the ball-and-stick representation of the trialanine dipeptide analog. Top right: Projection of the time series (all atomic positions) onto the torsion angle space spanned by Φ and Ψ, which reveals the metastable behavior. Bottom left: The Ramachandran plot of the torsion angle time series. At first glance, trialanine attains three different conformations, indicated by the three clusters. Bottom right: The discrete free energy, $-\log \pi$, associated with the stationary distribution π of a Markov jump process which models the effective dynamics of a system in terms of the torsion angles Φ and Ψ. The jump process was estimated from the underlying time series with respect to a 20×20 box discretization of the torsion angle space. The lighter the color of a box the more probable to encounter the process in that box.

1. Introduction

2. Theory: Time-continuous Markov Processes

The purpose of this chapter is to give an introduction to the theoretical framework of time-continuous Markov processes on a continuous and a discrete state space.

2.1. Markov Diffusion Processes

2.1.1. Markov Processes

In this section we give a brief mathematical description of Markov processes. For a detailed introduction see, e.g., [3],[86].

To begin at the beginning, a d-dimensional stochastic process $\{X_t, t \geq 0\}$ is a collection of random variable assuming its values in $\mathbb{R}^d$ (for $d \geq 1$) and the index t is referred to as the *time*. Formally, $\{X_t, t \geq 0\}$ is defined on the probability space $(\Omega, \mathcal{F}, \mathbb{P})$ with $\Omega = \{f : [0, \infty) \to \mathbb{R}^d\}$ is the set of $\mathbb{R}^d$-valued functions defined on the interval $[0, \infty)$, $\mathcal{F}$ is the sigma-algebra generated by the sets $\{f \in \Omega : f(s) \in \mathcal{B}\}, 0 \leq s < \infty, \mathcal{B} \in \mathcal{B}^d$ where $\mathcal{B}^d$ denotes the sigma algebra of Borel sets in $\mathbb{R}^d$, $\mathbb{P}$ is the probability measure defined by the finite-dimensional distributions of the process $\{X_t, t \geq 0\}$ on the space $(\Omega, \mathcal{F})$ and $X_t(\omega) = \omega(t)$ for all $\omega \in \Omega$. A *sample path* (realization, trajectory) $X_t(\omega)$ of the stochastic process is therefore an $\mathbb{R}^d$-valued function defined on the time interval $[0, \infty)$. In the following, we shall denote briefly the process by X_t.

Let $\mathcal{F}_T$ for $T \geq 0$ denote the sigma-algebra which is generated by the sets $\{f \in \Omega : f(s) \in \mathcal{B}\}, 0 \leq s < T, \mathcal{B} \in \mathcal{B}^d$. A stochastic process X_t is called *Markov process* if the so-called *Markov property* is satisfied:

$$\mathbb{P}(X_t \in \mathcal{B}|\mathcal{F}_s) = \mathbb{P}(X_t \in \mathcal{B}|X_s), \quad \forall\, 0 \leq s < t, \forall\, \mathcal{B} \in \mathcal{B}^d. \tag{2.1}$$

A verbal formulation of the Markov property (2.1) is as follows [3]:

> *If the state of the process at a particular time s (the presents) is known, additional information regarding the behavior of the process at $r < s$ (the past) has no effect on our knowledge of the probable development of the process at $t > s$ (in the future).*

A Markov process is called a *homogeneous Markov process* if the right hand side in (2.1) does only depend on the time difference $(t - s)$, i.e.

$$\mathbb{P}(X_{t+h} \in \mathcal{B}|X_t) = \mathbb{P}(X_h \in \mathcal{B}|X_0), \quad \forall\, 0 \leq t, h, \forall\, \mathcal{B} \in \mathcal{B}^d.$$

We write $X_0 \sim v_0$ if the Markov process X_t is initially distributed according to the probability density v_0, i.e. if $\mathbb{P}(X_0 \in \mathcal{B}) = \int_{\mathcal{B}} v_0(x)\mathrm{d}x$ for all $\mathcal{B} \in \mathcal{B}^d$.

2. Theory: Time-continuous Markov Processes

Let X_t be a homogeneous Markov process with initial distribution v_0. The probability $\mathbb{P}(X_t \in \mathcal{B})$ to observe X_t at the time T in the subset $\mathcal{B} \subset \mathcal{B}^d$ of the state space is given by

$$\mathbb{P}(X_t \in \mathcal{B}) = \int_{\mathbb{R}^d} p(t, x, \mathcal{B}) v_0(x) \mathrm{d}x,$$

where the function $p : [0, \infty) \times \mathbb{R}^d \times \mathcal{B}^d \to [0, 1]$ is called *stochastic transition function* and is defined according to

$$p(s, x, \mathcal{B}) \overset{def}{=} \mathbb{P}(X_s \in \mathcal{B} | X_0 = x), \quad s \in [0, \infty), x \in \mathbb{R}^d, \mathcal{B} \in \mathcal{B}^d. \tag{2.2}$$

The function $p : [0, \infty) \times \mathbb{R}^d \times \mathcal{B}^d \to [0, 1]$ has the following properties

1. $x \mapsto p(s, x, \mathcal{B})$ is measurable for fixed $s \in [0, \infty)$ and fixed $\mathcal{B} \in \mathcal{B}^d$.

2. $\mathcal{B} \mapsto p(s, x, \mathcal{B})$ is a probability measure for fixed $s \in [0, \infty)$ and fixed $x \in \mathbb{R}^d$.

3. $p(0, x, \mathbb{R}^d \setminus \{x\}) = 0$ for all $x \in \mathbb{R}^d$.

4. the *Chapman-Kolmogorov* equation

$$p(t + s, x, \mathcal{B}) = \int_{\mathbb{R}^d} p(t, x, \mathrm{d}z) p(s, z, \mathcal{B}) \tag{2.3}$$

holds for all $t, s \in [0, \infty), x \in \mathbb{R}^d$ and $\mathcal{B} \in \mathcal{B}^d$.

We say that the Markov process X_t admits an *invariant probability measure* μ, if

$$\int_{\mathbb{R}^d} p(t, x, \mathcal{B}) \mu(\mathrm{d}x) = \mu(\mathcal{B}) \quad \forall\, t \in [0, \infty), \quad \forall\, \mathcal{B} \in \mathcal{B}^d. \tag{2.4}$$

In many applications, it is important to guarantee that the Markov property (2.1) even holds if the fixed time s is replaced by a stopping time. A random variable $\nu : \Omega \to \mathbb{R}^+ \cup \{0\}$ is said to be a *stopping time* with respect to the Markov process X_t if

$$\{\nu \leq t\} = \{\omega \in \Omega : \nu(w) \leq t\} \in \mathcal{F}_t, \quad \forall t \geq 0.$$

In words, it should be possible to decide whether or not $\nu \leq t$ has occurred on the basis of the knowledge of the process up to the time t. A time-homogeneous Markov process X_t has the *strong Markov* property with respect to a stopping time ν if,

$$\mathbb{P}(X_{\nu+h} \in \mathcal{B} | X_\nu) = \mathbb{P}(X_h \in \mathcal{B} | X_0), \quad \forall t, h \leq 0, \quad \forall\, \mathcal{B} \in \mathcal{B}^d. \tag{2.5}$$

2.1.2. The Infinitesimal Operator

To every homogeneous Markov process X_t one can assign a *semigroup of Markov operators* $\{T_t, t \geq 0\}$, defined for any suitable function $u : \mathbb{R}^d \to \mathbb{R}$ by

$$T_t u(x) \overset{def}{=} \mathbb{E}_x[u(X_t)] = \int_{\mathbb{R}^d} u(y) p(t, x, \mathrm{d}y), \tag{2.6}$$

where $\mathbb{E}_x[u(X_t)]$ denotes the expectation of the observable u at time t conditional on $X_0 = x$. Moreover, the operator T_0 is the identity operator and the semigroup property, that is,

$$T_{s+t} = T_s T_t = T_t T_s, \quad \forall t, s \in [0, \infty)$$

follows from the Chapman-Kolmogorov equation (2.3). The *generator* $\mathcal{L}_{bw}$ of a homogeneous Markov process X_t is defined by an operator representing the derivative of the family $\{T_t, t \geq 0\}$ at the point $t = 0$,

$$\mathcal{L}_{bw} u(x) \stackrel{def}{=} \lim_{t \downarrow 0} \frac{T_t u(x) - u(x)}{t}. \tag{2.7}$$

The domain $D_{\mathcal{L}_{bw}}$ of definition of the operator $\mathcal{L}_{bw}$ is a subset of the space of bounded measurable scalar functions defined on $\mathbb{R}^d$ and consists of all functions for which the limit in (2.7) exists. The quantity $\mathcal{L}_{bw} u(x)$ is interpreted as the *mean infinitesimal rate of change* of $u(X_0)$ in case $X_0 = x$.

2.1.3. Diffusion Processes

Diffusion processes are special cases of Markov processes with continuous sample functions. There are basically two different approaches to the class of diffusion processes. On the one hand, one can define them in terms of the conditions on the stochastic transition function introduced above. On the other hand, one can study the state X_t itself and its variation with respect to time. This leads to a *stochastic differential equation*. That is what we shall do in the present section. A detailed introduction to stochastic differential equation can be found in, e.g., [70, 40].

In what follows, we restrict ourselves to *time-homogeneous Markov diffusion processes* X_t which are solutions or (or which are generated by) the stochastic differential equation (SDE) of the form

$$\mathrm{d}X_t = b(X_t)\mathrm{d}t + \sigma(X_t)\mathrm{d}W_t, \tag{2.8}$$

where $X_t \in \mathbb{R}^d$ and $W_t = (W_t^1, \ldots, W_t^d)$ is a d-dimensional standard Wiener process (see definition A.6.1 in the Appendix). The real vector field $b : \mathbb{R}^d \to \mathbb{R}^d$ is called the *drift field* or *mean velocity field* of the diffusion. The real symmetric matrix $a(x) = (a_{ij}(x)) \in \mathbb{R}^{d \times d}$, defined for all $x \in \mathbb{R}^d$ via the real matrix $\sigma(x) \in \mathbb{R}^{d \times d}$ according to

$$a(x) \stackrel{def}{=} \frac{1}{2}\sigma(x)\sigma(x)^T \tag{2.9}$$

is called the *diffusion matrix*. Here $\sigma^T(x)$ denotes the transposed matrix of the real matrix $\sigma(x)$.

Assumption 2.1.1. *Henceforth, we make the following additional assumptions on the coefficients of the SDE (2.8):*

- *The diffusion matrix $a(x)$ is for all $x \in \mathbb{R}^d$ **non-negative definite**, i.e.,*

$$\sum_{i,j=1}^{d} a_{ij}(x)\xi_i\xi_j \geq 0, \quad \forall \xi \in \mathbb{R}^d. \tag{2.10}$$

- *The drift field $b(x)$ and the diffusion matrix $a(x)$ are such that there exists an **unique solution** of (2.8). (See Theorem (A.6.1) in Appendix).*

2. Theory: Time-continuous Markov Processes

- *The drift field $b(x)$ and the diffusion matrix $a(x)$ are such that the diffusion process X_t is **ergodic** with respect to a unique invariant probability measure $d\mu(x) = \rho(x)\,dx$, i.e.,*

$$\lim_{T\to\infty} \frac{1}{T}\int_0^T f(X_s)\,ds = \int_{\mathbb{R}^d} f(y)\rho(y)\,dy \qquad (2.11)$$

for all $f \in L^1(\mathbb{R}^d)$.

2.1.4. Reversed-time Diffusion Process

Let $\{X_t, 0 \le t \le T\}$, $T > 0$ be a Markov diffusion process, satisfying the SDE

$$\mathrm{d}X_t = b(X_t)\mathrm{d}t + \sigma(x)\mathrm{d}W_t, \quad 0 \le t \le T$$

and denote by $v(t,x)$ the probability density of the law of X_t at time t, i.e.,

$$\mathbb{P}[X_t \in C] = \int_C v(t,y)\mathrm{d}y, \quad \forall C \in \mathcal{B}^d.$$

A Markov process remains a Markov process under time reversal, i.e., the reversed-time process $\{X_t^R, 0 \le t \le T\}$ according to

$$X_t^R \overset{def}{=} X_{T-t}$$

is again a Markov process, but in general the diffusion property is not preserved. Under mild conditions on the drift field $b(x)$, the matrix $\sigma(x)$ and the probability density $v_0(x)$ of the law of X_0, it is proven in [47] that the reversed-time process X_t^R is again a Markov diffusion process. In particular, it is shown that X_t^R satisfies a SDE

$$\mathrm{d}X_t^R = b^R(t, X_t^R)\mathrm{d}t + \sigma(X_t^R)\mathrm{d}W_t \qquad (2.12)$$

where the time-dependent *reversed drift field* $b^R(t,x) : \mathbb{R}^{d+1} \to \mathbb{R}^d$ is given by

$$b^R(t,x) = -b(x) + \frac{2}{v(T-t,x)}div\big(a(x)v(T-t,x)\big). \qquad (2.13)$$

If the diffusion process $\{X_t, 0 \le t \le \infty\}$ admits an invariant probability measure μ, induced by the probability density $\rho(x)$, then (2.13) reduces to

$$b^R(x) = -b(x) + \frac{2}{\rho(x)}div\big(a(x)\rho(x)\big) \qquad (2.14)$$

and $\mathrm{d}\mu(x) = \rho(x)\mathrm{d}x$ is the invariant probability measure of the reversed process too. If the diffusion process X_t is such that

$$b \equiv b^R$$

then the original process X_t and the reversed process X_t^R are statistically indistinguishable and the process X_t is called *reversible*.

2.1.5. Backward and Forward Equations

For a Markov diffusion process X_t of the form (2.8), the infinitesimal operator $\mathcal{L}_{bw}$ is a *linear second order partial differential operator* whose coefficients are determined by the drift field $b(x)$ and the diffusion matrix $a(x)$,

$$\mathcal{L}_{bw}u = \sum_{i,j=1}^{d} a_{ij} \frac{\partial^2 u}{\partial x_i \partial x_j} + \sum_{i=1}^{d} b_i \frac{\partial u}{\partial x_i} \tag{2.15}$$

acting formally on the space of twice partially differentiable functions $u : \mathbb{R}^d \to \mathbb{R}$. The first double sum in (2.15) is called the *principle part* of the differential operator.

Next, we establish the relation between the semigroup $\{T_t, 0 \leq t < \infty\}$ and the partial differential operator $\mathcal{L}_{bw}$.

Theorem 2.1.1. *([3], page 42-43) Let $g : \mathbb{R}^d \to \mathbb{R}$ denote a continuous bounded scalar function such that the function $u : [0, \infty) \times \mathbb{R}^d \to \mathbb{R}$ according to*

$$u(t,x) \stackrel{def}{=} \mathbb{E}_x \left[g(X_t) \right]$$

is continuous and bounded, as are its derivatives $\partial u / \partial x_i$ and $\partial^2 u / \partial x_i \partial x_j$. Then $u(t,x)$ satisfies the Kolmogorov's backward equation

$$\begin{cases} \dfrac{\partial u}{\partial t} & = \mathcal{L}_{bw} u \quad in \ (0,\infty) \times \mathbb{R}^d \\ u(0,\cdot) & = g \qquad on \ \mathbb{R}^d. \end{cases} \tag{2.16}$$

Loosely spoken, the backward equation describes the evolution of conditional expectations of observables with respect to X_t. The evolution of the probability density of the law of a diffusion process X_t is governed by the *Kolmogorov's forward equation*, also known as *Fokker-Planck equation*.

Theorem 2.1.2. *([57], page 360) If the functions σ_{ij}, $\partial\sigma_{ij}/\partial x_k$, $\partial^2 \sigma_{ij}/\partial x_k \partial x_l$, b_i, $\partial b_i/\partial x_j$, $\partial v/\partial t$, $\partial v/\partial x_i$, and $\partial^2 v/\partial x_i \partial x_j$ are continuous for $t > 0$ and $x \in \mathbb{R}^d$, and if b_i, σ_{ij} and their first derivatives are bounded, then $v(t,x)$ satisfies the equation*

$$\begin{cases} \dfrac{\partial v}{\partial t} & = \mathcal{L}_{fw} v \quad in \ (0,\infty) \times \mathbb{R}^d \\ v(0,\cdot) & = v_0 \qquad on \ \mathbb{R}^d, \end{cases} \tag{2.17}$$

where $X_0 \sim v_0$ and the operator $\mathcal{L}_{fw}$ is a linear second order partial differential operator, defined according to

$$\begin{aligned} \mathcal{L}_{fw}v &\stackrel{def}{=} \sum_{i,j=1}^{d} \frac{\partial^2 (a_{ij}v)}{\partial x_i \partial x_j} - \sum_{i=1}^{d} \frac{\partial (b_i v)}{\partial x_i} \\ &= \sum_{i=1}^{d} \frac{\partial}{\partial x_i} \left[\sum_{j=1}^{d} \frac{\partial (a_{ij}v)}{\partial x_j} - b_i v \right]. \end{aligned} \tag{2.18}$$

Notice, that the probability density function ρ of the invariant measure μ is the steady state solution of the Fokker-Plank equation (2.17), i.e.,

$$\mathcal{L}_{fw}\rho(x) = 0, \quad \forall x \in \mathbb{R}^d.$$

Remark 2.1.2. *The generator of a Markov diffusion process plays a key role in Transition Path Theory. For the sake of a compact presentation, we introduce a compact notation for differential operations on functions. Let $u : \mathbb{R}^d \to \mathbb{R}$ then the* **Nabla***-operator ∇ is defined as*

$$\nabla u = (\frac{\partial u}{\partial x_1}, \ldots, \frac{\partial u}{\partial x_d})$$

and the **Laplace***-operator Δ is given by*

$$\Delta u = \sum_{i=1}^{d} \frac{\partial^2 u}{\partial^2 x_i}.$$

Moreover, we abbreviate the **divergence** *of a vector field $b : \mathbb{R}^d \mapsto \mathbb{R}^d$ by*

$$\nabla \cdot b \stackrel{def}{=} div(b) = \sum_{i=1}^{d} \frac{\partial b_i}{\partial x_i}.$$

The divergence $\nabla \cdot a$ of a matrix $a(x) = (a(x)_{ij}) \in \mathbb{R}^{d \times d}$ is a vector field whose i^{th} component is defined by

$$(\nabla \cdot a)_i \stackrel{def}{=} \sum_{j=1}^{d} \frac{\partial a_{ij}}{\partial x_j}, \quad i = 1, \ldots, d.$$

Henceforth, we will write the generator (2.15) of a diffusion process as

$$\mathcal{L}_{bw} u = a : \nabla\nabla u + b \cdot \nabla u, \tag{2.19}$$

where we additionally abbreviate the principle part of $\mathcal{L}_{bw}$ by

$$a : \nabla\nabla u \stackrel{def}{=} \sum_{i,j=1}^{d} a_{ij} \frac{\partial^2 u}{\partial x_i \partial x_j}$$

and $b \cdot \nabla u$ denotes the scalar product between the vector field $b(x)$ and the gradient $\nabla u(x)$. In the introduced notation, the operator $\mathcal{L}_{fw}$, defined in (2.18), takes the form

$$\mathcal{L}_{fw} v = \nabla \cdot [\nabla \cdot (av) - bv],$$

where the vector field

$$J(x) \stackrel{def}{=} - \left[\nabla \cdot \big(a(x)v(x) \big) - b(x)v(x) \right] \tag{2.20}$$

is referred to as (probability) current.

2.1.6. Partial Differential Operators

In this work we are mainly concerned with two types of linear second order partial differential operators (PDEs): the *elliptic* and the *degenerate elliptic* type.

Consider the general linear second order partial differential operator

$$Gu = a : \nabla\nabla u + b \cdot \nabla u + cu \tag{2.21}$$

with real coefficients $a_{ij}(x), b_i(x), c(x)$ defined on a domain (open and connected) $\Omega \subset \mathbb{R}^d$. Because the Hesse matrix of a function $u \in C^2(\mathbb{R}^d)$ is symmetric, we may assume without loss of generality that the matrix $a(x) = (a_{ij}(x))$ is symmetric. Second-order PDEs are classified according the behavior of a quadratic form which is associated with their principle parts.

Definition 2.1.3. *The operator G is said to be of **elliptic** type (or elliptic) at a point $x_0 \in \Omega$ if the matrix $a(x_0)$ is positive definite, i.e.,*

$$\sum_{i,j=1}^{d} a_{ij}(x_0)\xi_i\xi_j > 0, \quad \forall \, \xi \in \mathbb{R}^d : \xi \neq 0. \tag{2.22}$$

The operator G is called elliptic in Ω if the matrix $a(x)$ is positive definite for all $x \in \Omega$. If there exists a positive constant $\theta > 0$ such that

$$\sum_{i,j=1}^{d} a_{ij}(x)\xi_i\xi_j \geq \theta \, \|\xi\|^2$$

*for all $x \in \Omega, \xi \in \mathbb{R}^d$, then we say that G is **uniformly elliptic** in Ω. If the matrix $a(x)$ is nonnegative definite, i.e.,*

$$\sum_{i,j=1}^{d} a_{ij}(x)\xi_i\xi_j \geq 0 \tag{2.23}$$

*for all $x \in \Omega, \xi \in \mathbb{R}^d$ then G is called **degenerate elliptic** [90].*

Remark 2.1.4. *Notice that besides the elliptic operators, the class of degenerate elliptic operators includes operators of parabolic types, first order equations, ultra-parabolic equations, and others. In the literature, a degenerate elliptic operator is also called semi-elliptic [70] or of nonnegative characteristic form [71].*

2.1.7. Relation between $\mathcal{L}_{bw}$ and $\mathcal{L}_{fw}$

In the language of the theory of partial differential equations, the operator $\mathcal{L}_{fw}$ (2.18) is the formal L^2-*adjoint* of the operator $\mathcal{L}_{bw}$ (2.15), i.e.,

$$\int_{\mathbb{R}^d} v\mathcal{L}_{bw}u \, \mathrm{d}x = \int_{\mathbb{R}^d} u\mathcal{L}_{fw}v \, \mathrm{d}x, \quad \forall u, v \in L^2(\mathbb{R}^d), \tag{2.24}$$

where $L^2(\mathbb{R}^d) = \{v : \mathbb{R}^d \to \mathbb{R} : \int_{\mathbb{R}^d} |v(x)|^2 \mathrm{d}x < \infty\}$. The operator $\mathcal{L}_{bw}$ is called *self-adjoint* if $\mathcal{L}_{bw} \equiv \mathcal{L}_{fw}$. If the domain of integration in (2.24) is restricted to a bounded domain $\Omega \subset \mathbb{R}^d$ with a sufficiently smooth boundary $\partial\Omega$ then by virtue of Green's theorem the identity (2.24) takes the form

$$\int_{\Omega} v\mathcal{L}_{bw}u \, \mathrm{d}x = \int_{\Omega} u\mathcal{L}_{fw}v \, \mathrm{d}x + \int_{\partial\Omega} R \cdot \hat{n} \, \mathrm{d}\sigma_{\partial\Omega}(x), \tag{2.25}$$

where $\hat{n}$ is the unit normal to the boundary $\partial\Omega$ pointing outward Ω, $\mathrm{d}\sigma_{\partial\Omega}$ is the surface element on $\partial\Omega$ and the real vector field $R : \mathbb{R}^d \to \mathbb{R}^d$ (the *concomitant* of $\mathcal{L}_{bw}$ [79]) is given by

$$R = va\nabla u - ua\nabla v + uv[b - \nabla \cdot a]. \tag{2.26}$$

The identity (2.25) will be useful to define adjoint boundary conditions in Section 2.1.9.

2.1.8. Stochastic Representation of Solutions of Boundary Value Problems

Theorem 2.1.1 states that for any suitable function g the function

$$u(t, x) = \mathbb{E}_x\left[g(X_t)\right]$$

satisfies the initial value problem

$$\begin{cases} \dfrac{\partial u}{\partial t} - \mathcal{L}_{bw}u = 0 & \text{in } (0, \infty) \times \Omega \\ u(0, \cdot) = g & \text{on } \Omega \end{cases} \tag{2.27}$$

where $\mathcal{L}_{bw}$ is the generator of the considered diffusion process X_t. In other words, the solution of (2.27) can be expressed in terms of the Markov diffusion process X_t associated with the generator $\mathcal{L}_{bw}$. Therefore, it is natural to ask the following question: Given a degenerate elliptic differential operator acting on $C^2(\mathbb{R}^d)$ of the form

$$Gu = a : \nabla\nabla u + b \cdot \nabla u,$$

and let $\Omega \subset \mathbb{R}^d$ be a domain (open and connected). Under what conditions on the coefficients $a(x), b(x)$ there exists a Markov diffusion process X_t such that the solution $u \in C^2(\Omega) \cap C(\overline{\Omega})$ of the *Dirichlet-Poisson problem* for given functions $f \in C(\Omega)$ and $g \in C(\partial\Omega)$,

$$\begin{cases} Gu = f & \text{in } \Omega \\ u = g & \text{on } \partial\Omega \end{cases} \tag{2.28}$$

can be expressed in terms of the Markov diffusion process X_t?

The idea of solution is to find a diffusion process X_t such that its generator $\mathcal{L}_{bw}$ coincides with G on $C^2(\mathbb{R}^d)$. This is formally achieved by setting

$$\mathrm{d}X_t = b(X_t)\mathrm{d}t + \sigma(X_t)\mathrm{d}W_t, \tag{2.29}$$

where $\sigma(x) \in \mathbb{R}^{d \times d}$ is chosen such that

$$\tfrac{1}{2}\sigma(x)\sigma(x)^T = a(x).$$

In order to guarantee that (2.29) admits a unique solution, we assume that the conditions on $b(x)$ and $a(x)$ in Theorem A.6.1 are satisfied. In particular, conditions which guarantee the Lipschitz-continuity of the square root of $a(x)$ are given in [40], Theorem 1.2, page 129.

The proof of the following uniqueness result is found in [70], page 168-169.

Theorem 2.1.3. *Suppose the function $g \in C(\partial\Omega)$ is bounded and the function $f \in C(\Omega)$ satisfies*

$$\mathbb{E}_x\left[\int_0^{\tau_\Omega} |f(X_s)|ds\right] < \infty, \quad \forall\, x \in \Omega,$$

where $\tau_\Omega = \inf\{t : X_t \in \partial\Omega\}$ is the first exit time from Ω. Suppose further that

$$\tau_\Omega < \infty, \quad a.s.\ \forall x \in \Omega.$$

Then if $u \in C^2(\Omega) \cap C(\overline{\Omega})$ is a solution of the Dirichlet-Poisson problem (2.28) we have

$$u(x) = \mathbb{E}_x\left[g(X_{\tau_\Omega})\right] - \mathbb{E}_x\left[\int_0^{\tau_\Omega} f(X_s)ds\right]. \tag{2.30}$$

Next we address the question of existence of a solution of the Dirichlet-Poisson problem in (2.28). Under the assumption that the operator G is uniformly elliptic in Ω, the following Theorem holds:

Theorem 2.1.4 ([40], page 144). *Let the conditions*

- *$(a_{ij}), b_i$ is uniformly Lipschitz-continuous in $\overline{\Omega}$*

- *f is uniformly Hölder continuous in $\overline{\Omega}$*

- *g is continuous on $\partial\Omega$*

- *$\partial\Omega \in C^2$*

Then (2.30) is the unique classical solution of the Dirichlet-Poisson problem in (2.28).

Unfortunately, it turned out that the existence problem for the case where G is degenerate elliptic, but not elliptic is a difficult question. Up to our knowledge there is no result which provides conditions under which a classical solution of (2.28) exists. For results on the existence of weak solutions of (2.28) we refer the interested reader to [71, 88].

2.1.9. Adjoint Boundary Condition

To motivate the concept of *adjoint boundary condition*, suppose we are interested in the invariant probability distribution of a Markov diffusion process *restricted* on a domain $\Omega \subset \mathbb{R}^d$. We mean by "restricted" that we require that the process must not escape the domain. As pointed out in Section 2.1.5, the probability density function $\rho(x)$ of the invariant probability distribution is the steady state solution of the Kolmogorov forward equation (2.17), hence we are interested in the solution of the equation

$$\mathcal{L}_{fw}v = 0 \quad \text{in } \Omega.$$

In order to reflect that the process must not escape the domain Ω, we have to impose additional conditions on the probability density function $v(x)$ on the boundary $\partial\Omega$. The natural choice is to require that the probability current (2.20) is tangential to the boundary which leads to the boundary conditions

$$BC(v) = (\nabla \cdot (av) - bv) \cdot \hat{n} = 0 \quad \text{on } \partial\Omega, \tag{2.31}$$

where $\hat{n}$ is the unit normal to $\partial\Omega$ pointing outward Ω. The adjoint boundary conditions $BC^*(u) = 0$ are chosen such that both operator $\mathcal{L}_{fw}$ and $\mathcal{L}_{bw}$ are adjoint *in* the domain Ω, i.e.,

$$\int_\Omega v\mathcal{L}_{bw}u\mathrm{d}x = \int_\Omega u\mathcal{L}_{fw}v\mathrm{d}x.$$

Recalling the integral identity (2.25), the adjoint boundary conditions $BC^*(u) = 0$ are formally defined [28] as a minimal set of homogeneous conditions on u such that

$$BC(v) = BC^*(u) = 0 \text{ on } \partial\Omega \implies R \cdot \hat{n} = 0 \text{ on } \partial\Omega.$$

A short calculation shows that the adjoint boundary conditions of the boundary conditions (2.31) take the form

$$BC^*(u) = a\nabla u \cdot \hat{n} = 0 \quad \text{on } \partial\Omega. \tag{2.32}$$

Notice that in the case $a = I = \mathrm{diag}(1, \ldots, 1) \in \mathbb{R}^{d\times d}$ the conditions (2.32) reduce to the Neumann-conditions.

2.1.10. Langevin and Smoluchowski Dynamics

In this work, we are mainly concerned with two classes of time-homogeneous Markov diffusion processes which arise from the stochastic modeling of the dynamics of particles in a potential landscape. Both dynamics incorporate a physical temperature and friction.

Langevin Dynamics

The first class of time-homogeneous diffusion process, we are interested in, is generated by the famous Langevin equation which is componentwise given in its traditional form by [76]

$$
\begin{aligned}
\dot{x}_i(t) &= m_i^{-1}p_i(t), \\
\dot{p}_i(t) &= -\frac{\partial V(x(t))}{\partial x_i} - \gamma_i m_i^{-1}p_i(t) + \sqrt{2\gamma_i\beta^{-1}}\zeta_i(t)
\end{aligned}
\tag{2.33}
$$

where $x = (x_1, \ldots, x_d)$ is the position of the particles, $p = (p_1, \ldots, p_d)$ is the momentum of the particles, $m_i > 0$ is the mass of x_i, the function $V(x)$ is the potential, $\gamma_i > 0$ is the friction coefficient on x_i and $\zeta_i(t)$ is a white noise (see Definition A.6.1 in Appendix). The inverse temperature $\beta > 0$ is related to the physical temperature T by $\beta = 1/k_B T$ where k_B is the Boltzmann-constant. A system governed by the Langevin dynamics can be regarded as a mechanical system with additional noise and dissipation (friction). The noise can be thought of modeling the influence of a heat bath surrounding the molecule and the dissipation is chosen such as to counterbalance the energy fluctuations due to the noise.

The Langevin dynamics (2.33) is ergodic with respect to the *equilibrium measure* (invariant probability measure)

$$\mathrm{d}\mu((x, p)) = Z^{-1}e^{-\beta H(x,p)}\mathrm{d}x\mathrm{d}p, \tag{2.34}$$

where the *Hamiltonian* $H(x,p)$ is defined as

$$H(x,p) = V(x) + \frac{1}{2}p^T M^{-1} p, \quad M^{-1} = \mathrm{diag}(m_1^{-1}, \ldots, m_d^{-1})$$

and $Z = \int_{\mathbb{R}^d \times \mathbb{R}^d} e^{-\beta H(x,p)}\, \mathrm{d}x \mathrm{d}p$ is the normalization constant. Notice that (2.33) can be put in the form of (2.8) by setting

$$b(x,p) = (M^{-1}p, -\nabla V(x) - \Gamma M^{-1}p)^T \ \in \mathbb{R}^{2d},$$

$$\sigma = \sqrt{2\beta^{-1}} \begin{pmatrix} 0 & 0 \\ 0 & \Gamma^{\frac{1}{2}} \end{pmatrix} \in \mathbb{R}^{2d \times 2d},$$

where $\Gamma^{\frac{1}{2}} = \mathrm{diag}(\sqrt{\gamma_1}, \ldots, \sqrt{\gamma_d})$.

According to (2.19), the generator of the Langevin dynamics (2.33) takes the form

$$\begin{aligned}
\mathfrak{L}_{bw}u =& \beta^{-1}\Gamma : \nabla_p \nabla_p u + M^{-1}p \cdot \nabla_x u \\
& - \nabla_x V \cdot \nabla_p u - \Gamma M^{-1}p \cdot \nabla_p u,
\end{aligned} \tag{2.35}$$

where ∇_x and ∇_p act only on the positions and momenta, respectively.

Remark 2.1.5. *Notice that the diffusion matrix of the Langevin dynamics*

$$a = \beta^{-1} \begin{pmatrix} 0 & 0 \\ 0 & \Gamma \end{pmatrix} \in \mathbb{R}^{2d \times 2d}$$

*is not positive definite but **nonnegative definite**. Hence the operator $\mathfrak{L}_{bw}$ is not elliptic but **degenerate elliptic**. In the literature, e.g. in [74], the Langevin process is also called a **hypoelliptic** diffusion process (see definition A.6.2 in Appendix)*

Next, we turn our attention to the reversed time Langevin dynamics. Recalling the relation (2.14) between the drift fields of a diffusion process and its reversed time process, the reversed drift field of the reversed time Langevin dynamics is given by

$$b^R((x,p)) = (-M^{-1}p, \nabla V(x) - \Gamma M^{-1}p)^T$$

and the generator of the reverse-time Langevin dynamics takes the form

$$\begin{aligned}
\mathfrak{L}_{bw}^R u =& \beta^{-1}\Gamma : \nabla_p \nabla_p u - M^{-1}p \cdot \nabla_x u \\
& + \nabla_x V \cdot \nabla_p u - \Gamma M^{-1}p \cdot \nabla_p u.
\end{aligned} \tag{2.36}$$

Since $b(x,p) \neq b^R(x,p)$, the Langevin dynamics is a *non-reversible* diffusion process on the phase space (x,p).

Smoluchowski Dynamics

A second important class of time-homogeneous diffusion processes is generated by the *overdamped Langevin* or *Smoluchowski* dynamics which arises in the high friction limit of the Langevin equation (2.33),

$$\dot{x}_i(t) = -\gamma_i^{-1}\frac{\partial V(x)}{\partial x_i} + \sqrt{2\gamma_i^{-1}\beta^{-1}}\zeta_i, \tag{2.37}$$

where $x = (x_1, \ldots, x_d)$ denotes the position of the particles and the other quantities are as in (2.33). For a sketch of the derivation of the Smoluchowski dynamics see [51]. The Smoluchowski dynamics (2.37) is ergodic with respect to the invariant measure $\mathrm{d}\mu(x) = \rho(x)\mathrm{d}x$, induced by the equilibrium probability density function

$$\rho(x) = Z^{-1}e^{-\beta V(x)}, \tag{2.38}$$

where $Z = \int_{\mathbb{R}^d} e^{-\beta V(x)}\mathrm{d}x$ is the normalization constant. In contrast to the Langevin dynamics, (2.37) defines a *reversible* diffusion process on the position space and the generator is given by the *elliptic* operator

$$\mathcal{L}_{bw}u = \beta^{-1}\Gamma^{-1} : \nabla\nabla u - \Gamma^{-1}\nabla V \cdot \nabla u, \tag{2.39}$$

where $\Gamma^{-1} = \mathrm{diag}(\gamma_1^{-1}, \ldots, \gamma_d^{-1})$.

2.2. Markov Jump Processes

In this section we will introduce time-continuous Markov processes on a *discrete* state space and will provide the basic facts about this class of processes which will be relevant for the derivation of discrete transition path theory. For further readings, see e.g. [86, 13, 69].

Let $\{X(t), t \geq 0\}$ be an S-valued stochastic process on a probability space $(\Omega, \mathcal{F}, \mathbb{P})$, with a discrete (countable) state space S and a continuous (time) parameter $0 \leq t < \infty$. We will denote by $\{X(t)\}_{t \in \mathbb{R}}$ an equilibrium sample path (or trajectory) of the Markov process, i.e. any path obtained from $\{X(t)\}_{t \in [T, \infty)}$ by pushing back the initial condition, $X(T) = x$, at $T = -\infty$.

A continuous-time stochastic process $\{X(t), t \geq 0\}$ with discrete state space S is called a *Markov process* if for any $t_{k+1} > t_k > \cdots > t_0 \geq 0$ and any $j, i_1, \cdots, i_k \in S$

$$\mathbb{P}(X(t_{k+1}) = j | X(t_k) = i_k, \cdots, X(t_1) = i_1) = \mathbb{P}(X(t_{k+1}) = j | X(t_k) = i_k) \tag{2.40}$$

holds. A continuous-time Markov process is called *homogeneous* if the right hand side of (2.40) only depends on the time increment $\tau_k = t_{k+1} - t_k$. The probability distribution μ_0 satisfying

$$\mu_0(i) = \mathbb{P}(X(0) = i), \quad \forall i \in S$$

is called the initial distribution. In the following we will focus on homogeneous continuous-time Markov processes on a *finite* state space $S \cong \{1, \ldots, d\}$ and we will denote that class of processes by *Markov jump processes*.

For a fixed time t, the transition probabilities

$$p_{ij}(t) = \mathbb{P}(X(t) = j | X(0) = i)$$

define a transition matrix $P(t) = (p_{ij}(t))_{i,j \in S}$ where $p_{ij}(0) = \delta_{ij}$ and $\delta_{ij} = 1$, if $i = j$ and zero otherwise. By definition, $P(t)$ is a stochastic matrix, i.e,

$$p_{ij}(t) \geq 0 \text{ and } \sum_{k \in S} p_{ik}(t) = 1, \quad \forall i, j \in S, \forall t \geq 0. \tag{2.41}$$

Throughout this thesis, we assume that the transition probabilities are continuous at $t = 0$, i.e.

$$\lim_{t \downarrow 0} p(t, i, j) = \delta_{ij}, \quad \forall i, j \in S. \tag{2.42}$$

which guarantees, that a trajectory of $\{X(t), t \geq 0\}$ is a right continuous function with left limits (*càdlàg*).

The family of transition matrices $\{P(t), t \geq 0\}$ is called the transition semigroup of the Markov jump process which is justified by the fact that $\{P(t), t \geq 0\}$ obeys the *Chapman-Kolmogorov equation*

$$P(t + s) = P(t)P(s), \ s, t \geq 0.$$

with $P(0) = I$ where $I = \text{diag}(1, \ldots, 1) \in \mathbb{R}^{d \times d}$ is the identity matrix.

Furthermore, a local characterization of the transition semigroup of a Markov jump process can be obtained by considering the infinitesimal changes of the transition probabilities. Under the assumption made in (2.42), one can show that the right-sided limit [13]

$$L = \lim_{t \to 0+} \frac{P(t) - I}{t}$$

exists (entrywise). The matrix $L = (l_{ij})_{i,j \in S}$ is referred to as the *infinitesimal generator* of the transition semigroup $\{P(t), t \geq 0\}$ because L 'generates' the transition semigroup via the relation

$$P(t) = \exp(tL) = \sum_{n=0}^{\infty} \frac{t^n}{n!} L^n.$$

Due to the finite state space S, the matrix L has a special structure, namely,

$$0 \leq l_{ij} < \infty \text{ and } \sum_{k \in S} l_{ik} = 0 \quad \forall i, j \in S, i \neq j. \tag{2.43}$$

where an entry $l_{ij}, \ i \neq j$ is interpreted as a transition rate: the average number of transitions from state i to state j per time unit. The diagonal entries of L, given by

$$l_{ii} = -\sum_{k \neq i} l_{ik}, \quad \forall i \in S,$$

are called the escape rates of the states.

The Markov property (2.40) of a Markov jump process even holds for a certain class of random times, the so-called *stopping times*. A real, non-negative random variable ν is called a stopping time with respect to the process $\{X(t), t \geq 0\}$ if for all $t \geq 0$, the event $\{\nu \leq t\}$ is expressible in terms of $(X(s), s \in [0, t])$, i.e. it should be possible to decide whether or not $\nu \leq t$ has occurred on the basis of the knowledge of the process up to the time t.

Now let $\{X(t), t \geq 0\}$ be a Markov jump process with generator L, ν a stopping time with respect to $\{X(t), t \geq 0\}$ and $i \in S$ an arbitrary state. Then, given that $X(\nu) = i$,

the process after ν and the process before ν are independent, and

the process after ν is a Markov jump process with generator L. $\tag{2.44}$

2. Theory: Time-continuous Markov Processes

The property (2.44) is called the *strong Markov* property.

Analogously to the case of a continuous state space, the evolution of conditional expectations of observables is governed by the infinitesimal generator. To be more precise, let $f : S \mapsto \mathbb{R}$ be an observable. Then the time derivative of the conditional expectations $u(i,t) = \mathbb{E}[f(X(t))|X(0) = i]$, $i \in S$ satisfies the backward Kolmogorov equations

$$\frac{d}{dt}u(i,t) = \sum_{j \in S} l_{ij} u(j,t), \quad u(i,0) = f(i) \quad \forall i \in S, \ t \geq 0 \tag{2.45}$$

or, in matrix-vector notation

$$\frac{du}{dt} = Lu, \quad u(0) = f \quad , t \geq 0.$$

Similarly, let $\mu(t) = (\mu_i(t))_{i \in S}^T = (\mathbb{P}(X(t) = i))_{i \in S}^T$ be the probability distribution of the Markov jump process at time t. Then the distribution $\mu(t)$ evolves in time according to the *forward Kolmogorov* equation

$$\frac{d\mu}{dt} = \mu^T L, \ t \geq 0, \tag{2.46}$$

also known as *Master equation*. A probability distribution $\pi = (\pi_i)_{i \in S}$ is called a *stationary distribution* if it satisfies

$$0 = \pi^T L.$$

In other words, π is a left eigenvector associated with the zero eigenvalue of L.

To further illuminate the characteristics of Markov Jump processes, denote by $t_0 = 0 < t_1 < t_2 < \dots$ the random jump times, at which the Markov process changes its state. For notational convenience, we denote the left-sided limit of the process at time t by

$$X^*(t) \stackrel{def}{=} \lim_{s \to t-} X(s). \tag{2.47}$$

Then the sequence of jump times $\{t_n, n \in \mathbb{N} \cup \{0\}\}$, formally given by

$$t_0 = 0, \qquad \forall n \in \mathbb{N} : t_n = \inf\{s : s > t_{n-1}, X(s) \neq X^*(s)\}.$$

defines according to

$$X_n \stackrel{def}{=} X(t_n)$$

the *embedded process* $\{X_n, n \in \mathbb{N}_0\}$ associated with the Markov jump process. It can be shown that $\{X_n, n \in \mathbb{N}_0\}$ is a discrete-time Markov chain and its transition matrix $\overline{P} = (\overline{p}_{ij})_{i,j \in S}$ is related to the infinitesimal generator L by

$$\overline{p}_{ij} = \begin{cases} -\frac{l_{ij}}{l_{ii}} & \forall i \neq j \\ 0, & \text{otherwise.} \end{cases} \tag{2.48}$$

A Markov jump process is called *irreducible* if the embedded process is irreducible, i.e., if for any pair (i,j), $i \neq j$ of states there exists an $m \in \mathbb{N}$ such that $(\overline{P}^m)_{i,j} > 0$ (cf. Sect. A.6).

Next, we turn our attention to the *reversed time* process $\{X^R(t), t \in \mathbb{R}\}$ defined by

$$X^R(t) \stackrel{def}{=} X^*(-t),$$

where $X^*(-t)$ denotes the left-sided limit of the process at time $-t$. If we assume that $\{X(t), t \in \mathbb{R}\}$ is irreducible and that it admits a unique stationary distribution $\pi = (\pi_i)_{i \in S}$, then the process $\{X^R(t), t \in \mathbb{R}\}$ is again a càdlàg Markov jump process with the same stationary distribution as $\{X(t)\}_{t \in \mathbb{R}}$, π, and the infinitesimal generator $L^R = (l_{ij}^R)_{i,j \in S}$ given by

$$l_{ij}^R = \frac{\pi_j}{\pi_i} l_{ji}. \tag{2.49}$$

If in particular the infinitesimal generator L satisfies the *detailed balance* equations

$$\pi_i l_{ij} = \pi_j l_{ji}, \quad \forall i, j \in S \tag{2.50}$$

then $L^R \equiv L$ and hence, the direct and the reversed time process are statistically indistinguishable. Such a process is called *reversible*.

We end this section by stating a strong law of large numbers for Markov jump processes, which says that the time average of an observable $f : S \mapsto \mathbb{R}$ with respect to the process equals the expectation of f with respect to the stationary distribution. Formally, we have

$$\lim_{t \to \infty} \frac{1}{t} \int_0^t f(X(s)) \mathrm{d}s = \sum_{i \in S} f(i) \pi_i \tag{2.51}$$

almost sure for all initial distributions μ_0 where π is the stationary distribution of the Markov jump process. In particular, the Markov jump process is said to be *ergodic* if it satisfies (2.51).

3. Transition Path Theory for Diffusion Processes

As explained in the introduction of this thesis, Transition Path Theory (TPT) provides a powerful framework to describe the statistical properties of the ensemble of reactive trajectories. In this chapter, we will recall the theoretical aspects of TPT in the context of Markov diffusion processes (Sect. 3.1) and, in particular, we will derive the main objects of TPT for the case of the Smoluchowski dynamics (Sect. 3.2) and for the Langevin dynamics (Sect. 3.3), respectively. The remainder of this chapter is devoted to illustrate TPT via several low dimensional examples where we will also explain briefly how the various quantities of TPT were computed on the simple examples. For the details of the numerical considerations, especially how we numerically solved the committor equation see Section A.1 in the Appendix. For more details, we refer the reader to the original references [34, 92, 65].

3.1. Theory: Transition Path Theory

Consider a system whose dynamics is governed by the following stochastic differential equation

$$\mathrm{d}X_t = b(X_t)\mathrm{d}t + \sigma \mathrm{d}W_t, \tag{3.1}$$

where $X_t \in \mathbb{R}^d$, $b(x) = (b_1(x), \ldots, b_d(x))^T \in \mathbb{R}^d$ is the drift vector, $\sigma \in \mathbb{R}^{d \times d}$ is a real matrix and W_t is a d-dimensional, standard Wiener process. The generator associated with the dynamics (3.1) is given by

$$
\begin{aligned}
\mathcal{L}_{bw}u(x) &= \sum_{i,j=1}^{d} a_{ij} \frac{\partial^2 u(x)}{\partial x_i \partial x_j} + \sum_{i=1}^{d} b_i(x) \frac{\partial u(x)}{\partial x_i} \\
&= a : \nabla\nabla u(x) + b(x) \cdot \nabla u(x),
\end{aligned} \tag{3.2}
$$

where $a = \frac{1}{2}\sigma\sigma^T$ is the diffusion matrix.

3.1.1. Ensemble of Reactive Trajectories

Let $X(t), -\infty < t < \infty$ be an infinity long trajectory solution of (3.1) which is ergodic with respect to the equilibrium probability density function $\rho(x)$, i.e. given any suitable observable $\phi(x)$, we have

$$\lim_{T \to \infty} \frac{1}{2T} \int_{-T}^{T} \phi(X(t))\mathrm{d}t = Z^{-1} \int_{\mathbb{R}^d} \phi(x)\rho(x)\mathrm{d}x, \tag{3.3}$$

where $Z = \int_{\mathbb{R}^d} \rho(x)\mathrm{d}x$. (3.3) is a property of any generic trajectory in the system which, during the time-interval $[-T, T]$, will be involved in any given reaction many
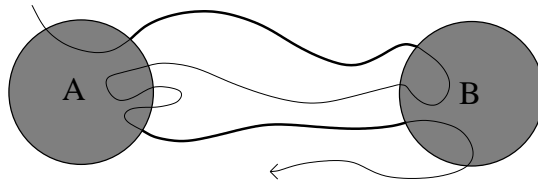
Figure 3.1.: Schematic representation of the reactant state A, the product state B and a piece of an equilibrium trajectory (shown in thin black). The subpieces connecting ∂A to ∂B (shown in thick black) are each a reactive trajectory, and the collection of all of them is the ensemble of reactive trajectories.

times when T is large (and infinitely often as $T \to \infty$). Suppose however that one is not interested in the statistical properties of such a generic trajectory, but rather in the statistical properties that this trajectory displays while involved in a reaction. This question can be made precise as follows. Suppose that $A \subset \mathbb{R}^d$ and $B \subset \mathbb{R}^d$ are two regions in configuration space that characterize the system while it is in the reactant and the product states, respectively, of a given reaction. Then, given any generic trajectory, $x(t)$, $-\infty < t < \infty$, we can prune this trajectory as illustrated in Figure 3.1 to consider only the pieces of this trajectory that connect ∂A (the boundary of A) to ∂B (the boundary of B). Each such piece is a reactive trajectory and the collection of all of them is the ensemble of reactive trajectories. By ergodicity, the statistical properties of this ensemble are independent of the particular trajectory used to generate the ensemble, and these properties are the object of TPT.

Formally, the ensemble of reactive trajectories is defined in

Definition 3.1.1 (ensemble of reactive trajectories).

$$
\begin{aligned}
&\textit{ensemble of reactive trajectories} \\
&= \{X(t) : t \in \mathcal{R}\} \textit{ where } t \in \mathcal{R} \textit{ if and only if} \\
&X(t) \notin A \cup B, \ X(t_{AB}^+(t)) \in B \textit{ and } X(t_{AB}^-(t)) \in A
\end{aligned}
\tag{3.4}
$$

where

$$
\begin{aligned}
t_{AB}^+(t) &= \textit{smallest } t' \geq t \textit{ such that } X(t') \in A \cup B, \\
t_{AB}^-(t) &= \textit{largest } t' \leq t \textit{ such that } X(t') \in A \cup B.
\end{aligned}
\tag{3.5}
$$

Each continuous piece of the trajectory going from A to B in the ensemble (3.1.1) is a specific reactive trajectory. The main objects of TPT are then defined in terms of the reactive trajectories and expressed in terms of $\rho(x)$ and the committor functions $q(x)$ and $q_b(x)$ which will be defined in the next section.

3.1.2. Committor Function

We will see in the next sections that the *forward committor function* $q(x)$, defined as the probability that the trajectory starting from $x \notin A \cup B$ reaches first B rather than A and the *backward committor function* $q_b(x)$, defined as the probability that the trajectory arriving at $x \notin A \cup B$ came rather from A than from B are the crucial objects to express, e.g., the probability density function of reactive trajectories.

Formally, the forward committor function $q(x)$ satisfies the backward Kolmogorov equation associated with (3.1):

$$\begin{cases} \mathcal{L}_{bw}q = 0 & \text{in } \mathbb{R}^d \setminus (A \cup B), \\ \quad q = 0 & \text{on } \partial A, \\ \quad q = 1 & \text{on } \partial B, \end{cases} \tag{3.6}$$

where $\mathcal{L}_{bw}$ is the operator in (3.2). To see (3.6) notice that the committor function $q(x)$ can be expressed in terms of a conditional expectation, i.e,

$$q(x) = \mathbb{E}_x \left[\mathbf{1}_B(X(\tau_{A \cup B})) \right],$$

where $\tau_{A \cup B}$ is the first hitting time of the process X_t with respect to the set $A \cup B$. If we define the auxiliary function $g : \partial A \cup \partial B \to \mathbb{R}$ by

$$g(x) = \begin{cases} 0, & \text{if } x \in \partial A \\ 1, & \text{if } x \in \partial B \end{cases}$$

and set $f \equiv 0$ then by virtue of Theorem 2.1.3 follows that if (3.6) possesses a (classical) solution, say $u(x)$, then we have $q \equiv u$, and therefore, $q(x)$ satisfies (3.6). For conditions on the differential operator $\mathcal{L}_{bw}$ and the boundary of the set $A \cup B$ which ensure the existence of a classical solution, see Theorem 2.1.4.

A similar reasoning as above shows that the backward committor function $q_b(x)$ satisfies the backward Kolmogorov equation associated with the reversed-time process (cf. Sect. 2.1.4):

$$\begin{cases} \mathcal{L}_{bw}^R q_b = 0 & \text{in } \mathbb{R}^d \setminus (A \cup B), \\ \quad q_b = 1 & \text{on } \partial A, \\ \quad q_b = 0 & \text{on } \partial B, \end{cases} \tag{3.7}$$

where

$$\mathcal{L}_{bw}^R q_b = a : \nabla\nabla q_b(x) + b^R(x) \cdot \nabla q_b(x) \tag{3.8}$$

with the drift field (cf. Theorem A.6.2)

$$b^R(x) = -b(x) + \frac{2}{\rho(x)} div\big(a(x)\rho(x)\big).$$

Notice that if the process X_t is reversible than in particular we have $\mathcal{L}_{bw} \equiv \mathcal{L}_{bw}^R$ and it follows that the backward committor function $q_b(x)$ can be expressed in terms of the forward committor function:

$$q_b(x) = 1 - q(x). \tag{3.9}$$

In large dimensional systems, the main question of interest then becomes how to solve (3.6), which is a highly nontrivial problem since (3.6) involves a partial differential equation for a function of many variables. The string method is a way to deal with this issue. In the context of the two-dimensional examples considered in this chapter, however, standard numerical techniques based on discretizing (3.6) by finite differences can be applied, as briefly explained in detail in the Appendix, Section A.1.

Remark 3.1.2. *Let $r(x)$ denote the **mean first passage time** (mean first hitting time) of the process X_t with respect to the set $\mathcal{S} \subset \mathbb{R}^d$, conditional on $X(0) = x$. Formally, $r(x)$ is given by*

$$r(x) = \mathbb{E}_x[\tau_{\mathcal{S}}],$$

where $\tau_{\mathcal{S}}$ is the hitting time of the process X_t with respect to the set $\mathcal{S}$. If we set $g \equiv 0$ and $f \equiv -1$ then a similar reasoning as for the committor function shows that $r(x)$ satisfies

$$\begin{cases} \mathcal{L}_{bw} r = -1 & in \ \mathbb{R}^d \setminus \mathcal{S}, \\ r = 0 & on \ \partial \mathcal{S}, \end{cases} \tag{3.10}$$

where $\mathcal{L}_{bw}$ is the operator in (3.2).

3.1.3. Probability Density Function of Reactive Trajectories

Let $A \subset \mathbb{R}^d$ and $B \subset \mathbb{R}^d$ denote the reactant and product states, respectively. What is the probability density to observe a reactive trajectory at position $x \notin A \cup B$ at time t, conditional on it being reactive at time t?

Intuitively, it should be clear that the probability density to observe any reactive trajectory is given by the probability density to observe any trajectory (reactive or not) at point x, which is $\rho(x)$, times the probability $q_b(x)$ that the trajectory came rather from A than from B and times the probability $q(x)$ that the trajectory reaches first B rather than A.

Formally, the probability density function of reactive trajectories $\rho_{AB}(x)$ is defined such that, giving any observable $\phi(x)$, we have

$$\lim_{T \to \infty} \frac{\int_{\mathcal{R} \cap [-T,T]} \phi(X(t)) \mathrm{d}t}{\int_{\mathcal{R} \cap [-T,T]} \mathrm{d}t} = \int_{\Omega_{AB}} \phi(x) \rho_{AB}(x) \mathrm{d}x, \tag{3.11}$$

where $\Omega_{AB} = \mathbb{R}^d \setminus (A \cup B)$. Indeed, it is proven in [34] that by exploiting both ergodicity and the strong Markov property of the dynamics the intuitive picture is right, namely that $\rho_{AB}(x)$ can be expressed in terms of $\rho(x)$, $q(x)$ and $q_b(x)$ as

$$\rho_{AB}(x) = Z_{AB}^{-1} q(x) q_b(x) \rho(x), \tag{3.12}$$

where the normalization constant Z_{AB},

$$Z_{AB} = \int_{\Omega_{AB}} q(x) q_b(x) \rho(x) \mathrm{d}x, \tag{3.13}$$

is the total probability to encounter a reactive trajectory.

3.1.4. Probability Current and Transition Rate

The probability density $\rho_{AB}(x)$ is not the only quantity of interest as it may not be sufficient to characterize the reaction pathway. To get a better understanding of this pathway, we may also ask about the probability current of reactive trajectories. Roughly, this current is such that, integrated over any surface in Ω_{AB}, it gives the probability flux of reactive trajectories across this surface, that is, the net balance

between the number of trajectories that cross this surface in one direction minus the number of them that cross this surface in the opposite direction during an infinitesimal time-interval.

More precisely, the probability current $J_{AB}(x)$ of reactive trajectories is the vector field defined in Ω_{AB} such that given any surface $\partial \mathcal{S}$ which is the boundary of a region $\mathcal{S} \subset \Omega_{AB}$, we have

$$
\lim_{s \to 0^+} \frac{1}{s} \lim_{T \to \infty} \frac{1}{2T} \int_{\mathcal{R} \cap [-T,T]} \big(\mathbf{1}_{\mathcal{S}}(X(t)) \mathbf{1}_{\mathbb{R}^d \setminus \mathcal{S}}(X(t+s))
$$
$$
- \mathbf{1}_{\mathbb{R}^d \setminus \mathcal{S}}(X(t)) \mathbf{1}_{\mathcal{S}}(X(t+s)) \big) \mathrm{d}t \tag{3.14}
$$
$$
= \int_{\partial \mathcal{S}} \hat{n}_{\partial \mathcal{S}}(x) \cdot J_{AB}(x) \mathrm{d}\sigma_{\partial \mathcal{S}}(x),
$$

where $\hat{n}_{\partial \mathcal{S}}(x)$ is the unit normal on $\partial \mathcal{S}$ pointing outward $\mathcal{S}$ and $\mathrm{d}\sigma_{\partial \mathcal{S}}(x)$ is the surface element on $\partial \mathcal{S}$. We want to emphasize that $J_{AB}(x)$ is independent of the surface $\partial \mathcal{S}$. As shown in Section A.4 in the Appendix, $J_{AB}(x)$ can be expressed componentwise as

$$
J_{AB,i}(x) = q(x) q_b(x) J_i(x)
$$
$$
+ q_b(x) \rho(x) \sum_{j=1}^{d} a_{ij}(x) \frac{\partial q(x)}{\partial x_j} \tag{3.15}
$$
$$
- q(x) \rho(x) \sum_{j=1}^{d} a_{ij}(x) \frac{\partial q_b(x)}{\partial x_j},
$$

where $J(x) = (J_1(x), \ldots, J_d(x))^T$ is the equilibrium probability current (recall that $\rho(x)$ is the equilibrium probability density function of the process):

$$
J_i(x) = b_i(x) \rho(x) - \sum_{j=1}^{d} \frac{\partial}{\partial x_j} (a_{ij}(x) \rho(x)). \tag{3.16}
$$

The current $J_{AB}(x)$ is divergence free, and its integral over any dividing surface $\partial \mathcal{S} \subset \Omega_{AB}$ gives the reaction rate:

$$
k_{AB} = \int_{\partial \mathcal{S}} \hat{n}_{\partial \mathcal{S}}(x) \cdot J_{AB}(x) \mathrm{d}\sigma_{\partial \mathcal{S}}(x), \tag{3.17}
$$

where $\hat{n}_{\partial \mathcal{S}}(x)$ is the unit normal to $\partial \mathcal{S}$ pointing toward B. Letting N_T^R be the number of reactive trajectories observed during the time interval $[-T,T]$ in the ensemble of reactive trajectories, k_{AB} is the limit

$$
k_{AB} = \lim_{T \to \infty} \frac{N_T^R}{2T}, \tag{3.18}
$$

i.e. it gives the exact mean frequency at which the reactive trajectories are observed within a given trajectory.

The expression (3.17) for the rate can be simplified and transformed into a volume integral over Ω_{AB}:

$$
k_{AB} = \int_{\Omega_{AB}} \rho(x) \sum_{i,j=1}^{d} a_{ij}(x) \frac{\partial q(x)}{\partial x_i} \frac{\partial q(x)}{\partial x_j} \mathrm{d}x. \tag{3.19}
$$

For a derivation of (3.19) see Section A.4 in the Appendix.

3.1.5. Transition Tubes

Another quantity of interest which can be extracted from the probability current of reactive trajectories are the streamlines of this current. These are the solutions of

$$\frac{dx_i(\tau)}{d\tau} = J_{AB,i}(x(\tau)).$$ (3.20)

(The "time" τ in this equation is artificial and unrelated to the physical time t). Solving (3.20) with the initial condition $x(0) \in \partial A$ one obtains a streamline connecting A to B; the ensemble of streamlines associated with all initial conditions $x(0) \in \partial A$ forms a bundle of curves in Ω_{AB} whose union is Ω_{AB} itself. The streamlines of the current are an indicator of the average trend of the reactive trajectories, and they allow to define reaction (or transition) tubes connecting A to B carrying a certain percentage of the probability flux of reactive trajectories. Indeed, suppose that $\partial'A \subset \partial A$ is a subset of the boundary of the reactant state A across which $p\%$ of the probability flux of reactive trajectories go, i.e.

$$
\begin{aligned}
&\int_{\partial'A} \hat{n}_{\partial A}(x) \cdot J_{AB}(x) \mathrm{d}\sigma_{\partial A}(x) \\
&= \frac{p}{100} \int_{\partial A} \hat{n}_{\partial A}(x) \cdot J_{AB}(x) \mathrm{d}\sigma_{\partial A}(x) \equiv \frac{p}{100} k_{AB},
\end{aligned}
$$ (3.21)

where we used (3.29) and the fact that ∂A is a dividing surface between A and B. Then, the ensemble of streamlines obtained by solving (3.20) for all initial conditions $x(0) \in \partial'A$ forms a reaction tube connecting A and B which carries $p\%$ of the probability flux of reactive trajectories. Sometimes, a rather localized tube can be found which carries a high percentage of the flux: then, the reactive trajectories must remain inside this tube with high probability, i.e. it is the preferred channel for the reaction.

3.2. TPT in the Smoluchowski Case

In this section we summarize the objects of TPT for a system which is governed by the Smoluchowski dynamics introduced in Section 2.1.10:

$$\dot{x}_i(t) = -\gamma_i^{-1} \frac{\partial V(x(t))}{\partial x_i} + \sqrt{2\beta^{-1}\gamma_i^{-1}} \, \eta_i(t),$$ (3.22)

where $x = (x_1, x_2, \ldots, x_d) \in \mathbb{R}^d$ denotes the position of the particles, $V(x)$ is the potential, γ_i is the friction coefficient on x_i, β is the inverse temperature and $\eta_i(t)$ is a white noise.

Recalling that the backward generator of the Smoluchowski dynamics in (3.22) takes the form

$$\mathcal{L}_{bw}u = \beta^{-1}\Gamma^{-1} : \nabla\nabla u - \Gamma^{-1}\nabla V \cdot \nabla u,$$ (3.23)

the forward committor function $q(x)$ satisfies the committor equation [29] (see also

Theorem 2.1.4)

$$
\begin{cases}
0 = \mathcal{L}_{bw} q \\
\quad = \beta^{-1}\Gamma^{-1} : \nabla\nabla q - \Gamma^{-1}\nabla V \cdot \nabla q & \text{in } \Omega_{AB} = \mathbb{R}^d \setminus (A \cup B), \\
q = 0 & \text{on } \partial A, \\
q = 1 & \text{on } \partial B,
\end{cases}
\tag{3.24}
$$

where $\Gamma^{-1} = \operatorname{diag}(\gamma_1^{-1}, \ldots, \gamma_d^{-1})$. Since the Smoluchowski dynamics is reversible, the backward committor function is given via the relation in (3.9). The probability density to observe a reactive trajectory at point $x \notin A \cup B$ at time t is

$$
Z^{-1} e^{-\beta V(x)} q(x)(1 - q(x)). \tag{3.25}
$$

This means that the total probability that the trajectory be reactive at time t is

$$
Z_{AB} = Z^{-1} \int_{\Omega_{AB}} e^{-\beta V(x)} q(x)(1 - q(x)) \mathrm{d}x, \tag{3.26}
$$

and the probability density to observe a reactive trajectory at point $x \notin A \cup B$ at time t conditional on it being reactive at time t is

$$
\rho_{AB}(x) = Z_{AB}^{-1} Z^{-1} e^{-\beta V(x)} q(x)(1 - q(x)). \tag{3.27}
$$

This expression was first derived in [52]. Furthermore, the probability current of reactive trajectories in (3.15) reduces to

$$
J_{AB}(x) = Z^{-1} \beta^{-1} e^{-\beta V(x)} \Gamma^{-1} \nabla q(x) \tag{3.28}
$$

and, consequently, the expressions for the rate in (3.17) and (3.19) take the form

$$
k_{AB} = Z^{-1} \beta^{-1} \int_{\partial \mathcal{S}} \hat{n}_{\partial \mathcal{S}}(x) \cdot e^{-\beta V(x)} \Gamma^{-1} \nabla q(x) \mathrm{d}\sigma_{\partial \mathcal{S}}(x), \tag{3.29}
$$

and

$$
k_{AB} = Z^{-1} \beta^{-1} \int_{\Omega_{AB}} e^{-\beta V(x)} \nabla q(x)^T \cdot \Gamma^{-1} \nabla q(x) \mathrm{d}x, \tag{3.30}
$$

respectively, where $\hat{n}_{\partial \mathcal{S}}(x)$ denotes the unit normal to the dividing surface $\partial \mathcal{S}$ pointing toward B and $\mathrm{d}\sigma_S(x)$ is the surface element on $\partial \mathcal{S}$.

3.3. TPT in the Langevin Case

The results of TPT can be generalized to systems described by the Langevin equation introduced in Section 2.1.10:

$$
\begin{aligned}
\dot{x}_i(t) &= m_i^{-1} p_i(t), \\
\dot{p}_i(t) &= -\frac{\partial V(x(t))}{\partial x_i} - \gamma_i m_i^{-1} p_i(t) + \sqrt{2\gamma_i \beta^{-1}} \zeta_i(t),
\end{aligned}
\tag{3.31}
$$

where $p = (p_1, p_2, \ldots, p_d) \in \mathbb{R}^d$ is the momentum of the particles, m_i is the mass of x_i and the other quantities are as in (3.22).

3. Transition Path Theory for Diffusion Processes

As mentioned earlier, the main difference is that the Langevin equation in (3.31) defines a non-reversible diffusion process on the phase space (x, p) and the associated generator $\mathfrak{L}_{bw}$ is a degenerated partial differential operator.

Let $A \subset \mathbb{R}^{2d}$ be the reactant and $B \subset \mathbb{R}^{2d}$ be the product state in phase-space (x, p). For the Langevin dynamics, the forward committor equation in (3.6) reduces to

$$
\begin{cases}
0 = \mathfrak{L}_{bw}q \\
\quad = \beta^{-1}\Gamma : \nabla_p\nabla_p q + M^{-1}p \cdot \nabla_x q, \\
\quad\quad - \nabla_x V \cdot \nabla_p q - \Gamma M^{-1}p \cdot \nabla_p q & \text{in } \mathbb{R}^{2d} \setminus (A \cup B) \\
q = 0 & \text{on } \partial A, \\
q = 1 & \text{on } \partial B,
\end{cases}
\tag{3.32}
$$

whereas the backward committor function $q_b(x, p)$ satisfies the backward committor equation

$$
\begin{cases}
0 = \mathfrak{L}_{bw}^R q_b \\
\quad = \beta^{-1}\Gamma : \nabla_p\nabla_p q_b - M^{-1}p \cdot \nabla_x q_b \\
\quad\quad + \nabla_x V \cdot \nabla_p q_b - \Gamma M^{-1}p \cdot \nabla_p q_b & \text{in } \mathbb{R}^{2d} \setminus (A \cup B), \\
q_b = 1 & \text{on } \partial A, \\
q_b = 0 & \text{on } \partial B.
\end{cases}
\tag{3.33}
$$

Notice that $q(x, p)$ can be related to $q_b(x, p)$ by

$$
q_b(x, p) = 1 - q(x, -p), \tag{3.34}
$$

provided that the sets A and B are point symmetric to each other with respect to the origin.

Remark 3.3.1. *The uniform ellipticity of the operator $\mathcal{L}_{bw}$ in the Smoluchowski case is essential for the existence a classical solution of the associated committor equation (cf. Theorem 2.1.4). Unfortunately, in case of the Langevin dynamics the backward operator $\mathcal{L}_{bw}$ is degenerate, but not elliptic (cf. Sect. 2.1.6) and up to our knowledge there does not exist any general theorem which states conditions for the existence of classical solutions of (3.32) and (3.33). Nevertheless, our numerical investigations on the committor equations in the Langevin case (as presented in Sect. 3.9) will show that at least for low-dimensional simple domains $\Omega \subset \mathbb{R}^2$ and reasonable parameters there exist sufficiently smooth solutions of (3.32) and (3.33).*

In terms of these quantities, the probability density to observe a reactive trajectory at (x, p) at time t conditional on the trajectory being reactive at time t now becomes (cf. (3.27))

$$
\rho_{AB}(x, p) = Z_{AB}^{-1}Z^{-1}e^{-\beta H(x,p)}q(x, p)q_b(x, p), \tag{3.35}
$$

where $H(x, p) = V(x) + \frac{1}{2}p^T M^{-1}p$ is the Hamiltonian, $Z = \int_{\mathbb{R}^d \times \mathbb{R}^d} e^{-\beta H(x,p)}\mathrm{d}x\mathrm{d}p$ is the partition function and Z_{AB} is the total probability that the trajectory be reactive at time t (cf. (3.26)):

$$
Z_{AB} = Z^{-1}\int_{\Omega_{AB}} e^{-\beta H(x,p)}q(x, p)q_b(x, p)\mathrm{d}x\mathrm{d}p, \tag{3.36}
$$

where $\Omega_{AB} = \mathbb{R}^{2d} \setminus (A \cup B)$. The probability current of the reactive trajectories can be obtained as well (cf. (3.28)):

$$J_{AB}(x,p) = Z^{-1}e^{-\beta H(x,p)}\big(J_{AB}^x(x,p), J_{AB}^p(x,p)\big), \tag{3.37}$$

where $J_{AB}^x(x,p)$ and $J_{AB}^p(x,p)$ are the components of the current in the directions of x and p, respectively, and given by

$$
\begin{aligned}
J_{AB}^x(x,p) =\,& q(x,p)q_b(x,p)p, \\
J_{AB}^p(x,p) = -\,& q(x,p)q_b(x,p)\nabla V(x) \\
& + \beta^{-1}q_b(x,p)\Gamma\nabla_p q(x,p) - \beta^{-1}q(x,p)\Gamma\nabla_p q_b(x,p).
\end{aligned}
$$

Out of the current the reaction rate can be computed (cf. (3.29))

$$k_{AB} = \int_{\partial\mathcal{S}} \hat{n}_{\partial\mathcal{S}}(x,p) \cdot J_{AB}(x,p)\mathrm{d}\sigma_{\partial\mathcal{S}}(x,p), \tag{3.38}$$

where $\partial\mathcal{S}$ is any dividing surface in phase-space between A and B, $\hat{n}_{\mathcal{S}}(x,p)$ is the unit normal on $\partial\mathcal{S}$ pointing toward B and $\mathrm{d}\sigma_{\mathcal{S}}(x,p)$ is the surface element on $\partial\mathcal{S}$. (3.38) can be re-expressed via (3.19) as a volume integral as (cf. (3.30))

$$
\begin{aligned}
k_{AB} = Z^{-1}\beta^{-1} \int_{\Omega_{AB}} &\nabla_p q(x,p)^T \cdot \Gamma\nabla_p q(x,p) \\
&\times e^{-\beta H(x,p)}\mathrm{d}x\,\mathrm{d}p.
\end{aligned} \tag{3.39}
$$

The streamlines of the probability current of reactive trajectories can also be defined as the ensemble of solutions of (cf. (3.20))

$$
\begin{cases}
\dfrac{dx(\tau)}{d\tau} = J_{AB}^x(x(\tau), p(\tau)), \\[2mm]
\dfrac{dp(\tau)}{d\tau} = J_{AB}^p(x(\tau), p(\tau)),
\end{cases} \tag{3.40}
$$

and they can be used to define reaction tubes carrying a given percentage of the probability flux of reactive trajectories as in the overdamped case.

The only additional difficulty with (3.32) absent with (3.24) is that, because the differential operator in (3.32) is degenerate (i.e. hypo-elliptic but not elliptic), in order to be able to impose the Dirichlet boundary conditions on ∂A and ∂B, the unit normal to these sets at (x,p) must span the velocity degrees of freedom everywhere except maybe on a set of zero measure on ∂A and ∂B. How to solve (3.32) in the context of the simple example considered in Section 3.9, is discussed in Section A.1 in the Appendix.

3.4. Numerical Aspects

Here we briefly discuss how we performed the numerics on the examples discussed below. In order to get an accurate approximation of the committor functions $q(x)$ and $q(x,p)$, we derived a stable finite differences scheme for the discretization of (3.24) and (3.32) and implemented the resulting scheme in MATLAB. In all numerical computations involving (3.24) we choose a rectangular domain $\Omega \subset \mathbb{R}^2$ and a uniform

mesh. The Dirichlet conditions for $q(x)$ are included into our scheme by defining discrete sets A and B via the mesh. For the details of the respective finite difference schemes and the proofs of stability and convergence see Section A.1 in the Appendix.

Remark 3.4.1. *We want to emphasize here that our extensive numerical experiments have shown that the results which will be presented in the next sections are stable under refinement of the underlying discretization meshes.*

To compare and test the predictions of TPT, we also computed some of the statistical quantities provided by TPT by means of direct numerical simulation (DNS) of the dynamical equations (3.22) and (3.31). As explained earlier, an ensemble of reactive trajectories can be computed by pruning a sufficiently long trajectory. This was done by discretizing (3.22) and (3.31) in such a way that long-term stability is achieved. The results presented below are based on the Euler-Maruyama-scheme for the Smoluchowski dynamics and an appropriate second order scheme for the Langevin dynamics [93] which both have been used with sufficiently small discretization time steps to guarantee stability. From the long trajectory generated by DNS, the approximation of the probability density function of reactive trajectories was obtained by binning the region between the reactant and product state and computing the ratio between the time spent by the reactive trajectories in each bin and the total time the long trajectory was reactive. The reaction rate was obtained by counting the number N of transitions from A to B in the long trajectory of length T, and dividing this number by T. It should be stressed that the trajectory must be extremely long in order to obtain a statistically accurate estimate of $q(x)$, $q(x,p)$ and k_{AB} by DNS, which makes the DNS much more expensive than the numerical solution of (3.24) and (3.32).

3.5. Diffusion in the Double-Well Potential

For our first example, we choose the two-dimensional potential (here and below we denote $(x,y) = (x_1, x_2)$):

$$V(x,y) = \tfrac{5}{2}(x^2 - 1)^2 + 5y^2 \tag{3.41}$$

which is a combination of a double well potential in x-direction and a harmonic potential in y-direction. The local minima at $(-1,0)$ and $(0,1)$ are separated by a saddle point at $(0,0)$. We choose the inverse temperature $\beta = 1$ such that the process spends most of its time within the two wells, and we also set $\gamma_x = \gamma_y = 1$. The equilibrium distribution of the Smoluchowski dynamics (3.22) associated with (3.41) is depicted in Figure 3.2.

For the reactant and product states, A and B, we choose the two neighborhoods of the two minima of the potential at $(-1,0)$ and $(1,0)$ such that they include all states x that satisfy $V(x,y) < 0.4$; as in all subsequent computations these sets are replaced by the sets of all mesh points satisfying this condition. We also restricted the computation to the domain $\Omega = [-1.5, 1.5] \times [-1, 1]$, which is large enough so that the potential is high at the boundaries (and hence the Boltzmann-Gibbs probability density is very small there). To discretize Ω, we used a uniform mesh of consisting of 500×500 mesh points.
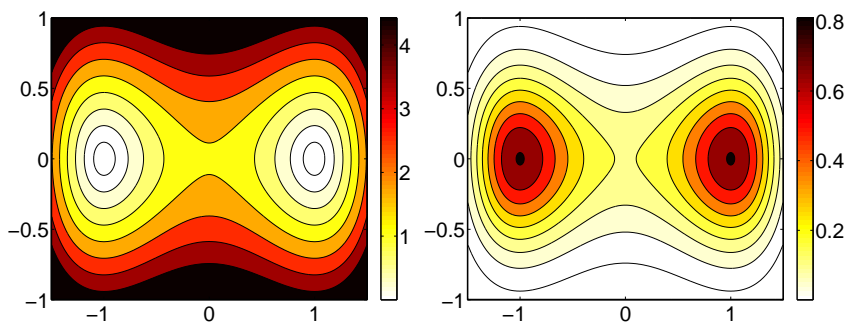
Figure 3.2.: Left: Contour plot of the double-well potential. Right: Contour plot of the Boltzmann-Gibbs probability density function $Z^{-1}e^{-\beta V(x,y)}$. Results for $\beta = 1$. The regions around the minima at $(-1,0)$ and $(1,0)$ contain most of the probability, i.e. they are metastable.
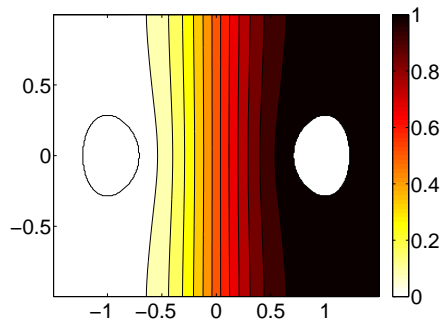
Figure 3.3.: Contour plot of the committor function solution $q(x,y)$ of (3.24) at inverse temperature $\beta = 1$. The white regions are the reactant state A and product state B (A is the left, B at the right). The level sets (isolines) of $q(x,y)$ are the regions from which the probability to reach first A rather B is uniform.

3.5.1. Committor Function

Figure 3.3 shows the level sets (isolines) of the committor function $q(x,y)$ obtained by solving (3.24) for this example. The left-right symmetry of the level sets of $q(x,y)$ with respect to the piece of the vertical axis $S = \{(0,y)| -1 \leq y \leq 1\}$ which includes the saddle point $(0,0)$ is a consequence of the choice of domain Ω, the symmetry of the potential (3.41) and the symmetry between A and B. In particular, it is clear that the probability to reach A before B should be $\frac{1}{2}$ for all points on S, i.e. $q(0,y) = \frac{1}{2}$ for all $-1 \leq y \leq 1$. This prediction is confirmed by the numerics.

3.5.2. Probability Density Function of Reactive Trajectories

Knowing $q(x,y)$ we can compute the probability density function of reactive trajectories $\rho_{AB}(x,y)$ via (3.27). This probability density function is shown in Figure 3.4. The density $\rho_{AB}(x,y)$ is peaked around the saddle point $(0,0)$ which indicates that the region around the saddle point is the dynamical bottleneck (transition state region) for the reaction.

For comparison, the probability density function of reactive trajectories $\rho_{AB}(x,y)$
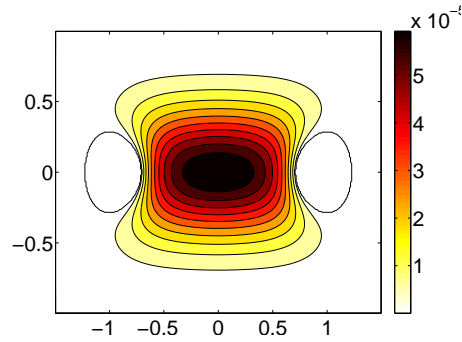
Figure 3.4.: Contour plot of the probability density function $\rho_{AB}(x, y)$ of reactive trajectories obtained via (3.27). Results for $\beta = 1$.
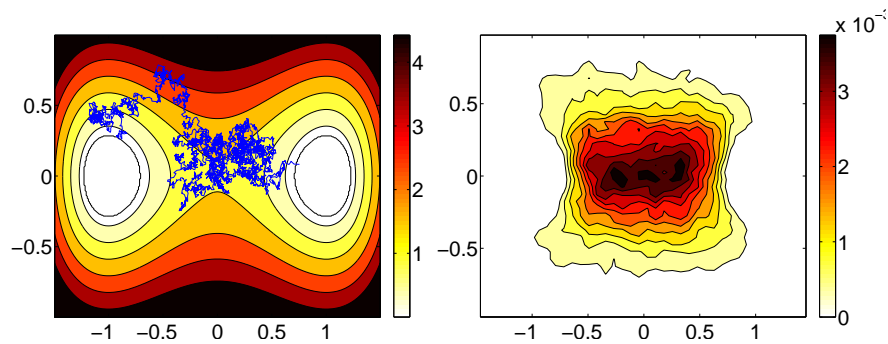
Figure 3.5.: Left: A typical reactive trajectory. Right: Probability density function of reactive trajectories computed via DNS based on 300 reactive trajectories and represented on a 40×40 box-discretization of the domain Ω. Results for $\beta = 1$.

was also computed by DNS. In the left panel of Figure 3.5 a typical reactive trajectory is shown.

In the right panel of Figure 3.5 the probability density function of reactive trajectories as computed via DNS is shown. The result of DNS agrees with the prediction of TPT shown in Figure 3.4. Notice however that the probability density $\rho_{AB}(x, y)$ obtained by DNS is subject to significantly larger errors of statistical origin.

3.5.3. Probability Current of Reactive Trajectories and its Streamlines

Knowing $q(x, y)$, we can also compute the probability current of reactive trajectories via (3.28) and its streamlines via (3.20). These streamlines are shown in the right panel of Figure 3.6.

In order to better visualize the probability current as well as the reaction tubes mentioned in Section 3.1, we did the following: First we computed the intensity of the probability current on a dividing surface of interest, for which we choose the isocommittor $\frac{1}{2}$ surface, $S_{1/2} = \{(x, y) : q(x, y) = \frac{1}{2}\}$. Since the isocommittor surface $S_{1/2}$ is simply the piece of the y-axis in Ω, the intensity $J_{AB} \cdot \hat{n}_{S_{1/2}}$ of the probability current on $S_{1/2}$ can be expressed by

$$J_{AB,1}(0, y) \cdot \hat{n}_{S_{1/2}} = \beta^{-1} Z^{-1} e^{-\beta V(0,y)} \frac{\partial q(0, y)}{\partial x}. \tag{3.42}$$

This intensity on $S_{1/2}$ is shown in the left panel of Figure 3.6. We observe that the intensity of the current is maximum at $(0, y) = (0, 0)$ which corresponds to the saddle point. This means that most reactive trajectories cross $S_{1/2}$ near the saddle point or, equivalently, that the probability flux of reactive trajectories across $S_{1/2}$ is concentrated near the saddle point.

Next, from each point $(0, y)$ on $S_{1/2}$ we transported the value of the current intensity $J_{AB}(0, y) \cdot \hat{n}_{S_{1/2}}$ backwards and forwards along each streamline of the current $J_{AB}(x, y)$ until it enters the states A and B. With this procedure, we give each point along a streamline the value of the current intensity evaluated at the point on $S_{1/2}$ through which the streamline goes. This is how the coloring in the right panel of Figure 3.6 was obtained: the darker the region, the higher the current intensity is. Regions in this figure which include all the greys down to a certain level form reactions tubes carrying a given percentage of the probability flux of reactive trajectories (the lower the level of grey, the higher the percentage; in this example, the tube in black already carries 42% of the flux).

3.5.4. Reaction Rate

Now we turn our attention to the reaction rate k_{AB}. Choosing $S_{1/2}$ as dividing surface in (3.29), this expression for the reaction rate reduces to

$$k_{AB} = \beta^{-1} Z^{-1} \int_{-1}^{1} e^{-\beta V(0,y)} \frac{\partial q(0, y)}{\partial x} dy. \tag{3.43}$$

Alternatively, we can compute k_{AB} via (3.30):

$$k_{AB} = \beta^{-1} Z^{-1} \int_{\Omega_{AB}} \left(\left(\frac{\partial q(x, y)}{\partial x} \right)^2 + \left(\frac{\partial q(x, y)}{\partial y} \right)^2 \right) \\ \times e^{-\beta V(x,y)} \mathrm{d}x \mathrm{d}y. \tag{3.44}$$
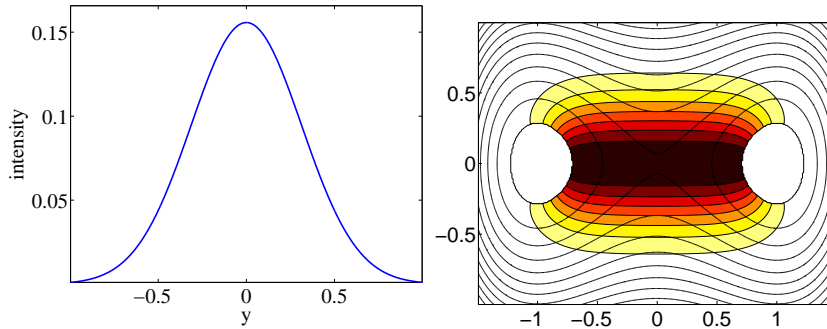
Figure 3.6.: Left: Intensity 3.42 of the probability current of reactive trajectories on the isocommittor surface $S_{1/2} = \{(x,y) : q(x,y) = 0.5\} = \{(0,y) : -1 \leq y \leq 1\}$. Right: Streamlines of the probability current $J_{AB}(x,y)$ colored according to the intensity of the current on the isocommittor surface $S_{1/2}$. Results for $\beta = 1$. The darker the color, the higher the intensity of the probability current of reactive trajectories through this region.

k_{AB} via (3.43)	$1.225 \cdot 10^{-1}$
k_{AB} via (3.44)	$1.226 \cdot 10^{-1}$
k_{AB} via DNS	$(1.230 \pm 0.029) \cdot 10^{-1}$

Table 3.1.: Reaction rate computed for the double-well potential for $\beta = 1$. The rate predicted by TPT is consistent with the rate computed via DNS (out of $N = 10^5$ reactive trajectories). The error given on the rate computed via DNS is the estimated statistical error. There is an additional error (not given) on all rates due to discretization of the domain; this error can be estimated from the difference between the rates obtained via (3.43) and via (3.44).

We approximate the partial derivatives $\partial q/\partial x$ and $\partial q/\partial y$ which are involved in both expressions for the rate on the mesh used to compute the committor function.

We compare the rate k_{AB} computed via DNS with the rates obtained from (3.43) and (3.44). Table 3.1 shows that the agreement of all different results is very good.

3.6. Entropic Barriers: Pure Diffusion

In our next example we consider pure diffusion in a square $\Omega = [0,1] \times [0,1]$ with two obstacles such that the domain becomes the S-shaped region shown in Figure 3.7. By pure diffusion we mean that we consider the Smoluchowski dynamics in a flat potential, $V(x,y) = 0$ in (3.22), except for the presence of hard walls at the boundary of the domain. We are interested in the statistics of the reactive trajectories starting in a region near the upper-right corner (set A) and ending in a region near the bottom-left corner (set B), see Figure 3.7. In contrast with the previous example where the transition between A and B is constrained by a potential barrier, here the dynamics has to overcome an *entropic barrier*: it has to find its way between the two obstacles. Suppose we start the dynamics in A. The closer the dynamics gets to the region enclosed by the obstacles the higher the probability that the dynamics will
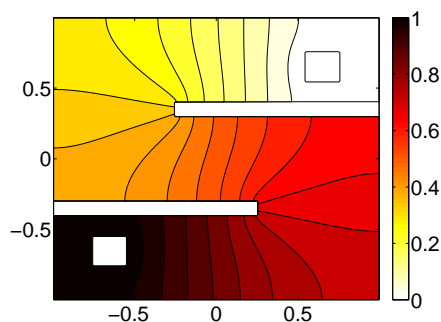
Figure 3.7.: Contour plot of the committor function $q(x,y)$ for the pure diffusion in the S-shaped domain. The reactant state A and product state B are the two squares in the upper-right and bottom-left corners, respectively. The two thin white rectangular regions connected to the vertical sides of the domain are hard walls. Results for $\beta = 1$. In this example, the Boltzmann-Gibbs probability density $Z^{-1}e^{-\beta V(x,y)}$ is uniform in the domain since $V(x,y) = 0$ except at the walls where it is infinity.
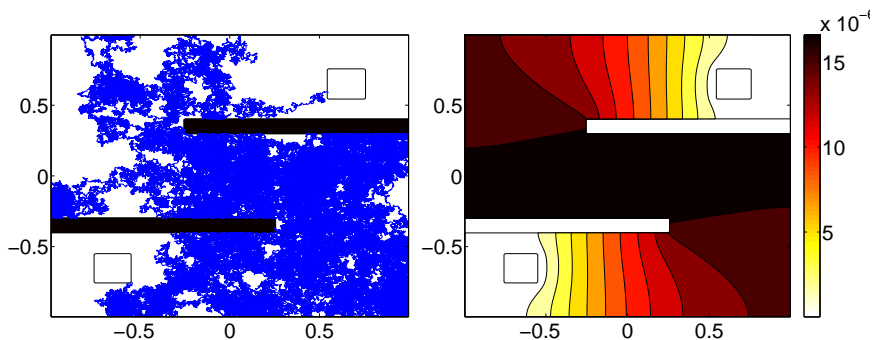
Figure 3.8.: Left: A typical reactive trajectory. Right: Contour plot of the probability density function of reactive trajectories $\rho_{AB}(x,y)$. Results for $\beta = 1$.

finally reach the left-down corner before returning to A because the probability to end up in B depends only on the distance between the current position and the set B. Figure 3.7 shows the committor function $q(x,y)$ as computed for this example; its isolines nicely illustrate the particular behavior of the dynamics. From the symmetry of the domain $\Omega \setminus (A \cup B)$ it is clear that the isocommittor $\frac{1}{2}$ surface goes through the point $(0,0)$. Therefore it is very likely to encounter a reactive trajectory between the obstacles, in the vicinity of isocommittor $\frac{1}{2}$ surface. In the left panel of Figure 3.8 we depict a typical reactive trajectory. One can see that the reactive trajectory spends most of its time between the obstacles. This is also obvious from the contour plot of the probability density function of reactive trajectories $\rho_{AB}(x,y)$ shown in the right hand panel of Figure 3.8. Notice how complicated the reactive trajectory is in this example and how much simpler $\rho_{AB}(x,y)$ is. The probability current of reactive trajectories (not shown) can also be computed in this example but it turns out to be very simple (basically, the streamlines follow the S-shape). In order to complete our observation for this example, Table 3.2 gives the values of the transition rates computed via TPT and via DNS. Again the values agree within numerical accuracy.

This example clearly shows that TPT is not restricted to situations in which the

rate via (3.29)	$4.455 \cdot 10^{-2}$
rate via (3.30)	$4.443 \cdot 10^{-2}$
rate via DNS	$(4.425 \pm 0.144) \cdot 10^{-2}$

Table 3.2.: The reaction rate k_{AB} for the pure diffusion in the S-shaped domain. Results for $\beta = 1$ and $N = 10^5$ in the DNS.
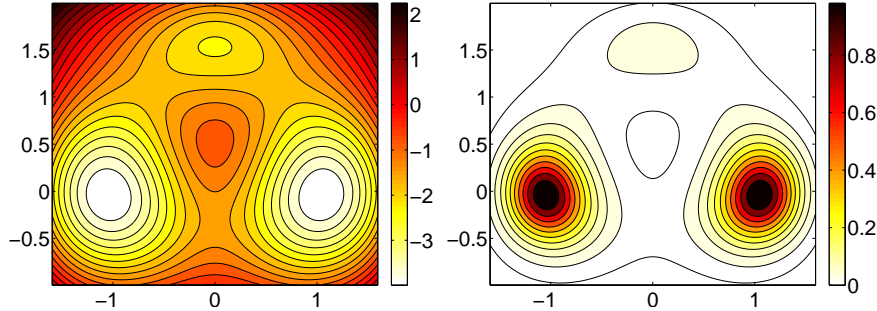
Figure 3.9.: Left: Contour plot of the three-hole potential. Right: Contour plot of the Boltzmann-Gibbs probability density function $Z^{-1}e^{-\beta V(x,y)}$ at $\beta = 1.67$.

reaction pathway is determined by energy effects, as in the example in Section 3.5, but it also allows one to handle situations where entropic effects dominate.

3.7. Entropic Switching

3.7.1. Diffusion in a Three-Hole Potential

In the next example, we study an example with two different reaction channels. For this purpose, we choose the three-hole potential

$$
\begin{aligned}
V(x,y) = &3e^{-x^2-(y-\frac{1}{3})^2} - 3e^{-x^2-(y-\frac{5}{3})^2} \\
&- 5e^{-(x-1)^2-y^2} - 5e^{-(x+1)^2-y^2} \\
&+ 0.2x^4 + 0.2(y-\frac{1}{3})^4
\end{aligned}
\tag{3.45}
$$

which has already been considered in [73, 25].

As one can see in the left panel of Figure 3.9 the potential (3.45) has two deep minima approximately at $(\pm 1, 0)$, a shallow minimum approximately at $(0, 1.5)$, three saddle points approximately at $(\pm 0.6, 1.1), (-1.4, 0)$ and a maximum at $(0, 0.5)$. Thus, the two deep minima are connected by an upper and a lower channel, and the upper channel contains the additional, less-pronounced minimum. The dynamical bottlenecks in the upper channel are the two saddle points with equal potential energy whereas the dynamics in the lower channel has only to overcome one saddle point whose potential energy is higher compared to the other two. It is known from large deviation theory [38] that in the limit $\beta \to \infty$ the reaction will occur via the upper channel with probability 1 since the energy barrier is lower there. Therefore we expect that the dynamics prefers the upper channel at low (finite) temperature. At higher temperature, however, the lower channel should be preferred (since it is direct). This entropic switching effect was first discovered and analyzed in [73].
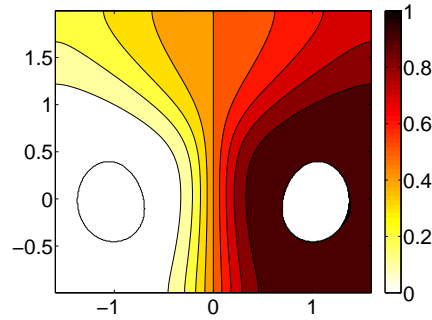
Figure 3.10.: Contour plot of the committor function $q(x, y)$ at $\beta = 1.67$. The isolines of the committor function are spread in the upper region of the potential because reactive trajectories get trapped in the upper shallow minima. The symmetry of the domain and the sets A and B implies that the isocommittor surface $\frac{1}{2}$ is $S_{1/2} = \{(0, y) : -2 \leq y \leq 2\}$. Results for a 350×350 mesh discretization.
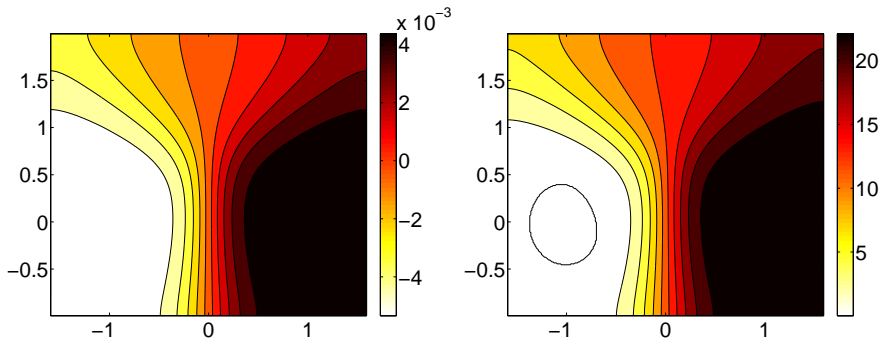
Figure 3.11.: Left: Contour plot of the eigenvector associated with the first non-trivial right eigenvalue of the discretization matrix $\overline{D}_h$ resulting from the finite differences discretization of the generator $\mathcal{L}_{bw}$ on the entire domain Ω together with Neumann boundary condition. Right: Contour plot of the MFPT with respect to the set A as also analyzed in [73]. Results for $\beta = 1.67$ and a 350×350 mesh discretization.

There the authors used the gradient of the mean first passage time (MFPT) (cf. Remark 3.1.2) with respect to a given state to detect the transition channels and their dependence on the temperature.

In this example, we performed experiments at two inverse temperature $\beta = 6.67$ (low temperature), which is such that the upper channel is the preferred reaction tube, and $\beta = 1.67$ (high temperature), which is such that the lower channel is the preferred reaction tube.

In Figure 3.10 we show the contour plot of the committor function at $\beta = 1.67$. As in the previous examples the symmetry of the domain Ω_{AB} explains that the isocommittor surface $\frac{1}{2}$ is $S_{1/2} = \{(0, y) : -2 \leq y \leq 2\}$. Notice how the presence of the shallow minima in the upper channel spreads the level sets of $q(x, y)$ in this region. This follows from the fact that the reactive trajectories going through the upper channel get trapped in the shallow well for a long period of time before exiting towards the set B. Notice that it also implies that the isocommittor $\frac{1}{2}$ surface goes
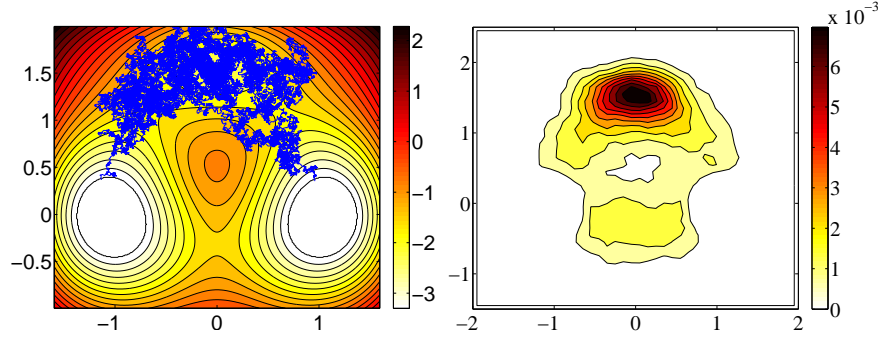
Figure 3.12.: Left: A typical reactive trajectory at a high temperature $\beta = 1.67$ taking the upper channel with the two saddle points with lowest energy. Right: Contour plot of the probability density function of reactive trajectories computed via DNS at $\beta = 1.67$ from 500 reactive trajectories using a 40×40 box-discretization of the domain $\Omega = [-2, 2] \times [-1.5, 1.5]$.
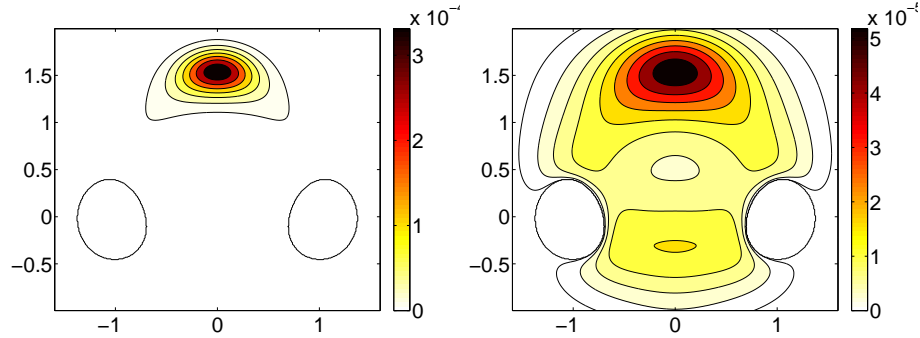
Figure 3.13.: Contour plots of the density $\rho_{AB}(x, y)$ for two different temperatures. Left: low temperature $\beta = 6.67$; Right: high temperature $\beta = 1.67$. In both cases $\rho_{AB}(x, y)$ attains its maximum in the shallow minima.

through the shallow minima and not through one of the two upper saddle points. The committor function at $\beta = 6.67$ (not shown) is very similar to the one at $\beta = 1.67$ (though, as we will see below, the probability density function and the probability current of reactive trajectories are very different). The left panel of Figure 3.11 reveals the similarity between the (forward) committor function and the eigenvector associated with the first non-trivial right eigenvalue of the discretization matrix $\overline{D}_h$ resulting from the finite differences discretization of the generator $\mathcal{L}_{bw}$ on the domain Ω_{AB}. Furthermore, the right panel of Figure 3.11 illustrates the similarity between the forward committor function and the MFPT with respect to the set A which is a specialty of this example and will not be guaranteed in general.

Now we turn our attention to the probability density function of reactive trajectories $\rho_{AB}(x, y)$ for this example. The panels in Figure 3.12 illustrate this situation for $\beta = 1.67$ (high temperature) as computed via DNS. In Figure 3.13 we depict the probability density function of reactive trajectories from TPT computed at two different temperatures. The left panel shows the density for a low temperature ($\beta = 6.67$) and the lower one for a high temperature ($\beta = 1.67$). The first observation is that both densities attain their maximum in the shallow minima.
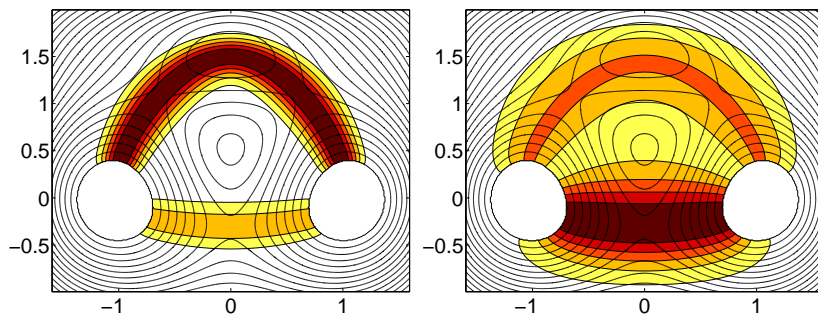
Figure 3.14.: Streamlines of the probability current of reactive trajectories colored according to the intensities of the probability current on the isocommittor $\frac{1}{2}$ surface for two different temperatures. Left: At the low temperature $\beta = 6.67$ the upper channel is the preferred reaction channel. Right: At the high temperature $\beta = 1.67$ most of the reactive trajectories take the lower channel.

This is because the shallow minima catches the dynamics on its way from A to B. As a consequence, the reactive trajectories spend a long time within this region and therefore the probability to encounter a reactive trajectory there increases. However, one can see that at the high temperature that there is a certain probability to encounter a reactive trajectory in the lower channel. But which reaction channel does the dynamics prefer depending on the temperature? From the viewpoint of the density $\rho_{AB}(x, y)$ we cannot answer this question since the long residency of reactive trajectories in the vicinity of the shallow minima spoils the information about the relative *number* of reactive trajectories going there.

To answer the question of which reaction channel is preferred at different temperatures we must consider the probability current of reactive trajectories $J_{AB}(x, y)$. In Figure 3.14 we show the transition tubes computed via its streamlines with colors induced by the intensity of the probability current on the isocommittor surface $\frac{1}{2}$, using the procedure explained in Section 3.5.3. One can clearly see that the transition tubes give the desired information. At the low temperature (left panel) the preferred transition channel is the upper one and at the high temperature (right panel) it is the lower one. This result is consistent with observations made in [73]. We complete this example by stating the reaction rate for the two temperatures in Table 3.3. As in the previous examples we choose the isocommittor surface $\frac{1}{2}$ for the rate computations via (3.43).

This example shows that TPT is able to handle situations with multiple reaction channels, possibly with intermediate metastable states along them, and can distinguish which channel is preferred depending on the temperature (entropic switching). It also shows that all the objects provided by TPT – the probability density of the reactive trajectories, their probability current and the associated streamlines – are necessary (and sufficient) to understand the mechanism of the reaction, while $\rho_{AB}(x, y)$ alone is not.

	$\beta = 6.67$	$\beta = 1.67$
rate via (3.29)	$9.47 \cdot 10^{-8}$	$1.912 \cdot 10^{-2}$
rate via (3.30)	$9.22 \cdot 10^{-8}$	$1.924 \cdot 10^{-2}$
rate via DNS		$(1.918 \pm 0.052) \cdot 10^{-2}$

Table 3.3.: Reaction rates for the three-hole potential for $\beta = 6.67$ and $\beta = 1.67$. One can see that for $\beta = 1.67$ the rate computed via DNS ($N = 10^5$) is consistent with those predicted from TPT. For $\beta = 6.67$ the rate is so small that any computation via DNS would lead to totally unreasonable effort (to obtain $N = 10^5$ reactive trajectories, it would require to generate a long trajectory of length $T \approx 10^5/k_{AB} = 10^{12}$). The computations via finite difference discretization of (3.24) take only a few seconds on a standard PC.
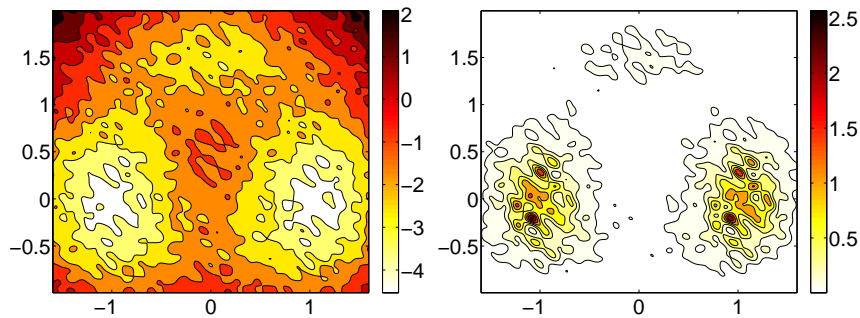
Figure 3.15.: Left: Contour plot of the perturbed three-hole potential in (3.46). Right: Contour plot of the associated Gibbs probability density function $Z^{-1}e^{-\beta\tilde{V}(x,y)}$ at $\beta = 1.67$. Results for the perturbation parameters $n = 5$ and $\delta = 0.05$.

3.7.2. Diffusion in a Rough Three-Hole Potential

In this section we are interested in the ensemble of reactive trajectories and its statistical properties for a Smoluchowski process in a *rough* potential landscape. To make things comparable, we perturbed the three-hole potential from the previous section by adding a periodic function with randomly drawn coefficients. To be more precise, we consider the potential

$$\tilde{V}(x,y) = V(x,y) + \sum_{k,l=1}^{n} \left[c_{kl} \cos(2\pi(kx + ly)) + d_{kl} \sin(2\pi(kx - ly)) \right], \quad (3.46)$$

where $V(x,y)$ is the three-hole potential in (3.45) and the real coefficients $c_{kl}, d_{kl}, 1 \leq k, l \leq n$ are drawn from a normal distribution $\mathcal{N}(0, \delta^2)$ with variance δ^2. For our numerical experiments, we chose $n = 5$ and $\delta = 0.05$. As one can see in Figure 3.15 the perturbed potential still exhibits three regions of attraction separated by a multitude of small barriers.

The guiding question is whether the entropic switching behavior is conserved despite the perturbation and, in particular, in which way the transition channels deviate from those resulting in a smooth potential (cf. Fig. 3.14). As the sets A and B, we chose the same sets as in the smooth three-hole potential example. The
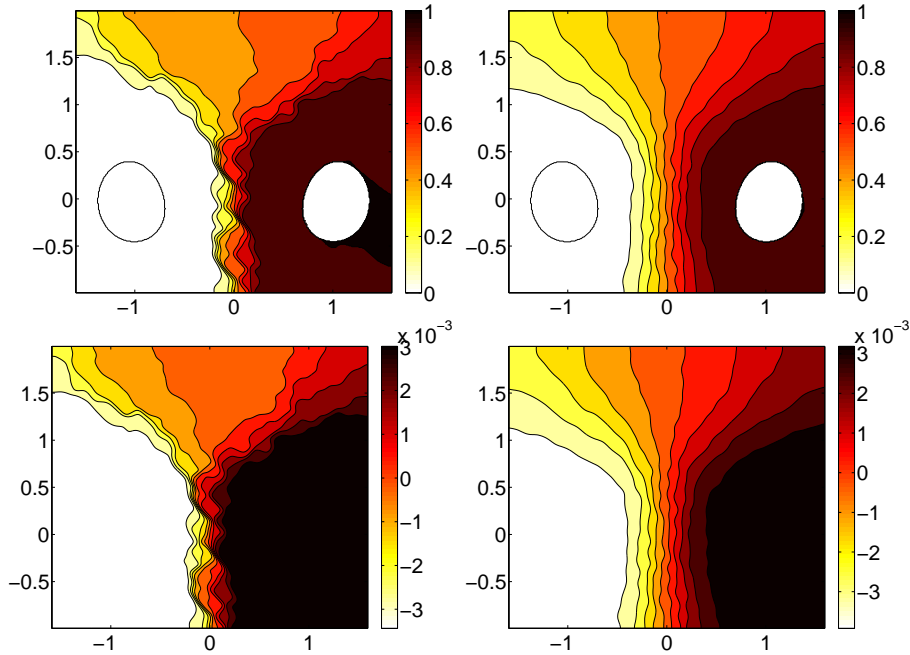
Figure 3.16.: Contour plot of the committor function $q(x, y)$ at low temperature $\beta = 6.67$ (upper left panel) and at high temperature $\beta = 1.67$ (upper right). The second row shows the contour plot of the eigenvector associated with the first non-trivial right eigenvalue of the discretization matrix $\overline{D}_h$: left lower panel at $\beta = 6.67$ and right lower panel at $\beta = 1.67$. Obviously, the geometry of the level sets of the eigenvector and the level sets of the committor function is very similar, respectively.

first row in Figure 3.16 shows the (forward) committor function at low temperature $\beta = 6.67$ (left upper panel) and at high temperature $\beta = 6.67$ (right upper panel). As expected, the lower the temperature the bigger the impact of the roughness of the potential landscape on the committor function because at low temperature the dynamics gets trapped in any local minima. Notice that even for the perturbed potential, the geometry of the level sets of the eigenvector associated with the first non-trivial right eigenvalue of the discretization matrix[1] $\overline{D}_h$ (shown in the second row of Figure 3.16) is very similar to the geometry of the level sets of the corresponding committor function, respectively.

We have seen that in the smooth three-hole potential example in Section 3.7.1, the distribution ρ_{AB} of reactive trajectories does not allow to make any prediction about the preferred reaction channel. As one can see in the panels of Figure 3.17, in the case of a rough potential landscape the distribution ρ_{AB} does not even give an idea of a single reaction channel. However, as illustrated in the panels of Figure 3.18, the streamlines of the probability current of reactive trajectories reveal the reaction channels and, furthermore, show that despite the perturbation of the landscape the global transition behavior is comparable to the transition behavior in the smooth potential landscape.

---

[1] $\overline{D}_h$ is meant to be the matrix which results from the finite difference discretization of the operator $\mathcal{L}_{bw}$ on the *entire* domain Ω under incorporation of the Neumann boundary conditions.
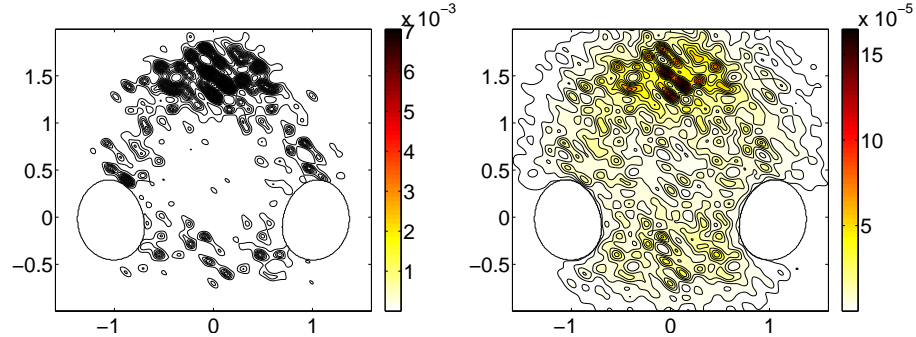
Figure 3.17.: In this figure we illustrate the probability density function $\rho_{AB}(x, y)$ of the reactive trajectories in the perturbed three-hole potential for two different temperatures. Left: low temperature $\beta = 6.67$; Right: high temperature $\beta = 1.67$.
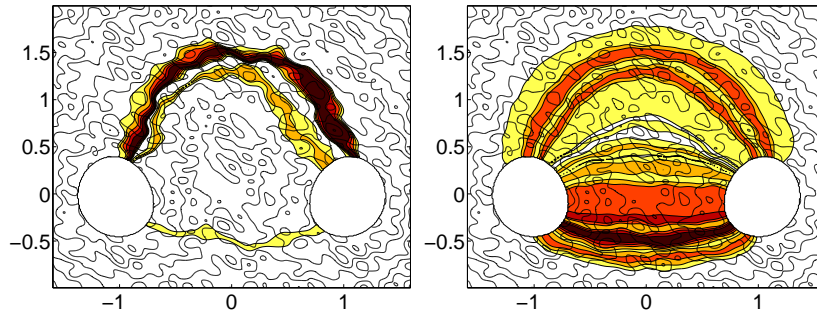
Figure 3.18.: Streamlines of the probability current of reactive trajectories in the perturbed three-hole potential colored according to the intensities of the probability current on the isocommittor $\frac{1}{2}$ surface for two different temperatures. Left: Despite the perturbation, at the low temperature $\beta = 6.67$ the upper channel is the preferred reaction channel whereas at the high temperature $\beta = 1.67$ (right panel) most of the reactive trajectories still take the lower channel.

δ^2	0.01	0.05	0.1	0.2	0.5
k_{AB}	$1.91 \cdot 10^{-2}$	$1.79 \cdot 10^{-2}$	$1.08 \cdot 10^{-2}$	$4.45 \cdot 10^{-3}$	$2.42 \cdot 10^{-5}$

Table 3.4.: The transition rate k_{AB} computed via (3.30) as a function of the variance δ^2. Results for $\beta = 1.67$ and $n = 5$.

We end this example by stating in Table 3.4 the transition rate k_{AB} (computed via (3.30)) as a function of the variance δ^2 of the normal distribution $\mathcal{N}(0, \delta^2)$. The decrease of the transition rate as δ^2 increases can be explained by noting that in a rough potential landscape the dynamics gets trapped in each local minima and, thus, as the roughness increases it becomes more difficult for the dynamics to make a transition from A to B.

3.8. Different Time-Scales: Fast-Slow Diffusion in a Double-Well Potential

In the last example for the Smoluchowski dynamics we consider a diffusion process with two variables subject to different friction coefficients leading to two different time scales. For this purpose we consider a process generated by

$$
\begin{aligned}
\dot{x}(t) &= -\frac{\partial V(x(t), y(t))}{\partial x} + \sqrt{2\beta^{-1}}\, \eta_x(t) \\
\epsilon \dot{y}(t) &= -\frac{\partial V(x(t), y(t))}{\partial y} + \sqrt{2\beta^{-1}\epsilon}\, \eta_y(t).
\end{aligned} \tag{3.47}
$$

This system is a special case of (3.22) with $\gamma_x = 1$ and $\gamma_y \equiv \epsilon > 0$. For $\epsilon \ll 1$, the variable y is fast compared to x. For details see [83]. Despite the different time scales, the equilibrium distribution still is given by the Boltzmann-Gibbs density $Z^{-1} e^{-\beta V(x,y)}$ for every value of $\epsilon > 0$. For the potential V, we choose a double-well potential in y-direction which is coupled to a harmonic potential in x-direction

$$
V(x, y) = 5(y^2 - 1)^2 + 1.25(y - \tfrac{1}{2}x)^2. \tag{3.48}
$$

The potential attains two local minima at $(-2, -1)$ and $(2, 1)$ which are separated by a saddle point at $(0, 0)$. For our computations we choose $\epsilon = 0.1$, so that the dynamics in the y-direction is roughly ten times faster than in the x-direction. The potential energy surface is shown in Figure 3.19 together with equilibrium probability density function for $\beta = 1$.

The key for understanding the reaction is to realize that the important barriers for the dynamics are the barriers in the y-direction. Suppose we fix an $x = x_0$ and consider the restricted potential $V(x_0, y)$, which then only depends on y. Due to the separation of time scale, this is the potential that the y-variable effectively feels while the x-variable is quasi-frozen and evolving only on a longer time scale. Consider the energy barriers for different x_0 in $V(x_0, y)$; denoting these barriers by $\Delta V(x_0)$, it can be seen that $\Delta V(x_0)$ attains a local maximum at $x_0 = 0$, and decreases as $|x_0|$ increases which is illustrated in Figure 3.20.

Because of this feature, one expects that the reactive trajectories will tend to wait near the reactant state A until they reach a fiber in the y-direction with a low barrier
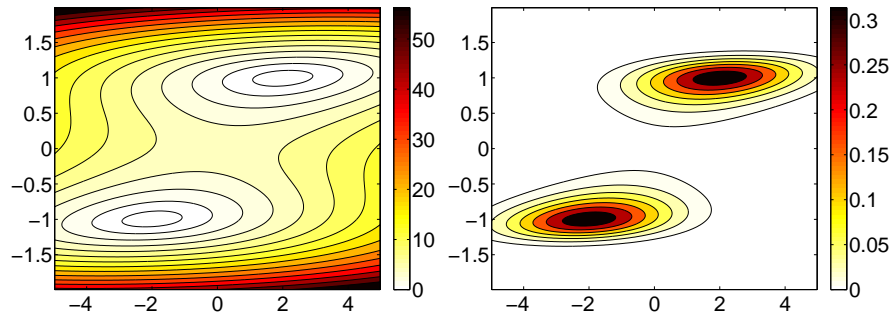
Figure 3.19.: Left: Contour plot of the potential (3.48). Right: Contour plot of Boltzmann-Gibbs equilibrium probability density function. Results for $\beta = 1$.
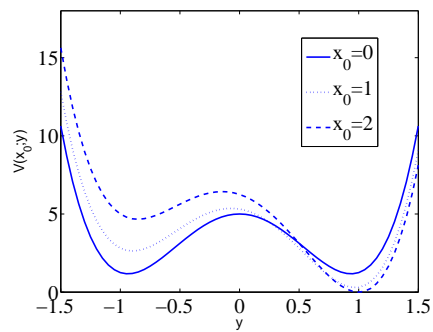
Figure 3.20.: The potential $V(x_0, y)$ of the fast-slow example as a function of y for $x_0 = 0$, $|x_0| = 1$ and $|x_2| = 2$. Thus, the barrier to overcome increases as $|x_0|$ increases.
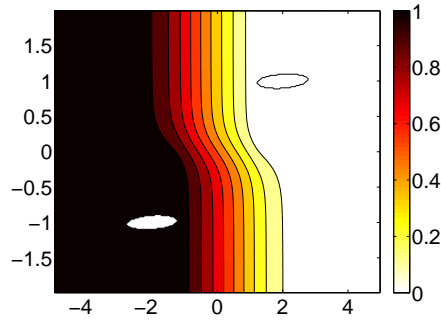
Figure 3.21.: Contour plot of the isocommittor function for the fast-slow example with $\beta = 1$ and $\epsilon = 0.1$.
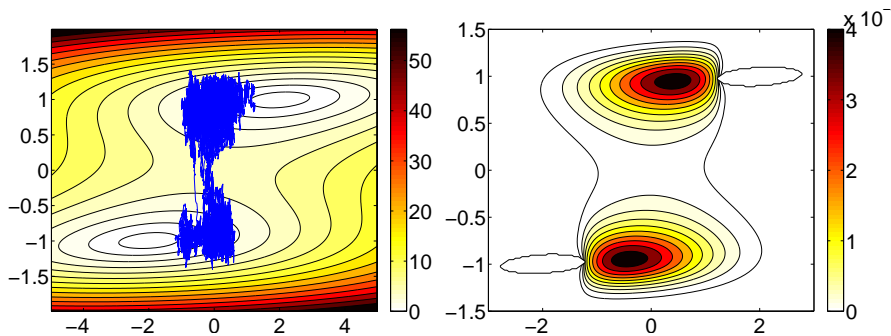
Figure 3.22.: Left: A typical reactive trajectories in (3.47). Right: Probability density function of reactive trajectories. Results for $\beta = 1$ and $\epsilon = 0.1$.

$\Delta V(x_0)$ to hop over. Since there is two groups of such fibers on either sides of the y-axis, there should be two predominantly vertical reaction channels. Let us now confirm this intuitive picture via TPT.

The contour plot of the committor function is shown in Figure 3.21. Consistent with the separation of time-scale it shows that the isocommittor surfaces are predominantly vertical except in a narrow strip around the x-axis.

A typical reactive trajectory is shown in the left panel of Figure 3.22. Consistent with the intuitive picture given above, because of the separation of time-scale, the trajectory spends a relatively long amount of time in the vicinity of the states A and B and a relatively short amount of time transiting between these states (the latter motion being predominantly in the fast y-direction). As explained in the previous example, this behavior of the dynamics affects the probability density function of the reactive trajectories which is peaked in the regions where the trajectories spend most time. The right panel of Figure 3.22 shows this effect. The probability density function $\rho_{AB}(x)$ is bimodal and attains local maxima in regions close to the states A and B. Notice that $\rho_{AB}(x)$ does not give much information about the reaction channels.

To visualize the reaction channels we proceed similarly as in the previous examples and choose the dividing surface $S = \{(x, 0) : -1.5 \leq x \leq 1.5\}$ to compute the intensity of the probability current used to color the streamlines of this current. The results are shown in Figure 3.23. Consistent with the intuitive picture given above, there are two predominantly vertical channels. Notice that most of the flux across S
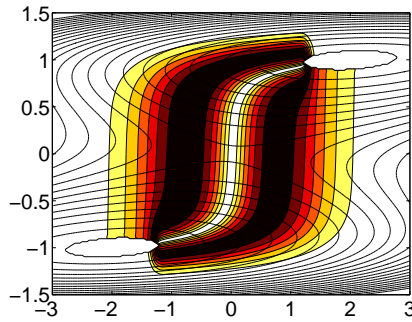
Figure 3.23.: Streamlines of the probability current colored according to the intensities on the dividing surface $S = \{(x, 0) : -1.5 \leq x \leq 1.5\}$. Result for $\beta = 1$.

k_{AB} via (3.38)	$3.278 \cdot 10^{-2}$
k_{AB} via (3.39)	$3.239 \cdot 10^{-2}$
k_{AB} via DNS	$(3.189 \pm 0.076) \cdot 10^{-2}$

Table 3.5.: Reaction rate computed for the fast-slow potential at $\beta = 1$. Results of DNS based on $N = 10^5$ reactive trajectories.

goes either at the left or the right of the saddle point.

Finally, the reaction rates predicted by TPT and computed by DNS are given in Table 3.5.

This example illustrates the subtle effects that time-scale separation may have on the reaction pathway and shows that TPT is able to capture these effects.

3.9. Langevin Dynamics

In this section we apply TPT to an example of the Langevin equation (3.31). Before we present in detail our numerical experiments, we want to point out again, that we can not analytically guarantee the differentiability of the forward and backward committor function as a solution of a hypoelliptic, mixed-boundary value problem of the form in A.3. However, the following numerical results show that for the particular choice of the domain Ω and the parameters of the Langevin dynamics the committor functions are sufficiently smooth.

Here we assume that $(x, v) \in \mathbb{R} \times \mathbb{R}$ and we set $\gamma_1 = m_1 = 1$ (Notice that if the mass is equal to one, the momentum is identical with the velocity of the particle). We also assume that the potential is the double-well potential given by

$$V(x) = (x^2 - 1)^2 \tag{3.49}$$

with minima at $x = -1$ and $x = 1$ and a local maximum at $x = 0$. In Figure 3.24 we show the Hamiltonian function $H(x, v)$ associated with the double-well potential in (3.49) and the Boltzmann-Gibbs equilibrium probability density function for $\beta = 1$. Although the structure of the potential is very simple, it allows us to illustrate how the reaction pathway depends on the friction constant γ. Keeping the temperature constant, we study three different scenarios: the high, medium and low friction cases.
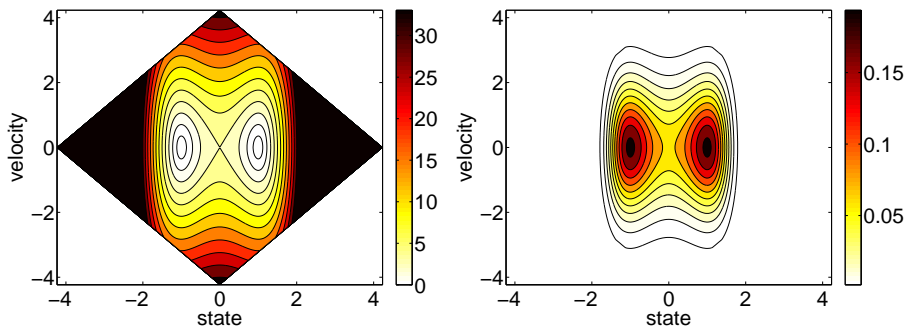
Figure 3.24.: Left: The contour plot shows the Hamiltonian $H(x, v)$ associated with the double-well potential in (3.49). Right: Contour plot of the Boltzmann-Gibbs equilibrium probability density function $Z^{-1}e^{-\beta H(x,v)}$. Results for $\beta = 1$.

	k_{AB} via DNS	k_{AB} via (3.39)	k_{AB} via (3.38)
$\gamma = 1$	$(3.833 \pm 0.061) \cdot 10^{-2}$	$3.778 \cdot 10^{-2}$	$3.721 \cdot 10^{-2}$
$\gamma = 2$	$(4.019 \pm 0.171) \cdot 10^{-2}$	$3.918 \cdot 10^{-2}$	$3.898 \cdot 10^{-2}$
$\gamma = 5$	$(2.634 \pm 0.106) \cdot 10^{-2}$	$2.523 \cdot 10^{-2}$	$2.483 \cdot 10^{-2}$
$\gamma = 10$	$(1.534 \pm 0.032) \cdot 10^{-2}$	$1.460 \cdot 10^{-2}$	$1.361 \cdot 10^{-2}$

Table 3.6.: Reaction rates computed for several friction coefficients via DNS of the Langevin dynamics and via TPT using (3.39) or (3.38). All computations are done for the same temperature $\beta = 1$.

For reasons of numerical stability we have to introduce a coordinate transformation which amounts to rotate the mesh by $\pi/4$ and solve the committor equation (3.32) on this mesh, see Appendix: Section A.1.3. This explains our unusual choice of the diamond-shaped domain Ω as visible in Figure 3.24. The reactant state A and the product state B are determined in a similar way as in the previous section, i.e., their union include all states (x, v) with $H(x, v) < 1$.

Before we start with a detailed description of the reaction pathways, we state the reaction rates in Table 3.6 computed for different friction coefficients via TPT and compare them with those obtained via direct numerical simulation of the Langevin dynamics (3.31). As one can see in Table 3.6 the rates agree within numerical error.

3.9.1. High Friction Case, $\gamma = 10$

As mentioned in Section 2.1.10, Langevin leads to Smoluchowski dynamics in the high friction limit $\gamma \to \infty$. In the present case, the overdamped equation is the one-dimensional equation

$$\dot{x}(t) = 4\gamma^{-1}(x(t) - x^3(t)) + \sqrt{2\beta^{-1}\gamma^{-1}}\, \eta(t) \qquad (3.50)$$

Since (3.50) involves the position $x(t)$ but not the velocity $v(t)$, in this limit the probability to reach the set B before the set A conditional on starting at point (x_0, v_0) must be independent of the velocity v_0. In other words, for large enough γ, $q(x, v) \approx q(x)$ where $q(x)$ is the committor function of (3.50) and the level sets of
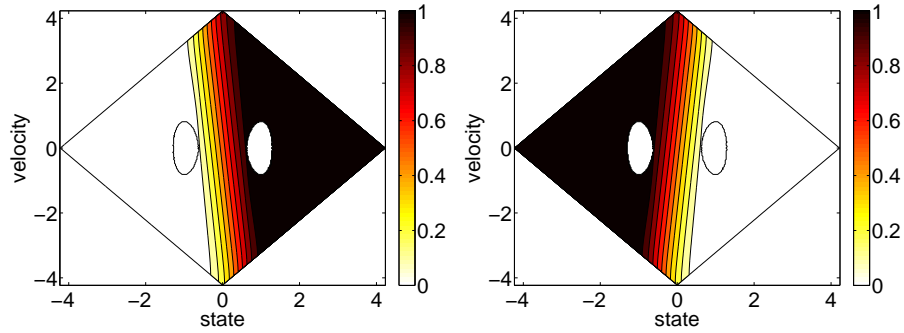
Figure 3.25.: Left: Contour plot of the committor function $q(x, v)$. Right: Contour plot of the backward committor function $q_b(x, v) = 1 - q(x, -v)$. Results for $\beta = 1$, $\gamma = 10$.
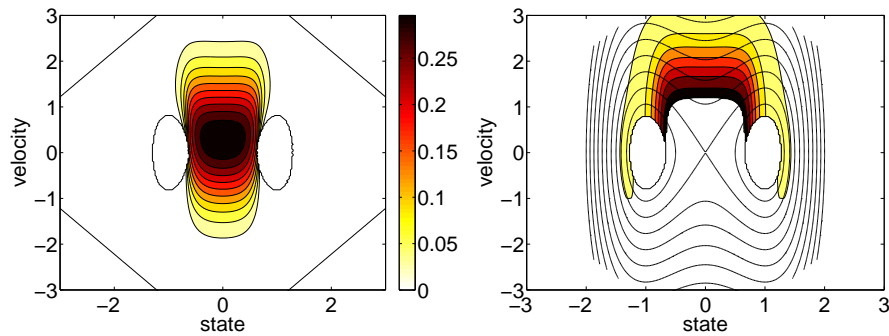
Figure 3.26.: Left: Probability density function of reactive trajectories $\rho_{AB}(x, v)$. Right: Reaction tube based on streamlines of the probability current colored according to the intensity of the probability current on the dividing surface $S = \{(0, v) : -3 \leq v \leq 3\}$. Results for $\beta = 1, \gamma = 10$.

the committor function are (almost) parallel to the velocity axis. This is confirmed by the results shown in Figure 3.25. The little deviations near the upper and lower corners are due to the Neumann boundary conditions which forces the level sets of the committor function to be perpendicular to the boundaries. Notice that $q(x, v) \approx q(x)$ also implies that $q_b(x, v) \approx 1 - q(x)$. This is also confirmed by the results shown in Figure 3.25.

The left panel of Figure 3.26 is a contour plot of the probability density function of reactive trajectories $\rho_{AB}(x, v)$. This density is peaked around the saddle point of the Hamilton function $H(x, v)$ at $(x, v) = (0, 0)$ and only shows a slight up-down asymmetry, consistent with the velocity playing no role in the mechanism of the reaction. In the right panel of Figure 3.26 we show the streamlines of the probability current (3.37) of reactive trajectories colored as in the previous example in function of the intensity of the current on $S = \{(0, v) : -3 \leq v \leq 3\}$. The reaction channel is predominantly horizontal.

3.9.2. Medium Friction Case, $\gamma = 1$

In the medium friction case, the reaction pathway changes dramatically and now involve the velocity as well as the position. This is apparent from the contour plot
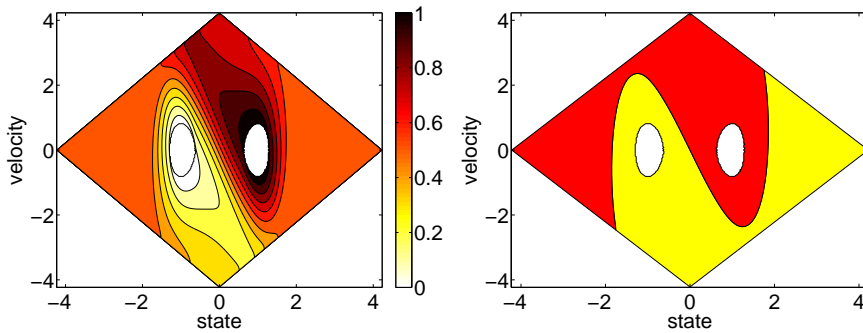
Figure 3.27.: Left: Contour plot of the committor function $q(x,v)$ for $\beta = 1$, $\gamma = 1$. Right: Decomposition of the domain Ω in phase-space into the two regions $\{(x,v) : q(x,v) < 0.5\}$ (light regime) and $\{(x,v) : q(x,v) > 0.5\}$ (dark regime). The dividing curve is the isocommittor $\frac{1}{2}$ surface where $q(x,v) = \frac{1}{2}$.

of the committor function $q(x,v)$ shown in the left panel of Figure 3.27 and the partition of the domain by the isocommittor $\frac{1}{2}$ surface shown in the right panel. Clearly, the committor function $q(x,v)$ now depends crucially on the velocity, unlike in the high friction case. In fact, the partition of the domain by the isocommittor $\frac{1}{2}$ surface is simple to understand: it is the ghost of the partition of the domain by the deterministic dynamics

$$\begin{cases} \dot{x}(t) = v(t), \\ \dot{v}(t) = -\dfrac{\partial V(x(t))}{\partial x} - \gamma v(t). \end{cases} \tag{3.51}$$

Because $\gamma > 0$ in this equation, every trajectory initiated at a point $(x,v) \in \mathbb{R}^{2d} \setminus (A \cup B)$ will asymptotically end up either in state A or in state B. Figure 3.28 shows the partition of phase-space that this induces: the dark grey region contains all the points which end up in B and the light grey region those which end up in A. Clearly, the resulting partition is close to the one by the isocommittor function $\frac{1}{2}$ shown in Figure 3.27, which indicates that the temperature is small enough so that it does not really affect this partition, except for wiping out the most external strips in the left and right corner in Figure 3.28 (though this wiping effect is also due to the external boundary conditions imposed when solving for $q(x,v)$ and is less pronounced in the low friction case, see Figure 3.31). Of course, in the absence of noise, there is no reaction, so the noise-free Langevin equation (3.51) is limited in the information that it can provide about the reaction and the full arsenal of TPT remains necessary to understand it.

The probability density function of reactive trajectories $\rho_{AB}(x,v)$ is shown in Figure 3.29. As expected we observe that the distribution is peaked around a point with $x = 0$ and $v > 0$, that is, around the maximum of the potential but in the region of positive velocities since these are needed to go from A to B.

The reaction tube from A to B is shown in Figure 3.30. This tube too indicates that the reaction pathway is asymmetric in the velocity (and in particular the reaction from A to B studied here is different from the one from B to A – the reaction tube for the latter can be visualized by flipping Figure 3.30 upside-down, that is, by
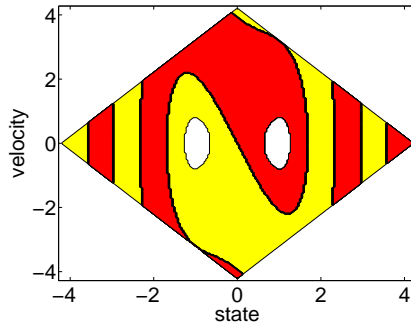
Figure 3.28.: Partition into regions that are asymptotically attracted to sets A or B, respectively, for the noise free Langevin equation (3.51). Notice the similarity in the core with the partition by the isocommittor $\frac{1}{2}$ surface shown in the right panel in Figure 3.27.
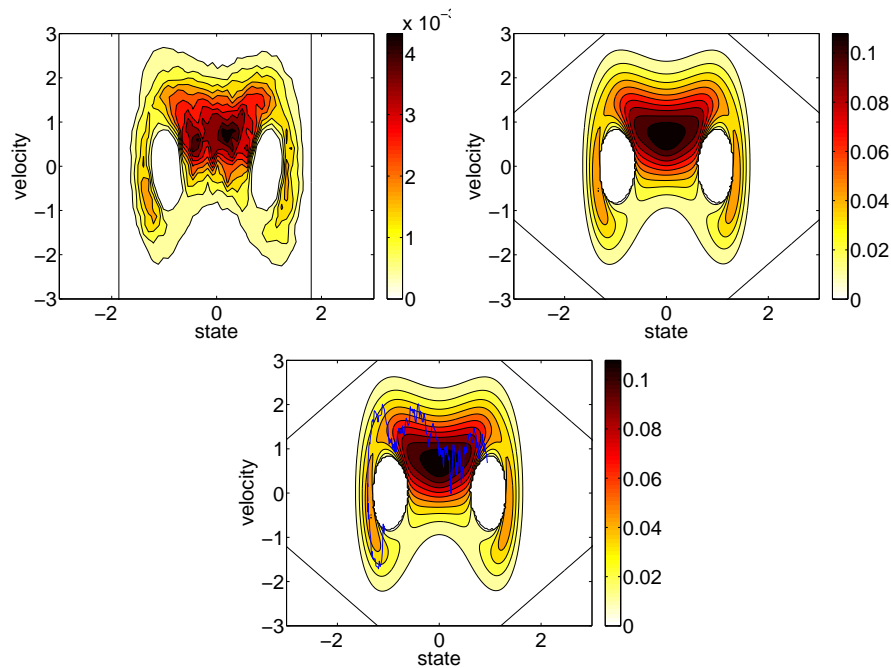
Figure 3.29.: Contour plot of the probability density function of reactive trajectories $\rho_{AB}(x, v)$ when $\beta = 1$, $\gamma = 1$. Top left: Result via DNS based on 300 reactive trajectories and a 40×40 box decomposition of the domain. Top right: Results from TPT. Bottom middle: A typical reactive trajectory embedded into the contour plot of $\rho_{AB}(x, v)$
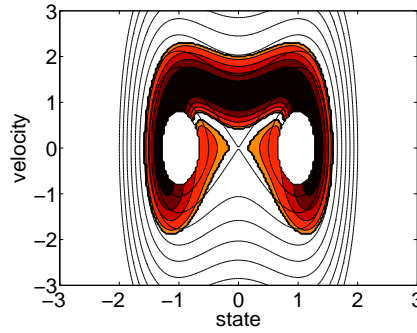
Figure 3.30.: Reaction tube based on streamlines of the probability current colored according to the intensity of the probability current on the dividing surface $S = \{(0, v) : -3 \leq v \leq 3\}$. Results for $\beta = 1$, $\gamma = 1$.
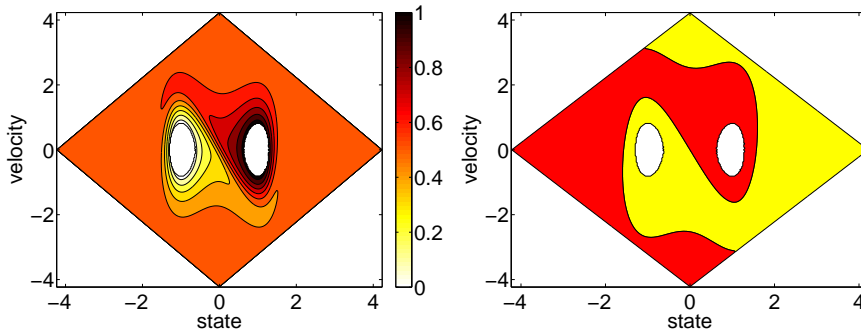
Figure 3.31.: Left: Contour plot of the committor function $q(x, v)$ in the low friction case. Right: Decomposition of the domain into the two regions $\{(x, v) : q(x, v) < 0.5\}$ (light regime) and $\{(x, v) : q(x, v) > 0.5\}$ (dark regime). The dividing curve is the isocommittor $\frac{1}{2}$ surface. Results for $\beta = 1$, $\gamma = 0.001$.

reverting the velocity.)

3.9.3. Low Friction Case, $\gamma = 0.001$

When the friction is as low as $\gamma = 0.001$, Langevin dynamics is now close to Hamiltonian dynamics. Nevertheless, at sufficiently long time scales the damping will force the dynamics to get attracted to the vicinity of the minima of the energy landscape which lie inside the states A and B, and the noise will eventually induce reactions between these states. Figure 3.31 shows the committor function $q(x, v)$ and the decomposition of the domain into the two regions $\{(x, v) : q(x, v) < 0.5\}$ and $\{(x, v) : q(x, v) > 0.5\}$ (dark grey) in the low friction case. Figure 3.32 shows the probability density function of reactive trajectories $\rho_{AB}(x, v)$ and the reaction tube. In the present case, the streamlines of the probability current of the reactive trajectories (not shown) are very winding around the states A and B and turn out to be difficult to compute accurately.
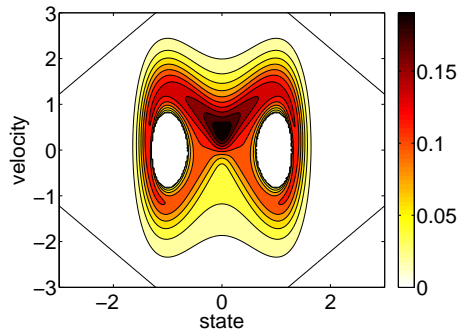
Figure 3.32.: Contour plot of the probability density function of reactive trajectories $\rho_{AB}(x,v)$. Result for $\beta = 1, \gamma = 0.001$.

3.9.4. Rough Potential Landscape

In the last example, we study the Langevin dynamics $(\beta = 1, \gamma = 1)$ in a perturbed double-well potential given by

$$\tilde{V}(x) = (x^2 - 1)^2 + \sum_{k=1}^{n} \big[a_k \cos(kx) + b_k \sin(kx) \big], \tag{3.52}$$

where the real coefficients $a_k, b_k, k = 1, \ldots, n$ are drawn from a normal distribution $\mathcal{N}(0, \delta^2)$ with variance δ^2 and mean zero. For our numerical example we chose $n = 20$ and $\delta = 0.01$. In the left top panel of Figure 3.33 we show the graph of the perturbed double-well potential together with the associated Hamiltonian (right top panel) and the associated Gibbs probability density function (bottom panel). To make things comparable, we chose the same mesh discretization of the phase-space domain Ω and the same sets A and B as in the unperturbed double-well potential case. One can see in the left panel of Figure 3.34 that the level sets of the forward committor function and, in particular, the $\frac{1}{2}$-committor surface (right panel) are rough but their overall shape is more or less comparable to the shape of the level sets depicted in Figure 3.27, respectively. As in opposite to the smooth case, here the probability density function of reactive trajectories $\rho_{AB}(x,v)$ (see top left panel of Figure 3.35) exhibits several peaks which are due to the several local minima in the perturbed potential landscape in which reactive trajectories get trapped on their way from A to B. A typical AB-reactive trajectory is given in the top right panel of Figure 3.35. Finally, we illustrate the resulting transition tube in the bottom panel of Figure 3.35.
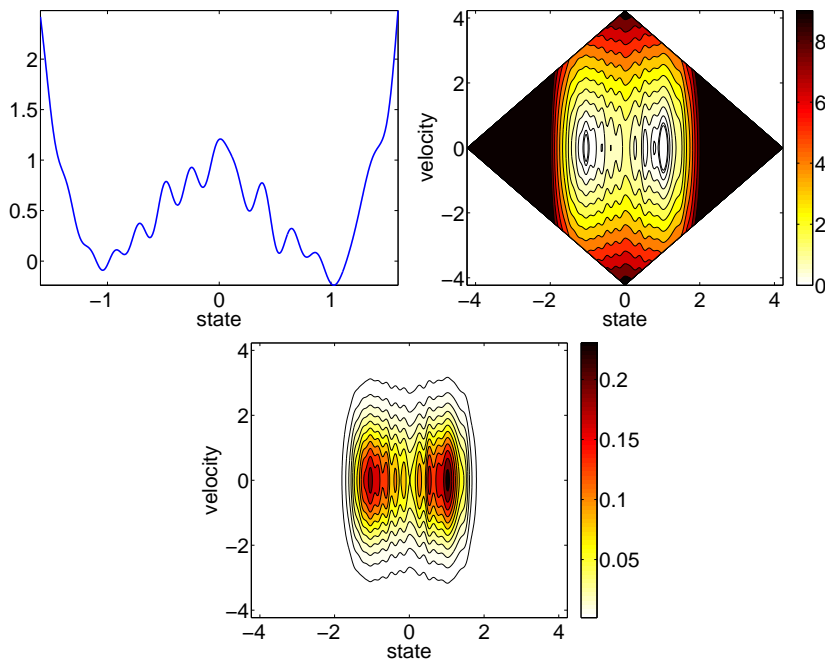
Figure 3.33.: Top left: The graph of the perturbed double-well potential in (3.52). Top right: Contour plot of the Hamiltonian $\tilde{H}(x,v)$ associated with the perturbed double-well potential. Bottom: Contour plot of the Gibbs equilibrium probability density function $\tilde{Z}^{-1}e^{-\beta\tilde{H}(x,v)}$. Results for $\beta = 1$.
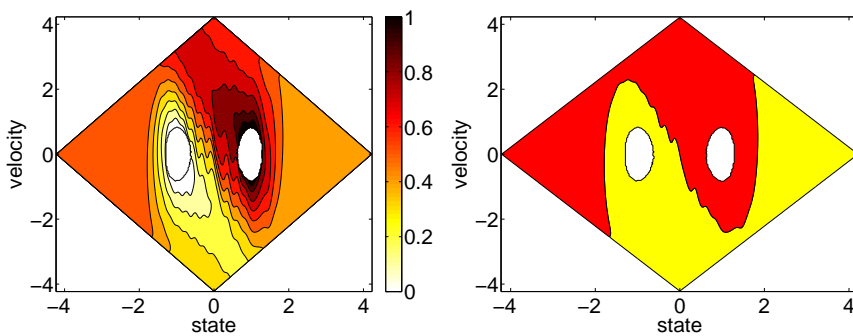
Figure 3.34.: Left: Contour plot of the committor function $q(x,v)$ for $\beta = 1$, $\gamma = 1$. Right: Decomposition of the domain Ω in phase-space into the two regions $\{(x,v) : q(x,v) < 0.5\}$ (light regime) and $\{(x,v) : q(x,v) > 0.5\}$ (dark regime). The dividing curve is the isocommittor $\frac{1}{2}$ surface where $q(x,v) = \frac{1}{2}$.
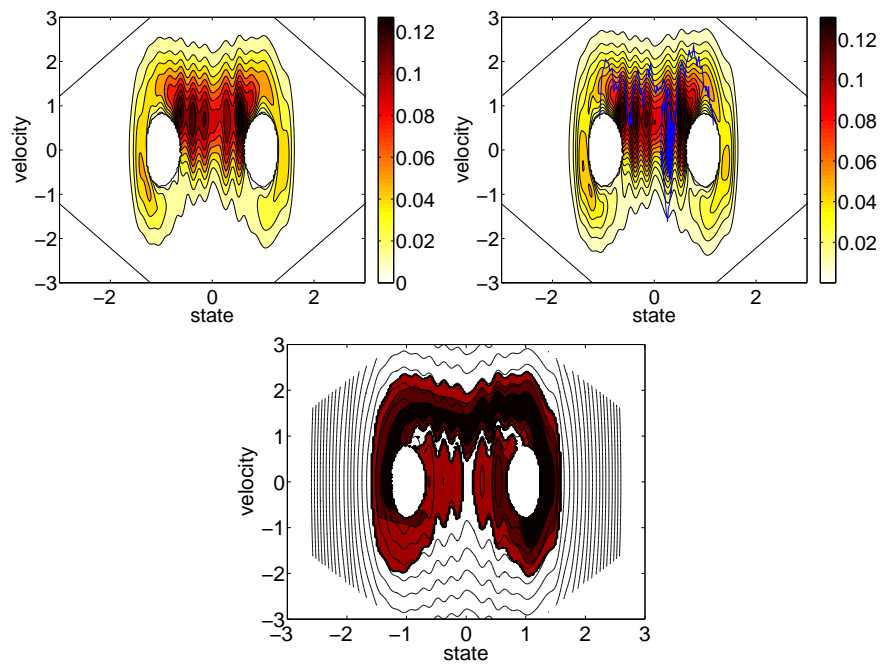
Figure 3.35.: Top left: Contour plot of the probability density function of reactive trajectories $\rho_{AB}(x,v)$. Top right: A typical reactive trajectory embedded in the contour plot of $\rho_{AB}(x,v)$. Bottom middle: Reaction tube based on streamlines of the probability current colored according to the intensity of the probability current on the dividing surface $S = \{(0,v) : -3 \leq v \leq 3\}$. Results for $\beta = 1$, $\gamma = 1$.

4. Transition Path Theory for Markov Jump Processes

Continuous-time Markov chains on discrete state-space have an enormous range of applications. In recent years, especially, with the explosion of new applications in network science, Markov chains have become the tool of choice not only to model the dynamics on these networks but also to study their topological properties [2, 68]. In this context, there is a need for new methods to analyze Markov chains on large state-space with no specific symmetries, as relevant for large complex networks.

A natural starting point to analyze a Markov chain is to use spectral analysis. This is especially relevant when the chain displays metastability, as was shown in [12, 24] in the context of time-reversible chains. By definition, the generator of a metastable chain possesses one or more clusters of eigenvalues near zero, and the associated eigenvectors provide a natural way to partition the chain (and hence the underlying network) in cluster of nodes on which the walker remains for a very long time before finding its way to another such cluster. This approach has been used not only in the context of Markov chains arising from statistical physics (such as e.g. glassy systems [4, 11] or bio-molecules [81]), but also in the context of data segmentation and embedding [84, 62, 78, 6, 26, 16, 55]. The problem with the spectral approach, however, is that not all Markov chains of interest are time-reversible and metastable, and when they are not, the meaning of the first few eigenvectors of the generator is less clear.

In this chapter, we take another approach which does not require metastability and applies for non-time-reversible chains as well. The basic idea is to single out two disjoint subsets of nodes of interest in the state-space of the chain and ask what is the typical mechanism by which the walker transits from one of these subsets to the other? We can also ask what is the rate at which these transitions occur, etc. The first object which comes to mind to characterize these transitions is the path of maximum likelihood by which they occur. However, this path can again be not very informative with respect to its relevance for the transition process. For an attempt to characterize transition pathways by means of the likelihood by which they occur see Chapter 6.

The main objective of this chapter, however, is to adapt the framework of transition path theory (TPT) on discrete state space which allows to give a precise meaning to the question of finding typical the mechanism and rate of transition even in chains which are neither metastable nor time-reversible. We will focus only on continuous-time Markov chains, but we note that the results can be straightforwardly extended to the case of discrete-time Markov chains.

Besides the illustration of the output of the theory on a test example, we will apply discrete TPT in order to study the conformational dynamics of the bio-molecule glycine as well as the dynamics of a genetic toggle switch model.

We want to point out that tools of TPT presented here can be used for data

segmentation as well. In this context, TPT provides an alternative to Laplacian eigenmaps [78, 6] and diffusion maps [16] which have become very popular recently in data analysis. In this thesis, we will not, however, develop these ideas any further.

4.1. Theoretical Aspects

4.1.1. Preliminaries: Notations and Assumptions

We will consider a Markov jump process on the countable state-space S with infinitesimal generator (or rate matrix) $L = (l_{ij})_{i,j \in S}$:

$$\begin{cases} l_{ij} \geq 0 & \text{for all } i, j \in S, i \neq j \\ \sum_{j \in S} l_{ij} = 0 & \text{for all } i \in S. \end{cases}$$

as introduced in Section 2.2. We assume that this process is irreducible and ergodic with respect to the unique, strictly positive stationary distribution $\pi = (\pi_i)_{i \in S}$. We will denote by $\{X(t)\}_{t \in \mathbb{R}}$ an equilibrium sample path (or trajectory) of the Markov jump process, i.e. any path obtained from $\{X(t)\}_{t \in [T,\infty)}$ by pushing back the initial condition, $X(T) = x$, at $T = -\infty$. Throughout that chapter, we do not assume reversibility.

For the algorithmic part of this chapter, it will be convenient to use the notations and concepts of Graph Theory. We will mainly consider directed graphs $G = G(S, E)$ where the vertex set S is the set of all states of the Markov jump process and two vertices i and j are connected by a *directed edge* if $(i, j) \in E \subseteq (S \times S)$. Let $E' \subset E$ be a subset of edges of a graph $G = G(S, E)$, then we denote by $G(S', E')$ the *induced subgraph*, i.e. the graph which consists of all edges in E' and the vertex set

$$S' = \{i \in S : \exists j \in S \text{ s.t. } (i, j) \in E' \text{ or } (j, i) \in E'\}.$$

We also recall that:

Definition 4.1.1. *A directed pathway $w = (i_0, i_2, \ldots, i_n)$, $i_j \in S, j = 0, \ldots, n$ in a graph G is a finite sequence of vertices such that $(i_j, i_{j+1}) \in E, j = 0, \ldots, n-1$. A directed pathway w is called* simple *if w does not contain any self-intersections (loops), i.e. $i_j \neq i_k$ for $j, k \in \{0, \ldots, n\}, j \neq k$.*

We will later consider several forms of weight-induced directed graphs:

Definition 4.1.2. *Whenever a $|S| \times |S|$-matrix $C = (C_{ij})$ with non-negative entries is given, the* weight-induced directed graph *is denoted by $G\{C\} = G(S, E)$. In this graph the vertex set S is the set of all states of the Markov jump process and two vertices i and j are connected by a* directed edge $(i, j) \in E \subseteq (S \times S)$ *if the corresponding* weight C_{ij} *is positive.*

4.1.2. Reactive Trajectories

Let A and B be two nonempty, disjoint subsets of the state space S. By ergodicity, any equilibrium path $\{X(t)\}_{t \in \mathbb{R}}$ oscillates infinitely many times between set A and set B. We are interested in understanding how these oscillations happen (mechanism, rate, etc). If we view A as a reactant state and B as a product state, each oscillation

from A to B is a reaction event, and so we are asking about the mechanism, rate, etc. of these reaction events. To properly define and characterize the reaction events, we proceed by pruning a long ergodic trajectory $\{X(t)\}_{t\in\mathbb{R}}$ into pieces during which it makes a transition from A to B, and ask about various statistical properties of these pieces, see Fig. 4.1. The pruning is done as follows.

First, given a trajectory $\{X(t)\}_{t\in\mathbb{R}}$ we define a set of exit and entrance times $\sigma = \{t_n^A, t_n^B\}_{n\in\mathbb{Z}}$ as:

Definition 4.1.3 (Exit and entrance times). *Given a trajectory $\{X(t)\}_{t\in\mathbb{R}}$, the exit time t_n^A and the entrance time t_n^B belong to σ if and only if*

$$\lim_{t\to t_n^A-} X(t) = x_n^A \in A, \quad X(t_n^B) = x_n^B \in B,$$
$$\forall t \in [t_n^A, t_n^B) : X(t) \notin A \cup B. \tag{4.1}$$

By ergodicity, we know that the cardinal of σ is infinite. It is also clear that the times t_n^A and t_n^B form an increasing sequence, $t_n^A \le t_n^B \le t_{n+1}^A$ for all $n \in \mathbb{Z}$. Notice however that we may have $t_n^A = t_n^B$ for some $n \in \mathbb{Z}$ corresponding to events when the trajectory jumps directly from A to B. If, on the other hand, $t_n^A < t_n^B$, then the trajectory visits states outside of A and B when it makes a transition from the former to the latter.

Next, given the set σ, we define:

Definition 4.1.4 (Reactive times). *The set R of reactive times is defined as*

$$R = \bigcup_{n\in\mathbb{Z}} (t_n^A, t_n^B) \subset \mathbb{R}. \tag{4.2}$$

Finally, we denote by $t_n^1 \equiv t_n^A \le t_n^2 \le \cdots \le t_n^{k_n} \le t_n^B$ the set of all the successive jumping times of $X(t)$ in $[t_n^A, t_n^B]$, i.e. all the times in $[t_n^A, t_n^B]$ such that

$$\lim_{t\to t_n^k-} X(t) \ne X(t_n^k) =: x_n^k, \qquad k = 1, \ldots, k_n \in \mathbb{N} \tag{4.3}$$

and we define:

Definition 4.1.5 (Reactive trajectories). *The ordered sequence*

$$P_n = [x_n^A, x_n^1, x_n^2 \ldots, x_n^{k_n} \equiv x_n^B]$$

consisting of the successive states visited during the nth transition from A to B (including the last state in A, x_n^A, and the first one in B, $x_n^B \equiv x_n^{k_n}$) is called the nth reactive trajectory. The set of all such sequences,

$$P = \bigcup_{n\in\mathbb{Z}} \{P_n\} \tag{4.4}$$

is called the set of reactive trajectories.

(Note that we have $k_n = 1$ when the trajectory hops directly from A to B at time $t_n^A = t_n^B$, in which case $P_n = [x_n^A, x_n^B]$.)

In the next sections we obtain various statistical properties of the objects defined in this section. Note that, because of the way we defined these objects they do depend on the particular trajectory $\{X(t)\}_{t\in\mathbb{R}}$ used to generate them. However, their law does not.

Figure 4.1.: Schematic representation of a piece of an ergodic trajectory. The sub-piece connecting A to B (shown in thick black) is a reactive trajectory, and the collection of reactive trajectories is the ensemble of reactive trajectories.

4.1.3. Probability Distribution of Reactive Trajectories

A first object relevant to quantify the statistical properties of the reactive trajectories is:

Definition 4.1.6. *The distribution of reactive trajectories $m^R = (m_i^R)_{i \in S}$ is defined so that for any $i \in S$ we have:*

$$\lim_{T \to \infty} \frac{1}{2T} \int_{-T}^{T} \mathbf{1}_{\{i\}}(X(t)) \mathbf{1}_R(t) \, dt = m_i^R, \tag{4.5}$$

where $\mathbf{1}_C(\cdot)$ denotes the characteristic function of the set C.

The distribution m^R gives the equilibrium probability to observe a reactive trajectory at state i and time t.

How can we find an expression for m^R? Suppose we encounter the process $X(t)$ in a state $i \in S$. What is the probability that $X(t)$ be reactive? Intuitively, this is the probability that the process came rather from A than from B times the probability that the process will reach B rather than A in the future. This indicates that the following objects will play an important role:

Definition 4.1.7. *The discrete forward committor $q^+ = (q_i^+)_{i \in S}$ is defined as the probability that the process starting in $i \in S$ will reach first B rather than A. Analogously, we define the discrete backward committor $q^- = (q_i^-)_{i \in S}$ as the probability that the process arriving in state i came last from A rather than B.*

In the next section we show that the forward and backward committor satisfy a discrete Dirichlet problem, respectively.

We have

Theorem 4.1.1. *The probability distribution of reactive trajectories defined in (4.5) is given by*

$$m_i^R = \pi_i q_i^+ q_i^-, \quad i \in S. \tag{4.6}$$

Proof. Denote by $x_i^{AB,+}(t)$ the first state in $A \cup B$ reached by $X(s)$, $s \geq t$, conditional on $X(t) = i$. Similarly, denote by $x_i^{AB,-}(t)$ the last state in $A \cup B$ left by $X(s)$, $s \leq t$, conditional on $X(t) = i$ or, equivalently, the first state in $A \cup B$ reached by $X^R(s)$, $s \geq -t$. In terms of these quantities, (4.5) can be written as

$$m_i^R = \lim_{T \to \infty} \frac{1}{2T} \int_{-T}^{T} \mathbf{1}_{\{i\}}(X(t)) \mathbf{1}_A(x_i^{AB,-}(t)) \mathbf{1}_B(x_i^{AB,+}(t)) \mathrm{d}t.$$

Taking the limit as $T \to \infty$ and using ergodicity together with the strong Markov property, we deduce that

$$m_i^R = \pi_i \, \mathbb{P}_i(\tau_B^+ < \tau_A^+) \mathbb{P}_i^R(\tau_B^- > \tau_A^-)$$

which is (4.6) by definition of q^+ and q^-. □

Notice that $m_i^R = 0$ if $i \in A \cup B$. Notice also that m^R is not a normalized distribution. In fact,

$$Z_{AB} = \sum_{j \in S} m_j^R = \sum_{j \in S} \pi_j q_j^+ q_j^- \leq 1$$

is the probability that the trajectory is reactive at some given instance t in time, i.e.

$$Z_{AB} = \mathbb{P}(t \in R). \tag{4.7}$$

The distribution

$$m_i^{AB} = Z_{AB}^{-1} m_i^R = Z_{AB}^{-1} \pi_i q_i^+ q_i^- \tag{4.8}$$

is then the normalized distribution of reactive trajectories which gives the probability to observe a reactive trajectory at state i at time t conditional on the trajectory being reactive at time t.

Remark 4.1.8. *If the Markov process is reversible (i.e. $\pi_i l_{ij} = \pi_j l_{ji}$), then $q_i^+ = 1 - q_i^-$ and the probability distribution of reactive trajectories reduces to*

$$m_i^R = \pi_i q_i^+ (1 - q_i^+) \qquad \text{(reversible process)}. \tag{4.9}$$

4.1.4. Discrete Committor Equations

The discrete forward and backward committors play a central role in TPT. Recall, that for a state $i \in S$ the discrete forward committor q_i^+ is defined as the probability that the Markov jump process starting in state i will reach B rather than A. In other words, q_i^+ is the first entrance probability of the process $\{X(t), t \geq 0, X(0) = i\}$ with respect to the set B *avoiding* the set A. The usual step in dealing with entrance or hitting probabilities with respect to a certain subset of states is the modification of the process such that these states become *absorbing* states. Let $L = (l_{ij})_{i,j \in S}$ be the infinitesimal generator of a Markov jump process and $A \subset S$ be a non-empty subset. Suppose we are interested in the process resulting from the declaration of the states in A to be absorbing states. Then the infinitesimal generator $\hat{L} = (\hat{l}_{ij})_{i,j \in S}$ of the modified process is given by, [89]

$$\hat{l}_{ij} = \begin{cases} l_{ij} & i \in A^c, j \in S \\ 0 & i \in A, j \in S \end{cases} \tag{4.10}$$

From this viewpoint, now it is simple to prove the following theorem.

4. Transition Path Theory for Markov Jump Processes

Theorem 4.1.2. *Let q_i^+ be the probability to reach B before A provided that the process has started in state $i \in S$. Then the discrete forward committor $q^+ = (q_i^+)_{i \in S}$ satisfies the equations*

$$\begin{cases} \sum_{k \in S} l_{ik} q_k^+ = 0, & \forall i \in (A \cup B)^c \\ q_i^+ = 0, & \forall i \in A \\ q_i^+ = 1, & \forall i \in B \end{cases} \tag{4.11}$$

Proof. If we make the states in the set A absorbing states then the discrete forward committor q^+ is the first entrance probability with respect to the set B under the modified process. Thus q^+ satisfies the discrete Dirichlet problem [89]

$$\begin{cases} \sum_{k \in S} \hat{l}_{ik} q_k^+ = 0, & \forall i \in B^c \\ q_i^+ = 1, & \forall i \in B \end{cases}$$

or, equivalently,

$$\begin{cases} \sum_{k \in S} l_{ik} q_k^+ = 0, & \forall i \in (A \cup B)^c \\ q_i^+ = 0, & \forall i \in A \\ q_i^+ = 1, & \forall i \in B \end{cases}$$

which ends the proof. $\square$

Observe that if we substitute the "boundary conditions" into the equations in (4.11) we end up with a linear system

$$U q^+ = v, \tag{4.12}$$

where the matrix $U = (u_{ij})_{i,j \in (A \cup B)^c}$ is given by

$$u_{ij} = l_{ij} \quad i,j \in (A \cup B)^c$$

and an entry of the vector $v = (v_i)_{i \in (A \cup B)^c}$ on the right hand side of (4.12) is defined by $v_i = -\sum_{k \in B} l_{ik}, \forall i \in (A \cup B)^c$. Now we can prove

Lemma 4.1.9. *If the matrix U is irreducible then the solution of (4.11) is unique.*

Proof. By the definition of the matrix U there exists at least an index $k \in (A \cup B)^c$ such that

$$|u_{kk}| > \sum_{j \neq k} u_{kj}.$$

But this implies that U is weakly diagonally dominant (see Definition A.58). Together with its assumed irreducibility, Theorem A.6.6 in the Appendix implies that it is invertible. $\square$

Next, we turn our attention to the discrete backward committor $q_i^-, i \in S$ which is defined as the probability that the process arriving at state i came rather from A than from B. The crucial observation is now that $q^- = (q_i^-)_{i \in S}$ is the discrete forward committor with respect to the *reversed time process*.

Theorem 4.1.3. *The discrete backward committor $q^- = (q_i^-)_{i \in S}$ satisfies the linear system of equations*

$$\begin{cases} \sum_{k \in S} l_{ik}^R q_k^- = 0, & \forall i \in (A \cup B)^c \\ q_i^- = 1, & \forall i \in A \\ q_i^- = 0, & \forall i \in B, \end{cases} \tag{4.13}$$

where $\pi = (\pi_i)_{i \in S}$ is a stationary distribution and $l_{ik}^R = \pi_k l_{ki}/\pi_i$ is the generator of the reversed time process (see (2.49)). Moreover, if the Markov jump process is reversible then the backward committor is simply related to the forward committor by

$$q^- = 1 - q^+. \tag{4.14}$$

Proof. The derivation of (4.13) is a straightforward generalization of the one of (4.11). To derive (4.14), note that if the Markov jump process is reversible, then the detailed balance 2.50 condition is satisfied and the discrete backward committor solves

$$\begin{cases} \sum_{k \in S} l_{ik} q_k^- = 0, & \forall i \in (A \cup B)^c \\ q_i^- = 1, & \forall i \in A \\ q_i^- = 0, & \forall i \in B. \end{cases} \tag{4.15}$$

On one hand the solution of the discrete Dirichlet problem (4.15) is unique (see Lemma 4.1.9). On the other hand, a short calculation shows that $1 - q^+$ also satisfies (4.15). Consequently, we have $q^- = 1 - q^+$ which ends the proof. □

Remark 4.1.10. *The committor q_i^+ is related to hitting times with respect to the sets A and B by*

$$q_i^+ = \mathbb{P}_i(\tau_B^+ < \tau_A^+). \tag{4.16}$$

Here $\mathbb{P}_i$ denotes expectation conditional on $X(0) = i$, $\tau_A^+ = inf\{t > 0 : X(t) \in A\}$ denotes the first entrance time of the set A and $\tau_B^+ = inf\{t > 0 : X(t) \in B\}$ the first entrance time of the set B; q_i^- can be defined similarly using the time-reversed process as

$$q_i^- = \mathbb{P}^R_i(\tau_B^- > \tau_A^-), \tag{4.17}$$

where $\mathbb{P}^R_i$ denotes expectation with respect to the time-reversed process conditional on $X^R(0) = i$, $\tau_A^- = inf\{t > 0 : X^R(t) \in A\}$ denotes the last exit time of the subset A and $\tau_B^- = inf\{t > 0 : X^R(t) \in B\}$ the last exit time of the subset B.

4.1.5. Probability Current of Reactive Trajectories

In this section we are interested in the average current of reactive trajectories flowing from state i to state j per time unit. More precisely:

Definition 4.1.11. *The probability current of reactive trajectories $f^{AB} = (f_{ij}^{AB})_{i,j \in S}$ is defined so that for all pairs of states $(i, j), i, j \in S, i \neq j$ we have*

$$\lim_{s \to 0+} \frac{1}{s} \lim_{T \to \infty} \frac{1}{2T} \int_{-T}^{T} \mathbf{1}_{\{i\}}(X(t)) \mathbf{1}_{\{j\}}(X(t+s))$$

$$\times \sum_{n \in \mathbb{Z}} \mathbf{1}_{(-\infty, t_n^B]}(t) \mathbf{1}_{[t_n^A, \infty)}(t+s) dt = f_{ij}^{AB}. \tag{4.18}$$

In addition, we set $f_{ii}^{AB} = 0$ for all $i \in S$.

4. Transition Path Theory for Markov Jump Processes

We have

Theorem 4.1.4. *The discrete probability current of reactive trajectories is given by*

$$f_{ij}^{AB} = \begin{cases} \pi_i q_i^- l_{ij} q_j^+, & \text{if } i \neq j \\ 0, & \text{otherwise} \end{cases} \tag{4.19}$$

Proof. Using the same notations as in the proof of Theorem 4.1.1, equation (4.18) can also be written as

$$f_{ij}^{AB} = \lim_{s \to 0^+} \frac{1}{s} \lim_{T \to \infty} \frac{1}{2T} \int_{-T}^{T} \mathbf{1}_{\{i\}}(X(t)) \mathbf{1}_{\{j\}}(X(t+s)) \\ \times \mathbf{1}_A(x_i^{AB,-}(t)) \mathbf{1}_B(x_j^{AB,+}(t+s)) \mathrm{d}t. \tag{4.20}$$

Taking the limit $T \to \infty$ and using ergodicity, we deduce that

$$f_{ij}^{AB} = \lim_{s \to 0^+} \frac{1}{s} \pi_i q_i^- \mathbb{E}_i[q_{X(s)}^+, \mathbf{1}_{\{j\}}(X(s))],$$

where $\mathbb{E}_i$ denotes the expectation conditional on $X(0) = i$. To take the limit $s \to 0^+$ we use

$$\forall \Phi : S \mapsto \mathbb{R} : \lim_{s \to 0^+} \frac{1}{s}(\mathbb{E}_i[\Phi(X(s))] - \Phi(i)) = \sum_{j \in S} l_{ij} \Phi(j)$$

and we are done since $i \neq j$. $\qquad \square$

This result implies an expected property, the conservation of the discrete probability current or flux in each node:

Theorem 4.1.5. *For all $i \in (A \cup B)^c$ the probability current is conserved, i.e.*

$$\sum_{j \in S}(f_{ij}^{AB} - f_{ji}^{AB}) = 0, \quad \forall i \in (A \cup B)^c. \tag{4.21}$$

Proof. By definition of f^{AB} for $i \in (A \cup B)^c$:

$$\sum_{j \in S}(f_{ij}^{AB} - f_{ji}^{AB}) = \pi_i q_i^- \sum_{j \neq i} l_{ij} q_j^+ - \pi_i q_i^+ \sum_{j \neq i} \frac{\pi_j}{\pi_i} l_{ji} q_j^-$$
$$= -q_i^- q_i^+ \pi_i l_{ii} + q_i^- q_i^+ \pi_i l_{ii}^R = 0,$$

where we used $\sum_{j \in S} l_{ij} q_j^+ = 0$ if $i \in (A \cup B)^c$ from (4.11) and $\sum_{j \in S} l_{ij}^R q_j^- = 0$ if $i \in (A \cup B)^c$ from (4.15). $\qquad \square$

For later use we should also mention that conservation of the current in every state $i \in (A \cup B)^c$ immediately implies the following total conservation of the current,

$$\sum_{i \in A, j \in S} f_{ij}^{AB} = \sum_{j \in S, i \in B} f_{ji}^{AB}, \tag{4.22}$$

where we used that $f_{ij}^{AB} = 0$ if $i \in S$ and $j \in A$, and $f_{ij}^{AB} = 0$ if $i \in B$ and $j \in S$.

4.1.6. Transition Rate and Effective Current

In this section we derive the average number of transitions from A to B per time unit or, equivalently, the average number of reactive trajectories observed per time unit. More precisely, let $N_T^-, N_T^+ \in \mathbb{Z}$ be such that

$$R \cap [-T, T] = \bigcup_{N_T^- \leq n \leq N_T^+} (t_n^A, t_n^B), \tag{4.23}$$

that is, $N_T^+ - N_T^-$ is the number of reactive trajectories in the interval $[-T, T]$ in time.

Then:

Definition 4.1.12. *The transition (reaction) rate k_{AB} is defined as*

$$k_{AB} = \lim_{T \to \infty} \frac{N_T^+ - N_T^-}{2T}. \tag{4.24}$$

We have:

Theorem 4.1.6. *The transition rate is given by*

$$k_{AB} = \sum_{i \in A, j \in S} f_{ij}^{AB} = \sum_{j \in S, k \in B} f_{jk}^{AB}. \tag{4.25}$$

Proof. From (4.20) we get

$$\sum_{i \in A, j \in S} f_{ij}^{AB} = \lim_{s \to 0^+} \frac{1}{s} \lim_{T \to \infty} \frac{1}{2T} \tag{4.26}$$

$$\times \int_{-T}^{T} \mathbf{1}_A(X(t)) \sum_{j \in S} \mathbf{1}_B(x_j^{AB,+}(t+s)) \mathrm{d}t.$$

Let us consider the integral; we can always restrict our attention to generic values of T such that there is no $n \in \mathbb{Z}$ for which $T = t_n^A$ or $T = t_n^B$. The integrand in this expression is nonzero *iff* $X(t) \in A$, $X(t+s) \in A^c$ and $t+s \in R$, i.e. if $t_n^A \in (t, t+s)$ for some $n \in \mathbb{Z}$. But this means that the integral of $\mathbf{1}_A(X(t)) \mathbf{1}_B(x_j^{AB,+}(t+s))$ on every interval $t \in (t_n^A - s, t_n^A)$ is equal to s and the only contributions to the integral in (4.26) come from the intervals in $[-T, T] \cap \cup_{n \in \mathbb{Z}} (t_n^A - s, t_n^A)$. But these are exactly $N_T^+ - N_T^-$ intervals such that the whole integral amounts to $(N_T^+ - N_T^-)s$. From (4.26) and (4.23), this implies the first identity for the rate k_{AB}. The second identity follows from (4.22). $\square$

Notice that the rate can also be expressed as

$$k_{AB} = \sum_{i \in A, j \in S} f_{ij}^+, \tag{4.27}$$

where:

Definition 4.1.13. *The effective current is defined as*

$$f_{ij}^+ = \max(f_{ij}^{AB} - f_{ji}^{AB}, 0). \tag{4.28}$$

Identity (4.27) follows from (4.25) and the fact that $\forall i \in A \; : \; f_{ij}^+ = f_{ij}^{AB}$ since $f_{ji}^{AB} = 0$ and $f_{ij}^{AB} > 0$ if $i \in A$. The effective current gives the net average number of reactive trajectories per time unit making a transition from i to j on their way from A to B. The effective current will be useful to define transition pathways in Section 4.1.8.

Remark 4.1.14. *If the Markov process is reversible, then the effective current reduces to*

$$f_{ij}^+ = \begin{cases} \pi_i l_{ij}(q_j^+ - q_i^+), & \text{if } q_j^+ > q_i^+ \\ 0, & \text{otherwise} \end{cases} \qquad \text{(reversible process)} \qquad (4.29)$$

and the reaction rate can be expressed as

$$k_{AB} = \tfrac{1}{2} \sum_{i,j \in S} \pi_i l_{ij}(q_j^+ - q_i^+)^2. \qquad \text{(reversible process)} \qquad (4.30)$$

The last identity can also be written as $k_{AB} = -\sum_{i \in S, j \in B} \pi_i l_{ij} q_i^+$ (for reversible processes!) which in turn is identical to the expression that we know from Theorem 4.1.6

$$k_{AB} = \sum_{\substack{i \in S, j \in B \\ i \neq j}} \pi_i l_{ij}(1 - q_i^+). \qquad \text{(reversible process)}$$

4.1.7. Relations with Electrical Resistor Networks

Before proceeding further, it is interesting to revisit our result in the context of electrical resistor networks [27]. Recall that an *electrical resistor network* is a directed weighted graph $G(S, E) = G\{C\}$ where $C = (c_{ij})$ is an entry-wise nonnegative symmetric matrix (cf. Def. 4.1.2), called *conductance matrix* of G. The reciprocal r_{ij} of the conductance c_{ij} is called the *resistance* of the edge (i, j). Establishing a voltage $v_a = 0$ and $v_b = 1$ between two vertices a and b induces a voltage $v = (v_i)_{i \in S \setminus \{a,b\}}$ and an electrical current F_{ij} which are related by Ohm's Law

$$F_{ij} = \frac{v_i - v_j}{r_{ij}} = (v_i - v_j)c_{ij}, \; i, j \in S, i \neq j. \qquad (4.31)$$

Furthermore, the Kirchhoff's Current Law, that is

$$\sum_{j \in S} F_{ij} = 0 \quad \forall i \in S \setminus \{a, b\} \qquad (4.32)$$

requires that the voltages have the property

$$v_i = \sum_{j \neq i} \frac{c_{ij}}{c_i} v_j, \quad \forall i \in, S \setminus \{a, b\}, \qquad (4.33)$$

where $c_i = \sum_{j \in S} c_{ij}$. A *reversible* Markov jump process, given by its infinitesimal generator L, can be seen as an electrical resistor network by setting up the conductance matrix C via

$$c_{ij} = \pi_i l_{ij},$$

where $\pi = (\pi_i)_{i \in S}$ is the unique stationary distribution. Now observe that equation (4.33) reduces to

$$0 = \sum_{j \in S} l_{ij} v_j, \quad \forall i \in S \setminus \{a, b\}.$$

But this means that the forward committor q^+ with respect to the sets $A = \{a\}$ and $B = \{b\}$ can be interpreted as a voltage. Moreover, a short calculation shows that the effective flux, defined in (4.28), pertains to the electrical current.

4.1.8. Dynamical Bottlenecks and Reaction Pathways

The transition rate k_{AB} is a quantity which is important to describe the global transition behavior. In this section we characterize the local *bottlenecks* of the ensemble of reactive trajectories which determine the transition rate. In order to get a detailed insight into the local transition behavior we characterize reaction pathways by looking on the amount of reactive trajectories which is conducted from A to B by a sequence of states.

We use the notations of Graph Theory introduced at the end of Section 4.1.1. Let $G(S, E) = G\{f^+\}$ be the weight induced directed graph associated with the effective current $f^+ = (f_{ij}^+)$, $i_j \in S$. A simple pathway in the graph G, starting in $A \subset S$ and ending in $B \subset S$, is the natural choice for representing a specific reaction from A to B because any loop during a transition would be redundant with respect to the progress of the reaction.

Definition 4.1.15. *A reaction pathway* $w = (i_0, i_1, \ldots, i_n)$, $i_j \in S, j = 0, \ldots, n$ *from A to B is a simple pathway such that*

$$i_0 \in A, i_n \in B, i_j \in (A \cup B)^c \quad j = 1, \ldots, n-1.$$

The crucial observation which leads to a characterization of bottlenecks of reaction pathways is that the amount of reactive trajectories which can be conducted by a reaction pathway per time unit is confined by the minimal effective current of a transition involved along the reaction pathway.

Definition 4.1.16. *Let* $w = (i_0, i_1, \ldots, i_n)$ *be a reaction pathway in $G\{f^+\}$. We define the* min-current *of w by*

$$c(w) = \min_{e=(i,j) \in w} \{f_{ij}^+\}. \tag{4.34}$$

The dynamical bottleneck *of a reaction pathway is the edge with the minimal effective current*

$$(b_1, b_2) = arg \min_{e=(i,j) \in w} \{f_{ij}^+\}. \tag{4.35}$$

We call such an edge (b_1, b_2) *a* bottleneck.

Here and in the following we somewhat misuse our notation by writing $e = (i, j) \in w$ whenever the edge e is involved in the pathway $w = (i_0, i_1, \ldots, i_n)$, i.e. if there is an $m \in \{0, \ldots, n-1\}$ such that $(i, j) = (i_m, i_{m+1})$.

Now it is straightforward to characterize the "best" reaction pathway, namely, that is the one with the *maximal min-current*.

$$G[\mathcal{W}_\mathcal{D}]$$
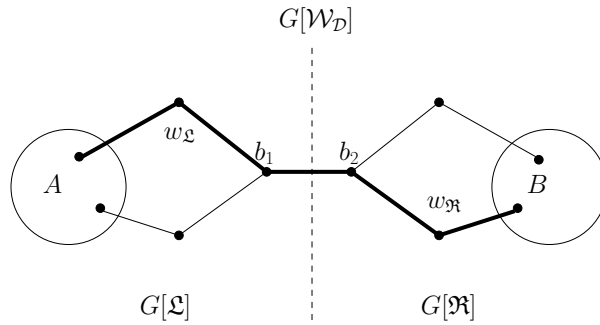
Figure 4.2.: Schematic representation of the decomposition of $\mathcal{W}_\mathcal{D}$. A reaction pathway w (shown in thick black) can be decomposed into two simple pathways $w_\mathfrak{L}$ and $w_\mathfrak{R}$.

Remark 4.1.17. *Notice that the problem of finding a pathway which maximizes the minimal current is known as the* maximum capacity augmenting path problem *[1] in the context of solving the maximal flow problem in a network.*

In general, one cannot expect to find a unique "best" reaction pathway because the bottleneck corresponding to the maximal min-current could be the bottleneck of other reaction pathways too.

Definition 4.1.18. *Let* **W** *be the set of all reaction pathways and denote the maximal min-current by c_{max}. Then we define the set of the* dominant reaction pathways $\mathcal{W}_\mathcal{D} \subset \mathbf{W}$ *by*

$$\mathcal{W}_\mathcal{D} = \{w \in \mathbf{W} : c(w) = c_{max}\}.$$

Remark 4.1.19. *To guarantee uniqueness of the bottleneck, we henceforth assume that the positive currents of the effective current f^+ are pairwise different, i.e. $f_e^+ \neq f_{e'}^+$ for all pairs of edges $e = (i,j), e' = (i',j')$. Nevertheless, we are aware that in applications the situation could show up where more than one bottleneck exists because the corresponding currents are more or less equal. This ambiguity is taken into account in an hierarchical decomposition of the set of all reaction pathways described at the end of this section.*

Let $G[\mathcal{W}_\mathcal{D}] = G(S_\mathcal{D}, E_\mathcal{D})$ be the directed graph induced by the set $\mathcal{W}_\mathcal{D}$, i.e., the graph whose vertex/edge set is composed of all vertices/edges that appear in at least one of the pathways in $\mathcal{W}_\mathcal{D}$. The next Lemma shows that the graph $G[\mathcal{W}_\mathcal{D}] = G(S_\mathcal{D}, E_\mathcal{D})$ possesses a special structure which is crucial for the definition of a *representative dominant reaction pathway*.

Lemma 4.1.20. *Let $b = (b_1, b_2)$ denote the unique bottleneck in $G[\mathcal{W}_\mathcal{D}]$. Then the graph $G(S_\mathcal{D}, E_\mathcal{D} \setminus \{b\})$ decomposes into two disconnected parts $G[\mathfrak{L}]$ and $G[\mathfrak{R}]$ such that every reaction pathway $w \in \mathcal{W}_\mathcal{D}$ can be decomposed into two pathways $w_\mathfrak{L}$ and $w_\mathfrak{R}$*

$$w = (\underbrace{i_{l_1}, \ldots, i_{l_n} = b_1}_{=w_\mathfrak{L}}, \underbrace{b_2 = i_{r_1}, \ldots, i_{r_m}}_{=w_\mathfrak{R}}),$$

where $w_\mathfrak{L} \in \mathfrak{L}$ is a simple pathway in $G[\mathfrak{L}]$ starting in $i_{l_1} \in A$ and ending in $\{b_1\}$ and $w_\mathfrak{R}$ is a simple pathway in $G[\mathfrak{R}]$ starting in $\{b_2\}$ and ending up in $i_{r_m} \in B$. Whenever we have $\mathfrak{L} = \emptyset$ then $G[\mathfrak{L}] = (\{i_{l_1}\}, \emptyset)$; for $\mathfrak{R} = \emptyset$ likewise.

Here and in the following we write $w_{\mathfrak{L}} \in \mathfrak{L}$ (and $w_{\mathfrak{R}} \in \mathfrak{R}$, respectively) if we want to express that for every edge $e \in w_{\mathfrak{L}}$ we have $e \in \mathfrak{L}$.

Proof. It immediately follows from the definition of $\mathcal{W}_{\mathcal{D}}$ that the bottleneck b is involved in every dominant reaction pathway because otherwise there would exist a pathway $w \in \mathcal{W}_{\mathcal{D}}$ such that $c(w) > c_{max}$ which leads to a contradiction. By definition, a reaction pathway does not possess any loops. Consequently, the bottleneck b separates $\mathcal{W}_{\mathcal{D}}$ which proofs the assertion. $\qquad\square$

According to the Lemma, the set of dominant reaction pathways $\mathcal{W}_{\mathcal{D}}$ can be represented as

$$\mathcal{W}_{\mathcal{D}} = \mathfrak{L} \times \mathfrak{R} := \{(w_{\mathfrak{L}}, w_{\mathfrak{R}}) : w_{\mathfrak{L}} \in \mathfrak{L}, w_{\mathfrak{R}} \in \mathfrak{R}\} . \tag{4.36}$$

In Figure 4.2 we give a schematic representation of the decomposition of $\mathcal{W}_{\mathcal{D}}$.

Next, we address the most likely case in applications where more than one dominant reaction pathway exists. By definition, each dominant reaction pathway conducts the same amount of current from A to B but they differ with respect to the maximal amount of current which they conduct, e.g., from the set A to the bottleneck, respectively. Now observe that the simple pathways in the set $\mathfrak{L}$ could be seen as reaction pathways with respect to the set A and the B-set $\{b_1\}$. Hence, $\mathfrak{L}$ possesses itself again a set of dominant reaction pathways $\mathcal{W}_{\mathcal{D}}(\mathfrak{L})$ and so on. This motivates the following recursive definition of the a *representative* dominant reaction pathway.

Definition 4.1.21. *Let $\mathcal{W}_{\mathcal{D}} = \mathfrak{L} \times \mathfrak{R}$ and suppose $b = (b_1, b_2)$ is its (unique) bottleneck. Then we define the* representative *dominant reaction pathway w^* of $\mathcal{W}_{\mathcal{D}}$ by*

$$w^* = (w_{\mathfrak{L}}^*, w_{\mathfrak{R}}^*), \tag{4.37}$$

where $w_{\mathfrak{L}}^*$ is the representative dominant pathway of the set $\mathcal{W}_{\mathcal{D}}(\mathfrak{L})$ with respect to the set A and the B-set $\{b_1\}$ and $w_{\mathfrak{R}}^*$ is the representative of $\mathcal{W}_{\mathcal{D}}(\mathfrak{R})$ with respect to the A-set $\{b_2\}$ and the set B. If $\mathfrak{L} = \emptyset$ and $G[\mathfrak{L}] = (\{i\}, \emptyset)$ then $w_{\mathfrak{L}}^* = \{i\}$; if $\mathfrak{R} = \emptyset$ then $w_{\mathfrak{R}}^*$ is defined likewise.

Notice that the representative w^* is unique under the assumption made in Remark 4.1.19. Furthermore, it follows immediately from the recursive definition of w^* that

$$\begin{aligned}
w^* &= \arg \max_{w \in \mathcal{W}_{\mathcal{D}}} \min_{\substack{e=(i,j)\in w, \\ (i,j)\neq(b_1,b_2)}} \{f_{ij}^+\} \\
&= \arg \max_{w \in \mathcal{W}_{\mathcal{D}}} \min_{\substack{e=(i,j)\in w, \\ (i,j)\neq(b_1,b_2)}} \{f_{ij}^+ - c_{max}\}.
\end{aligned} \tag{4.38}$$

Finally, we turn our attention to the *residuum current* which results from updating the effective current of each edge along the representative pathway $w_1^* = w^*$ by subtracting the min-current $c_{max}^{(1)} = c_{max}$. That is, the residuum current is defined as

$$f_{ij}^{r,1} = \begin{cases} f_{ij}^+ - c_{max}^{(1)}, & \text{if } (i,j) \in w_1^* \\ f_{ij}^+, & \text{otherwise.} \end{cases} \tag{4.39}$$

71

The graph $G_1 = G\{f_{ij}^{r,1}\}$ induced by the residuum current satisfies the current conservation property in analogy to (4.21). It possesses again a bottleneck, say $\tilde{b}$, a set of dominant pathways and a representative pathway, say w_2^*. If we denote the min-current of w_2^* with respect to the residuum current by $c_{max}^{(2)}$ then it should be clear that $c_{max} = c_{max}^{(1)} > c_{max}^{(2)}$ holds. The property (4.38) of w_1^* guarantees that $c_{max}^{(2)}$ is maximal with respect to all possible residuum currents. We can obviously repeat this procedure by introducing the residuum current $f_{ij}^{r,2}$ by subtracting $c_{max}^{(2)}$ from $f_{ij}^{r,1}$ along the edges belonging to w_2^*, and so on. The resulting iteration terminates when the resulting induced graph $G_{M+1} = G\{f_{ij}^{r,M+1}\}$ no longer contains reaction pathways and leads to a hierarchical enumeration $(w_1^*, w_2^*, \ldots, w_M^*)$ of the set $\mathbf{W}$ of all reaction pathways such that

$$
\begin{aligned}
&c_{max}^{(i)} > c_{max}^{(j)}, \quad 0 \leq i < j \leq M, \\
&\sum_{i=1}^{M} c_{max}^{(i)} = k_{AB},
\end{aligned}
\tag{4.40}
$$

where the last identity simply follows from the following equation for the rates $k_{AB}(G_i)$ associated with the graphs $G_1, \ldots, G_M$:

$$
k_{AB}(G_i) = k_{AB}(G_{i-1}) - c_{max}^{(i)},
$$

where G_0 denotes the original graph $G\{f_{ij}^+\}$, and $k_{AB}(G_{M+1}) = 0$.

Remark 4.1.22. *The composition of the total rate into fraction coming from currents along reactive pathways is a quite general concept in graph theory. We herein just presented a specification of it. We refer the interested reader to, e.g. [1], Section 3.5.*

4.1.9. Relation with Laplacian Eigenmaps and Diffusion Maps

Let us briefly comment about the relevance of our results in the context of data analysis (in particular data segmentation and embedding, i.e., low dimensional representation). Recently, two classes of methods have been introduced to this aim: Laplacian eigenmaps [84, 62, 78, 6, 26] and diffusion maps [16, 55]. The idea behind these approaches is quite simple. Given a set of data points, say $S = \{x_1, x_2, \ldots, x_n\}$, one associates a weight induced graph with weight function $w(x, y)$. This graph is constructed locally, e.g. by connecting all points with equal weights that are below a cut-off distance from each other. These weights are then renormalized by the degree of each node, which means that $w(x, y)$ can be re-interpreted as the stochastic matrix of a continuous Markov chain. Alternatively, it is also possible to interpret the weights as rates and thereby build the generator of a continuous-time Markov chain. In both cases, the properties of the chain are then investigated via spectral analysis of the stochastic matrix or the generator. In particular, the first N eigenvectors with leading eigenvalues, say, $\phi_j(x)$, $j = 1, \ldots, N$ can be used to embed the chain into $\mathbb{R}^N$ via: $x \mapsto (\phi_1(x), \ldots, \phi_N(x))$. The eigenvectors can also be used to segment the original data set into important components (segmentation).

As explained in the introduction, the spectral approach is particularly relevant if the Markov chain displays metastability, i.e. if their exists one or more clusters

of eigenvalues which are either very close to 1 (in the case of discrete-time Markov chains) or 0 (in the case of continuous-time Markov chains). When the chain is not metastable, however, the meaning of the first few eigenvectors is less clear, which makes the spectral approach less appealing. In these situations, TPT may provide an interesting alternative. For instance, if several points (or groups of points) with some specific properties can be singled out in the data set, by analyzing the reaction between pairs of such groups, one will disclose global information about the data set (for instance, the committor functions between these pairs may be used for embedding instead of the eigenvectors). The current of reactive trajectories and dominant reaction pathways will also provide additional information about the global structure of the data set which are not considered in the spectral approach.

4.2. Algorithmic Aspects

In this section we explain the algorithmic details for the computation of the various quantities in TPT. Given the generator L and the two sets A and B, the stationary distribution $\pi = (\pi_i)_{i \in S}$ is computed by solving $\pi^T L = 0$, whereas the discrete forward and backward committors, $q^+ = (q_i^+)_{i \in S}$ and $q^- = (q_i^-)_{i \in S}$, are computed by solving (4.11) and (4.15). Solving these equations numerically can be done using any standard linear algebra package. These objects allow one to compute the probability distribution of reactive trajectories $m^R = (m_i^R)_{i \in S}$ in (4.6), its normalized version $m^{AB} = (m_i^{AB})_{i \in S}$ in (4.8), the probability current of reactive trajectories $f^{AB} = (f_{ij}^{AB})_{i,j \in S}$ in (4.19), and the effective current $f^+ = (f_{ij}^+)_{i,j \in S}$ in (4.28). This also gives the reaction rate k_{AB} via (4.25) or (4.27). Next we focus on the computation of the bottlenecks and representative dominant reaction pathways which is less standard.

4.2.1. Computation of Dynamical Bottlenecks and Representative Dominant Reaction Pathways

From the definition in (4.35) of the bottleneck $b = (b_1, b_2)$ associated with the set of dominant reaction pathways $\mathcal{W}_\mathcal{D}$, it follows that

$$f_e^+ > f_b^+, \quad \forall e \in E_\mathcal{D}, \ e \neq b,$$

where $f^+ = (f_{ij}^+)_{i,j \in S}$ is the effective current and $E_\mathcal{D}$ is the edge set of the induced graph $G = G[\mathcal{W}_\mathcal{D}]$. This observation leads to a characterization of the bottleneck which is algorithmically more convenient. Let $E_{sort} = (e_1, e_2, \ldots, e_{|E|})$ be an enumeration of the set of edges of $G = G\{f^+\}$ sorted in ascending order according to their effective current. Then the edge $b = e_m$ in E_{sort} is the bottleneck if and only if the graph $G(S, \{e_m, \ldots, e_{|E|}\})$ contains a reaction pathway but the graph $G(S, \{e_{m+1}, \ldots, e_{|E|}\})$ does not. The bisection-algorithm stated in Algorithm 1 is a direct consequence of this alternative characterization of the bottleneck and is related to the *capacity scaling algorithm* ([1], section 7.3) for solving the maximum flow algorithm. For an alternative algorithm in the context of distributed computing which is based on a modified Dijkstra algorithm see [43].

We also have:

Algorithm 1 Computation of the bottleneck

Input: Graph $G = G\{f^+\}$.
Output: Bottleneck $b = (b_1, b_2)$.
  (1) Sort edges of G according to their weights in ascending order
      $\Longrightarrow E_{sort} = (e_1, e_2, \ldots, e_{|E|})$.
  (2) **IF** the edge $e_{|E|}$ connects A and B **THEN RETURN** bottleneck $b := e_{|E|}$.
  (3) Initialize $l := 1, r := |E|$.
  (4) **WHILE** $r - l > 1$
  (5)   Set $m := \lfloor \frac{r-l}{2} \rfloor, E'(m) := \{e_m, \ldots, e_{|E|}\}$.
  (6)   **IF** there exists an reaction pathway in $G(S, E'(m))$
  (7)   **THEN** $l := m$ **ELSE** $r := m$.
  (8) **ENDWHILE**
  (9) **RETURN** bottleneck $b := e_l$.

Lemma 4.2.1. *The computational cost of Algorithm 1 in the worst case is $\mathcal{O}(n \log n)$ where $n = |E|$ denotes the number of edges of the graph $G = G\{f^+\}$.*

Proof. Assume that $n = 2^k, k > 1$. First notice that the sorting of the edges of $G = G\{f^+\}$ can be performed in $\mathcal{O}(n \log n)$. In the worst case scenario, the edge $e_1 \in E_{Sort}$ is the bottleneck.[1] When this is the case, the number of edges in the jth repetition of the while-loop would be

$$\frac{n}{2^j},$$

and we would have $k - 1$ repetitions. The cheapest way to determine whether there exists an reactive trajectory is to perform a breadth-first search starting in A; the computational cost of that step depends only linearly on the number of edges to be considered, such that we deduce for the worst case effort $T(n)$ of the entire procedure

$$
\begin{aligned}
T(n) &= \mathcal{O}(kn) + \mathcal{O}(\frac{n}{2}) + \mathcal{O}(\frac{n}{4}) + \ldots + \mathcal{O}(\frac{n}{2^{k-1}}) \\
&= \mathcal{O}\left(kn + n(\frac{1}{2} + \frac{1}{4} + \ldots + \frac{1}{2^{k-1}})\right) \\
&= \mathcal{O}(kn)
\end{aligned}
$$

which by noting that $k = log(n)$ ends the proof. $\qquad\square$

The algorithm for computing the unique representative pathway w^* of the set of dominant reaction pathways is a direct implementation of the recursive definition of w^* given in (4.37). Recalling that $\mathcal{W}_\mathcal{D}$ can be decomposed as stated in (4.36) and assuming that f^+ takes different values for every edge (i, j), we end up with the Algorithm 2. A rough estimation of the computational cost of this algorithm is $\mathcal{O}(mn \log n)$ where m is the number of edges of the resulting representative pathway w^* and $n = |E|$.

---

[1] We are aware that the edge e_1 could never be the bottleneck unless all effective currents are equal which is by Remark 4.1.19 excluded. Nevertheless, the following reasoning with respect to e_1 leads only to a slight over-estimation of the computational cost.

Algorithm 2 Representative Pathways

Input: Graph $G = G\{f^+\}$, set A, set B.
Output: Representative $w^* = (w_{\mathfrak{L}}^*, w_{\mathfrak{R}}^*)$ of $\mathcal{W}_{\mathcal{D}}(G)$.
  (1) Determine bottleneck $b = (b_1, b_2)$ in G via Algorithm 1.
  (2) Determine all edges E_{AB} of dominant reaction pathways in G.
  (3) Set $w_{\mathfrak{L}}^* := \begin{cases} b_1, & \text{if } b_1 \in A \\ \text{result of the recursion with } (G[E_{AB}], A, \{b_1\}), & \text{if } b_1 \notin A. \end{cases}$
  (4) Set $w_{\mathfrak{R}}^* := \begin{cases} b_2, & \text{if } b_2 \in B \\ \text{result of the recursion with } (G[E_{AB}], \{b_2\}, B), & \text{if } b_2 \notin B. \end{cases}$
  (5) **RETURN** $(w_{\mathfrak{L}}^*, w_{\mathfrak{R}}^*)$

4.3. Illustrative Examples

In this section we illustrate the discrete transition path theory on three examples. The first is the discrete equivalent of a diffusion process in the three-hole potential, which we chose because the results of discrete TPT can directly be compared with the results in Section 3.7.1. This example also establishes a link to the case of continuous state space. The second example deals with a problem from molecular dynamics, the glycine-molecule, and shows that TPT allows to characterize reaction pathways between molecular conformations. In this example we follow two different approaches: In the first approach the dynamics of glycine is given by an incomplete observation of the system in a certain time interval, meaning that we have to deal with the issue of reconstructing the generator of the process given the time series. In the second approach we utilize a discrete analog of diffusion in a free energy landscape to approximate the effective dynamics of glycine in the torsion angle space. The third example arise from the modeling of a genetic toggle switch in chemical kinetics.

4.3.1. Discrete Analog of a Diffusion in a Potential Landscape

In Chapter 3, TPT for diffusion processes was illustrated on the example of a particle whose dynamics is governed by the Smoluchowski dynamics

$$\begin{cases} \mathrm{d}x(t) = -\dfrac{\partial V(x(t), y(t))}{\partial x} \mathrm{d}t + \sqrt{2\beta^{-1}} \, \mathrm{d}W_x(t) \\ \mathrm{d}y(t) = -\dfrac{\partial V(x(t), y(t))}{\partial y} \mathrm{d}t + \sqrt{2\beta^{-1}} \, \mathrm{d}W_y(t), \end{cases} \tag{4.41}$$

where $(x(t), y(t)) \in \mathbb{R}^2$ denotes the position of the particle, $V(x, y)$ is the potential, and the remaining parameters are as in (3.22).

For $V(x, y)$ we chose again the three-hole potential

$$\begin{aligned} V(x, y) = {}& 3e^{-x^2 - (y - \frac{1}{3})^2} - 3e^{-x^2 - (y - \frac{5}{3})^2} \\ & - 5e^{-(x-1)^2 - y^2} - 5e^{-(x+1)^2 - y^2} \\ & + \frac{2}{10}x^4 + \frac{2}{10}(y - \frac{1}{3})^4 \end{aligned} \tag{4.42}$$

which has been already considered in Section 3.7.1. As one can see in Figure 4.3 the potential (4.42) has two deep minima approximately at $(\pm 1, 0)$, a shallow minimum approximately at $(0, 1.5)$, three saddle points approximately at $(\pm 0.6, 1.1), (-1.4, 0)$ and a maximum at $(0, 0.5)$. As already mentioned, the process defined by (4.42) is ergodic with respect to the invariant measure

$$d\mu(x, y) = Z^{-1} \exp\left(-\beta V(x, y)\right) dxdy, \tag{4.43}$$

where $Z = \int_{\mathbb{R}^2} \exp\left(-\beta V(x, y)\right) dx\, dy$ is a normalization constant. If β is small enough, the measure is strongly peaked on the deep minima of the potential (see the left panel of Figure 4.4), and the system displays metastability, i.e. the particle makes transitions between the vicinity of these minima only very rarely. In it was shown that TPT can be used to describe the mechanism of the transition and compute their rates. In particular, it was shown that transitions preferably occur by the upper channel visible in Figure 4.3 when β is very small, but that they proceed by the lower channel when β is somewhat increased. The reasons for this entropic switch were elucidated in Section 3.7.1 and we refer the reader to this section for details. Our purpose here is to apply TPT on a discrete analog of (4.41).

In order to construct this analog, we exploit the well-known fact that a diffusion process can be approximated by a Markov jump process after discretization of state space. For details on the derivation of the generator, given in (4.44), see Section A.3 in the Appendix. Here we approximate the dynamics (4.41) on a two dimensional, rectangular domain $\Omega = [a, b] \times [c, d] \subset \mathbb{R}^2$ via a Birth-Death process on the discrete state space (mesh) $S = (a + h\mathbb{Z} \times b + h\mathbb{Z}) \cap ([a, b] \times [c, d])$ where the mesh width $h > 0$ is chosen such that the corners of Ω are covered by the mesh S. The generator is given by

$$
\begin{aligned}
(Lf)(x, y) = \quad & k_x^+(x + h, y)(f(x + h, y) - f(x, y)) \\
& + k_x^-(x - h, y)(f(x - h, y) - f(x, y)) \\
& + k_y^+(x, y + h)(f(x, y + h) - f(x, y)) \\
& + k_y^-(x, y - h)(f(x, y - h) - f(x, y)),
\end{aligned}
\tag{4.44}
$$

where

$$
k_x^+(x + h, y) =
\begin{cases}
\dfrac{\beta^{-1}}{h^2} - \dfrac{1}{2h}\dfrac{\partial V(x, y)}{\partial x}, & \text{if } x \in (a, b) \cap (a + h\mathbb{Z}) \\
0, & \text{if } x = b \\
\dfrac{1}{h}, & \text{if } x = a
\end{cases}
$$

$$
k_x^-(x - h, y) =
\begin{cases}
\dfrac{\beta^{-1}}{h^2} + \dfrac{1}{2h}\dfrac{\partial V(x, y)}{\partial x}, & \text{if } x \in (a, b) \cap (a + h\mathbb{Z}) \\
0, & \text{if } x = a \\
\dfrac{1}{h}, & \text{if } x = b
\end{cases}
$$

and the coefficients k_y^+ and k_y^- are defined analogously with respect to $\partial V(x, y)/\partial y$. In the left panel of Figure 4.4 we show the level sets of the density function $\exp(-\beta V(x, y))$ associated with the Gibbs measure (4.43). In the right panel of Figure 4.4 we illustrate the stationary distribution $\pi = (\pi_i)_{i \in S}$ of the Birth-Death process as a *box plot*.

We now present the results of TPT on this example. The panels in Figure 4.5
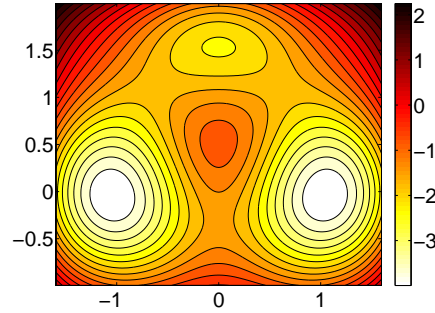
Figure 4.3.: The figure shows the level sets of the three-hole potential given in (4.42). In principal, the dynamics can make a transition between the two main minima via the direct lower channel or via the upper channel through the shallow minima.
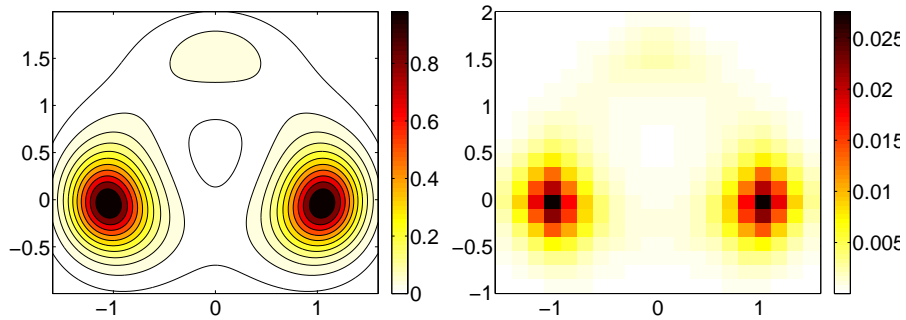
Figure 4.4.: Left: Contour plot of the equilibrium density function $\exp(-\beta V(x))$. Right: Box-plot of the stationary distribution $(\pi_i)_{i \in S}$. Results for $\beta = 1.67$ and a 20×20 mesh discretization.
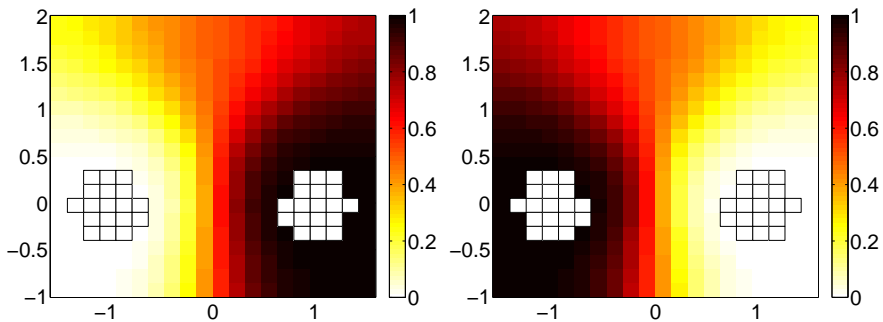
Figure 4.5.: Box-plot of the discrete committors. Left: Forward committor q^+. Right: Backward committor q^-. Results for $\beta = 1.67$ and a 20×20 mesh discretization.

77
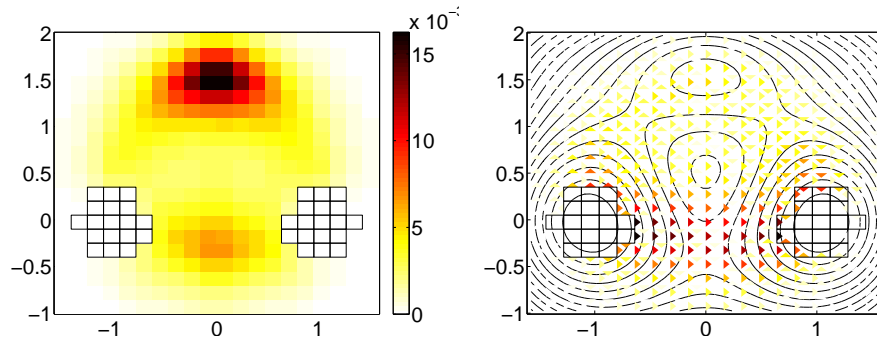
Figure 4.6.: Left: Box-plot of the discrete probability distribution of reactive trajectories m^{AB}. Right: Visualization of the effective current f^+ between mesh points (boxes). An edge (i, j) with positive effective current f_{ij}^+ is depicted by a triangle pointing from the box which corresponds to the state i towards the box identified with $j \in S$. The darker the color of a triangle, the higher the effective current is.

show the box plots of the forward committor q^+ (left panel) and the backward committor q^- (right panel). The set $A \subset S$ is chosen such that it sufficiently covers the region around the left minimum. The set B is defined analogously for the right minimum. The symmetry of the potential together with the symmetry of the sets A and B implies that the particular $\frac{1}{2}$-committor surface, defined as the set $\{i \in S : q_i^+ = 0.5\}$, should correspond to the symmetry axis in y-direction, which is confirmed in Figure 4.5. Notice how the presence of the shallow minima in the upper part of the potential spreads the "level sets" of q^+ in this region. This follows from the fact that the reactive trajectories going through the upper channel get trapped in the shallow well for a long period of time before exiting towards the set B. Next, we turn our attention to the probability distribution of the reactive trajectories, shown in the left panel of Figure 4.6. One can see that the distribution has a peak in the upper shallow minima whereas the effective current, visualized in the right panel of Figure 4.6, suggests that most of the reactive trajectories prefer the lower channel. This again can be explained by the fact that the reactive trajectories going through the upper channel get trapped in the shallow well whereas the reactive trajectories in the lower channel just need to overcome the barrier. We end this example by discussing the family of dominant reaction pathways resulting from the procedure described in the end of Section 4.2.1. In Figure 4.7 we plot the family of reaction pathways which covers about 50% of the probability flux of reactive trajectories for two different temperature, respectively. The pathways are colored according to the values of their min-currents. The darker the color, the larger the current conducted by the corresponding reaction pathway is. At the high temperature ($\beta = 1.67$, left panel), the reaction happens mostly via the lower channel, whereas at low temperature ($\beta = 6.67$, right panel) it occurs mostly via the upper channel. This is consistent with the results presented in [73] and in Section 3.7.1. Finally, we present in Figure 4.8 the family of dominant reaction pathways in the perturbed three-hole potential which has already been considered in Section 3.7.1. We used the same perturbation of three-hole potential as well as the same (discrete) sets A and B as for the smooth three-hole potential above. As one can see, the
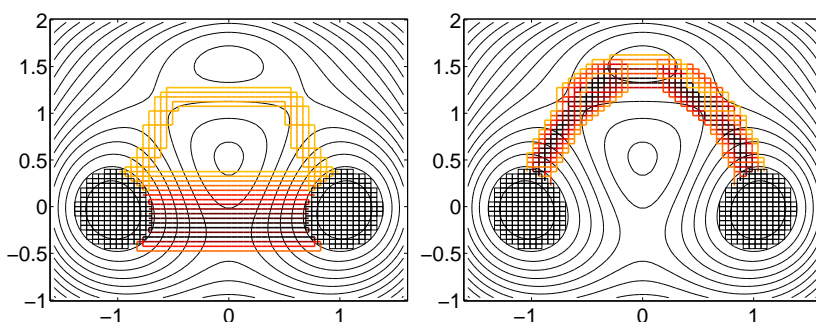
Figure 4.7.: Reaction pathway families for two different temperatures. Both families cover about 50% of the probability flux of reactive trajectories, respectively. The pathways are colored according to the values of their min-currents. The darker the color the more current is conducted by the corresponding reaction pathway. Left: Reaction pathway family at a high temperature $\beta = 1.67$. Right: Reaction pathway family at a low temperature $\beta = 6.67$. Results for a 60×60 mesh discretization; for the sake of illustration the mesh is chosen finer than before.

transition behavior described in Section 3.7.1 is recovered by the discrete TPT.

4.3.2. Molecular Dynamics : Glycine

In this example we use discrete TPT to study conformation changes of the glycine-molecule which is shown in ball-and-stick representation in the left panel of Figure 4.9. We have seen that the essential object in discrete TPT is the generator of the considered Markov jump process. Unlike in the previous example, here the generator of the process is not directly available. Nevertheless, we will present two approaches both yielding a generator of a Markov jump process which describes the dynamics of glycine in terms of the torsion angles Φ and Ψ at room temperature $300K$.

In the first approach the dynamics of the glycine-molecule in solvent is given by a time series of the two torsion angles Φ and Ψ. The main challenge here was to estimate a generator of a Markov jump process representing the dynamics on a coarse grained state space of the torsion angle space (Φ, Ψ). The details of the estimation procedure are described in Chapter 5. For a more detailed analysis of the conformation see [61]. In the second approach we apply the technique presented in the previous section in order to approximate the dynamics of glycine in an interpolated discrete free energy landscape via a Birth-Death process.

Time Series Approach

The time series used herein was extracted out of a molecular simulation of the glycine-molecule embedded in a cubic box of edge length 3.51 nm with 1402 water molecules. The integration of the trajectory with total length $T = 5$ nanoseconds was realized with $\tau = 2$ fs time steps in the Leapfrog-integration scheme with GROMACS force field [8, 59] at room temperature of 300K. In the right panel of Figure 4.9 we give a snapshot of a trajectory where the glycine-molecule is shown together with
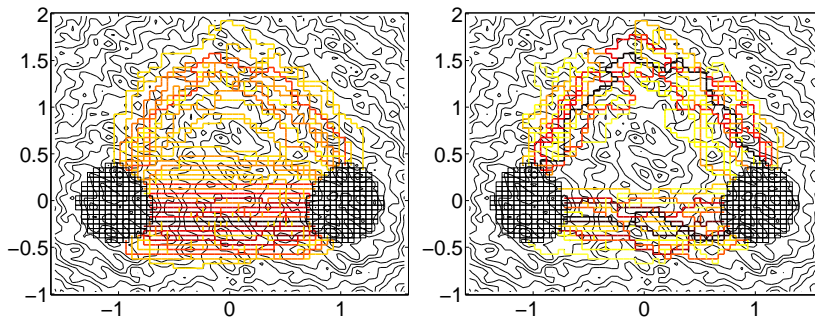
Figure 4.8.: Reaction pathway families in the perturbed three-hole potential in (3.46) at high temperatures $\beta = 1.67$ (left panel) and at low temperature $\beta = 6.67$ (right panel). We used the same perturbation of the potential as in Section 3.7.1. Both families cover about 50% of the probability flux of reactive trajectories, respectively. The pathways are colored according to the values of their min-currents. The darker the color the more current is conducted by the corresponding reaction pathway. Results for a 60×60 mesh discretization.
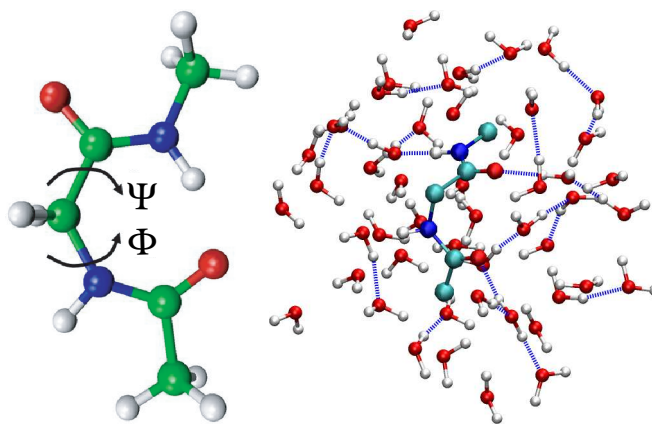
Figure 4.9.: Left: The glycine-molecule shown in ball-and-stick representation and the two torsion angles Φ and Ψ. Right: This panel shows a snapshot of the respective trajectory where the glycine-molecule is shown together with the nearest water molecules.
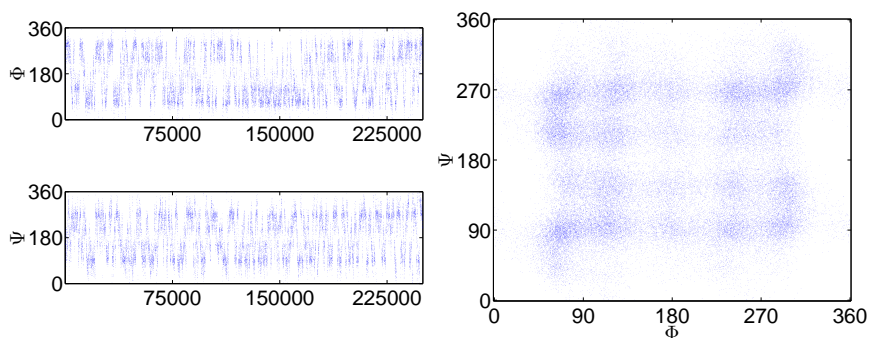
Figure 4.10.: Left: Projection of the time series (all atomic positions) onto the torsion angle space spanned by Φ and Ψ. Right: The Ramachandran plot of the time series in the torsion angle space (Φ, Ψ) reveals the metastable behavior of the dynamics. At first glance, the molecule attains four main conformations where each conformation could be decomposed further into four conformations. We will focus, however, on the four main conformations.

the nearest water molecules. In order to ensure the Markov property later on, we considered only every 100th step of the original trajectory. Before explaining how we constructed a Markov jump process with discrete state space (and especially its generator) out of this time series, let us give some background about this example.

Metastability and Conformation states   A conformation of a molecule is understood as a mean geometric structure of the molecule which is conserved on a large time scale compared to the fastest molecular motions. From the dynamical point of view, a conformation typically persists for a long time (again compared to the fastest molecular motions) such that the associated subset of configurations is *metastable* [82]. In the left panel of Figure 4.10 we show the projection of the time series of the torsion angles Φ and Ψ which clearly reveals the metastable behavior. The Ramachandran plot of the time series in the right panel of Figure 4.10 illustrates the dependency of the conformation states on the two torsion angles. At first glance, the molecule attains four main conformations in the torsion angle space.

Generator Estimation   The first step towards the application of discrete TPT is to determine a coarse grained model of the dynamics in the torsion angle space based on the given time series. We discretized the two-dimensional torsion angle space with a 20×20 equidistant box discretization and identified each element of the time series with the box by which it is covered. Assuming that the resulting discrete time series is Markovian, we estimated a reversible Markov jump process on the discrete state space of boxes which most likely explains the discrete time series. This is done by using an efficient generalization of the maximum-likelihood method presented in detail in Chapter 5. For details on the estimation of the generator for this example see Section 5.4.5.

In the following, we denote by $\tilde{L}_{MLE} = (\tilde{l}_{ij})_{i,j \in S}$ the infinitesimal generator of the estimated Markov jump process. For the sake of illustration, we show in the left panel of Figure 4.11 the *discrete free energy*, $-log\,\pi_i$, where $(\pi_i)_{i \in S}$ is the stationary distri-
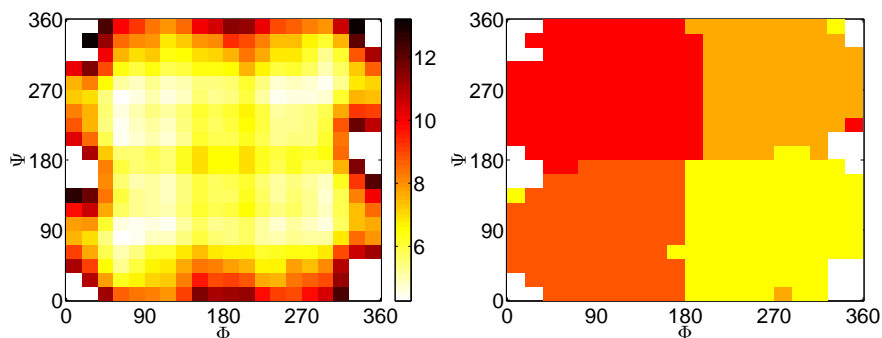
Figure 4.11.: Left: Box plot of the discrete free energy, $-log(\pi_i)$, where $(\pi_i)_{i \in S}$ is the stationary distribution computed from the estimated generator $\tilde{L}_{MLE}$. The lighter the color of a box is the more probable to encounter the equilibrated jump process in the corresponding state. Right: The decomposition of the torsion angle space into four metastable subsets resulting from PCCA .

bution computed from the estimated generator $\tilde{L}_{MLE}$ with respect to a 20×20 box discretization. The lighter the color of a box is the more probable it is to encounter the equilibrated process in the corresponding state. In order to determine the number of metastable subsets and the subsets itself, we have to look at the dominant eigenvalues of the transition matrix $\tilde{P}(\tau) = \exp(\tau \tilde{L}_{MLE}), \tau = 2 \cdot 10^{-13}$ as listed in Table 5.3 in Section 5.4.5). The gap between the fourth and the fifth dominant eigenvalue suggests a decomposition of the state space (torsion angle space) into four metastable subsets. Algorithmically, the decomposition was performed via the Perron Cluster Cluster Analysis (PCCA) [24, 17]. The symmetry of the resulting four metastable subsets, as illustrated in the left panel of Figure 4.11, shows that the estimated generator captures the dynamics in the coarse grained torsion angle space.

Analysis within Transition Path Theory   We were interested in the reaction pathways between two main conformations - the upper left one and the lower right one. As the set B we chose the box in which the discrete free energy restricted on the upper left conformation attains its minimum. The set A was selected analogously with respect to the lower right conformation. The discrete forward committor q^+ is given in the left panel of Figure 4.12. Comparison of the distribution of reactive trajectories m^{AB} (illustrated in the right panel of Figure 4.12) with the family of dominant reaction pathways (right panel of Figure 4.13) reveals again that m^{AB} is insufficient to describe the effective dynamics from A to B. To see this, notice that since we deal with a periodic boundary the distribution of reactive trajectories m^{AB} does not tell anything about the orientation of the direction in which a reaction takes place.

The family of dominant reaction pathways which cover about 20% of the transition rate is given in the left panel of Figure 4.13. The darker the color of a pathway the more current it conducts from A to B. Each of the two darkest reaction pathways covers about 6% of the rate which shows that the upper and lower reaction channel are more or less equivalent. That observation is consistent with the symmetry of the
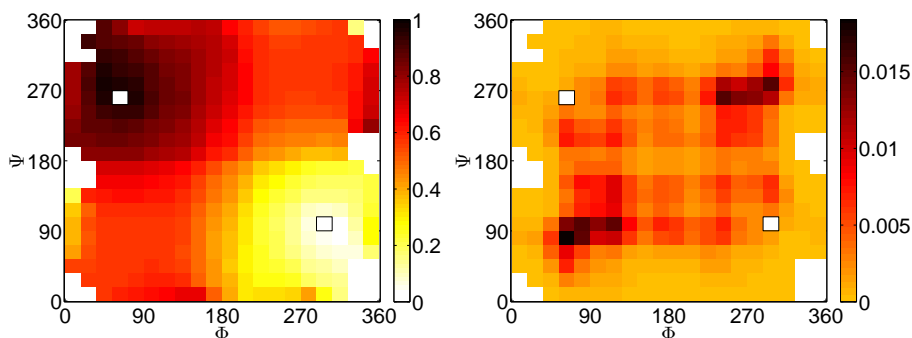
Figure 4.12.: Left: This figure shows the forward committor q^+ computed via (4.11). As the set A we chose the box (shown as a white box with black boundary) which covers the peak of the restricted stationary distribution on the lower right conformation. The set B for the upper left conformation (shown as a white box) was chosen analogously. Right: Box plot of the discrete probability distribution of reactive trajectories m^{AB}. Results are for an equidistant discretization of the torsion angle space into 20×20 boxes.

glycine-molecule in terms of the considered torsion angles. The family of dominant reaction pathways with respect to 30% of the reaction rate (shown in the right panel of Figure 4.13) reveals that there exists an additional third reaction pathways with an opposite orientation.

Free Energy Landscape Approach

In the timeseries approach we consider the dynamical information (the trajectory) to derive the generator of the underlying process. In the free energy approach we assume that the dynamics of the observables (here the two torsion angles) can be described by a Smoluchowski dynamics in a free energy landscape associated with these observables. For a short account to free energy with respect to Smoluchowski dynamics see Section A.5 in the Appendix.

Suppose that we are given a periodic potential landscape $V(\Phi, \Psi) : [0, 2\pi] \times [0, 2\pi] \to \mathbb{R}$ such that the dynamics in the torsion angles Φ and Ψ is governed by

$$\begin{cases} \mathrm{d}\Phi(t) = -\dfrac{\partial V(\Phi(t), \Psi(t))}{\partial \Phi}\mathrm{d}t + \sqrt{2\beta^{-1}}\,\mathrm{d}W_\Phi(t) \\ \mathrm{d}\Psi(t) = -\dfrac{\partial V(\Phi(t), \Psi(t))}{\partial \Psi}\mathrm{d}t + \sqrt{2\beta^{-1}}\,\mathrm{d}W_\Psi(t). \end{cases} \tag{4.45}$$

Our crucial observation now is that the approach presented on the three-hole example in Section 4.3.1 can straightforwardly be generalized to that situation. The only difference for the approximation of the dynamics in (4.45) via a Birth-Death process is that we have to incorporate *periodic* boundary conditions instead of reflecting boundary conditions. To be more precise, we discretized the square $\Omega = [0, 2\pi) \times [0, 2\pi)$ with a total uniform mesh

$$\Omega_h = \{(\Phi_0 + ih, \Psi_0 + jh) : 0 \le i, j \le N\}$$
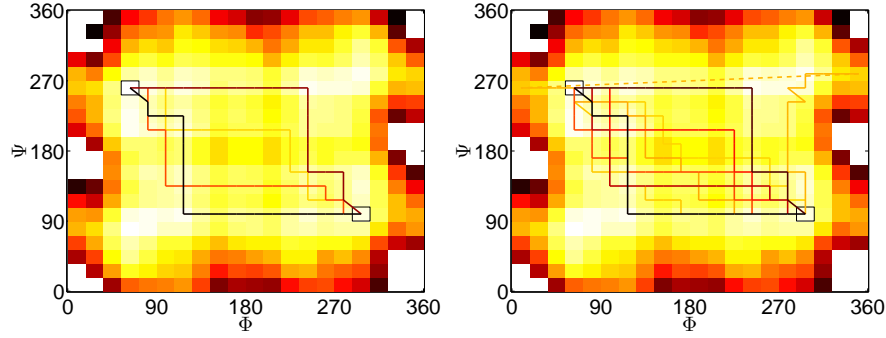
Figure 4.13.: Family of dominant reaction pathways which cover about 20% (left panel) and 30% (right panel) of the reaction rate k_{AB}. The darker the color of a pathway the more current it conducts from A to B. For the sake of illustration, the dominant reaction pathways are embedded in the box plot of the discrete free energy. Each of the two darkest reaction pathways covers about 6% of the rate which shows that the upper and lower reaction channel are more or less equivalent which is consistent with the symmetry of the glycine-molecule. The family shown in the right panel reveals that there exists an additional third reaction pathway, indicated by the long edge in the upper part of the panel.

such that

$$\Phi_0 \equiv (\Phi_0 + (N+1)h) \bmod 2\pi \text{ and } \Psi_0 \equiv (\Psi_0 + (N+1)h) \bmod 2\pi.$$

The condition on the boundary mesh points accounts for the periodicity of the torsion angle space. Then the generator L of the Birth-Death process is given by (cf. (4.44) and Sect. A.3))

$$\begin{aligned}
(Lf)(\Phi, \Psi) = \; & k_\Phi^+(\Phi + h, \Psi)(f(\Phi + h, \Psi) - f(\Phi, \Psi)) \\
& + k_\Phi^-(\Phi - h, \Psi)(f(\Phi - h, \Psi) - f(\Phi, \Psi)) \\
& + k_\Psi^+(\Phi, \Psi + h)(f(\Phi, \Psi + h) - f(\Phi, \Psi)) \\
& + k_\Psi^-(\Phi, \Psi - h)(f(\Phi, \Psi - h) - f(\Phi, \Psi)),
\end{aligned} \tag{4.46}$$

where

$$k_\Phi^+(\Phi + h, \Psi) = \frac{\beta^{-1}}{h^2} - \frac{1}{2h}\frac{\partial V(\Phi, \Psi)}{\partial \Phi}, \quad \text{if } \Phi \in (0, 2\pi) \cap (\Phi_0 + h\mathbb{Z})$$

$$k_\Phi^-(\Phi - h, \Psi) = \frac{\beta^{-1}}{h^2} + \frac{1}{2h}\frac{\partial V(\Phi, \Psi)}{\partial \Phi}, \quad \text{if } \Psi \in (0, 2\pi) \cap (\Phi_0 + h\mathbb{Z})$$

and the coefficients k_Ψ^+ and k_Ψ^- are defined analogously with respect to $\partial V(\Phi, \Psi)/\partial \Psi$.

Analysis within Transition Path Theory Our crucial step towards the comparison of the time series approach with the free energy approach is to interpolate the discrete free energy on a mesh consisting of the box centers of the torsion angle space decomposition.
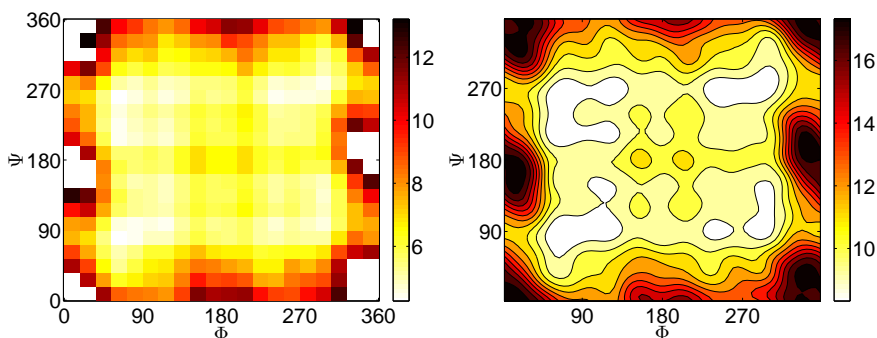
Figure 4.14.: Left: The discrete free energy, $-\log \pi_i$, resulting from the time series approach with respect to the decomposition of the torsion angle space (Φ, Ψ) into 20×20 boxes. Right: The continuous representation of the discrete free energy via a Fourier ansatz.

To be more precise, consider the 20×20 box-decomposition of the torsion angle space (Φ, Ψ) from the analysis of the time series in the previous section. Let (Φ_i, Ψ_i), $i = 1, \ldots, 20^2$ denote the centers of a decomposition boxes. Since the time series does not visit all boxes of the decomposition, the free energy for the empty boxes (depicted as the white regions in left panel of Figure 4.14) is not defined. For the numerical interpolation, however, we set the free energy of not visited boxes to a sufficiently high value such that they result in a barrier for the diffusion dynamics.

Due to the periodicity of the torsion angle space, we can use a Fourier ansatz for the numerical interpolation:

$$V(\Phi_i, \Psi_i) = \pi_i = \sum_{k,l=0}^{M} \left[(a_k \sin(k\Phi_i) + b_k \cos(k\Phi_i))(c_l \sin(l\Psi_i) + d_l \cos(l\Psi_i)) \right],$$

where $i = 1, , \ldots, 20^2$ and determine the coefficients $a_k, b_k, c_l, d_l, 0 \leq l, k \leq M$ by means of the least square method. The right panel in Figure 4.14 illustrates the interpolated discrete free energy landscape[2]. For our numerical experiment we set $M = 12$.

The main question is now if the Birth-Death process (given via the construction in (4.46)) in the interpolated landscape exhibits the same transition behavior as detected with the time series approach? To answer this question, we constructed a generator L via (4.46) on a 70×70 (periodic) mesh discretization of the square $[0, 360] \times [0.360]$. The inverse temperature β was set such that it corresponds to room temperature of 300K. As the set A, we chose the set of mesh points which are covered by the single discretization box associated with the reactant state in the time series approach. The B was chosen analogously. The forward committor q^+ and the distribution m^{AB} of reactive trajectories are given in Figure 4.15.

Finally, we present in the panels of Figure 4.16 two families of reaction pathways, one family with respect to 10% (left panel) of the rate k_{AB} and the other family is with respect to 20% (right panel). In comparison to the time series approach, one can see that the symmetry of the two dominant reaction channels is reproduced and

---

[2]For illustrative convenience, we present the results in a continuous manner (contour plots) rather than using box plots as in the previous sections.
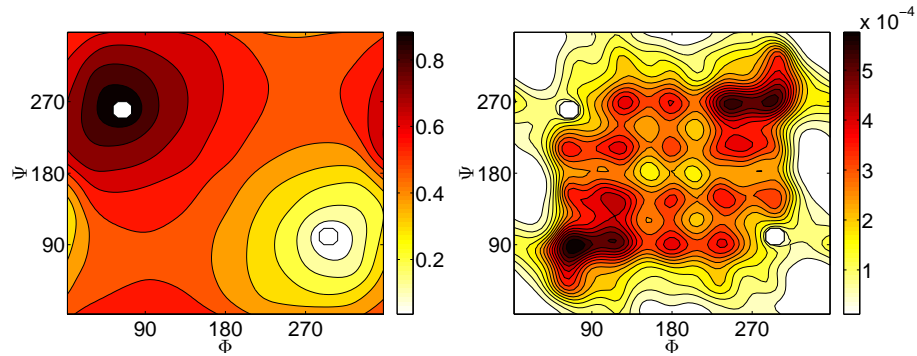
Figure 4.15.: The left panel shows the committor function q^+ with respect to the sets A (bottom right) and B (top left). The distribution m^{AB} is illustrated via a contour plot in the right panel.
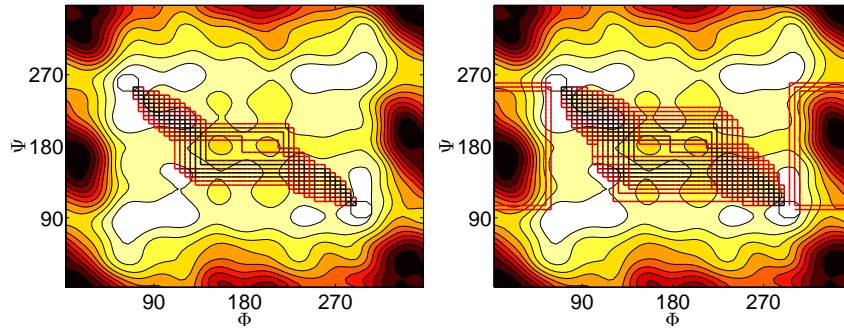
Figure 4.16.: In this figure we illustrate two families of reaction pathways. The family which covers 10% of the transition rate (left panel) reveals that there are two dominant symmetric reaction channels. In the family with respect to 20% (right panel) two additional reaction channels appear but with opposite orientation.

more or less their spatial relation to each other (cf. right panel of Figure 4.13). The family with respect to 20% of reaction rate clearly reveals two additional channels where the upper one is consistent with the third channel in the time series approach.

At the end of this example, we want to point out that the (infinitesimal) generator L in (4.46) can also be used to compute the objects of the continuous TPT since L results from the finite differences discretization of the generator $\mathcal{L}_{bw}$ associated with the diffusion process in (4.45). For example, in Figure 4.17 we show the transition tubes resulting from the streamlines associated with the probability current in (3.28) (cf. Sect. 3.1.5). As a dividing surface we chose a circle with radius $r = 1$ around the center of the set A. The resulting tubes are consistent with the reaction pathways found within the discrete setting.

The results of this section have shown that discrete TPT can be used to analyze transition events in conformational dynamics. We have presented two different approaches - TPT in combination with the generator estimation and the free energy approach. Both approaches lead to reasonably and comparable results.
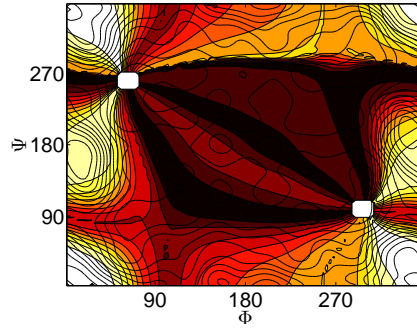
Figure 4.17.: The transition tubes resulting from the streamlines associated with the probability current in (3.28). Results for .

4.3.3. Chemical Kinetics

In the last example, we consider a Markov jump process which arises as a stochastic model of a genetic toggle switch consisting of two genes that repress each others' expression [77].

The expression of the each of the two respective genes results in the production of a specific type of protein; gene G_A produces protein P_A and gene G_B protein P_B. Denote the number of available proteins of type P_A by x and of type P_B by y, the model for the toggle switch proposed in [77] is a Birth-Death process on the discrete state space $S = (\mathbb{Z} \times \mathbb{Z}) \cap ([0, d_1] \times [0, d_2]), d_1, d_2 > 0$, whose generator is given by:

$$
\begin{aligned}
(Lf)(x, y) = {} & c_1(x + 1, y)(f(x + 1, y) - f(x, y)) \\
& + \frac{x}{\tau_1}(f(x - 1, y) - f(x, y)) \\
& + c_2(x, y + 1)(f(x, y + 1) - f(x, y)) \\
& + \frac{y}{\tau_2}(f(x, y - 1) - f(x, y)),
\end{aligned}
\tag{4.47}
$$

where

$$
c_1(x + 1, y) = \begin{cases} \dfrac{a_1}{1 + (y/K_2)^n}, & \text{if } x \in [0, d_1) \\ 0, & \text{if } x = d_1, \end{cases}
$$

$$
c_2(x, y + 1) = \begin{cases} \dfrac{a_2}{1 + (x/K_1)^m}, & \text{if } y \in [0, d_2) \\ 0, & \text{if } y = d_2. \end{cases}
$$

We refer to [77] for the biological interpretation of the parameters in (4.47). For our numerical experiments, we used the parameters $a_1 = 156, a_2 = 30, n = 3, m = 1, K_1 = K_2 = 1, \tau_1 = \tau_2 = 1$, consistent with [77]. With these parameters the system's dynamical behavior is as follows: There are two "metastable" states; in the first of these only gene G_A is expressed and protein P_A is produced until a certain number (around $x = 155$ for the parameters chosen) is reached which then is rather stable, while gene G_B is repressed and almost no protein P_B is produced (so that typically $y = 0$ or $y = 1$). After some rather long period of fluctuation in this metastable state the system is able to exit from it which leads to expression of gene G_B and repression of G_A. Then the system gets into a metastable state where the
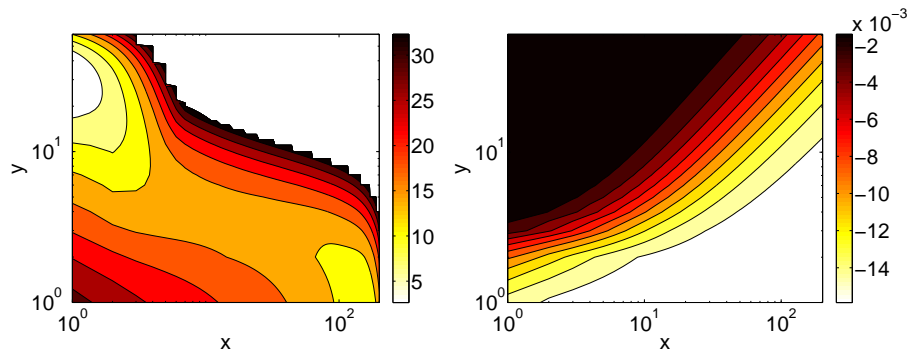
Figure 4.18.: Left: Contour plot of the discrete free energy, $-log\pi_i$, of the Birth-Death process (4.47) on the state space $S = \mathbb{Z} \times \mathbb{Z} \cap ([0, 200] \times [0, 60])$. The white region in the right upper part of the panel indicates the subset of states with almost vanishing stationary distribution (all boxes with distribution less than machine precision have been colored white). Right: Contour plot of the eigenvector of the first non-trivial right eigenvalue of L. Results for $a_1 = 156, a_2 = 30, n = 3, m = 1, K_1 = K_2 = 1, \tau_1 = \tau_2 = 1$.

number of protein P_B fluctuates around a certain non-vanishing number ($y = 30$ for our parameters) and P_A is rather not produced (typically $x = 0$ or $x = 1$).

It is well-known that in the limit of large protein numbers the dynamics of the jump process or, more precisely, of the associated Master equation is given by a deterministic model of the biochemical kinetics in terms of the associated concentrations. The authors in [77] also consider this deterministic model in order to get a rough understanding of the switch dynamics. The model consists of two coupled ordinary differential equations,

$$
\begin{aligned}
\dot{x} &= \frac{a_1}{1 + (y/K_2)^n} - \frac{x}{\tau_1}, \\
\dot{y} &= \frac{a_2}{1 + (x/K_1)^m} - \frac{y}{\tau_2},
\end{aligned}
\tag{4.48}
$$

where the parameters are the same as in the stochastic model (4.47). For our particular choice of parameters the deterministic dynamics in (4.48) has two stable stationary points approximately at $(x, y) = (155, 0)$ and $(x, y) = (0, 30)$.

For the sake of illustration, we illustrate in the left panel of Figure 4.18 the Gibbs energy, $-\log \pi$, of the Birth-Death process instead of its stationary distribution π itself. Moreover, we neglected all states with almost vanishing stationary distribution (depicted by the white region) and in order to emphasize the states of interest, we chose a log-log representation. The color scheme is chosen such that the darker the color of a region the more probable to find the process there. One can clearly see that the process spends most of its time near the two metastable core sets $(x, y) \in \{(155, 0), (155, 1)\}$ and $(x, y) \in \{(0, 30), (1, 30)\}$.

We were interested in the reaction from the set $A = \{(155, 0), (155, 1)\}$ towards the set $B = \{(0, 30), (1, 30)\}$. The different shapes of the level sets of the discrete forward and backward committor, as shown in the left and right panel of Figure 4.19, indicate the high non-reversibility of the Birth-Death process. Notice that the geometry of
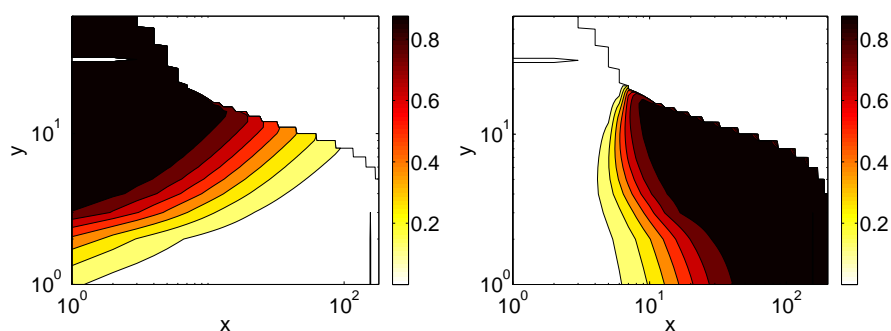
Figure 4.19.: Contour plots of the discrete forward and backward committor. Due to the logarithmic scaling, the set $A = \{(155, 0), (155, 1)\}$ is depicted as a vertical black line and the set $B = \{(0, 30), (1, 30)\}$ as an ellipsoid. Left: Discrete forward committor q^+. Right: Discrete backward committor q^-.
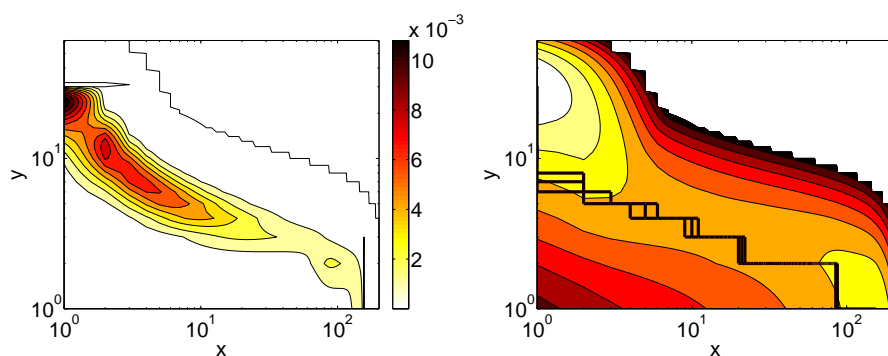
Figure 4.20.: Left: Contour plot of the distribution of reactive trajectories m^{AB}. Right: Edge plot of the three dominant reaction pathways which cover about 6% of the current.

the level sets of the forward committor q^+ looks very similar to the geometry of the eigenvector associated with the first non-trivial right eigenvalue of L, as plotted in the right panel of Figure 4.18. Finally, the edges of the three most dominant reaction pathways are plotted in the right panel of Figure 4.20. Again, the reaction pathways deviate from the channel which is suggested by the distribution m^{AB} of reactive trajectories, shown in the left panel of Figure 4.20.

89

5. Generator Estimation of Markov Jump Processes

We have seen that discrete TPT is a powerful tool for the investigation of the ensemble of reaction trajectories of Markov jump processes. The central object of discrete TPT is the committor function which satisfies a system of linear equation involving the infinitesimal generator of the process. In applications, however, the generator is not given but only an *incomplete* observation of the process is available. This chapter is devoted to the problem of finding a generator of a Markov jump process based on an *incomplete* observation of the process. The results of this chapter are published in [63, 64].

We will focus on two methods for the estimation of a generator. The maximum likelihood method (MLE-method) introduced by Asmussen 1996 in [5] and reinvented by Bladt and Sørensen 2005 in [9] finds a generator via an EM-algorithm which maximizes the likelihood of the given incomplete observation. Furthermore, we will discuss a significant algorithmic improvement of the MLE-method, we call it *enhanced* MLE-method, which was independently derived by Holmes and Rubin 2002 in [49]. Moreover, we introduce an adaption of the enhanced MLE-method to the case of reversible Markov jump processes. The quadratic programming approach introduced by Crommelin and Vanden-Eijnden in [19], determines a generator via the approximation of the eigenstructure of the empirical transition matrix.

After a comparison of both methods via their numerical performance on small test examples, we will apply the enhanced MLE-method to data from a molecular dynamics simulation of glycine in water. The resulting estimated generator is the basis for the investigation of the conformational dynamics of glycine via discrete TPT (cf. Chap. 4). Finally, we will demonstrate the performance of the enhanced MLE-method on an example with non-constant observation time steps.

5.1. The Embedding Problem

Let $\{X(t), t \geq 0\}$ be a Markov jump process on a finite state space $S \cong \{1, \ldots, d\}$ and let $L \in \mathbb{R}^{d \times d}$ be its generator. Then the time-dependent transition matrix $P(t)$ of the process can be expressed as the matrix exponential (cf. Sect. 2.2)

$$P(t) = \exp(tL) = \sum_{k=0}^{\infty} \frac{t^k}{k!} L^k.$$

In the following, the set of all generators with respect to a fixed dimension d will be denoted by

$$\mathfrak{G} = \left\{ L = (l_{ij})_{i,j} \in \mathbb{R}^{d \times d} : l_{ij} \geq 0 \quad \text{for all } i \neq j, \quad l_{ii} = -\sum_{j \neq i} l_{ij} \right\}. \qquad (5.1)$$

Now suppose that a process is only partially observed, i.e. the process is only given by a finite sampling $Y = \{y_0 = X(t_0), \ldots, y_N = X(t_N)\}$ at discrete times $t_0 < t_1 < \ldots < t_N$. In this chapter we consider the problem of how to determine the generator if only an incomplete observation Y is available.

Several difficulties must be taken into account. First, from a finite number of samples it is impossible to tell if the underlying process is actually Markovian. Second, it is not clear if the observed data originates indeed from discrete samples of a continuous-time Markov chain with some generator L, or rather from a discrete-time Markov chain which cannot be embedded into a time-continuous counterpart. In the latter case, a generator does not exist because the transition matrix of the discrete chain does not belong to the set

$$\mathfrak{P} = \left\{ P \in \mathbb{R}^{d \times d} : \text{ there is a } L \in \mathfrak{G} \text{ such that } P = \exp(L) \right\}.$$

It is well-known that $\mathfrak{P}$ is a subset of all stochastic matrices, but the so-called *embedding problem*, i.e. the question what characterizes the elements of $\mathfrak{P}$, is widely open for $d > 3$ (cf. [9, 19] and references therein). A third difficulty is the fact that the matrix exponential function *is not injective* if the eigenvalues of the generator are complex. Hence, some matrices $P \in \mathfrak{P}$ can be represented as $P = \exp(L) = \exp(\bar{L})$ with two different generators $L \neq \bar{L}$. And finally, the question whether the time points t_n of the observations are equidistant plays an important role. In case of a constant time lag $\tau = t_{n+1} - t_n$ an estimate of the transition matrix $P(\tau)$ is available by counting the number of transitions between each pair of states, but in case of variable time lags the sampled data is typically not sufficient for reasonable approximations of the transition matrix.

Due to these problems the above question has to be modified: how can we find the generator that "agrees best" with a finite observation $Y = \{y_0 = X(t_0), \ldots, y_N = X(t_N)\}$ of a process?

5.2. The Maximum Likelihood Method

In this section we explain in detail the maximum likelihood method introduced in [5] and elaborated further in [9]. Furthermore, we present in detail the enhanced MLE-methods which is based on results in [49]. The idea behind the MLE-method is to find a generator $\tilde{L}$ such that it maximizes the *discrete likelihood* of the given time series.

5.2.1. Continuous and Discrete Likelihood Functions

The basis objects in the MLE-method is the continuous and discrete likelihood function. Suppose that the Markov jump process $X(t)$ has been observed continuously in a certain time interval $[0, T]$. Let the random variable $R_i(T)$ be the time the process spent in state i before time T

$$R_i(T) = \int_0^T \mathbf{1}_{\{i\}} X(s) \mathrm{d}s$$

and denote by $N_{ij}(T)$ the number of transitions from state i to state j in the time interval $[0, T]$. The *continuous time likelihood function* $\mathcal{L}_c$ of an observed trajectory

$\{X_t : 0 \leq t \leq T\}$ is given by [9]

$$\mathcal{L}_c(L) = \prod_{i=1}^{d} \prod_{j \neq i} l_{ij}^{N_{ij}(T)} \exp(-l_{ij} R_i(T)), \qquad L = (l_{ij}). \tag{5.2}$$

By definition, the *maximum likelihood estimator* (MLE) $\tilde{L}$ maximizes the likelihood function (5.2). Exploiting the monotonicity of the *log*-function, $\tilde{L}$ is also the maximizer of

$$\log \mathcal{L}_c(L) = \sum_{i=1}^{d} \sum_{j \neq i} \left[N_{ij}(T) \log(l_{ij}) - l_{ij} R_i(T) \right], \tag{5.3}$$

i.e. $\tilde{L}$ is the null of the partial derivatives of $\log \mathcal{L}_c(L)$ with respect to l_{ij} and the Hessian matrix of $\log \mathcal{L}_c(L)$ evaluated at $\tilde{L}$ is negative definite. A short calculation shows

$$\frac{\partial \log \mathcal{L}_c(\tilde{L})}{\partial l_{ij}} = 0 \iff \tilde{l}_{ij} = \frac{N_{ij}(T)}{R_i(T)} \tag{5.4}$$

and

$$\frac{\partial \log \mathcal{L}_c(\tilde{L})}{\partial l_{ij} \partial l_{kl}} = -\frac{N_{ij}(T)}{\tilde{l}_{ij}^2} \mathbf{1}_{\{k\}}(i) \mathbf{1}_{\{l\}}(j) \leq 0.$$

In the case where the process has only been observed at discrete time points $0 = t_0 < t_1 < \ldots < t_N = T$ the *discrete likelihood function* $\mathcal{L}_d$ of a time series $Y = \{y_0 = X(t_0), \ldots, y_N = X(t_N)\}$ is given in terms of the transition matrix $P(t) = \exp(tL)$,

$$\mathcal{L}_d(L) = \prod_{k=0}^{N-1} p_{y_k, y_{k+1}}(\Delta t_k) = \prod_{s=1}^{r} \prod_{i,j \in S} [p_{ij}(\tau_s)]^{c_{ij}(\tau_s)}, \tag{5.5}$$

where $p_{y_k, y_{k+1}}(\Delta t_k)$ is the probability that the process makes a transition from state y_k to the state y_{k+1} in time Δt_k, $\tau_s \in \{\tau_1, \ldots, \tau_r\} = \cup_{k=1}^{N-1} \{\Delta t_k\}$ is an observed time lag and the entry $c_{ij}(\tau_s)$ in the *frequency matrix* $C(\tau_s) = (c_{ij}(\tau_s))$, $i, j \in S$, defined according to

$$c_{ij}(\tau_s) \stackrel{def}{=} \sum_{n=1}^{N-1} \mathbf{1}_{\{i\}}(X(t_n)) \mathbf{1}_{\{j\}}(X(t_{n+1})) \mathbf{1}_{\{\tau_s\}}(\Delta t_n), \tag{5.6}$$

provides the number of consecutively observed transitions in Y from state i to state j in time τ_s.

Unfortunately, even in the simplified case of a constant time lag, i.e. $\tau = const$, the derivative of the discrete log-likelihood function,

$$\log \mathcal{L}_d(L) = \sum_{k=0}^{N-1} \log p_{y_k, y_{k+1}}(\tau) = \sum_{i,j \in S} [\log p_{ij}(\tau)]^{c_{ij}(\tau)}, \tag{5.7}$$

with respect to the entries of L, that is

$$\frac{\partial}{\partial L} \log \mathcal{L}_d(L) = \sum_{n=1}^{\infty} \sum_{k=1}^{n} \frac{\tau^n}{n!} (L^T)^{k-1} Z (L^T)^{n-k},$$
$$\text{with } Z = (z_{ij})_{i,j \in S}, z_{ij} = c_{ij} / \exp(\tau L)_{ij},$$

has such a complicated form that the null cannot be found analytically. Hence no analytical expression for the MLE with respect to L is available. The derivative of $\log \mathcal{L}_d$ with respect to the transition matrix $P(\tau)$ can analytical be obtained and the maximizer is simply given by

$$\hat{P} = (\hat{p}_{ij})_{i,j} \quad \text{with entries} \quad \hat{p}_{ij} = \frac{c_{ij}(tau)}{\sum_{j=1}^{d} c_{ij}(tau)}, \tag{5.8}$$

where $c_{ij} = c_{ij}(\tau)$. Notice that reversibility of the transition matrix $\hat{P}$ can easily be achieved by considering the symmetric frequency matrix $C^{REV}(\tau) = (c_{ij}^{REV})$ with entries given by

$$c_{ij}^{REV}(\tau) = c_{ij}(\tau) + c_{ji}(\tau).$$

Then the transition matrix which results via 5.8 on the basis of $C^{REV}(\tau)$ is reversible with respect to the probability distribution

$$\pi = Z^{-1} \left(\sum_{k=1}^{d} c_{1k}^{REV}(\tau), \dots, \sum_{k=1}^{d} c_{dk}^{REV}(\tau) \right),$$

where $Z = \sum_{i,j=1}^{d} c_{ij}^{REV}$ is the normalization constant.

In the following neither we assume a constant observation time lag nor we assume reversibility.

5.2.2. Likelihood Approach Revisited

In the likelihood approach, introduced by Bladt and Sørensen in [9], a generator $\tilde{L}$ for a given time series is determined such that $\tilde{L}$ maximizes the discrete likelihood function (5.5) for the time series. As pointed out in the previous section the discrete likelihood function $\mathcal{L}_d$ does not permit an analytical maximum likelihood estimator. On the other hand, the MLE (5.4) for a continuous time observation can be obtained analytically but for an incomplete observation the information between two consecutive observations is *hidden* and, hence, the observables $R_i(T)$ and $N_{ij}(T)$ are unknown.

Nevertheless, the discrete likelihood $\mathcal{L}_d$ can iteratively be maximized by means of an *Expectation-Maximization algorithm* (EM-algorithm). The idea is to approximate the hidden (not observed) information between the incomplete observations in Y by the *expected* (averaged) information *conditional* on the data and on a given guess of the hidden process. This step is called expectation step (E-Step) and formally consists of the computation of the *conditional log-likelihood* function

$$\mathcal{G} : L \mapsto \mathbb{E}_{\tilde{L}_0} \left[\log \mathcal{L}_c(L) | Y \right], \tag{5.9}$$

where $L \in \mathfrak{G}$ and for reasons of algebraical simplicity and without loss of generality the *log-likelihood* function $\log \mathcal{L}_c$ is considered. The crucial observation is now that the maximizer (M-step),

$$\tilde{L}_1 = \arg \max_{L \in \mathfrak{G}} \mathcal{G}(L; \tilde{L}_0)$$

, of the conditional log-likelihood function $\mathfrak{G}(L; \tilde{L}_0)$ satisfies [23]

$$\mathcal{L}_d(\tilde{L}_1) \geq \mathcal{L}_d(\tilde{L}_0).$$

Hence, taking the maximizer as a new guess of the hidden process, the iteration of the two described steps allows to approximate a (local) maximum of the discrete likelihood function $\mathcal{L}_d$. The resulting algorithm is stated in Algorithm 3.

Algorithm 3 General EM-algorithm

Input: Time series $Y = \{y_0 = X(t_0), \ldots, y_N = X(t_N)\}$, initial guess of generator $\tilde{L}_0$.

Output: MLE $\tilde{L}$.
   (1) Expectation step (E-step):
         Compute the function $L \mapsto \mathcal{G}(L; \tilde{L}_k)$.
   (2) Maximization step (M-Step):
         $\tilde{L}_{k+1} = \arg\max_{L \in \mathfrak{G}} \mathcal{G}(L; \tilde{L}_k)$
   (3) Go to Step (1), unless a certain convergence criterion is satisfied.

For our particular likelihood function in (5.2) the conditional log-likelihood function $\mathcal{G}$ in the E-Step reduces to

$$\mathcal{G}(L; \tilde{L}_0) = \sum_{i=1}^{d} \sum_{j \neq i} \left[\log(l_{ij}) \mathbb{E}_{\tilde{L}_0} \left[N_{ij}(T)|Y \right] - l_{ij} \mathbb{E}_{\tilde{L}_0} \left[R_i(T)|Y \right] \right] \tag{5.10}$$

and the maximizer $\tilde{L} = (\tilde{l}_{ij}), \ i,j \in S$ of (5.10) takes the form (cf. (5.4))

$$\tilde{l}_{ij} = \begin{cases} \dfrac{\mathbb{E}_{\tilde{L}_0} \left[N_{ij}(T)|Y \right]}{\mathbb{E}_{\tilde{L}_0} [R_i(T)|Y]}, & i \neq j \\ -\sum_{k \neq i} \tilde{l}_{ik}, & \text{otherwise.} \end{cases} \tag{5.11}$$

The non-trivial task which remains is to evaluate the conditional expectations $\mathbb{E}_{\tilde{L}_0} \left[N_{ij}(T)|Y \right]$ and $\mathbb{E}_{\tilde{L}_0} \left[R_i(T)|Y \right]$, respectively. The first step towards their computation is the observation that by the Markov property and the homogeneity of the Markov jump process the conditional expectations in (5.10) can be expressed as sums [9]

$$\mathbb{E}_{\tilde{L}_0} \left[R_i(T)|Y \right] = \sum_{s=1}^{r} \sum_{k,l=1}^{d} c_{kl}(\tau_s) \mathbb{E}_{\tilde{L}_0} \left[R_i(\tau_s)|X(\tau_s) = l, X(0) = k \right],$$

$$\mathbb{E}_{\tilde{L}_0} \left[N_{ij}(T)|Y \right] = \sum_{s=1}^{r} \sum_{k,l=1}^{d} c_{kl}(\tau_s) \mathbb{E}_{\tilde{L}_0} \left[N_{ij}(\tau_s)|X(\tau_s) = l, X(0) = k \right]. \tag{5.12}$$

Next, the conditional expectations in the right hand sides in (5.12) can be decomposed further by using the identities

$$\mathbb{E}_L \left[R_i(t)|X(t) = l, X(0) = k \right] = \frac{\mathbb{E}_L \left[R_i(t) \mathbf{1}_{\{l\}}(X(t))|X(0) = k \right]}{p_{kl}(t)},$$

$$\mathbb{E}_L \left[N_{ij}(t)|X(t) = l, X(0) = k \right] = \frac{\mathbb{E}_L \left[N_{ij}(t) \mathbf{1}_{\{l\}}(X(t))|X(0) = k \right]}{p_{kl}(t)}. \tag{5.13}$$

Finally, the authors in [5, 9] realized that the auxiliary functions defined by

$$M_{kl}^i(t) \stackrel{def}{=} \mathbb{E}_L \left[R_i(t) \mathbf{1}_{\{l\}}(X(t))|X(0) = k \right],$$

$$F_{kl}^{ij}(t) \stackrel{def}{=} \mathbb{E}_L \left[N_{ij}(t) \mathbf{1}_{\{l\}}(X(t))|X(0) = k \right] \tag{5.14}$$

satisfy systems of ordinary differential equations. For example, let $i, j \in S$ be fixed. Then the vectors $M_k^i(t) = (M_{k1}^i(t), \ldots, M_{kd}^i(t))$ and $F_k^{ij}(t) = (F_{k1}^{ij}(t), \ldots, F_{kd}^{ij}(t))$ satisfy the two systems of ODEs

$$
\begin{aligned}
\frac{\mathrm{d}}{\mathrm{d}t} M_k^i(t) &= M_k^i(t)L + A_k^i(t), \quad M_k^i(0) = 0 \\
&\text{with } A_k^i(t) = p_{ki}(t)e_i, \\
\frac{\mathrm{d}}{\mathrm{d}t} F_k^{ij}(t) &= F_k^{ij}(t)L + A_k^{ij}(t), \quad F_k^{ij}(0) = 0 \\
&\text{with } A_k^{ij}(t) = l_{ij}p_{ki}(t)e_j,
\end{aligned}
\tag{5.15}
$$

where e_i and e_j are the ith and j^{th} unit vectors. To summarize, the computation of the function $\mathcal{G}(L; \tilde{L})$ in the E-step reduces to solving the systems of ODEs given in (5.15). Solving these ODEs numerically, however, causes prohibitive computational costs when the number of states of the system is large. Another option is to approximate the matrix-exponentials which are involved in the analytic solutions of (5.15)

$$
\begin{aligned}
M_k^i(t) &= \int_0^t A_k^i(s) \exp((t-s)L)\mathrm{d}s, \\
F_k^{ij}(t) &= \int_0^t A_k^{ij}(s) \exp((t-s)L)\mathrm{d}s
\end{aligned}
\tag{5.16}
$$

via the so-called uniformization method [67]. Choose $\alpha = \max_{i=1,\ldots,d}\{-l_{ii}\}$, and define $B = I + \alpha^{-1}L$. Then, e.g., $M^i(t) = (M_{kl}^i(t))_{k,l \in S}$ is given by

$$
M^i(t) = \exp(-\alpha t)\alpha^{-1} \sum_{n=0}^{\infty} \frac{(\alpha t)^{n+1}}{(n+1)!} \sum_{j=0}^n B^j (e_i e_i^T) B^{n-j}.
$$

with e_i^T denoting the transpose of the unit vector e_i. However this expansion is fairly time consuming and for high dimensional matrices intractable. Moreover the infinite sum has to be cut off at a finite n which entails inaccuracies.

We will choose an alternative way to compute the left hand sides in (5.13) which avoids the treatment of the ODEs. We will explain the approach in detail in the next subsection. In Algorithm 4, we state the resulting EM-algorithm due to [9].

5.2.3. Enhanced Computation of the Maximum Likelihood Estimator

In [48], the authors showed that the conditional expectations $\mathbb{E}_L[N_{ij}(t)|X(t) = l, X(0) = k]$ and $\mathbb{E}_L[R_i(t)|X(t) = l, X(0) = k]$ can analytically be expressed in terms of the generator L. Recalling the notation of the transition matrix $P(s) = \exp(sL)$, they proved the identities

$$
\begin{aligned}
\mathbb{E}_L[R_i(t)|X(t) = l, X(0) = k] &= \frac{1}{p_{kl}(t)} \int_0^t p_{ki}(s)p_{il}(t-s)\mathrm{d}s, \\
\mathbb{E}_L[N_{ij}(t)|X(t) = l, X(0) = k] &= \frac{l_{ij}}{p_{kl}(t)} \int_0^t p_{ki}(s)p_{jl}(t-s)\mathrm{d}s.
\end{aligned}
\tag{5.17}
$$

The crucial observation is now that an eigendecomposition of the generator L leads to closed form expressions of the integrals in (5.17). To be more precise, consider

---

Algorithm 4 MLE-method (Bladt,Sørensen,[5, 9])

Input: Time series $Y = \{y_0 = X(t_0), \ldots, y_N = X(t_N)\}$, initial guess of generator $\tilde{L}_0$.

Output: MLE $\tilde{L}$.

    (1) E-step: **FOR ALL** $\tau_s \in \{\tau_1, \ldots, \tau_r\}$ **DO**

         i) Compute for $i, j, l, k = 1, \ldots, d$ the conditional expectations

             $\mathbb{E}_{\tilde{L}_k}[R_i(\tau_s)|X(\tau_s) = l, X(0) = k]$,

             $\mathbb{E}_{\tilde{L}_k}[N_{ij}(\tau_s)|X(\tau_s) = l, X(0) = k]$, $i \neq j$ via (5.15),(5.13).

         END FOR

         ii) Compute $\mathbb{E}_{\tilde{L}_k}[R_i(T)|Y]$ and $\mathbb{E}_{\tilde{L}_k}[N_{ij}(T)|Y]$ via (5.12).

    (2) M-Step: Setup the next guess $\tilde{L}_{k+1}$ of the generator by

$$\tilde{l}_{ij} = \begin{cases} \mathbb{E}_{\tilde{L}_k}[N_{ij}(T)|Y] / \mathbb{E}_{\tilde{L}_k}[R_i(T)|Y], & i \neq j \\ -\sum_{k \neq i} \tilde{l}_{ik}, & \text{otherwise.} \end{cases}$$

    (3) Go to Step (1), unless a certain convergence criterion is satisfied.

---

the eigendecomposition of a generator L, that is

$$L = U D_\lambda U^{-1}, \tag{5.18}$$

where the columns of the matrix U consist of all eigenvectors to the corresponding eigenvalues of L in the diagonal matrix $D_\lambda = \text{diag}(\lambda_1, \ldots, \lambda_d)$. Consequently, the expression of the transition matrix $P(t)$ simplifies to

$$P(t) = \exp(tL) = U \exp(tD_\lambda)U^{-1}$$

and we finally end up with a closed form expression of the integrals in (5.17), that is [49]

$$\int_0^t p_{ab}(s)p_{cd}(t-s)\mathrm{d}s = \sum_{p=1}^d u_{ap}u_{pb}^{-1} \sum_{q=1}^d u_{cq}u_{qd}^{-1} \Psi_{pq}(t), \tag{5.19}$$

where the symmetric matrix $\Psi(t) = (\Psi_{pq}(t))_{p,q \in S}$ is defined as

$$\Psi_{pq}(t) = \begin{cases} te^{t\lambda_p} & \text{if } \lambda_p = \lambda_q \\ \frac{e^{t\lambda_p} - e^{t\lambda_q}}{\lambda_p - \lambda_q} & \text{if } \lambda_p \neq \lambda_q. \end{cases} \tag{5.20}$$

Remark 5.2.1. *We are aware of the fact that in general an eigenvalue decomposition does not have to exist. For example, consider the matrix*

$$L = \begin{pmatrix} -4 & 2 & 2 \\ 1 & -4 & 3 \\ 1 & 1 & -2 \end{pmatrix} \in \mathfrak{G}.$$

The characteristic polynomial of L is $-x(x+5)^2$, hence -5 is an eigenvalue with multiplicity two but the dimension of the corresponding eigenspace is one. However, in all of our numerical experiments this non-decomposable case did not show up.

For the convenience of the reader we state the resulting *enhanced MLE-method* in Algorithm 5. In a single iteration step for each single observation time lag, d^2 conditional expectations have to be computed where each one is decomposed into d^2 conditional expectations. Hence, the computational cost of a single iteration step in Algorithm 4 and in Algorithm 5 is $\mathcal{O}(r \cdot d^4 \cdot T_{\mathbb{E}})$ where r is the number of the different observed time lags and $T_{\mathbb{E}}$ denotes the computational cost to compute a single conditional expectation in the E-Step. The numerical considerations in [9] lead to a total computational cost per iteration in Algorithm 4 of at least $\mathcal{O}(r \cdot d^6)$. According to the closed form expressions for the expectations (5.19), the computational cost of a single iteration in the enhanced MLE-method (Algorithm 5) is $\mathcal{O}(r \cdot d^5)$ which is achieved by a simultaneously computation of the unknowns via matrix multiplication. For example, define for a fixed $i \in S$ the matrix $M^i_{kl} = \mathbb{E}_L\left[R_i(\tau)|X(\tau) = l, X(0) = k\right]$. Let U_i^{-1} denote the ith row of the matrix U^{-1} and U_i the ith column of U. Then M^i can be computed by

$$M^i = U\left[(U_i^{-1}U_i) * \Psi\right]U^{-1},$$

where $A * B$ is the Hadamard (entrywise) product of two matrices A and B. We want to emphasize that the algorithm works in principal even in the case of pairwise different time lags, i.e. $r = N - 1$ where N is the number of observations, but in practise this would lead to unacceptable computational costs.

Algorithm 5 Enhanced MLE-method

Input: Time series $Y = \{y_0 = X(t_0), \ldots, y_N = X(t_N)\}$, the set of observed time
lags $\{\tau_1, \ldots, \tau_r\}$, the tolerance TOL, initial guess of generator $\tilde{L}_0$.
Output: MLE $\tilde{L}$.
(1) Compute eigendecomposition (5.18) of $\tilde{L}_k$.
(2) E-step: **FOR ALL** $\tau_s \in \{\tau_1, \ldots, \tau_r\}$ **DO**
      i)   Compute the auxiliary matrix $\Psi(\tau_s)$ (5.20).
      ii) Compute for $i, j, l, k = 1, \ldots, d$ the conditional expectations
         $\mathbb{E}_{\tilde{L}_k}\left[R_i(\tau_s)|X(\tau_s) = l, X(0) = k\right],$
         $\mathbb{E}_{\tilde{L}_k}\left[N_{ij}(\tau_s)|X(\tau_s) = l, X(0) = k\right], i \neq j$ via (5.19),(5.17).
      END FOR
      iii) Compute $\mathbb{E}_{\tilde{L}_k}\left[R_i(T)|Y\right]$ and $\mathbb{E}_{\tilde{L}_k}\left[N_{ij}(T)|Y\right]$ via (5.12).
(3) M-Step: Setup the next guess $\tilde{L}_{k+1}$ of the generator by
$$\tilde{l}_{ij} = \begin{cases} \mathbb{E}_{\tilde{L}_k}\left[N_{ij}(T)|Y\right]/\mathbb{E}_{\tilde{L}_k}\left[R_i(T)|Y\right], & i \neq j \\ -\sum_{k \neq i} \tilde{l}_{ik}, & \text{otherwise.} \end{cases}$$
(4) Go to Step (1) unless $\|\tilde{L}_{k+1} - \tilde{L}_k\| < TOL$.

5.2.4. Reversible Case

In the reversible case the homogeneous Markov jump process, given by its generator L, admits a unique stationary distribution $\pi = (\pi_i)_{i \in S}$ and, moreover, *detailed balance* holds:

$$l_{ji} = \frac{\pi_i}{\pi_j} l_{ij}.$$

This has two important consequences for the EM-algorithm. The first one is that detailed balance guarantees a special representation of L which improves the stability

and accuracy of the EM-algorithm. Furthermore, one has to take into account that the M-step in general does not preserve the reversibility. To understand the first issue, notice that L can be written as

$$L = D_\pi^{-1/2} \mathbf{S} D_\pi^{1/2} \tag{5.21}$$

with a symmetric matrix $\mathbf{S}$ which can be decomposed as

$$\mathbf{S} = V D_\lambda V^T,$$

where $\lambda_1, \dots, \lambda_d \in \mathbb{R}$ are the eigenvalues of $\mathbf{S}$ and V is an orthogonal matrix, i.e. $VV^T = I$. Combining things, we end up with [48]

$$P(t) = D_\pi^{-1/2} V \exp(D_\lambda) V^T D_\pi^{1/2},$$

where $D_\pi^{1/2} = \mathrm{diag}(\sqrt{\pi_1}, \dots, \sqrt{\pi_d})$. Consequently, the integrals in (5.17) reduce to

$$\int_0^t p_{ab}(s) p_{cd}(t-s) \mathrm{d}s = \left(\frac{\pi_b \pi_d}{\pi_a \pi_c} \right)^{1/2} \sum_{p=1}^d v_{ap} v_{bp} \sum_{q=1}^d v_{cq} v_{dq} \Psi_{pq}(t), \tag{5.22}$$

where Ψ is defined in (5.20).

Next, we turn our attention to the problem of the non-preservation of the reversibility in the M-Step. The first idea could be to exploit the fact that detailed balance implies the bisection of the unknowns because l_{ji} is determined by π_i, π_j and l_{ij}. Then one could proceed as follows: Firstly, compute the MLE $\tilde{L}$ via the EM-algorithm as usual and then define a reversible generator $\tilde{L}^{REV} = (\tilde{l}_{ij}^{REV})_{i,j \in S}$ by

$$\tilde{l}_{ij}^{REV} = \begin{cases} \tilde{l}_{ij} & \text{if } i \leq j \\ \dfrac{\pi_j}{\pi_i} \tilde{l}_{ji} & \text{otherwise.} \end{cases}$$

This would work in principle but it does not guarantee that the resulting generator $\tilde{L}^{REV}$ is the MLE *subject* to the space of reversible generators. As a remedy, we include the restriction to that space explicitly in the log-likelihood function (5.10) via Lagrange multiplier:

$$\mathcal{G}^{REV}(L; \tilde{L}_0) = \mathcal{G}(L; \tilde{L}_0) + \sum_{i=1}^d \sum_{j>i}^d \mu_{ij} \left(\pi_i l_{ij} - \pi_j l_{ji} \right).$$

Performing the usual steps, we end up with the MLE $\tilde{L}^{REV}$, given by

$$\tilde{l}_{ij}^{REV} = \begin{cases} \dfrac{\mathbb{E}_{\tilde{L}_0} [N_{ij}(T)|Y]}{-\mu_{ij} \pi_i + \mathbb{E}_{\tilde{L}_0} [R_i(T)|Y]}, & i < j \\ \dfrac{\pi_i}{\pi_j} \tilde{l}_{ij}^{REV}, & \text{otherwise} \end{cases} \tag{5.23}$$

where the Lagrange multiplier can be determined by

$$\mu_{ij} = \left[\frac{\mathbb{E}_{\tilde{L}_0} [R_j(T)|Y]}{\pi_j \mathbb{E}_{\tilde{L}_0} [N_{ji}(T)|Y]} - \frac{\mathbb{E}_{\tilde{L}_0} [R_i(T)|Y]}{\pi_i \mathbb{E}_{\tilde{L}_0} [N_{ij}(T)|Y]} \right]$$
$$\times \left[-\frac{\mathbb{E}_{\tilde{L}_0} [N_{ij}(T)|Y] \cdot \mathbb{E}_{\tilde{L}_0} [N_{ji}(T)|Y]}{\mathbb{E}_{\tilde{L}_0} [N_{ij}(T)|Y] + \mathbb{E}_{\tilde{L}_0} [N_{ji}(T)|Y]} \right]. \tag{5.24}$$

Combining both issues leads to Algorithm 6.

Algorithm 6 Enhanced MLE-method for the reversible case

Input: Time series $Y = \{y_0 = X(t_0), \ldots, y_N = X(t_N)\}$, the set of observed time lags $\{\tau_1, \ldots, \tau_r\}$, the tolerance TOL, initial guess of reversible generator $\tilde{L}_0^{REV}$.
Output: Reversible MLE $\tilde{L}^{REV}$.
  (1) Compute eigendecomposition (5.21) of $\tilde{L}_k^{REV}$.
  (2) E-step: **FOR ALL** $\tau_s \in \{\tau_1, \ldots, \tau_r\}$ **DO**
      i)   Compute the auxiliary matrix $\Psi(\tau_s)$ (5.20).
      ii) Compute for $i, j, l, k = 1, \ldots, d$ the conditional expectations
           $\mathbb{E}_{\tilde{L}_k^{REV}}[R_i(\tau_s)|X(\tau_s) = l, X(0) = k]$,
           $\mathbb{E}_{\tilde{L}_k^{REV}}[N_{ij}(\tau_s)|X(\tau_s) = l, X(0) = k], i \neq j$ via (5.22),(5.17).
        END FOR
      iii) Compute $\mathbb{E}_{\tilde{L}_k^{REV}}[R_i(T)|Y]$ and $\mathbb{E}_{\tilde{L}_k^{REV}}[N_{ij}(T)|Y]$ via (5.12).
  (4) Compute Lagrange multipliers μ_{ij} via (5.24).
  (5) M-Step: Setup the next guess $\tilde{L}_{k+1}^{REV}$ of the generator via (5.23).
  (4) Go to Step (1) unless $\|\tilde{L}_{k+1}^{REV} - \tilde{L}_k^{REV}\| < TOL$.

5.2.5. Scaling

We prove that the maximizer (5.11) in the (enhanced) MLE-method respects the time invariance of the semigroup $P(t) = \exp(tL)$. Consequently, in the case of a constant observation time step τ we can estimate a generator $\tilde{L}(\tau')$ with respect to $\tau' = 1$ and regain the generator with respect to τ by $\tilde{L}(\tau) = \tilde{L}(1)/\tau$.

Lemma 5.2.2. *Let $\tilde{L}(\tau)$ be the MLE with respect to the time lag τ and $\tilde{L}(1)$ with respect to $\tau' = 1$. Then for both cases the general and the reversible case the following relation holds:*

$$\tilde{L}(\tau) = \frac{1}{\tau}\tilde{L}(1). \tag{5.25}$$

Proof:
A short calculation shows that

$$\int_0^\tau p_{ab}(s)p_{cd}(\tau - s)\mathrm{d}s = \tau \int_0^1 [\exp(s\bar{L})_{ab}(\exp((1-s)\bar{L})_{cd}]\mathrm{d}s,$$

where $\bar{L} = \tau L$. But this immediately implies

$$\mathbb{E}_L[R_i(\tau)|X(\tau) = l, X(0) = k] = \tau \mathbb{E}_{\bar{L}}[R_i(1)|X(1) = l, X(0) = k]$$

and, by noting that $l_{ij} = \frac{1}{\tau}\bar{l}_{ij}$,

$$\mathbb{E}_L[N_{ij}(\tau)|X(\tau) = l, X(0) = k] = \mathbb{E}_{\bar{L}}[N_{ij}(1)|X(1) = l, X(0) = k]$$

which proves (5.25). In the reversible case, the same reasoning shows that the Lagrange multipliers scale linearly with τ and therefore (5.25) also holds.

5.2.6. Enhanced MLE-Method vs. MLE-Method

The eigendecomposition approach has several advantages compared to the numerical considerations proposed in [9]. Let d be the dimension of the discrete state space. As

explained in Section 5.2.2, the computational cost is reduced to $\mathcal{O}(r \cdot d^5)$ thanks to the closed form expression (5.19). Moreover, there is no longer an explicit dependency on the length of the time series. The second advantage is the exact computation of the conditional expectations involved in the E-step of the EM-algorithm. The steps which introduce numerical errors are the eigendecomposition and the computation of U^{-1}. As before, the explicit inversion of U can be avoided by considering the left eigenvectors of $\tilde{L}$. We are aware that the eigendecomposition of non-symmetric matrices can be *ill-conditioned*, but any reliable numerical solver should indicate this. Nevertheless, the computational cost of both steps ($\mathcal{O}(d^3)$) and their numerical stability are superior compared to any numerical approximation scheme for solving the ODEs in (5.15).

5.3. An Alternative Approach: The Quadratic Optimization Method

The approach introduced by Crommelin and Vanden-Eijnden [19] yields an estimate $\tilde{L}$ such that the spectral properties of the empirical transition matrix $\hat{P}$, i.e. eigenvalues and eigenvectors, are well approximated by the spectral properties of $\exp(\tau\tilde{L})$.

Let $\hat{P} \approx P(\tau)$ be the approximative transition matrix computed by Equation (5.8). Now suppose an eigendecomposition

$$\hat{P} = U\Lambda U^{-1} \tag{5.26}$$

with a diagonal matrix $\Lambda = \mathrm{diag}(\lambda_1, \ldots, \lambda_d)$ containing the eigenvalues exists, and that $\lambda_k \neq 0$ for all k. (Note that U^{-1} can be obtained without explicit matrix inversion since its rows are the left eigenvectors of $\hat{P}$.) Then, the matrix

$$\tilde{L} \;=\; UZU^{-1} \quad \text{with} \quad Z = \mathrm{diag}(z_1, \ldots, z_d), \quad z_k = \frac{\log(\lambda_k)}{\tau} \tag{5.27}$$

can be defined, and the approximative transition matrix can be expressed in terms of the matrix exponential

$$\exp(\tau\tilde{L}) = \exp\left(U \log(\Lambda) U^{-1}\right) = U\Lambda U^{-1} = \hat{P}.$$

In spite of this relation, $\tilde{L}$ cannot be considered as a reasonable estimate for the generator because $\tilde{L} \notin \mathfrak{G}$ in many cases. In order to find an estimate with the correct structural properties, Crommelin and Vanden-Eijnden propose to compute the generator $\tilde{L} \in \mathfrak{G}$ which agrees best with the eigendecomposition (5.27). This is motivated by the fact that many properties of a continuous-time Markov chain (such as, e.g., its stationary distribution) depend strongly on the eigenvalues and eigenvectors of its generator. Therefore, in [19] the generator is estimated by solving the quadratic minimization problem

$$\tilde{L}_{QP} = \arg\min_{L \in \mathfrak{G}} \sum_{k=1}^{d} \Big(\alpha_k |U_k^{-1}L - z_k U_k^{-1}|^2 \quad + \quad \beta_k |LU_k - z_k U_k|^2$$
$$+ \quad \gamma_k |U_k^{-1}LU_k - z_k|^2 \Big), \tag{5.28}$$

where U_k denotes the kth column of U, U_k^{-1} is the kth row of U^{-1}, and

$$\alpha_k = a_k |z_k U_k^{-1}|^{-2}, \quad \beta_k = b_k |z_k U_k|^{-2} \quad \text{and} \quad \gamma_k = c_k |z_k|^{-2}$$

are weights with suitably chosen coefficients a_k, b_k, c_k. The problem (5.28) can be solved with a standard quadratic optimizer such as the MATLAB `quadprog` command after reformulating (5.28) as

$$\tilde{L}_{QP} = \arg\min_{L \in \mathfrak{G}} \frac{1}{2}\langle L, HL \rangle + \langle F, L \rangle + E_0$$

with a tensor $H \in \mathbb{R}^{d \times d \times d \times d}$ and a matrix $F \in \mathbb{R}^{d \times d}$; see [19] for details. If d is so large that the tensor H cannot be stored, the problem (5.28) can still be solved with `quadprog`, but this requires a function for the evaluation of Hv for arbitrary v without composing H explicitly.

5.4. Numerical Examples for Equidistant Observation Times

5.4.1. Preparatory Considerations

In order to compare the performance of the quadratic programming approach (QP) and the maximum likelihood method (MLE), we will first restrict ourselves to the case of equidistant observation times and we will apply the approaches to a series of model problems. In Section 5.5, we will focus on the case of non-equidistant observation times.

A rather straightforward test would proceed as follows:

1. Choose an arbitrary generator $L \in \mathfrak{G}$ and a time lag τ.

2. Compute the corresponding transition matrix $P(\tau) = \exp(\tau L)$.

3. Produce a time series $Y = \{y_0 = X(t_0), \ldots, y_N = X(t_N)\}$ by sampling from $P(\tau)$.

4. Pass this data to each of the two methods and compute an estimate $\tilde{L} \approx L$.

5. Compare the errors of the two approaches.

Although such a test seems to be somewhat reasonable, we will *not* use this procedure. The reason for our refusal is the fact that the time series produced in step 3 is just a single realization. Hence, the result of this test is random, too, and applying the test several times to the methods yields different results even though the input L remains unchanged. In fact, both methods are affected by the sampling error

$$\|P(\tau) - \hat{P}\| \quad \text{with} \quad \hat{P} = (\hat{p}_{ij})_{i,j} \quad \text{and} \quad \hat{p}_{ij} = \frac{c_{ij}}{\sum_{j=1}^{d} c_{ij}}. \tag{5.29}$$

(Here and below, $\|\cdot\|$ denotes the matrix 2-norm.) Roughly speaking, the sampling error indicates how well the frequency matrix of a time series "represents" the underlying transition matrix. In the limit $N \to \infty$ one may expect the sampling error to vanish, but for a finite number of observations the deviation can be considerable. Since the outcome of a numerical method cannot be better than the input data, the error of both methods are bounded from below by the sampling error.

Therefore, our numerical experiments are designed in a different way:

1. a) Choose a generator $L \in \mathfrak{G}$ and a time lag τ and compute the corresponding transition matrix $P(\tau) = \exp(\tau L)$,

   or

   b) choose a transition matrix P. This allows to test the performance of the methods in situations where no underlying generator exists. In this case, the time lag does not matter, and we can set $\tau = 1$.

2. Define a virtual frequency matrix by multiplying each row of the transition matrix $P(\tau)$ with the corresponding entry of the stationary distribution $\pi = (\pi_i), i \in S$ and the length N of the (virtual) time series:

$$c_{ij} = \text{round}(N\pi_i p_{ij}). \tag{5.30}$$

   This is the frequency matrix which, up to rounding errors, reflects the underlying transition matrix in an optimal way.

3. Based on the virtual frequency matrix, define the virtual transition matrix

$$\hat{P}_{virt} = (\hat{p}_{ij})_{i,j} \quad \text{and} \quad \hat{p}_{ij} = \frac{c_{ij}}{\sum_{j=1}^{d} c_{ij}} \tag{5.31}$$

   and compute an estimate $\tilde{L} \approx L$ for the generator.

4. For both methods, compute and compare the errors:

   a) $\|\tilde{L} - L\|$ (only if L is available, i.e. if variant (a) of step 1 was used)
   b) $\|P(\tau) - \exp(\tau\tilde{L})\|$
   c) $\|\hat{P}_{virt} - \exp(\tau\tilde{L})\|$ with $\hat{P}_{virt}$ defined in (5.31).

The advantage of this approach to numerical experiments is illustrated by a simple example in the next section.

Of course, the choice of the initial value $\tilde{L}_0$ for the MLE-method is crucial for the convergence. If the matrix logarithm of $\hat{P}_{virt}$ exists, then a good initial value $\tilde{L}_0$ can easily be obtained by taking the absolute values of the off-diagonal entries of $\log(\hat{P}_{virt})/\tau$ and setting the diagonal entries to the corresponding negative row sums, respectively.

A Simple Example Illustrating the Effect of Sampling Errors

This example illustrates the influence of the sampling error on the optimal generator estimate. The transition matrix of the generator

$$L = \begin{pmatrix} -0.2 & 0.2 \\ 0.2 & -0.2 \end{pmatrix}$$

with respect to the time lag $\tau = 1$ is

$$P(\tau) = \begin{pmatrix} 0.8352 & 0.1648 \\ 0.1648 & 0.8352 \end{pmatrix}.$$

Suppose that sampling according to the transition matrix produces the time series

time t_n	0	1	2	3	4	5	6	7	8	9	10
state $X(t_n)$	2	1	1	1	1	2	2	1	1	2	1

such that the corresponding frequency matrix is

$$C = \begin{pmatrix} 4 & 2 \\ 3 & 1 \end{pmatrix}.$$

According to this data, the transition matrix seems to be

$$\hat{P} = \begin{pmatrix} 2/3 & 1/3 \\ 3/4 & 1/4 \end{pmatrix} \tag{5.32}$$

and since $\hat{P} = \exp(\hat{L})$ with

$$\hat{L} \approx \begin{pmatrix} -0.5003 & 0.5003 \\ 0.3752 & -0.3752 \end{pmatrix} \in \mathfrak{G} \tag{5.33}$$

the best result we can expect to obtain based on the time series is $\hat{L}$ instead of L. The errors $\|\hat{P} - P\| \approx 0.2670$ and $\|\hat{L} - L\| \approx 0.4916$ are caused by the time series and cannot be avoided by the two methods. However, these errors decrease if, according to the second test procedure, the frequency matrix is replaced by the virtual frequency matrix (5.30). Since in our example the stationary distribution is $\pi = (0.5, 0.5)$, one obtains

$$C = \begin{pmatrix} 4 & 1 \\ 1 & 4 \end{pmatrix}.$$

The corresponding transition matrix

$$\hat{P}_{virt} = \begin{pmatrix} 0.8 & 0.2 \\ 0.2 & 0.8 \end{pmatrix}$$

is obviously a better approximation of the true transition matrix P than (5.32), and the generator estimate

$$\tilde{L} = \log(\hat{P}_{virt}) \approx \begin{pmatrix} -0.2554 & 0.2554 \\ 0.2554 & -0.2554 \end{pmatrix}$$

is evidently better than (5.33). In fact, the new errors are only $\|P - \hat{P}_{virt}\| \approx 0.0703$ and $\|L - \tilde{L}\| \approx 0.1108$.

5.4.2. Transition Matrix with Underlying Generator

In a first example we follow variant (a) of step 1 and consider the generator

$$L = \begin{pmatrix} -4.29 & 0.678 & 0.301 & 0.819 & 0.592 & 0.149 & 0.543 & 0.411 & 0.774 & 0.023 \\ 0.033 & -3.83 & 0.633 & 0.260 & 0.636 & 0.878 & 0.485 & 0.527 & 0.147 & 0.231 \\ 0.857 & 0.995 & -5.46 & 0.704 & 0.532 & 0.021 & 0.441 & 0.920 & 0.148 & 0.845 \\ 0.682 & 0.499 & 0.005 & -4.69 & 0.208 & 0.923 & 0.626 & 0.379 & 0.639 & 0.726 \\ 0.801 & 0.430 & 0.816 & 0.082 & -4.26 & 0.632 & 0.077 & 0.638 & 0.093 & 0.694 \\ 0.917 & 0.829 & 0.690 & 0.875 & 0.241 & -5.58 & 0.544 & 0.173 & 0.928 & 0.383 \\ 0.388 & 0.116 & 0.981 & 0.077 & 0.720 & 0.632 & -4.66 & 0.785 & 0.485 & 0.479 \\ 0.472 & 0.598 & 0.069 & 0.741 & 0.400 & 0.753 & 0.270 & -4.43 & 0.163 & 0.967 \\ 0.088 & 0.221 & 0.045 & 0.125 & 0.394 & 0.769 & 0.291 & 0.776 & -3.49 & 0.783 \\ 0.925 & 0.398 & 0.740 & 0.443 & 0.411 & 0.808 & 0.822 & 0.342 & 0.131 & -5.02 \end{pmatrix} \in \mathfrak{G}. \tag{5.34}$$
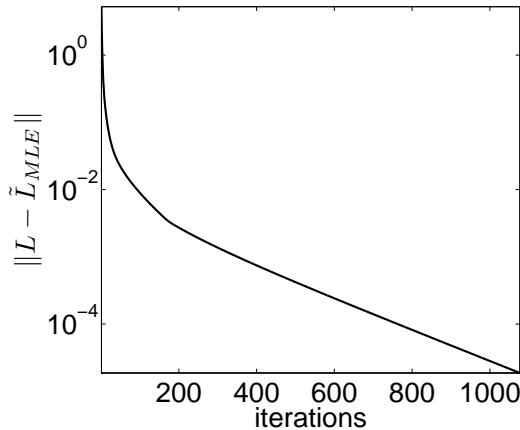
Figure 5.1.: Approximation error of $\tilde{L}_{MLE}$ with respect to the generator L in (5.34) as a function of the iteration steps.

	$\|L - \tilde{L}\|$	$\|\exp(\tau L) - \exp(\tau \tilde{L})\|$	$\|\hat{P}_{virt} - \exp(\tau \tilde{L})\|$
QP	$2.07 \cdot 10^{-8}$	$1.39 \cdot 10^{-9}$	$1.18 \cdot 10^{-14}$
MLE	$1.88 \cdot 10^{-5}$	$1.19 \cdot 10^{-6}$	$1.19 \cdot 10^{-6}$

Table 5.1.: Approximation errors of the estimated generators $\tilde{L}_{QP}$ and $\tilde{L}_{MLE}$ with respect to the given generator (5.34), the exact transition matrix $P(\tau)$ and the transition matrix $\hat{P}_{virt}$ constructed via (5.31). Results for the time lag $\tau = 0.2$ and the length of the virtual time series $N = 10^{10}$.

Based on the exact transition matrix $P(\tau)$ with $\tau = 0.2$, we computed the virtual transition matrix $\hat{P}_{virt}, N = 10^{10}$ via (5.31) and estimated the generator with both methods. The enhanced MLE-method (5) stopped after 1132 iteration steps because the increment-based stopping criterion $\|\tilde{L}_k - \tilde{L}_{k-1}\| \leq tol$ with $tol = 10^{-7}$ had been met. Figure 5.1 shows the error of $\tilde{L}_{MLE}$ with respect to L (5.34) as a function of the iteration steps.

Obviously, the convergence of the enhanced MLE-method is very slow. In contrast to the MLE-method, the QP-method converged after only one iteration step. In Table 5.1 the errors of both approaches are compared. The QP-approach approximates the original generator clearly better than the enhanced MLE-method. This is, however, not surprising because it has to be taken into account that the QP-approach approximates the eigendecomposition of $\hat{P}_{virt}$ and for the length $N = 10^{10}$ of a virtual time series the difference between the exact and the virtual transition matrix is only $\|P(0.2) - \hat{P}_{virt}\| = 1.39 \cdot 10^{-9}$.

Next, we investigate the influence of the sampling error on both estimation methods. Instead of considering realizations of the Markov jump process, we compute estimations of L for a number of virtual time series of increasing length N. Figure 5.2 shows the resulting errors of $\tilde{L}_{MLE}$ and $\tilde{L}_{QP}$ with respect to the generator L (5.34) as a function of the length N of the virtual time series. It reveals that for a time series of a realistic length ($N \leq 10^7$), the errors of $\tilde{L}_{QP}$ and $\tilde{L}_{MLE}$ are almost identical. The fact that the error of the MLE-method remains larger than 10^{-5} regardless of N is due to the chosen stopping criterion.
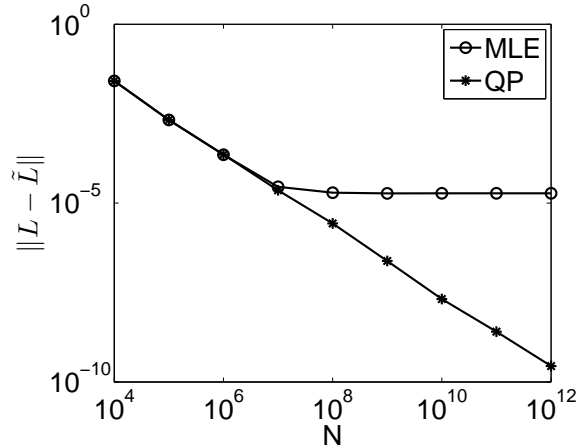
Figure 5.2.: Graphs of the errors of $\tilde{L}_{MLE}$ and $\tilde{L}_{QP}$ with respect to the generator L in (5.34), respectively, as a function of the length N of the virtual time series. The error of the MLE-method remains larger than 10^{-5} regardless of N due to the stopping criterion $\|\tilde{L}_k - \tilde{L}_{k-1}\| \leq 10^{-7}$.

	$\|P - \exp(\tau\tilde{L})\|$	$\|\hat{P}_{virt} - \exp(\tau\tilde{L})\|$
QP	$1.74 \cdot 10^{-2}$	$1.74 \cdot 10^{-2}$
MLE	$2.86 \cdot 10^{-2}$	$2.86 \cdot 10^{-2}$

Table 5.2.: Approximation errors of $\exp(\tilde{L}_{QP})$ and $\exp(\tilde{L}_{MLE})$ with respect to the given transition matrix (5.35) and the transition matrix $\hat{P}_{virt}$ constructed via (5.31). Results of MLE-method for $tol = 10^{-7}$.

5.4.3. Transition Matrix without Underlying Generator

In contrast to the first case both estimation procedures are now applied to a transition matrix which does not possess a generator:

$$P = \begin{pmatrix} 0.645 & 0.037 & 0.033 & 0.039 & 0.046 & 0.062 & 0.040 & 0.003 & 0.031 & 0.059 \\ 0.014 & 0.792 & 0.054 & 0.06 & 0.010 & 0 & 0 & 0 & 0.016 & 0.051 \\ 0.049 & 0.065 & 0.751 & 0.069 & 0.000 & 0 & 0 & 0 & 0.046 & 0.015 \\ 0.020 & 0.056 & 0.057 & 0.723 & 0.061 & 0 & 0 & 0 & 0.022 & 0.057 \\ 0.037 & 0.044 & 0.039 & 0.061 & 0.707 & 0 & 0 & 0 & 0.066 & 0.043 \\ 0.010 & 0.057 & 0.025 & 0.012 & 0.020 & 0.727 & 0.032 & 0.053 & 0.050 & 0.009 \\ 0 & 0 & 0 & 0.069 & 0.047 & 0.016 & 0.753 & 0.069 & 0.029 & 0.014 \\ 0 & 0 & 0 & 0.019 & 0.019 & 0.040 & 0.055 & 0.770 & 0.052 & 0.042 \\ 0 & 0 & 0 & 0.019 & 0.035 & 0.057 & 0.004 & 0.059 & 0.776 & 0.047 \\ 0 & 0 & 0 & 0.065 & 0.004 & 0.039 & 0.045 & 0.032 & 0.033 & 0.778 \end{pmatrix} \notin \mathfrak{P} \quad (5.35)$$

One can immediately verify via Theorem A.6.8 cited in the Appendix that (5.35) cannot be generated since, e.g, the state 6 is accessible from state 2 via state 1 but $p_{2,6} = 0$. As Table 5.2 shows, the errors of the estimated transition matrices $\exp(\tau\tilde{L})$ are of the same order of magnitude and are larger than in the first example due to the additional difficulty that no generator exists. The error $\|P - \exp(\tilde{L}_{MLE})\|$ as a function of the first 10 iteration steps is shown in the left panel of Figure 5.3. Surprisingly, the best accuracy is obtained after only one iteration, but the following iterations increase the error again. The reason for this behavior is the fact that the MLE-method aims to maximizing the likelihood instead of minimizing the error, and the graph of the discrete log-likelihood, depicted in the right panel of Figure 5.3, clearly shows that the maximum likelihood was not attained after the first iteration.
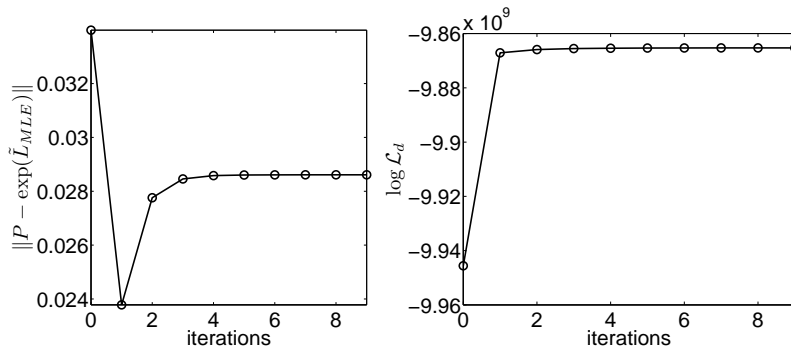
Figure 5.3.: Left: Error of $\exp(\tilde{L}_{MLE})$ with respect to the transition matrix P (5.35) as a function of the first 10 iteration steps. Right: The discrete log-likelihood $\mathcal{L}_d$ as a function of the 10 first iteration steps.
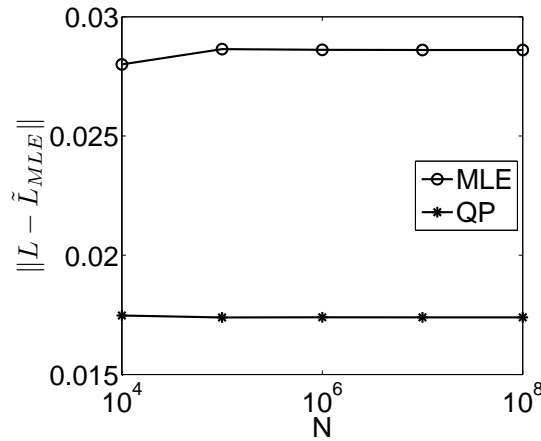
Figure 5.4.: The graphs of the errors of $\exp(\tilde{L}_{MLE})$ and $\exp(\tilde{L}_{QP})$ with respect to the transition matrix (5.35), respectively, as a function of the length N of the virtual time series.

In contrast to the first example, Figure 5.4 shows that here increasing the length of the virtual time series does not improve the estimation significantly in both methods.

5.4.4. Transition Matrix with Exact Generator under Perturbation

In the next example, we consider again the transition matrix $P(\tau)$ with $\tau = 0.2$ which is generated by the generator (5.34) given in the first example. In order to investigate the impact of perturbations due to, e.g., sampling from a time series, we estimate a generator based on a perturbed transition matrix

$$P_\epsilon(\tau) = \exp(\tau L) + k\epsilon, \quad k = 0, ..., 19,$$
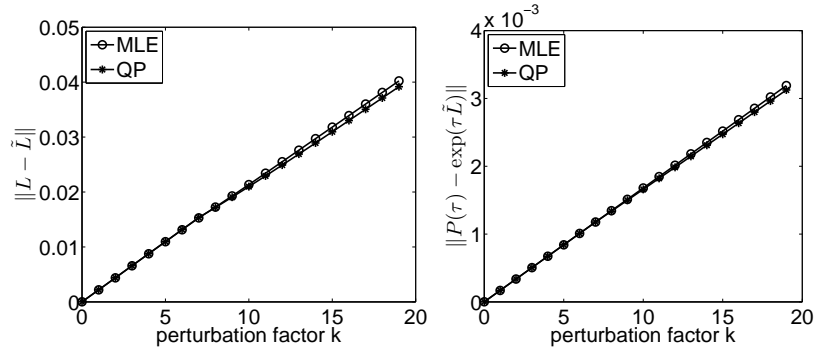
Figure 5.5.: Left: Approximation error of the generator estimates $\tilde{L}_{QP}$ and $\tilde{L}_{MLE}$ with respect to the unperturbed generator (5.34) as a function of the perturbation factor k. Right: Error of the estimated transition matrices $\exp(\tau\tilde{L}_{QP})$ and $\exp(\tau\tilde{L}_{MLE})$ with respect to the unperturbed transition matrix $\exp(\tau L)$ as a function of the perturbation factor k. Results for $\tau = 0.2$.

, where ϵ is the perturbation matrix

$$\epsilon = 10^{-5} \cdot \begin{pmatrix} 4.05 & -3.55 & 1.75 & 0.80 & -4.09 & -3.51 & 4.71 & 0.04 & 0.69 & -0.91 \\ 3.10 & -3.50 & -1.60 & 2.87 & 1.31 & -0.67 & 2.02 & 1.45 & 1.27 & -6.26 \\ -3.22 & -0.97 & -2.61 & 5.67 & -3.65 & 2.38 & 5.72 & -2.47 & 0.15 & -0.99 \\ 4.46 & -1.23 & -5.22 & 1.94 & -1.02 & -3.49 & 2.43 & -2.04 & 2.68 & 1.49 \\ 4.69 & -4.18 & -1.27 & 1.94 & -4.19 & -0.45 & -0.85 & 3.64 & -4.33 & 4.99 \\ 4.37 & -2.33 & -1.60 & 3.41 & 1.55 & 1.85 & -4.52 & -2.27 & 4.35 & -4.80 \\ 1.20 & -2.23 & 5.50 & -4.12 & -1.15 & -0.13 & -3.34 & -3.63 & 4.11 & 3.78 \\ 2.83 & -1.00 & 2.73 & -3.00 & -1.06 & -4.55 & 2.69 & 2.61 & 3.19 & -4.43 \\ -1.47 & 4.04 & -0.31 & -3.72 & -0.41 & 1.24 & 0.45 & -2.99 & -2.15 & 5.33 \\ -1.46 & -1.56 & 5.23 & -0.77 & -2.61 & 4.25 & -2.00 & -0.25 & 0.70 & -1.51 \end{pmatrix}.$$

The left panel of Figure 5.5 shows the deviation of the estimated generators from the unperturbed generator as a function of the perturbation factor k. The QP-method performs slightly better but both errors $\|L - \tilde{L}_{QP}\|$ and $\|L - \tilde{L}_{MLE}\|$ are of the same order of magnitude. Furthermore, the errors scale linearly with the perturbation factor k. This observation is plausible since for small perturbations the logarithm $\log(P + \epsilon)$ can be approximated by $\log(P) + \mathcal{O}(\epsilon)$. The right panel of Figure 5.5 illustrates the behavior of the errors of the estimated transition matrices $\exp(\tau\tilde{L}_{QP})$ and $\exp(\tau\tilde{L}_{MLE})$, respectively. A similar reasoning as above explains the linear scaling.

Finally, we consider the error of the estimated transition matrices $\exp(\tau\tilde{L}_{QP})$ and $\exp(\tau\tilde{L}_{MLE})$ with respect to the perturbed transition matrix $P_\epsilon(\tau) = \exp(\tau L) + k\epsilon$, depicted in Figure 5.6. Notice that the error $\|P_\epsilon(\tau) - \exp(\tau\tilde{L})\|$ is bounded from above, namely

$$\|P_\epsilon(\tau) - \exp(\tau\tilde{L})\| \leq \|\exp(\tau L) - \exp(\tau\tilde{L})\| + k\|\epsilon\|.$$

Indeed, Figure 5.6 shows that both errors obey that bound. For the perturbation factors up to $k = 8$, the matrix logarithm of P_ϵ is still a generator whereas for $k = 9, \ldots, 19$ the perturbation is apparently high enough to destroy the generator structure of the matrix logarithm of P_ϵ. However, the accuracy of both methods is again of the same order of magnitude.
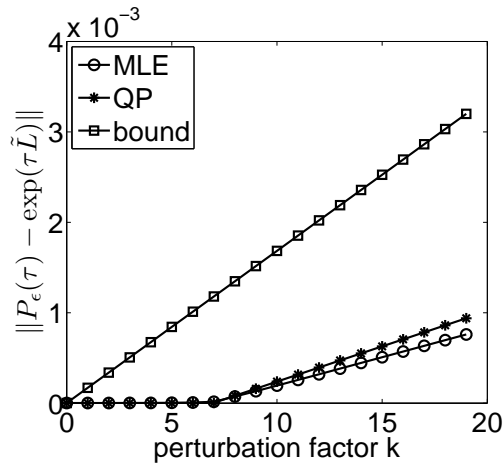
Figure 5.6.: Error of the estimated transition matrices $\exp(\tau \tilde{L}_{QP})$ and $\exp(\tau \tilde{L}_{MLE})$ with respect to the perturbed transition matrix $P_\epsilon(\tau) = \exp(\tau L) + k\epsilon$ as a function of the perturbation factor k. The upper bound was computed via $\tilde{L}_{MLE}$.

5.4.5. Application to a Time Series from Molecular Dynamics

In this example, we apply the enhanced MLE-method to a time series of two torsion angles extracted from a molecular simulation of glycine in water. The ball-and-stick representation of glycine together with the two considered torsion angles Φ and Ψ is shown in Figure 4.9(Sect. 4.3.2). The time series used herein was extracted out of a molecular simulation of the glycine-molecule embedded in a cubic box of edge length 3.51 nm with 1402 water molecules. The integration of the trajectory with total length $T = 5$ nanoseconds was realized with 2 femtoseconds time steps in the Leapfrog-integration scheme with GROMACS force field [8, 59] at room temperature of 300K. The left panel of Figure 5.7 shows the projection of the time series onto the torsion angles Φ and Ψ which reveals the metastable behavior. The Ramachandran plot of the time series, given in the right panel of Figure 5.7, illustrates the dependency among both torsion angles and indicates that the glycine-molecule attains four different main conformations.

As explained in Section 4.3.2, the identification of conformations amounts to identify metastable states in a coarse grained model of the dynamics. We considered a 20×20 box discretization of the torsion angle space which results in a state space of 374 visited boxes. In order to ensure the Markov property, we considered only every 100th step of the original trajectory and estimated a reversible generator with respect to the reversible transition matrix $\hat{P}$ (cf. (5.8)) via the Algorithm 6. Moreover, instead of using the time lag $\tau = 2 \cdot 10^{-13}$, we performed the estimation with respect to $\tau = 1$ and re-scaled the resulting generator $\tilde{L}_{MLE}$ afterwards (cf. Sect. 5.2.5). As one can see in Figure 5.8, the estimation algorithm is already converged after 200 steps (here we used the log-likelihood function as an indicator for convergence).

In Table 5.3 we compare the dominant eigenvalues of the transition matrix $\hat{P}$ with those of $\tilde{P} = \exp(\tau \tilde{L}_{MLE})$. The spectral gap as well as the eigenvalues are more or less well reproduced. The panels of Figure 5.9 illustrate the decomposition of the state space via PCCA which is based on the eigenvectors corresponding to

109
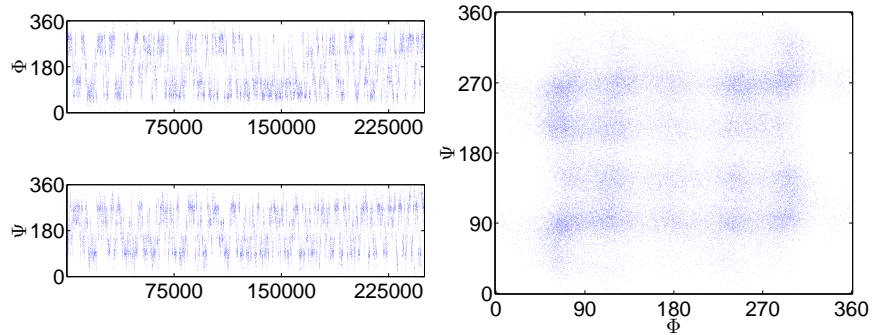
Figure 5.7.: Left: We show the projection of the time series (all atomic positions) on the torsion angles Φ and Ψ. Right: To illustrate the dependency of the torsion angles, we show the Ramachandran plot of the time series of the torsion angles Φ and Ψ. At first glance, the glycine-molecule attains four different main conformations indicated by the four clusters.

	λ_1	λ_2	λ_3	λ_4	λ_5
$\hat{P}$	1	0.9944	0.9942	0.9890	0.9718
$\exp(\tau \tilde{L}_{MLE})$	1	0.9988	0.9987	0.9977	0.9931

Table 5.3.: The five largest eigenvalues of the transition matrix $\hat{P}$ and the transition matrix computed from the estimated generator $\tilde{L}_{MLE}$. Results for an equidistant 20×20 box-discretization of the torsion angle space.

the largest eigenvalues. The decomposition in the left panel results from $\hat{P}$ and the right panel corresponds to the transition matrix $\exp(\tau \tilde{L}_{MLE})$. The almost identical decompositions of the torsion angle space show that despite the slight deviations in the dominant eigenvalues, the estimated generator contains the essential information on the coarse grained dynamics. For a further analysis of the estimated Markov jump process via discrete TPT see Chapter 4.

5.5. Numerical Examples for Non-Equidistant Observation Times

In this section we demonstrate the performance of the enhanced MLE-method for non-equidistant observation times on a test example and for a process arising in the approximation of a genetic toggle switch. In both examples, we re-identify a generator L of a Markov jump process from an associated artificially generated incomplete observation. To be more precise, we drew from a generator L a continuous time realization $\{X(t), 0 \leq t \leq T\}$ for a prescribed $T > 0$ and extracted out of it an incomplete observation $Y = \{y_0 = X(t_0), \ldots, y_N = X(t_N)\}$ with respect to a prescribed set of time lags $\{\tau_1, \ldots, \tau_r\}$, $r > 1$, as follows: Suppose $t_k < T$ is the observation time last considered then the next observation time t_{k+1} is given by $t_{k+1} = t_k + \tau$ where τ is uniformly drawn from the set of time lags $\{\tau_1, \ldots, \tau_r\}$. We terminate that procedure if $t_{k+1} > T$.

Figure 5.8.: The figure shows the log-likelihood function $\log \mathcal{L}_d$ as a function of the EM-steps. The constancy of the log-likelihood function indicates that the estimation procedure is converged already after 50 iteration steps.
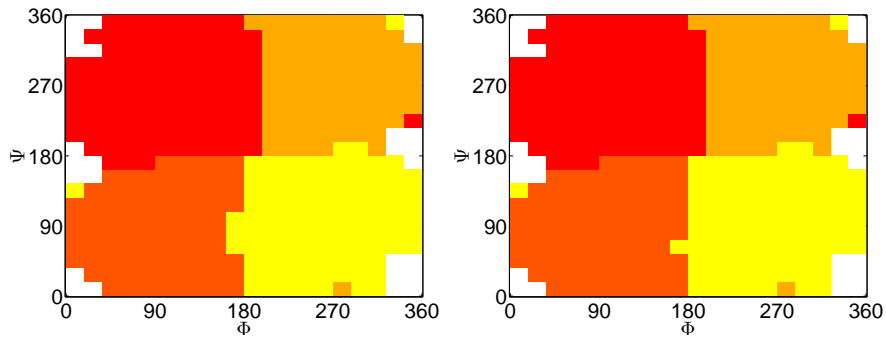
Figure 5.9.: Decomposition of the torsion angle state space into four metastable sets via PCCA. Left: Decomposition with respect to the observed transition matrix $\hat{P}$. Right: Decomposition with respect to the transition matrix $\tilde{P} = \exp(\tau \tilde{L}_{MLE})$. The decompositions are almost identical which indicates that the estimated process captures the essential dynamics in the coarse grained torsion angle space.

5.5.1. Test Example

In the first example we consider a five-state Markov jump process given by its generator

$$L = \begin{pmatrix} -6 & 2 & 2 & 1 & 1 \\ 1 & -4 & 0 & 1 & 2 \\ 1 & 0 & -4 & 2 & 1 \\ 2 & 1 & 0 & -3 & 0 \\ 1 & 1 & 1 & 1 & -4 \end{pmatrix} \in \mathfrak{G}. \tag{5.36}$$

For the reconstruction of L, we extracted from a realization of total time $T = 3.7 \cdot 10^6$ a time series of $N = 10^7$ observations with respect to the set of time lags $\{\tau_1 = 0.01, \tau_2 = 0.1, \tau_3 = 1\}$. In (5.37) we state the estimated generator resulting from Algorithm 5 with the prescribed tolerance $TOL = 10^{-6}$. One clearly can see that $\tilde{L}$ approximates the original one very well.

$$\tilde{L} = \begin{pmatrix} -5.9803 & 2.0054 & 1.9863 & 0.9911 & 0.9975 \\ 1.0002 & -4.0018 & 0.0010 & 0.9938 & 2.0068 \\ 0.9921 & 0.0001 & -3.9768 & 1.9938 & 0.9909 \\ 1.9909 & 0.9951 & 0.0004 & -2.9871 & 0.0006 \\ 0.9982 & 1.0051 & 0.9993 & 1.0050 & -4.0075 \end{pmatrix} \in \mathfrak{G}. \tag{5.37}$$

Next, we address the question of how the length of the respective time series and the number of different time lags do affect the outcome of the estimation procedure. To make things comparable, we generated three different time series of length $N = 10^8$ with respect to the time lags sets $\{0.01\}, \{0.01, 0.1\}$ and $\{0.01, 0.1, 1\}$, all subsampled from the same underlying continues time realization, respectively, and estimated for each time series a generator on the basis of the first $N = 10^3, N = 10^4 \ldots, N = 10^8$ observed states, respectively. Furthermore, we used for all estimations the same initial guess $\tilde{L}_0$. In Figure 5.10 we illustrate the dependence of the approximation error $\|\tilde{L} - L\|$ (measured in the 2-norm) with respect to the length N of the respective time series and the number of different time lags. The graphs reveal that the error $\|\tilde{L} - L\|$ decays exponentially with the length of the underlying time series approximately as $N^{\frac{1}{2}}$. The second observation is that the estimations based on multiple observation time lags give better results than the estimation on a single time lag. The authors are not aware of how to explain this observation.

5.5.2. Application to a Genetic Toggle Switch Model

In the last example we apply the enhanced MLE-method to a *Birth-Death process* which arises as a stochastic model of a genetic toggle switch consisting of two genes that repress each others' expression [77]. Expression of the two different genes produces two different types of proteins; let us name them P_A and P_B. If we denote the number of molecules of type P_A by x and of type P_B by y, then the generator in (4.47) describes their dynamics. For details on that process and its investigation via discrete TPT we refer the reader to Chapter 4, Section 4.3.3.

For the numerical experiments to be presented, we used the parameters $a_1 = 156, a_2 = 30, n = 3, m = 1, K_1 = K_2 = 1, \tau_1 = 1/7$ and $\tau_2 = 1/3$. For this particular
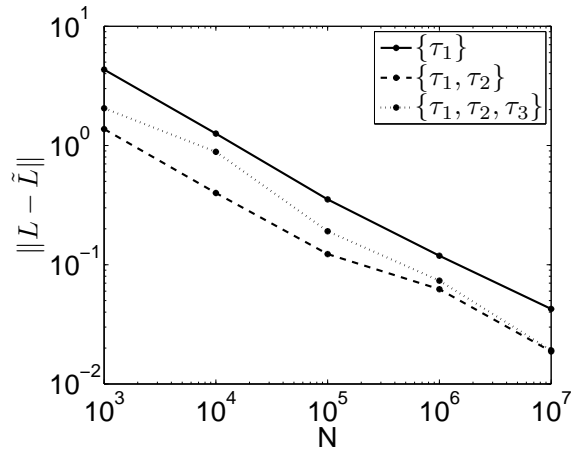
Figure 5.10.: Error of the estimated generator $\tilde{L}$ with respect to the original generator (5.36), measured in the 2-norm $\|\tilde{L} - L\|$, as a function of the length N of the respective time series. Results for the three different sets of time lags $\{0.01\}, \{0.01, 0.1\}$ and $\{0.01, 0.1, 1\}$ and the tolerance $TOL = 10^{-6}$.

choice the deterministic dynamics (4.48) has two stable stationary points approximately at $(x, y) = (20, 0)$ and $(x, y) = (0, 8)$ and one unstable point approximately at $(x, y) = (6, 1)$. This insight in the deterministic approximation helps to understand the following analysis of the jump process:

For the sake of illustration, the left panel of Figure 5.11 shows the discrete free energy, $-\log \pi$, of the jump process instead of its stationary distribution π itself. All states with almost vanishing stationary distribution are depicted by the white region and in order to emphasize the states of interest, we chose a log-log representation. The color scheme is chosen such that the darker the color of a region the higher the probability of finding the process there. One can clearly see that the process spends most of its time near the two stable stationary points approximately at $(x, y) = (20, 0)$ and $(x, y) = (0, 8)$.

A single realization of the jump process generated by L models the evolution of the numbers of proteins with respect to a specific initial value (x_0, y_0). The resulting evolution of the associated probability density function (PDF) in time is governed by the *Master-equation*: Let $p_0 \in \mathbb{R}^{|S|}$ be the initial PDF, then the PDF evolves in time according to

$$\frac{\partial p(t)}{\partial t} = L^T p(t), \quad p(0) = p_0, \ t > 0, \tag{5.38}$$

where L^T denotes the transpose of the generator given in (4.47). In order to motivate the relevance of the following numerical experiment, suppose you measure the numbers of proteins of types P_A and P_B discretely in time; without knowing the generator, you are interested in fitting a Markov jump process. Assuming that the hidden process is Markovian, one can apply the enhanced MLE-method.

Before we describe our numerical example in detail, notice that the structure of a transition matrix P, i.e. the occupation of the entries in P, does not allow to infer on the structure of the underlying generator. For example, the generator of a dense transition matrix does not have to be dense too. This means that there is some
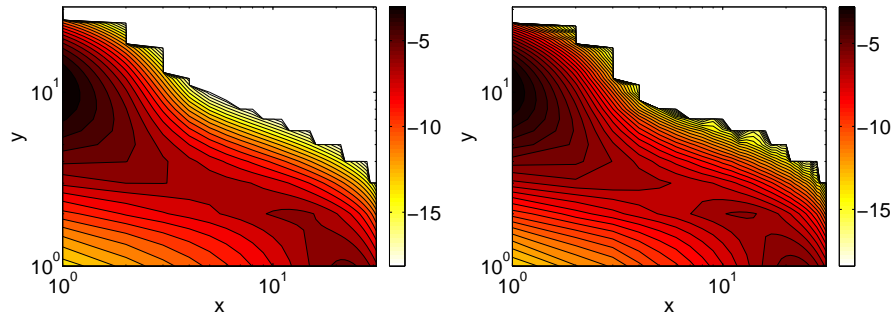
Figure 5.11.: Left: Log-log contour plot of the Gibbs energy, $-log\pi$, where $\pi = (\pi_i), i \in S$ is the stationary distribution computed via $\pi^T L = 0$. Right: Log-log contour plot of the Gibbs energy resulting from the observed distribution $\hat{\pi}$ of states in the time series. Result for $N = 10^8$.

freedom in the choice of the structure of the estimated generator $\tilde{L}$. In this example, we follow two options. One option – we call it option A – is to use the structure of the observed transition matrix as a blueprint for the structure of $\tilde{L}$. In option B we exploited knowledge about the hidden process. We know that the number of a gene's molecule can only increase or decrease by one in a single reaction while the number of the other one remains constant. Hence, it is natural to estimate the entries $\tilde{l}_{ij}$ if the states i and j (the numbers) have been observed and are adjacent in the sense of a single reaction.

For our numerical experiment, we generated a sufficiently long realization of the Birth-Death process on the state space $\mathbb{Z}^2 \cap ([0, 30] \times [0, 30])$ and extracted out of it a time series of length $N = 10^8$ with respect to the set of time lags $\{\tau_1 = 0.0001, \tau_2 = 0.001, \tau = 0.01\}$. The Gibbs energy resulting from the distribution of the observed states in the time series is shown in the right panel of Figure 5.11. As one can see, the relative occupation of the states is consistent with the exact stationary distribution depicted in the left panel.

The generated time series visits 225 states of 900 possible states, hence we had to estimate a generator $\tilde{L} \in \mathfrak{G}$ on the state space $S \cong \{1, \ldots, 225\}$. In the following $\tilde{L}_A$ denotes the estimated generator resulting from the estimation option A and $\tilde{L}_B$ via option B. For both estimation options we used the tolerance $TOL = 10^{-2}$. The Figure 5.12 shows the free energies associated with $\tilde{L}_A$ (left panel) and with $\tilde{L}_B$ (right panel). From the viewpoint of stationarity, one can see that both estimated generators are good approximations of the original one (cf. left panel of Figure 5.11). In order to make things more precise, we compare in the following the estimated generators with the original generators of (4.47) *restricted* on the set of observed states. Formally, we consider the restricted generator $\bar{L} \in \mathfrak{G}, S \cong \{1, \ldots, 225\}$ defined according to

$$\bar{l}_{ij} = \begin{cases} l_{ij}, & \text{if } i \neq j \text{ were visited by the time series,} \\ -\sum_k \bar{l}_{ik}, & \text{if } i = j \text{ was visited by the time series.} \end{cases} \quad (5.39)$$

Now we compare the spectral properties of the estimated generators with those of the restricted generator from (5.39) in more detail. In the left panel of Figure 5.13 we depict the real parts of the 30 largest eigenvalues of $\tilde{L}_A$ and $\tilde{L}_B$ with those of
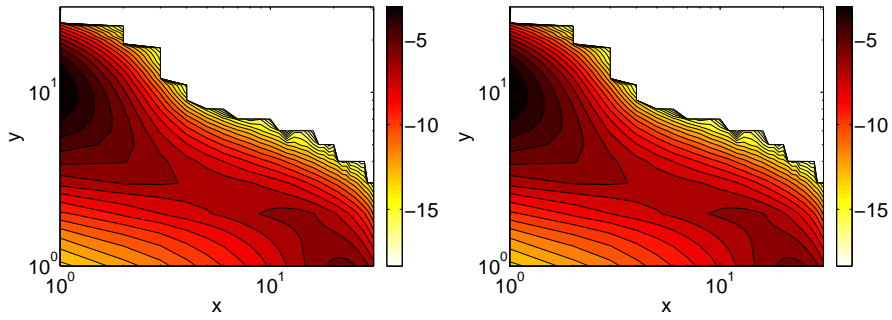
Figure 5.12.: Log-log contour plot of the free energies, $-\log \tilde{\pi}$, associated with the estimated generators $\tilde{L}_A$ (left panel) and $\tilde{L}_B$ (right panel) where $\tilde{\pi}$ is the stationary distribution of the estimated generators computed via $\tilde{\pi}^T \tilde{L} = 0$, respectively.

the restricted generator $\bar{L}$, respectively. Although the enhanced MLE-method is not designed to approximate spectral properties, notice that the real parts of considered eigenvalues of $\bar{L}$ are well reconstructed by both estimation options. Another important quantity in time series analysis is the auto-correlation function (ACF) of a process which reflects the speed of memory loss of the process. For a Markov jump process, it is easy to see that the ACF reduces to [19]

$$\mathbb{E}(X_{t+\tau} X_t) = \sum_{k=1}^{d} e^{\tau \lambda_k} \sum_{i,j \in S} i \cdot j \cdot \pi_i U_{ik} U_{kj}^{-1}, \qquad (5.40)$$

where $L = U \operatorname{diag}(\lambda_1, \ldots, \lambda_d) U^{-1}$ is the eigendecomposition of the generator L of the Markov jump process and $\pi = (\pi_i)$, $i \in S$ its stationary distribution. The graphs of the normalized ACFs associated with $\tilde{L}_A$ and $\tilde{L}_B$ together with the ACF of the restricted generator $\bar{L}$ are given in Figure 5.14. As one can see, the ACFs associated with $\tilde{L}_A$ and $\tilde{L}_B$ are consistent with the ACF of the restricted process which shows that besides the eigenvalues even the eigenvectors of the restricted generator $\bar{L}$ are well reproduced by both estimated generators, respectively. The almost identical reproduction of the ACF of $\bar{L}$ by $\tilde{L}_B$ shows that the incorporation of theoretical knowledge of the hidden process leads to sightly better results.
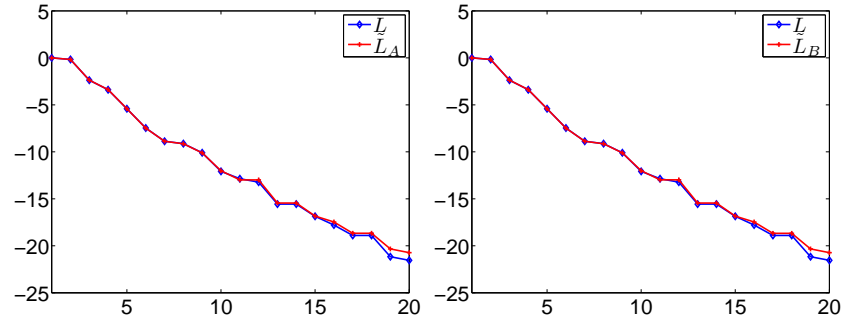
Figure 5.13.: The real parts of the first 30 largest eigenvalues of the estimated generators compared to the eigenvalues of the restricted generator $\bar{L}$ (5.39). Left: Real parts of eigenvalues of $\tilde{L}_A$. Right: Real parts of eigenvalues of $\tilde{L}_B$.
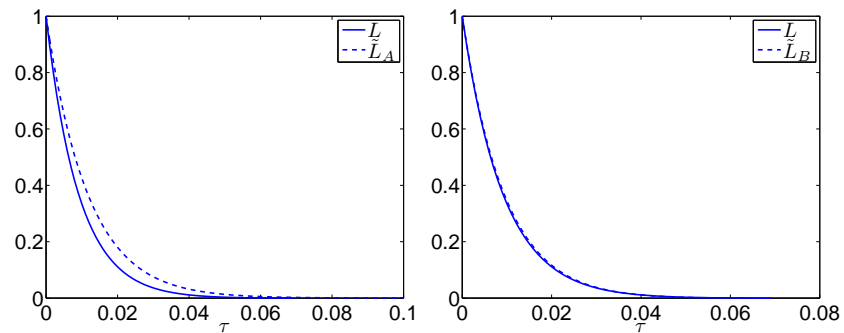
Figure 5.14.: The graphs of the ACFs associated with $\tilde{L}_A$ (left panel) and $\tilde{L}_B$ (right panel) compared to the ACF of the restricted generator $\bar{L}$, respectively.

6. Detecting Reaction Pathways via Shortest Paths in Graphs

We have demonstrated that discrete TPT is a powerful tool to analyze transition events in Markov jump processes. The central object is the infinitesimal generator of the process which finally allows to compute reaction rates and to determine a hierarchy of dominant reaction pathways. In the case where the process is only discretely observed in time the generator of the underlying Markov jump process has to be estimated. Alternatively, if the observation time lag is constant, the underlying process can be modeled as a Markov chain, i.e., as a Markov process discrete in space and time.

In this chapter, we will consider the use of shortest-path algorithms in the context of reaction pathway computation in Markov chains. The crucial question for this undertaking is the choice of a weight function that defines the *length* of an edge. We will present two such functions [22] which both have a natural motivation. We will apply both resulting methods on the examples which have already been investigated with discrete TPT in Section 4.3 and we will compare the results.

6.1. Shortest Path in Graphs

6.1.1. Dijkstra Algorithm

The standard algorithm used for computing shortest paths in a graph $G = G(V, E)$ is the Dijkstra algorithm. It solves the so called *Single Source Shortest Path Problem* where the shortest paths from one source vertex $v_s \in V$ to all other vertices $v \in V$ have to be determined. The *Single Source, Single Destination Shortest Path Problem* is a special case in which only one path from v_s to a designated destination vertex v_d has to be determined. In both cases the runtime of the Dijkstra algorithm is $O(|V| \log(|V|) + |E|)$. For a profound discussion of this standard algorithm we refer to, e.g. [54, 18]. In the following we will only roughly sketch its basic principle.

Given a vertex v_s as starting vertex, the algorithm maintains a list of distances to v_s assigned to every other vertex that is initialized with the value ∞ and in the end contains the lengths of the shortest paths from v_s to any vertex. In the first step, the distances of all neighbors of v_s are set to the weight of the edge connecting them to v_s. These vertices form the initial *halo set*, i.e. they are the vertices for which one path from v_s is known but it is not known whether this path is a shortest path. In the main loop of the algorithm, it removes a vertex v_{min} with the minimum known distance from the halo set, and considers all neighbors of v_{min}. If a neighbor is also in the halo set, the algorithm checks whether a path through v_{min} would result in a distance from v_s less than the current known distance. If a neighbor is not yet in the halo set, it is added to it, with its distance value being the sum of the distance of v_{min} and the length of the edge connecting the neighbor to v_{min}. The algorithm

terminates when a prescribed target vertex is reached or when the halo set becomes empty.

By a slight modification, the Dijkstra algorithm can be generalized to find a shortest path from any vertex of a source set $V_s \subset V$ to all remaining vertices $w \in V \setminus V_s$. Unlike in the original algorithm, here the source set V_s forms the initial halo set and in the initialization step all vertices of V_s are assigned the distance value zero.

Algorithm 7 Generalized Dijkstra's Algorithm

Input: A directed graph $G = (V, E)$, weights $w : E \to \mathbb{R}_+$. Source set $V_s \subset V$
Output: Shortest paths from all $v \in V_s$ to all $u \in V$ and their lengths.
  (1) Set $\mathrm{dist}(v_s) = 0 \;\; \forall v_s \in V_s$, $\mathrm{dist}(v) := \infty \;\; \forall v \in V \setminus V_s$.
  (2) Initialize halo set $H := V_s$.
  (3) $v := \mathrm{argmin}_{u \in H}\mathrm{dist}(u)$, set $H := H \setminus \{v\}$.
  (4) **FOR ALL** $(v, u) \in E$ **DO**:
  (5)   **IF** $\mathrm{dist}(u) > \mathrm{dist}(v) + w(v, u)$
  (6)   **THEN** Set $\mathrm{dist}(u) := \mathrm{dist}(v) + w(v, u)$, $\mathrm{pred}(u) := v$.
  (7)   **IF** $u \notin H$ **THEN** $H := H \cup \{u\}$.
  (8) **END FOR**
  (9) **IF** $H \neq \emptyset$ **THEN** go to step (3).

If a vertex $v \in V \setminus V_s$ is not reachable from the source set V_s then $\mathrm{dist}(v) = \infty$ and $\mathrm{pred}(v)$ is not defined. Otherwise, the shortest path from V_s to a vertex v can be reconstructed by following recursively the predecessors until a vertex in $v_s \in V_s$ is reached. If we subsequently reverse the order of the vertices in that path, we end up with a shortest path $z(v)$ from V_s to v,

$$z(v) = (v_s, \ldots, \mathrm{pred}(\mathrm{pred}(v)), \mathrm{pred}(v), v).$$

6.1.2. Bidirectional Dijkstra Algorithm

The purely graph theoretic consideration of shortest paths in the previous section has to be extended by some ideas related to the specialized setting of graphs describing spatial discretizations of Markov diffusion processes. In particular we have in mind the fact that the numerical realizations of these graphs necessarily come with a discretization error which makes it doubtful whether the notion of *the* shortest path between two vertices v_s and v_d is really a meaningful quantity in our applications – even leaving out the possible existence of several shortest paths. Furthermore, we are interested in the revealing of *all* dominant transition channels between metastable sets. Therefore, we are not only interested in one (or all) precisely shortest paths, but we are also interested in a *family of shortest paths* which consists of short paths being only slightly longer than a path with the shortest length.

Edge based family of shortest paths   Let $\mathrm{dist}(v_s, v_d)$ denote the length of the shortest path between the vertex $v_s \in V_s$ and the vertex $v_d \in V_d$. We want to calculate all paths from v_s to v_d which have a slightly longer length than the shortest path. To be more precise, we determine all paths in the graph which have a length

of at most

$$(1 + \epsilon)\mathrm{dist}(v_s, v_d),$$

where $0 \leq \epsilon$. In order to do so, we need to apply the generalized Dijkstra algorithm, as stated in Algorithm 7, only twice: Firstly, we calculate all distances from v_s to all other vertices and denote these distances by $\mathrm{dist}_1(v)$ for all vertices $v \in V$. Among all distances this also includes the distance between v_s and v_d. Secondly, we consider a new graph $= (V, E^R)$ where E^R consists of the edges in E with direction reversed. Then, we calculate all distances from v_d to all other vertices in G^R, and denote these distances by $\mathrm{dist}_2(v)$ for all vertices $v \in V$. Note that $\mathrm{dist}_2(v)$ is also the distance from v to v_d in G for any vertex $v \in V$.

It is now simple to decide whether or not an edge $(v_i, v_j) \in E$ lies on a path between v_s and v_d of length at most $(1 + \epsilon)\mathrm{dist}(v_s, v_d)$. Such a path has to consist of three parts: a path from v_s to v_i, the edge (v_i, v_j) itself and a path from v_j to v_d. The shortest length for the first part is $\mathrm{dist}_1(v_i)$ and the shortest length of the last part is $\mathrm{dist}_2(v_j)$. Thus, an edge (v_i, v_j) lies on a path between v_s and v_d of length at most $(1 + \epsilon)\mathrm{dist}(v_s, v_d)$ if and only if

$$\mathrm{dist}_1(v_i) + w(v_i, v_j) + \mathrm{dist}_2(v_j) \leq (1 + \epsilon)\mathrm{dist}(v_s, v_d).$$

The result is a subset $E_{sp}(\epsilon) \subset E$ of edges belonging to the family of short paths. The algorithm can easily be extended to the case of more than one source and destination vertex and is stated in Algorithm 8. The computational cost of Algorithm 8 is the

---

Algorithm 8 Bidirectional Dijkstra algorithm

Input: A directed graph $G = (V, E)$, weights $w : E \to \mathbb{R}_+$, source set $V_s \subset V$ and destination set $V_d \subset V$, threshold ϵ.

Output: Set of edges $E_{sp}(\epsilon) \subset E$ belonging to the family of short paths.
  (1) Compute all distances $\mathrm{dist}_1(v)$ in G from V_s to all vertices $v \in V$.
  (2) Construct new graph $G^R = (V, E^R)$ by reversing all edges in E.
  (3) Compute all distances $\mathrm{dist}_2(v)$ in G^R from V_d to all vertices in $v \in V(G^R)$.
  (4) $\mathrm{dist}_{min} := \min_{v_d \in V_d}\{\mathrm{dist}_1(v_d)\}$.
  (5) **FOR ALL** edges in $(v_i, v_j) \in E$ **DO**
  (6)   **IF** $\mathrm{dist}_1(v_i) + w(v_i, v_j) + \mathrm{dist}_2(v_j) \leq (1 + \epsilon)\mathrm{dist}_{min}$
  (7)   **THEN** $E_{sp}(\epsilon) := E_{sp}(\epsilon) \cup \{(v_i, v_j)\}$.
  (8) **END FOR**

---

same as of Dijkstra's algorithm (cf. Algorithm 7).

Vertex based family of shortest paths In order to motivate the vertex based approach, consider for an edge $(v_i, v_j) \in E_{sp}(\epsilon)$ the associated shortest path

$$z_S(v_i, v_j) = \left(z(v_i), z^R(v_j)\right),$$

where $z^R(v_j)$ denotes the shortest path from v_j to V_d in G. The crucial observation is now that in general the path $z(v_i, v_j)$ is different from the shortest path composed of the shortest path from V_s to v_i and the shortest path from v_i to V_d. In other words, the edge (v_i, v_j) does not have to lie on the shortest path connecting V_s and V_d via v_i. The same argument holds for the vertex v_j too.

For this reason, we consider in the vertex based approach the vertex set $V_{sp}(\epsilon) \subset V$ which comprises all vertices being involved on a short path with length at most $(1 + \epsilon)\text{dist}_{min}$. Formally, a vertex $v \in V$ lies on a short path between V_s and V_d of length of at most $(1 + \epsilon)\text{dist}_{min}$ if and only if

$$\text{dist}_1(v) + \text{dist}_2(v) < (1 + \epsilon)\text{dist}_{min}.$$

Reaction pathways and short paths   It immediately follows from the definition of a shortest path that it does not have any self-intersections (loops). Unfortunately, both presented approaches - the edge and vertex based approach - lead to short paths which could have self-intersections. To see this, notice that in both approaches a short path is composed of two shortest paths which are computed independently of each other. Since we are eventually interested in reaction pathways (cf. Def. 4.1.15), we finally have to sort out from the family of short paths all short paths with loops.

6.2. Choice of Edge Weights

The choice of the edge weights depends on the way how to compare paths. The first natural choice of edge weights is based on the *likelihood* of sample paths. Unfortunately, this approach leads in our context to reaction pathways which are in contradiction to the underlying dynamics and its physical interpretation. As a remedy, we follow an alternative approach which takes into account the *free energy* barriers along a reaction pathway. This approach is more adapted to the underlying dynamics and, moreover, is less sensitive with respect to the underlying box discretization of the state space. In what follows we interpret a Markov chain, described by its transition matrix $P = (p_{ij})_{i,j \in S}$, as a directed graph $G = (V, E)$ (cf. notations introduced in Section 4.1.1).

6.2.1. Likelihood Approach

Suppose we are given two sample paths p_1 and p_2 of a Markov chain and, moreover, suppose that both starting in a state i_A and ending in the state i_B. One option to compare these two paths is to ask which of both is the more preferred one by the dynamics, i.e. which one is more *likely*? The respective likelihoods of the sample paths can be expressed in terms of the transition probabilities of the Markov chain. Let $z = (i_1, i_2, i_3, \ldots, i_n)$ be a finite sample path of the Markov chain. Then the likelihood of z is given by

$$\mathcal{L}_d(z) = \prod_{k=1}^{n-1} p_{i_k, i_{k+1}},$$

being the probability that the Markov chain produces that sample path conditional on starting in the state i_1. The edge weights are now chosen such that the more likely a sample paths is the less is its length. To this end, we define the weight of an edge $(i, j) \in E$ by

$$w_L(i, j) \stackrel{def}{=} -\log(p_{ij}) \tag{6.1}$$

and the resulting length of a path p,

$$l(z) = \sum_{k=1}^{n-1} w_L(i_k, i_{k+1}) = -\log(\prod_{k=1}^{n-1} p_{i_k, i_{k+1}}),$$

is the negative *log-likelihood* of that sample path (cf. Sect. 5.2). It should be clear that the shortest path with respect to the weights in (6.1) between two different states is the most probable one and vice versa.

6.2.2. Free Energy Approach

Motivational Example To motivate the alternative free energy approach we present an example for which the likelihood approach yields misleading results. To this end we consider a pure diffusion process, i.e. a diffusion process in a flat potential landscape, on a squared domain with reflecting boundary conditions. Additionally, we cut out of the domain a small square and apply reflecting boundary conditions on its boundary too. In Figure 6.1 we give a schematic picture of the situation. The decomposition of the domain is chosen such that the probability to encounter the equilibrated process in the boxes $A, 1, 2, 3$ and B is $1/8$ and for the box 4 is $3/8$. The dynamics between the boxes is given by a reversible Markov chain where the transition probabilities between adjacent boxes are given by

$$
\begin{aligned}
p(A, 1) &= p(1, A) = p(1, 2) = p(2, 1) \\
&= P(2, 3) = p(3, 2) = p(3, B) = p(B, 3) \\
&= p(A, 4) = p(B, 4) = a, \; 0 < a < \frac{1}{2}, \\
p(4, A) &= p(4, B) = \frac{1}{3}a,
\end{aligned}
$$

where the probability a depends on the size of the squares. The condition $0 < a < \frac{1}{2}$ guarantees that the probability to make a self-transition is positive.

Suppose, we start the diffusion process in box A. From the symmetry of the domain and the nature of diffusion, it should be clear that the probability to reach the box B via the upper way is the same, namely $\frac{1}{2}$, as for the lower way. The discrete likelihoods of the upper and lower way in the Markov chain are given by

$$
\begin{aligned}
\mathcal{L}_d\big((A, 1, 2, 3, B)\big) &= a^4, \\
\mathcal{L}_d\big((A, 4, B)\big) &= \frac{1}{3}a^2.
\end{aligned}
$$

The likelihoods of both discrete paths are equal if and only if $a = \sqrt{1/3} \approx 0.577 > 0.5$ which contradicts the condition $0 < a < 0.5$. But this means that the likelihood approach would indicate that one of the paths is preferred which is not consistent with the continuous picture.

New Choice of Edge Weight

The new choice of edge weights is based on the discrete analog of the free energy (cf. Sect. A.5).
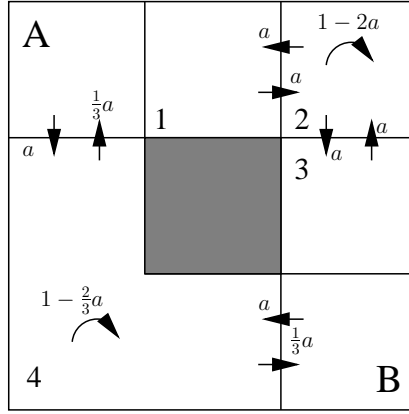
Figure 6.1.: Schematic representation of the motivational example.

Recall that under the assumption that the Markov chain admits a unique stationary distribution $\pi = (\pi_i)_{i \in S}$ the discrete free energy $F = (F_i)_{i \in S}$ is defined by

$$F_i \stackrel{def}{=} -\log \pi_i > 0, \quad i \in S.$$

The new edge weights are constructed such that the shortest path between two states is the one which overcomes the lowest discrete free energy barriers. To this end, we introduce the weights

$$w_F(i,j) = |F_j - F_i|. \tag{6.2}$$

In order to explain that the free energy weights yield the desired result, firstly consider a path $z = (i_1, \ldots, i_s)$ with monotonously increasing discrete free energies along it, i.e.,

$$F_{i_j} \leq F_{i_{j+1}} \Leftrightarrow \pi_{i_j} \geq \pi_{i_{j+1}}, \quad j = 1, \ldots, s-1. \tag{6.3}$$

Then the length of such a path z,

$$l(p) = \sum_{j=1}^{s-1} w_F(i_j, i_{j+1}) = F_{i_s} - F_{i_1},$$

is simply given by the free energy difference between the last and the first state of the path. Moreover, if we fix the states i_1 and i_s, then all paths connecting these two states and satisfying (6.3), have the same length. Next, consider a path $p = (i_1, \ldots, i_n)$ which can be decomposed into two parts $p_1 = (i_1, \ldots, i_s)$ and $p_2 = (i_s, \ldots, i_n)$ such that

$$\begin{cases} F_{i_j} \leq F_{i_{j+1}}, & j = 1, \ldots, s-1, \\ F_{i_j} \geq F_{i_{j+1}}, & j = s, \ldots, n-1. \end{cases}$$

One immediately verifies that again the length of the path p,

$$l(p) = 2F_{i_s} - (F_{i_1} + F_{i_n}) \geq 0,$$

only depends on free energy differences, namely the barriers $F_{i_s} - F_{i_1}$ and $F_{i_s} - F_{i_n}$. Consequently, if we fix the states i_1 and i_n then the shortest path between i_1 and i_n with respect to the weights in (6.2) is the one which crosses the lowest free energy barriers.

Remark 6.2.1. *Notice that in the free energy approach every barrier along a certain path contributes to the length twofold: first from V_s towards V_d and second from V_d towards V_s. However, in a post-processing step one can determine all barriers along a reaction pathway and use these information for a further analysis or a re-computation of the shortest paths. Notice further that in our motivational example the free energy approach would also tell that the lower discrete path is the preferred path of the underlying diffusion. Nevertheless, our numerical experiments will show that the free energy approach is more insensitive with respect to a decomposition of a diffusion process.*

6.3. Numerical Experiments

In this section we will illustrate the method of detecting reaction pathways via shortest paths in graphs on some examples which have already been investigated via discrete TPT. In the following, we only use the vertex based approach.

In the first example we consider the Smoluchowski dynamics in the three-hole example introduced in Section 3.7.1. In order to start with the shortest paths method, we have to provide a transition matrix which captures the dynamics on a coarse grained level. Instead of generating such a transition matrix via a time series resulting from a direct numerical simulation of the Smoluchowski dynamics in (3.22), we utilized the generator L, given in (4.44), of the approximating Birth-Death process (cf. Sect. 4.3.1). For the time lag $\tau = 1.2$ we generated a transition matrix $P(\tau)$ via the relation

$$P(\tau) = \exp(\tau L).$$

As the source set $A(= V_s)$, we chose the states (mesh points) in S which cover the left deep minima. The destination set $B(= V_d)$ was chosen with respect to the right minima. The stationary distribution $\pi = (\pi_i)_{i \in S}$ was numerically computed via $P(\tau)^T \pi = \pi$. In the following results, we always used the vertex based approach.

For the comparison of the likelihood approach and the free energy approach, we asked two questions:

1. Do both approaches detect the two transition channels?

2. Do both approaches reproduce the entropic switching behavior?

The Figure 6.2 gives an answer to the first question. In the left column we plot the families of reaction pathways resulting from the likelihood approach. From top to bottom we used the thresholds $\epsilon = 0.1, \epsilon = 0.3$ and $\epsilon = 0.6$. The right column shows the families of reaction pathways resulting from the free energy approach for the thresholds $\epsilon = 0.05$ (top),$\epsilon = 0.06$ and $\epsilon = 0.08$ (bottom). The darker the color of a drawn edge is the shorter is the path in which the edge is involved, i.e, the more likely is the path in the likelihood approach and the lower is the overcome barrier in the free energy approach, respectively. One can clearly see, that with increasing threshold the likelihood approach results rather in reaction pathways which cross the local maximum than in pathways proceeding from A to B in the upper channel. This behavior is in contradiction to the underlying diffusion and can be ascribed to the sensitivity of the likelihood approach with respect to the underlying
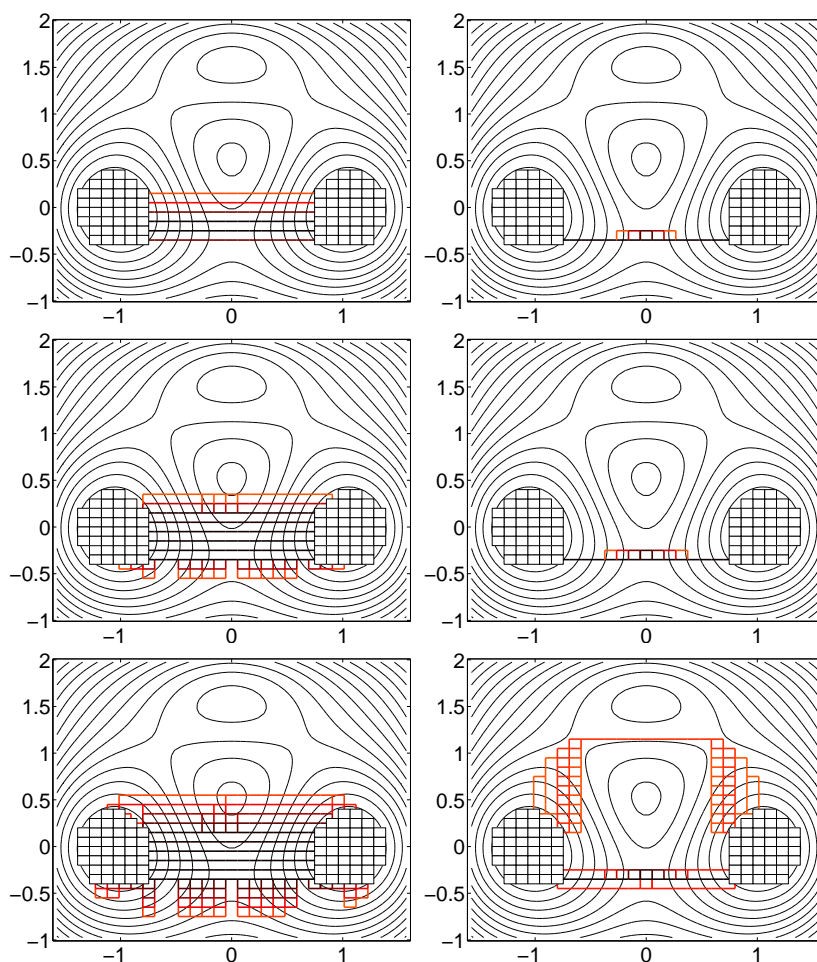
Figure 6.2.: Comparison of vertex based families of reaction pathways resulting from the likelihood approach (left column) and from the free energy approach (right column). The darker the color of an edge the shorter is the pathway in which the edge is involved. For the likelihood approach we chose from top to the bottom the threshold $\epsilon = 0.1, \epsilon = 0.3$ and $\epsilon = 0.6$. For the free energy approach we chose $\epsilon = 0.05, \epsilon = 0.06$ and $\epsilon = 0.08$. The sets A and B (depicted by boxes) were chosen such that they cover the two local minima, respectively. Results for a 30×30 mesh discretization of the rectangular state space and temperature $\beta = 1.67$.
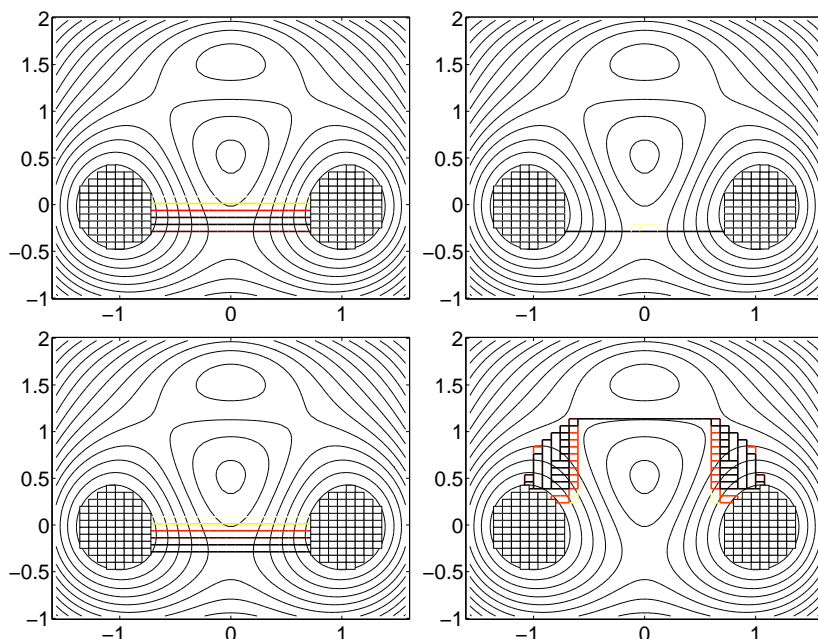
Figure 6.3.: Comparison of reaction pathways resulting from the likelihood approach (left column, $\epsilon = 0.1$) and from the free energy approach (right column, $\epsilon = 0.01$) at two different temperatures: $\beta = 6.67$ (top row) and $\beta = 1.67$ (bottom row). Results for a 40×40 mesh discretization of the rectangular state space.

discretization. As expected, the families of reaction pathways resulting from the free energy approach are less sensitive to the respective discretization because for the low threshold $\epsilon = 0.08$ both channels were detected.

The Figure 6.3 reveals the behavior of both approaches if the temperature in the underlying diffusion is varied. In the first column we show the reaction pathways ($\epsilon = 0.1$) resulting from the likelihood approach for the low temperature $\beta = 6.67$ (top) and the high temperature $\beta = 1.67$ (bottom). The right column shows the results of the free energy approach ($\epsilon = 0.01$) for the same temperatures. Apparently, only the free energy approach reproduces an entropic switching behavior of the underlying dynamics. But if we compare the preferred channels with the channels obtained via the discrete TPT (cf. Fig. 4.7 in Section 4.3.1) we see that the results are in opposite to each other; e.g., the preferred channel resulting from the shortest path methods at $\beta = 6.67$ corresponds to the preferred channel resulting from discrete TPT at $\beta = 1.67$. This observation can be explained by recalling that the length of a path in the free energy approach reflects barriers which the path overcomes. At low temperature ($\beta = 6.67$) the only chance to encounter the underlying process is in one of the minima. Hence, the upper shallow minima is separated from the rest by a extremely high free energy barrier and, hence, the lower direct channel is detected.

We end this section by presenting the results of the free energy approach applied to two others examples which have been investigated with discrete TPT in Section 4.3. The reaction pathways for the genetic toggle switch example (cf. Sect. 4.3.3 extracted from the vertex based family of short paths ($\epsilon = 0.005$) are depicted in the left panel of Figure 6.4. Apparently, the reaction pathway crossing the lowest discrete free
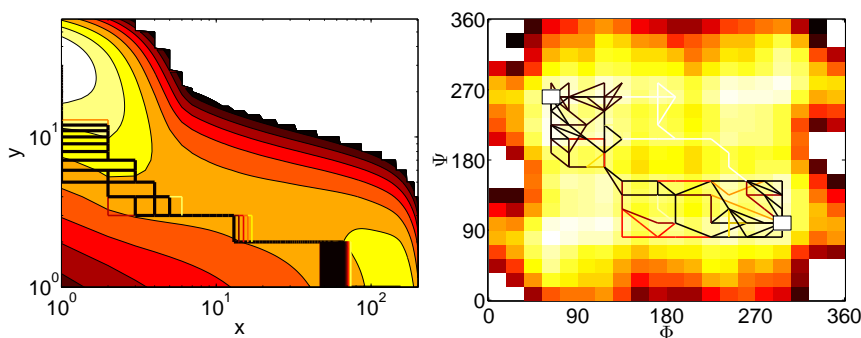
Figure 6.4.: Left: Reaction pathways for the genetic toggle switch example (cf. Fig. 4.20 in Section 4.3.3) extracted from the vertex based family of short paths ($\epsilon = 0.005$) in the free energy approach. Right: Reaction pathways in the torsion angles space of the glycine in solvent example (cf. Sect. 4.3.2) extracted from the vertex based family of short paths ($\epsilon = 0.01$) in the free energy approach. The darker the color of an edge is the shorter is the length of the pathway in which the edge is involved, i.e., the lower is the overcome free energy barrier of the pathways. The reaction pathways are embedded in a log-log contour plot of the discrete free energy, respectively.

energy barrier is consistent with dominant reaction pathways found via discrete TPT (cf. Fig. 4.20).

The right panel of Figure 6.4 illustrates the reaction pathways in the torsion angles space of the glycine in solvent example (cf. Sect. 4.3.2) extracted from the family of short paths ($\epsilon = 0.01$). The detected reaction pathways suggest that the lower channel is the preferred one which stands in contradiction to the results found via discrete TPT (cf. Fig. 4.13).

Finally, we draw the conclusion that only the free energy approach is able to detect different transition channels which are consistent with the underlying diffusion. But in the case of multiple reaction channels it does not allow to make any predictions about which channel is preferred one by the underlying diffusion. Nevertheless, the shortest-path approach is useful to get a first impression of possible reaction channels.

7. Variance of the Committor Function

A natural question arising the context of committor function computation on the basis of time series is of how the discrete committor function q does depend on uncertainties in the underlying data. In this chapter we will present an approach which allows to estimate these uncertainties element-wise. We will restrict ourselves to the case of Markov chains, i.e. discrete in time and *in space*. The idea behind that approach is to estimate the uncertainties in terms of the element-wise variances of a discrete committor function ensemble resulting from an ensemble of transition matrices distributed according to the discrete likelihood function $\mathcal{L}_d$. We will devise an appropriate Monte Carlo Markov Chain (MCMC) sampling procedure and will illustrate the approach on examples. The extension to Markov jump processes will not be discussed here and will be subject to further investigations.

7.1. The Discrete Committor Function

Let $P \in \mathbb{R}^{d \times d}$ be the transition matrix of a Markov chain on the state space $S \cong \{1, \dots, d\}$. As shown for example in [10] via *first step analysis*, the discrete committor function $q : S \mapsto [0, 1]$ with respect to two disjoint, non-empty sets $A, B \subset S$ satisfies the discrete committor equation:

$$\begin{cases} \sum_{j=1}^{d} (p_{ij} - \delta_{ij}) q_j = 0 & \forall\, i \in S \setminus (A \cup B), \\ q_i = 0 & \forall\, i \in A, \\ q_i = 1 & \forall\, i \in B, \end{cases} \tag{7.1}$$

where δ_{ij} is the Kronecker symbol. When only a finite observation $Y = \{y_0 = X(t_0), \dots, y_N = X(t_N)\}$ of the Markov chain is available, the transition matrix of the underlying Markov chain is not accessible and has to be estimated from the data. Unlike to the case of Markov jump processes, the inverse modeling of a Markov chain, i.e. reconstructing a Markov chain on the basis of a finite observation Y, is easy. It is defined as the Markov chain which most likely explains the observed data, i.e. which maximizes its discrete likelihood. Recall that the discrete likelihood function of an observation Y is given by (cf. Sect. 5.2)

$$\mathcal{L}_d(Y; P) = \prod_{k=0}^{N-1} p_{y_k, y_{k+1}} = \prod_{i,j \in S} p_{ij}^{c_{ij}}, \tag{7.2}$$

where $P = (p_{ij})_{i,j \in S}$ is the transition matrix of the underlying Markov chain and the frequency matrix $C = (c_{ij})_{i,j \in S}$ provides the number of consecutively observed transitions between states.

Remark 7.1.1. *We want to point out that here and in the following we assume that the prior probability over the transition matrices **before** observing any data is simply a uniform distribution. In particular, that assumption implies*

$$\mathcal{L}_d(Y; P) = \mathcal{L}_d(P; Y).$$

Henceforth, we will denote for a fixed observation Y the discrete likelihood function in (7.2) by $\mathcal{L}_d(P)$.

The maximum likelihood estimator (MLE) $\hat{P} = (\hat{p}_{ij})_{i,j \in S}$, i.e. the transition matrix which maximize the discrete likelihood function (7.2) given the observation Y, is unique and its entries $\hat{p}_{ij}$ can be expressed in terms of the frequency matrix,

$$\hat{p}_{ij} = \frac{c_{ij}}{c_i}, \tag{7.3}$$

where $c_i = \sum_{k \in S} c_{ik}$ is the total number of observed transitions leaving the state i.

Due to the finite number of observations, the transition probabilities in the MLE $\hat{P}$ are afflicted with uncertainty. The question is how do these uncertainties affect the committor function $\hat{q}$ computed via

$$\begin{cases} \sum_{j=1}^d (\hat{p}_{ij} - \delta_{ij})\hat{q}_j = 0 & \forall\, i \in S \setminus (A \cup B), \\ \hat{q}_i = 0 & \forall\, i \in A, \\ \hat{q}_i = 1 & \forall\, i \in B. \end{cases} \tag{7.4}$$

In other words, we are interested in the error $\|q - \hat{q}\|$ given an observation Y but, unfortunately, that error cannot directly be measured since the "true" committor function $q = (q_i)$, $i \in S$ is unknown and the MLE $\hat{P}$ does not indicate the involved uncertainties. However, following standard reasonings, the error $\|q - \hat{q}\|$ can be estimated via the *variance* of the committor function given an observation Y.

7.2. Metropolis Markov Chain Monte Carlo

One way to estimate the variance of the committor is to draw an ensemble of transition matrices $\{P_1, \ldots, P_k\}$ from the *conditional probability distribution* of all possible transition matrices given the observation Y. Then the variance of the committor $\hat{q}$ is approximately given by the variance of the resulting ensemble of committor functions $\{q_1, \ldots, q_k\}$ computed via (7.1), respectively. One option to generated such an ensemble of transition matrices can be found in [85]. They follow a Bayesian approach to derive a *conditional probability distribution* of all possible transition matrices given the observation Y by assuming that the prior probability over the transition matrices before observing any data is given by Dirichlet distributions. Moreover, they derive efficient methods to sample from the resulting posterior distribution. However, the resulting ensembles do depend *explicitly* on the choice of parameters for the prior Dirichlet distributions and, therefore, the Bayesian approach is from our point of view inappropriate for the computation of the variance of the committor function $\hat{q}$.

We follow an alternative approach via Markov Chain Monte Carlo (MCMC) simulation. For notational convenience we denote the set of all transition matrices by

$$\mathfrak{P} = \left\{ P = (p_{ij})_{i,j \in S} : p_{ij} \in [0,1], \sum_{k \in S} p_{ik} = 1 \;\; \forall i, j \in S \right\}.$$

We devise an MCMC Metropolis scheme to generate an ensemble of transition matrices which is distributed according to the discrete likelihood function $\mathcal{L}_d$ restricted on the set $\mathfrak{P}$. Compared to the Bayesian approach, we do not assume any prior distribution of transition matrices.

A MCMC Metropolis scheme works basically as follows. Suppose you want to sample from a probability distribution which is induced by a density function $f \in L^1(\mathbb{R}^d)$. Let $x_\mathcal{C} \in \mathbb{R}^d$ be the current state under consideration in the ensemble. In the proposal step a new state $x_\mathcal{N} \in \mathbb{R}^d$ is generated. In the acceptance step the proposed state $x_\mathcal{N}$ is accepted with the probability

$$p_{acc} = \min \left\{ 1, \frac{f(x_\mathcal{N}) \cdot p(x_\mathcal{C} \to x_\mathcal{N})}{f(x_\mathcal{C}) \cdot p(x_\mathcal{N} \to x_\mathcal{C})} \right\}, \tag{7.5}$$

where $p(x_\mathcal{C} \to x_\mathcal{N})$ is probability of generating the state $x_\mathcal{N}$ conditional on the state $x_\mathcal{C}$ and $p(x_\mathcal{N} \to x_\mathcal{C})$ is defined analogously. If the new state is accepted than $x_\mathcal{N}$ is added to the ensemble and the scheme restarts with $x_\mathcal{N}$ as the current state. Otherwise, the current state $x_\mathcal{C}$ is added to the ensemble and is considered again in the next iteration of the scheme.

Let us in the following comment on several issues concerning the MCMC sampling procedure:

- The target density function $f \in L^1(\mathbb{R}^d)$ does not have to be normalized because only the ratio $f(x_\mathcal{N})/f(x_\mathcal{C})$ is involved in the acceptance probability in (7.5).

- The sampling of a probability distribution *restricted* on a subset of the state space, say $R \subset \mathbb{R}^d$, can easily be achieved by modifying the density function f according to

$$f_R(x) \stackrel{def}{=} \mathbb{1}_R(x) f(x).$$

  If the MCMC sampling procedure is started with $x_\mathcal{C} \in R$ then the ratio in the acceptance probability in (7.5),

$$\frac{f_R(x_\mathcal{N})}{f_R(x_\mathcal{C})} = \frac{\mathbb{1}_R(x_\mathcal{N}) f(x_\mathcal{N})}{\mathbb{1}_R(x_\mathcal{C}) f(x_\mathcal{C})} = \mathbb{1}_R(x_\mathcal{N}) \frac{f(x_\mathcal{N})}{f(x_\mathcal{C})},$$

  is well defined during the sampling procedure and the resulting ensemble is distributed according to f restricted on R.

- In principle, one can use any strategy for the generation of a new state in the proposal step as long as one is able to evaluate the probabilities $p(x_\mathcal{C} \to x_\mathcal{N})$ and $p(x_\mathcal{N} \to x_\mathcal{C})$. The choice of the proposal step strategy, however, is crucial for the efficiency and the convergence of the sampling procedure. For a discussion on these issues see, e.g., [13].

7.3. Ensemble of Transition Matrices via MCMC

We are interested in sampling the distribution induced by the discrete likelihood function $\mathcal{L}_d(P)$. In the following, it is convenient to represent the target density function $f(P) = \mathcal{L}_d(P)$ as

$$f(P) = e^{-g(P)} \text{ with } g(P) \stackrel{def}{=} -\log(\mathcal{L}_d(P)). \tag{7.6}$$

7.3.1. Dynamics on the Transition Matrix Space

For the generation of a proposal state $P_{\mathcal{N}}$ we exploit the fact that the non-normalized probability density function $\rho(P)$ of the invariant measure associated with the SDE

$$\mathrm{d}P_t = -\nabla g(P_t)dt + \sqrt{2}\ \mathrm{d}W_t \tag{7.7}$$

is given by

$$\rho(P) = e^{-g(P)} = \mathcal{L}_d(P),$$

where $P \in \mathbb{R}^{d^2}$ is understood as a d^2-dimensional vector and W_t is a d^2-dimensional standard Wiener process. A scheme for the generation of a proposal state $P_{\mathcal{N}}$ is obtained by discretizing the SDE in (7.7) by means of the Euler-Maruyama-scheme,

$$P_{\mathcal{N}} = P_{\mathcal{C}} - \nabla g(P_{\mathcal{C}})\Delta t + \sqrt{2\Delta t}\ \eta, \tag{7.8}$$

where $0 < \Delta t \in \mathbb{R}$ denotes the discretization time step and the random variable η is drawn from a d^2-dimensional standard Gaussian distribution with mean $0 \in d^2$ and covariance matrix $I = \mathrm{diag}(1, \dots, 1) \in \mathbb{R}^{d^2 \times d^2}$. Unfortunately, the proposal step equation in (7.8) does not preserve the transition matrix property, i.e. $P_{\mathcal{N}} \notin \mathfrak{P}$, because the Gaussian random variable η is unbounded. One option is to choose a sufficiently small time discretization step Δt such that $p_{ij} \in [0, 1]$, $0 \leq i, j \leq d$ but in general $P_{\mathcal{N}}$ is not a stochastic matrix, i.e. $\sum_{m \in S} p_{im} \neq 1$.

7.3.2. MCMC on the Frequency Matrix Space

Motivation

As a preparation for an alternative approach, recall that if only an incomplete observation of a Markov chain with discrete state space S is available, the transition matrix $\hat{P} = (\hat{p}_{ij})$, $i, j \in S$ which most likely explains the data is given by

$$\hat{p}_{ij} = \frac{c_{ij}}{\sum_{k \in S} c_{ik}}, \tag{7.9}$$

where an entry c_{ij} of the frequency matrix $C = (c_{ij})$, $i, j \in S$ provides the number of observed transitions from i to j. The relation in (7.9) can be written in compact form,

$$\hat{P} = u(C),$$

where the function $u(C) : \mathbb{R}^{d^2} \mapsto \mathfrak{P}$ is defined as

$$u(C) \stackrel{def}{=} \left(\frac{c_{11}}{\sum_{m \in S} c_{1m}}, \dots, \frac{c_{dd}}{\sum_{m=1}^{d} c_{dm}} \right) \in \mathfrak{P}.$$

To avoid any notational confusion with respect to the empirical frequency matrix, we will denote in the following a general frequency matrix by K.

The crucial idea is now to generate an ensemble of frequency matrices $\mathcal{K} = \{K \in \mathbb{R}_+^{d^2}\}$ via an MCMC procedure which is distributed according to the likelihood function $\mathcal{L}_d(u(C))$. We will show that the ensemble $\mathcal{P} = \{P = u(K) : K \in \mathcal{K}\}$ is distributed according to $\mathcal{L}_d(P)$.

Derivation of the MCMC Procedure on the Frequency Matrix Space

We consider a dynamics on the state space of frequency matrices,

$$\mathrm{d}K_t = -\nabla \tilde{g}(K_t)dt + \sqrt{2\beta^{-1}} \, \mathrm{d}W_t, \tag{7.10}$$

where $K_t = (k_{ij})_{i,j \in S} \in \mathbb{R}^{d^2}$, the factor β^{-1} can be seen as an artificial temperature. The function $\tilde{g} : \mathbb{R}^{d^2} \mapsto \mathbb{R}$ is defined according to

$$\tilde{g}(K) \stackrel{def}{=} g(u(K)),$$

where the function g is defined in (7.6). Then the probability density function $\rho(K)$ of the invariant distribution of (7.10) is given by

$$\rho(K) = e^{-\beta \tilde{g}(K)} = [\mathcal{L}_d(u(K))]^\beta. \tag{7.11}$$

The time discretization of (7.10) via the Euler-Maruyama-scheme yields an equation for the proposal step,

$$K_\mathcal{N} = K_\mathcal{C} - \nabla \tilde{g}(K_\mathcal{C})\Delta t + \sqrt{2\beta^{-1}\Delta t} \, \eta, \tag{7.12}$$

where the gradient $\nabla \tilde{g}(K)$ takes the form

$$\nabla \tilde{g}(K) = (\frac{c_1}{k_1} - \frac{c_{11}}{k_{11}}, \ldots, \frac{c_d}{k_d} - \frac{c_{dd}}{k_{dd}})^T, \tag{7.13}$$

with $k_i = \sum_{m=1}^d k_{im}$ and Δt and η are as in (7.8).

It remains to derive an expression for the probability $p(K_\mathcal{C} \to K_\mathcal{N})$ but this immediately follows by realizing that the difference $\Delta K = K_\mathcal{N} - K_\mathcal{C}$ is distributed according to a d^2-dimensional Gaussian distribution with mean $-\Delta t \nabla \tilde{g}(K_\mathcal{C}) \in \mathbb{R}^{d^2}$ and covariance matrix $2\beta^{-1}\Delta t I \in \mathbb{R}^{d^2 \times d^2}$. Consequently, the probability to generate the proposal state $K_\mathcal{N}$ while being in the current state $K_\mathcal{C}$ is

$$p(K_\mathcal{C} \to K_\mathcal{N}) = Z^{-1} \exp\left[-\frac{1}{4\beta^{-1}\Delta t}\|\Delta K + \nabla \tilde{g}(K_\mathcal{C})\Delta t\|^2\right],$$

where Z is a normalization factor.

In order to ensure that the matrix $u(K_\mathcal{N})$ is a transition matrix, i.e. $u(K_\mathcal{N}) \in \mathfrak{P}$, we generate an ensemble of frequency matrices restricted on the subset (cf. Sect. 7.2)

$$\mathfrak{K} = \left\{K \in R_+^{d^2} : k_i^- < \sum_{m=1}^d k_{im} < k_i^+\right\}, \tag{7.14}$$

where $0 < k_i^- < k_i^+$, $i = 1, \ldots, d$. The particular choice of the boundary conditions for $\mathfrak{K}$ will become clear in Section 7.3.3.

Combining all issues, we finally end up with the Metropolis algorithm, as stated in Algorithm 9, to generate an ensemble of transition matrices distributed according to the discrete likelihood function $\mathcal{L}_d(P)$.

Algorithm 9 Metropolis algorithm

Input: Frequency matrix $C = (c_{ij})_{i,j \in S}$, number of MCMC steps $nMCMC$, time
   step Δt, temperature β^{-1}.

Output: Ensemble $\mathcal{P}$ of transition matrices.

   (1) Initialize $K_\mathcal{C} := C$.

   (2) **FOR** $n = 1$ **TO** $nMCMC$ **DO**

   (3)   Generate proposal frequency vector $K_\mathcal{N} = (k_{ij})$:
   $$K_\mathcal{N} = K_\mathcal{C} - (\tfrac{c_1}{k_1} - \tfrac{c_{11}}{k_{11}}, \ldots, \tfrac{c_d}{k_d} - \tfrac{c_{dd}}{k_{dd}})^T + \sqrt{2\Delta t}\ \eta.$$

   (4)   Accept $K_\mathcal{N}$ with acceptance probability ($\Delta K = K_\mathcal{N} - K_\mathcal{C}$):
   $$p_{acc} = \min \left\{ 1, \mathbb{1}_\mathfrak{K}(K_\mathcal{N}) \frac{\mathcal{L}_d(u(K_\mathcal{N})) \exp\left[-\frac{1}{4\beta^{-1}\Delta t}\|\Delta K + \nabla \tilde{g}(K_\mathcal{C})\Delta t\|^2\right]}{\mathcal{L}_d(u(K_\mathcal{C})) \exp\left[-\frac{1}{4\beta^{-1}\Delta t}\|-\Delta K + \nabla \tilde{g}(K_\mathcal{N})\Delta t\|^2\right]} \right\}.$$

   (5)   **If** $K_\mathcal{N}$ is accepted **THEN** set $K_\mathcal{C} := K_\mathcal{N}$.

   (6)   Add $u(K_\mathcal{C})$ to the transition matrix ensemble $\mathcal{P}$.

   (7) **END FOR**

7.3.3. Proof of Correctness

It remains to prove that resulting ensemble of transition $\mathcal{P} = \{u(\mathcal{K})\}$ is indeed
distributed according to $\mathcal{L}_d(P)$.

Theorem 7.3.1. *Let $\mathcal{K} = \{K \in \mathfrak{K}\}$ be an ensemble of frequency matrices distributed
according to $\mathcal{L}_d(u(K))$. Then the ensemble $\mathcal{P} = \{u(K) : K \in \mathcal{K}\}$ is distributed
according to $\mathcal{L}_d(P)$.*

Proof. We prove that for all $P \in \mathfrak{P}$ holds

$$\mathbb{P}[u(K) = P] \propto \mathcal{L}_d(P).$$

Without loss of generality, we restrict ourselves to the first row vector $K^{(1)} = (k_{11}, \ldots, k_{1d})$ of a frequency matrix $K \in \mathcal{K}$. For the sake of notational simplicity we
write in the following

$$u(k_{11}, \ldots, k_{1d}) = (\frac{k_{11}}{\sum_{m=1}^d k_{1m}}, \ldots, \frac{k_{1d}}{\sum_{m=1}^d k_{1m}}),$$

$$\mathcal{L}_d(p_{11}, \ldots, p_{1d}) = \prod_{j=1}^d (p_{1j})^{c_{1j}}.$$

Let $\mathfrak{P}^{(1)} = \{p = (p_{11}, \ldots, p_{1d}) : p \in \mathbb{R}_+^d, \sum_{j=1}^d p_{1j} = 1\}$. Since $\mathfrak{P}^{(1)} \subset \mathbb{R}^d$ is an
(d-1)-dimensional manifold we represent an element $p \in \mathfrak{P}^{(1)}$ by

$$p = (p_{11}, \ldots, p_{1(d-1)}, 1 - \sum_{j=1}^{d-1} p_{1j}).$$

Furthermore, we will denote in the following by $\Pi(p), p \in \mathfrak{P}^{(1)}$ the projection onto
the first (d-1) components of p, i.e,

$$\Pi(p) = (p_{11}, \ldots, p_{1(d-1)}).$$

The crucial observation now is that due to the particular choice of the set $\mathfrak{K}$ in (7.14) we have

$$\{K^{(1)} : u(K^{(1)}) = (p_{11}, \ldots, p_{1d})\} = \{(\alpha p_{11}, \ldots, \alpha p_{1d}) : k_1^- < \alpha < k_1^+\}, \qquad (7.15)$$

which motivates to consider the new observable $\tilde{K}^{(1)} = \tilde{T}(K^{(1)})$,

$$\tilde{T} : \mathbb{R}_+^d \to \mathbb{R}_+ \times \Pi(\mathfrak{P}^{(1)})$$
$$\tilde{T}(k_{11}, \ldots, k_{dd}) \mapsto (\alpha, p_{11}, \ldots, p_{1(d-1)}), \qquad (7.16)$$
$$\alpha = \sum_{m=1}^{d} k_{1m}, \quad p_{1j} = \frac{k_{1j}}{\sum_{m=1}^{d} k_{1m}}, \; j = 1, \ldots, d-1.$$

If we denote the probability density function associated with the new observable $\tilde{K}^{(1)}$ by $\tilde{\mathcal{L}}$ then it should be clear that

$$\mathbb{P}[u(K^{(1)}) = (p_{11}, \ldots, p_{1d})] \propto \int_{k_1^-}^{k_1^+} \tilde{\mathcal{L}}(\alpha, p_{11}, \ldots, p_{1(d-1)}) \mathrm{d}\alpha.$$

In Lemma 7.3.1 we show that $\tilde{\mathcal{L}}$ is simply given by

$$\tilde{\mathcal{L}}(\alpha, p_{11}, \ldots, p_{1(d-1)}) = \mathcal{L}_d(p_{11}, \ldots, p_{1d}) \alpha^{(d-1)},$$

where $p_{1d} = (1 - \sum_{j=1}^{d-1} p_{1j})$. But this immediately implies

$$\mathbb{P}[u(K^{(1)}) = (p_{11}, \ldots, p_{1d})] \propto \mathcal{L}_d(p_{11}, \ldots, p_{1d}).$$

and we are done. $\qquad\qquad\square$

It remains to prove

Lemma 7.3.1.

$$\tilde{\mathcal{L}}(\alpha, p_{11}, \ldots, p_{1(d-1)}) = \mathcal{L}_d(p_{11}, \ldots, 1 - \sum_{j=1}^{d-1} p_{1j}) \alpha^{(d-1)}$$

Proof. The probability density function $\tilde{\mathcal{L}}(\tilde{K}^{(1)})$ associated with $\tilde{K}^{(1)} = (\alpha, p_{11}, \ldots, p_{1(d-1)})$ is given by [58]

$$\tilde{\mathcal{L}}(\tilde{K}^{(1)}) = \mathcal{L}_d(u(\tilde{T}^{-1}(\tilde{K}^{(1)}))) \left| \det(J(\tilde{T}^{-1})(\tilde{K}^{(1)})) \right|, \qquad (7.17)$$

where

$$\tilde{T}^{-1} : \mathbb{R}_+ \times \Pi(\mathfrak{P}^{(1)}) \to \mathbb{R}_+^d$$
$$\tilde{T}^{-1}(\alpha, p_{11}, \ldots, p_{1(d-1)}) \mapsto (\alpha p_{11}, \ldots, \alpha p_{1(d-1)}, \alpha(1 - \sum_{j=1}^{d-1} p_{1j})). \qquad (7.18)$$

The first factor in (7.17) reduces to

$$\mathcal{L}_d(u(\tilde{T}^{-1}(\tilde{K}^{(1)}))) = \mathcal{L}_d(u(\alpha p_{11}, \ldots, \alpha p_{1(d-1)}, \alpha(1 - \sum_{j=1}^{d-1} p_{1j})))$$
$$= \mathcal{L}_d(p_{11}, \ldots, p_{1d}),$$

where $p_{1d} = (1 - \sum_{j=1}^{d-1} p_{1j})$.

Finally, we compute the determinant in (7.17):

$$
\det J(\tilde{T}^{-1}) =
\begin{vmatrix}
p_{11} & \alpha & 0 & 0 & \ldots \\
p_{12} & 0 & \alpha & 0 & \ldots \\
\vdots & & \vdots & \ddots & \ddots & \vdots \\
p_{1(d-1)} & 0 & \ldots & \ldots & \alpha \\
1 - \sum_{j=1}^{d-1} p_{1j} & -\alpha & \ldots & \ldots & -\alpha
\end{vmatrix}
$$

$$
=
\begin{vmatrix}
p_{11} & \alpha & 0 & 0 & \ldots \\
p_{12} & 0 & \alpha & 0 & \ldots \\
\vdots & \vdots & \ddots & \ddots & \vdots \\
p_{1(d-1)} & 0 & \ldots & \ldots & \alpha \\
1 & 0 & \ldots & \ldots & 0
\end{vmatrix}
$$

$$
=(-1)^{(d-1)}
\begin{vmatrix}
1 & 0 & \ldots & \ldots & 0 \\
p_{11} & \alpha & 0 & 0 & \ldots \\
p_{12} & 0 & \alpha & 0 & \ldots \\
\vdots & \vdots & \ddots & \ddots & \vdots \\
p_{1(d-1)} & 0 & \ldots & 0 & \alpha
\end{vmatrix}
= (-1)^{(d-1)} \alpha^{(d-1)}.
$$

$\square$

7.4. Numerical Experiments

7.4.1. Dirichlet Distribution

In the first example we use the derived MCMC method to sample from a two-dimensional (non-normalized) Dirichlet-distribution

$$
\mathcal{L}(p_1, p_2) = (p_1)^{c_1} \cdot (p_2)^{c_2} \cdot (1 - p_1 - p_2)^{c_3} \tag{7.19}
$$

on the state space $D = \{p_1 + p_2 + p_3 = 1 : p_1, p_2, p_3 \geq 0\}$ with parameters $c_1, c_2, c_3 > 0$. For our numerical experiments we chose two different sets of parameters, namely $\mathcal{C}_1 = (c_1 = 3, c_2 = 8, c_3 = 10)$ and $\mathcal{C}_2 = (c_1 = 43, c_2 = 8, c_3 = 15)$. We sampled both distribution at the "temperature" $\beta^{-1} = 10$ via Algorithm 9 and generated an ensemble consisting of 10^6 transition matrices, respectively. As boundary conditions for the restriction $\mathfrak{K}$ in (7.14) we chose $k_1^- = (\sum_{j=1}^{3} c_j) - 5$ and $k_1^+ = (\sum_{j=1}^{3} c_j) + 5$. For the simulation with respect to the parameter set $\mathcal{C}_1$ we had for the time step $\Delta t = 10^{-3}$ an acceptance rate of 93% and with respect to $\mathcal{C}_2$ for $\Delta t = 10^{-2}$ an acceptance rate of 96%.

In Figure 7.1 we compare the distribution of the ensemble from the simulation with respect to the parameter set $\mathcal{C}_1$ (top right panel) with the corresponding analytical distribution (top left panel). For the sake of comparison, we normalized all distributions such that their respective maximal value is one. The distributions resulting for the parameter set $\mathcal{C}_2$ are given in the second row of Figure 7.1. One can see both distributions are well sampled.

Let us comment on the choice of the simulation parameters. The simulation's temperature $\beta^{-1} = 5$ ensures that even states with a very low statistical weight
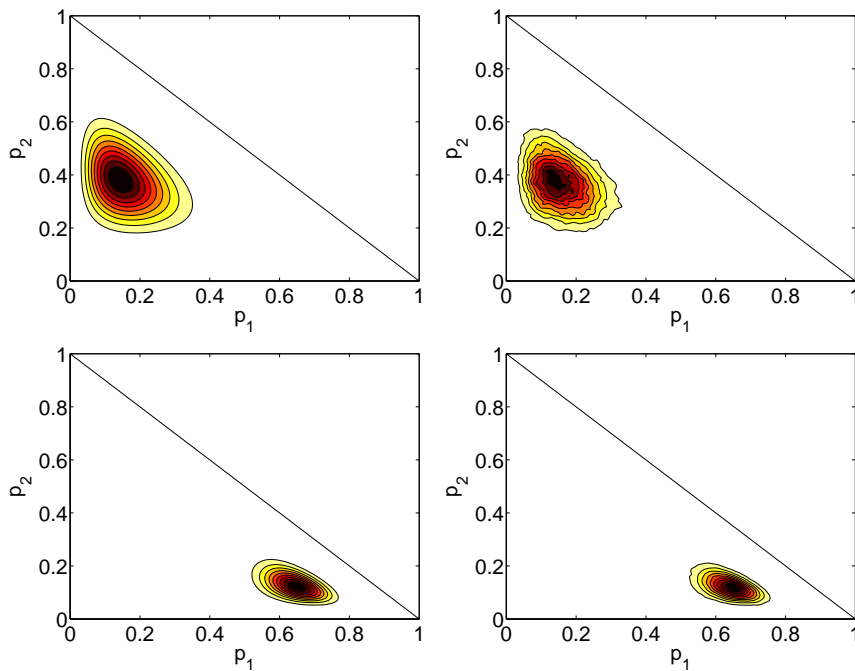
Figure 7.1.: We compare the distributions of the Dirichlet distribution in (7.19) (first column) with the distributions of the ensembles generated via Algorithm 9 (second column) with respect to the parameter set $\mathcal{C}_1 = (c_1 = 3, c_2 = 8, c_3 = 10)$ (first row) and $C_2 = (c_1 = 43, c_2 = 8, c_3 = 15)$ (second row). For example, the analytical distribution with respect to $\mathcal{C}_1$ attains its maximum at $(\frac{c_1}{c1+c2+c3}, \frac{c_2}{c1+c2+c3}) \approx (0.14, 0, 38)$.

with respect to the target distribution $\mathcal{L}_d(u(K))$ are sufficiently often proposed such that the variance is right reproduced. For realistic values of the parameters ($c_i > 100$), however, our extensive numerical experiments have shown that the Dirichlet distribution in (7.19) is already well sampled at a low temperature $\beta^{-1} = 1$.

7.4.2. Small Example

In this section we demonstrate the performance of the derived Algorithm 9 on a Markov chain with a small state space $S \cong \{1, \ldots, 25\}$. This example is constructed such that it allows to relate the element-wise variances of the resulting ensemble of committor functions to an underlying discretized potential landscape.

As exemplified in the Section 4.3.1, a Smoluchowski diffusion process in a potential landscape can be approximated by a Markov jump process where the infinitesimal generator L of the approximating Markov jump process results from a finite differences discretization scheme of the generator, associated with the diffusion process (cf. Sect. A.3). Doing so, a transition matrix can easily be obtained because the generator L generates a semigroup of transition matrices via $P(t) = \exp(tL)$. For a particular choice of $t > 0$ we will call $P(t) = \exp(tL)$ transition matrix.

For our numerical experiments, we utilized the generator given in (4.44) which results from an approximation of the Smoluchowski dynamics in the three-hole potential landscape. We approximated the diffusion (at temperature $\beta^{-1} = 1$) on a
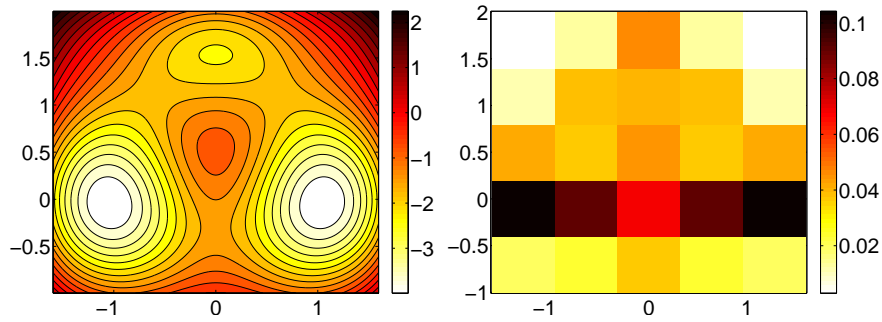
Figure 7.2.: Left: Contour plot of the three-hole potential (3.45). Right: Box plot of the stationary distribution associated with the 25-state Markov chain $P = \exp(1.2L)$.
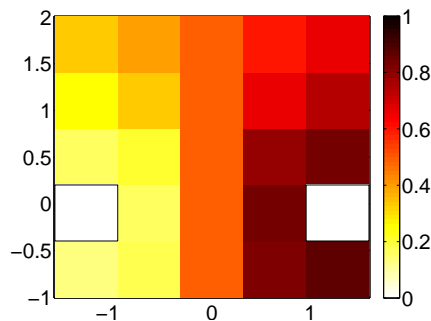
Figure 7.3.: Box plot of the committor function associated with the transition matrix $P = \exp(1.2L)$. As the sets A and B, we chose the two states with the highest stationary distribution. The set A consists of the state corresponding to the left white box and the set B consists of the state corresponding to the right white box.

5×5 mesh of the domain $\Omega = [-1.5, 1.5] \times [-1, 1.5]$ which results in a generator $L \in \mathbb{R}^{25 \times 25}$ on a discrete state space of 25 states.

The potential landscape of the three-hole potential in (3.45) is illustrated as a contour plot in the left panel of Figure 7.2. In the right panel, we show a box plot of the stationary distribution of the transition matrix $P(1.2) = \exp(1.2 \cdot L) \in \mathbb{R}^{25 \times 25}$. Although we used an extremely coarse-grained mesh (5×5), one can clearly see that the equilibrated dynamics of the Markov chain reflects the topology of the potential landscape, e.g., the two states in the Markov chain with highest stationary probability correspond to the two deep minima in the potential landscape, respectively. The discrete committor function with respect to $P(1.2)$ is illustrated in Figure 7.3. As the set A and B we chose the two states with the highest stationary distribution (depicted by white boxes). The main question we were interested in is of how the element-wise variances of a committor ensemble do depend on the length N of the observed time series of the Markov chain. For this purpose, we generated via Algorithm 9 a sequence of committor function ensembles $\{q_1^{(N)}, \ldots, q_6^{(N)}\}$ for time series of length $N = 10^3, \ldots, N = 10^8$ where the respective time series were all subsampled from a fixed realization of the Markov chain. For each ensemble we sampled $m = 500000$ committor functions where we used the discretization time

N	10^3	10^4	10^5	10^6	10^7	10^8
κ	13.34	14.03	12.27	11.97	11.91	11.94

Table 7.1.: The condition number κ of the matrix $\hat{P}^{(N)} - I$ *after* elimination of the condition $q_i = 0, \forall i \in A, q_i = 1, \forall i \in B$ which arises from solving of the discrete committor equation (7.4). The table gives the condition number κ as a function of the length N of the considered time series. Results for time series all subsampled from the same realization.

step $\Delta t = 10^{-3}$ in the proposal step equation (7.12). As boundary conditions for the restriction $\mathfrak{K}$ in (7.14) we chose $k_i^- = c_i - 15$ and $k_i^+ = c_i + 15$ where $c_i = \sum_{j=1}^{d} c_{ij}$. In all simulations we had an acceptance rate of about $> 93\%$.

In the following $\hat{P}^{(N)}$ denotes the MLE transition matrix resulting from the time series of length N and $\hat{q}^{(N)}$ is the associated committor function. The mean committor function of an ensemble $\{q_1^{(N)}, \ldots, q_6^{(N)}\}$ is denoted by $\bar{q}^{(N)}$ and the variance by $var(\bar{q}^{(N)})$. In Figure 7.4 we illustrate the committor function $\hat{q}^{(N)}$ (first column), mean committor function $\bar{q}^{(N)}$ (second column) and its variance $var(\bar{q}^{(N)})$ (third column) for all ensembles, respectively. At first glance, one can see that the committor functions $\hat{q}^{(N)}$ are almost identical with the corresponding mean committor function $\bar{q}^{(N)}$ of the ensemble, except for the length $N = 10^3$. Beside the observation that the variance of the ensembles decreases by the same order of magnitude as the length N increases, the box plots in third column reveal that the states with the lowest stationary distribution exhibit the highest variance in the committor function. The observations are confirmed by the graphs shown in Figure 7.5. In the left panel, we plot the maximal variance $\|var(\bar{q}^{(N)})\|_\infty$ of the mean committor functions $\bar{q}^{(N)}$ as a function of the length N of the respective time series whereas in the right panel the error $\|\bar{q}^{(N)} - \hat{q}^{(N)}\|$ (measured in the 2-norm) between the mean committor function $\bar{q}^{(N)}$ and the committor function $\hat{q}^{(N)}$ is shown as a function of the length N of the respective time series.

Our numerical experiments have shown that the committor function $\hat{q}^{(N)}$ even for short time series ($N = 10^3$) almost coincides with the expected committor function with respect to the discrete likelihood function $\mathcal{L}_d$.
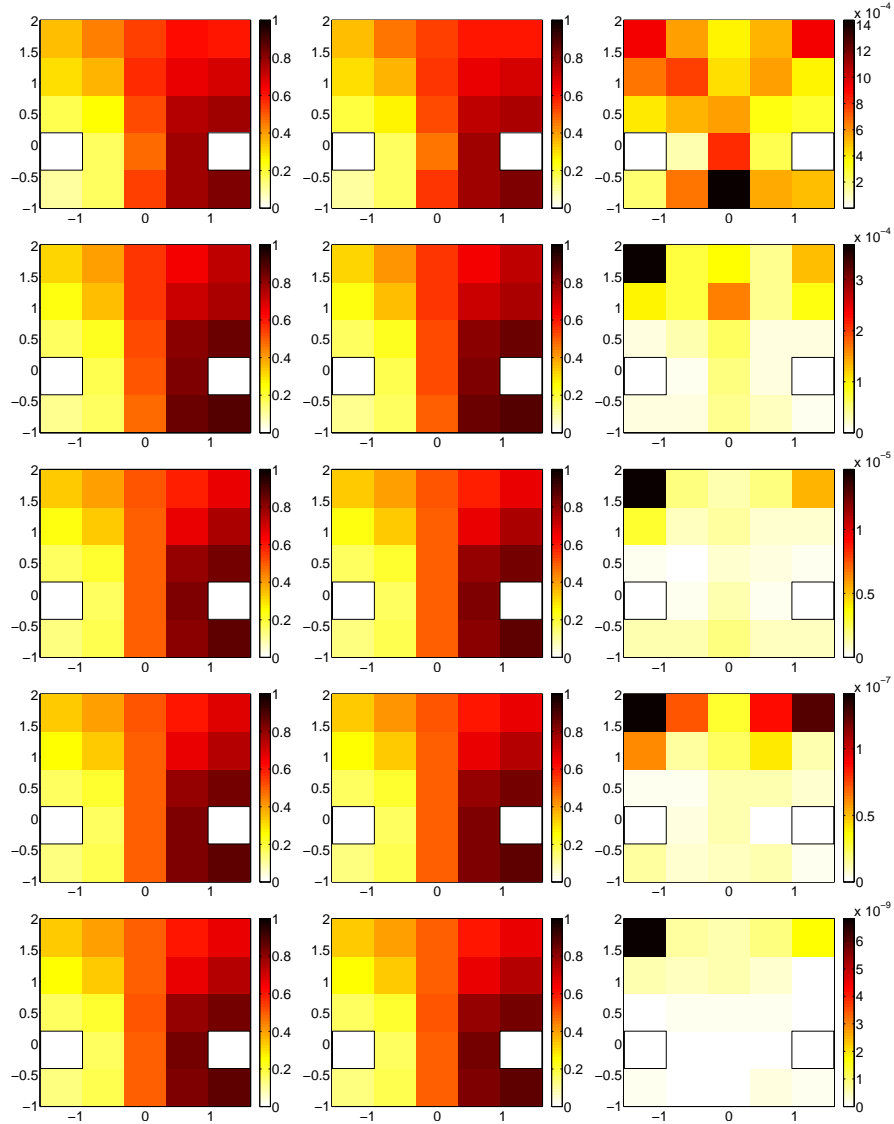
Figure 7.4.: Left column: Box plots of the committor functions $\hat{q}^{(N)}$ resulting from the MLE transition matrix $\hat{P}^{(N)}$ (7.3), respectively. Middle column: Box plots of the mean committor functions $\bar{q}^{(N)}$ of the committor function ensembles $\{q_1^{(N)}, \ldots, q_5^{(N)}\}$, respectively. Right column: Box plots of the variances $var(\bar{q}^{(N)})$ of the mean committor functions, respectively. Results for different lengths $N = 10^3$ (top), ..., $N = 10^7$ (bottom) of respective time series all subsampled from the same realization.
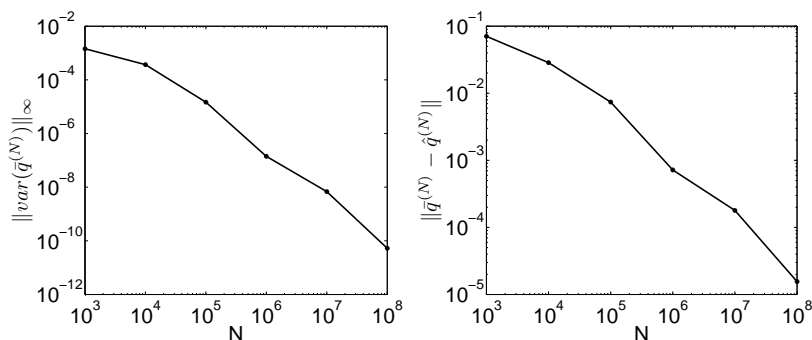
Figure 7.5.: Left: The maximal variance $\|var(\bar{q}^{(N)})\|_\infty$ of the mean committor functions $\bar{q}^{(N)}$ as a function of the length N of the respective time series. Right: The error $\|\bar{q}^{(N)} - \hat{q}^{(N)}\|$ (measured in the 2-norm) between the mean committor function and the committor function resulting from the MLE transition matrix $\hat{P}^{(N)}$ in (7.3) as a function of the length N of the respective time series. Results for time series all subsampled from the same realization.

7.4.3. Glycine

In the last example we apply the MCMC methods in order to estimate the uncertainties of the forward committor function q^+ in the glycine in solvent example from Section 4.3.2. We are aware that in the glycine-example the forward committor function q^+ is computed via an (estimated) generator L of a Markov jump process and *not* via the transition matrix of a Markov chain. Nevertheless, the MCMC method allows to get an idea of the uncertainties because q^+ is almost identical with the discrete committor function $\hat{q}^+$ based on the MLE $\hat{P}$ and computed via (7.4). Both committor functions are illustrated in the panels of Figure 7.6.

For the estimation of the variance of the committor function $\hat{q}^+$ we generated an ensemble of $7 \cdot 10^6$ transition matrices ($\Delta t = 10^{-5}$) and computed the element-wise variances of the resulting ensemble of committor functions. The boundary conditions for the restriction $\mathfrak{K}$ were the same as in the previous example. To be more precise, instead of generating a full transition (counts) matrix in each step of the simulation, we used the structure of the MLE $\hat{P}$ as a template, i.e., we only generated entries k_{ij} if $c_{ij} > 0$. In each iteration step of the Algorithm 9 we solved the discrete committor equation in (7.4) with respect to the current transition matrix. Finally, a clever update-scheme allowed us to compute the element-wise variances of the committor function ensemble $\{q^+_{MCMC}\}$ *on the fly* (see the end of this section).

The final variances are illustrated in the left panel of Figure 7.7 where the boxes are colored according to the log-values of the respective variances in order to emphasize the different orders of magnitudes. Again, the comparison of the variances element by element with the Gibbs energy of the Markov chain $\hat{P}$ reveals what intuitively should be clear; the states with high variance correspond to those with very high discrete free energy which is equivalent to a very small stationary distribution. In Figure 7.8 we show the maximal variance $\|var(\{q^+_{MCMC}\})\|_\infty$ as a function of the MCMC-steps.

We end this section by deriving the update-scheme for the "on the fly" com-
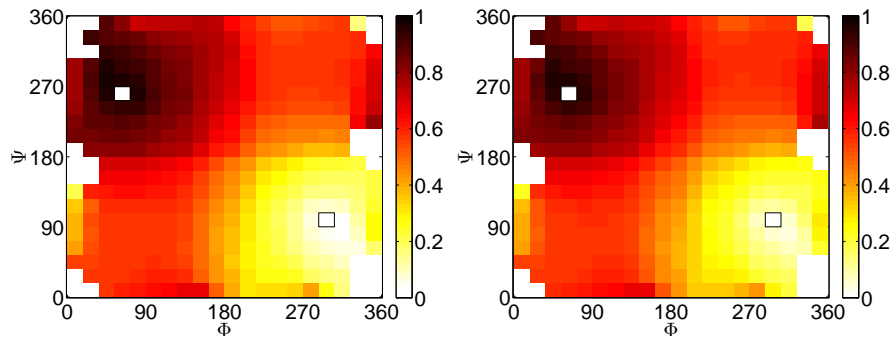
Figure 7.6.: Right: The panel shows the forward committor q^+ based on an estimated generator $\tilde{L}$ (cf. Sect. 4.3.2) and computed via (4.11). Left: The corresponding box plot of the discrete committor $\hat{q}^+$ based on the MLE $\hat{P}$ and computed via (7.4). As the set A we chose the box (shown as a white box with black boundary) which covers the peak of the restricted stationary distribution on the lower right conformation. The set B for the upper left conformation (shown as a white box) was chosen analogously. Results for an equidistant discretization of the torsion angle space into 20×20 boxes.

putation of the variances. We derive the scheme for a one-dimensional time series $(x_1, \ldots, x_N), x_i \in \mathbb{R}$. A short calculation shows that the estimator of the variance of the time series reduces to

$$\frac{1}{N+1} \sum_{i=1}^{N} \left(x_i - \sum_{j=1}^{N} x_j \right)^2 = \frac{1}{N+1} \left(s_1(N) - \frac{1}{N} s_2^2(N) \right), \qquad (7.20)$$

where $s_1(N) = \sum_{j=1}^{N} x_j^2$ and $s_2(N) = \sum_{j=1}^{N} x_j$. But this means if one is interested in the in the variance of the time series $(x_1, \ldots, x_N, x_{N+1})$ then only the sums s_1 and s_2 have to be updated and the right hand side in (7.20) yields the desired result with respect to $N' = N + 1$.
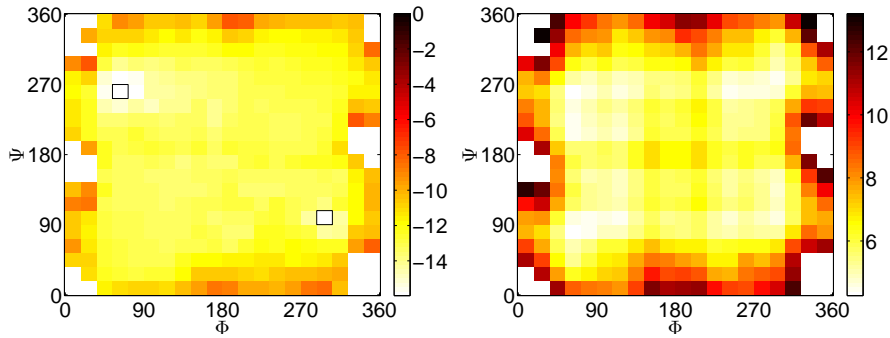
Figure 7.7.: The left panel illustrates the element-wise variances of the committor functions ensemble $\{q^+_{MCMC}\}$. In order to emphasize the variances' magnitudes of order, we chose a logarithmical scale. The comparison of the variances with the discrete free energy of the MLE Markov chain $\hat{P}$, as shown in the right panel, again reveals that the states with the highest variances correspond to those with the lowest statistical weights.
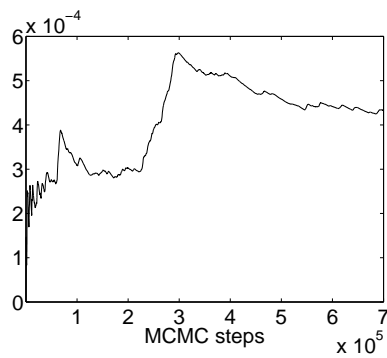
Figure 7.8.: The maximal variance $\|var(\{q^+_{MCMC}\})\|_\infty$ as the function of the MCMC steps.

7. Variance of the Committor Function

8. Summary and Conclusion

In this thesis, we have presented the framework of transition path theory (TPT) for time continuous Markov processes with continuous and discrete state space. TPT provides statistical properties of the ensemble of reactive trajectories between some start and target sets and yields properties such as the committor function, the probability distribution of the reactive trajectories, their probability current and their rate of occurrence. We have shown that knowing these objects allows one to arrive at a complete understanding of the mechanism of the reaction.

The main objects of TPT for Markov diffusion processes have been explicitly derived for the Langevin and Smoluchowski dynamics and we have illustrated them on a various number of low-dimensional examples. Despite the simplicity of these examples compared to those encountered in real applications, they already demonstrate the ability of TPT to handle complex dynamical scenarios. The main challenge in TPT for diffusion processes is the numerical computation of the committor function as a solution of a Dirichlet-Neumann boundary value problem involving the generator of the process.

Beside the derivation of TPT for Markov jump processes, we have focused on the development of efficient graph algorithms to determine reaction pathways in discrete state space. One approach via shortest-path algorithms has turned out to give only a rough picture of possible reaction channels whereas the network approach allows a hierarchical decomposition of the set of reaction pathways such that the dominant channels can be identified. We have successfully applied the latter approach to an example of conformational dynamics of a bio-molecule. In particular, we have made use of a maximum likelihood method to estimate the infinitesimal generator of a jump process from an incomplete observation. Finally, we have addressed the question of error propagation in the committor function computation for Markov chains.

The discrete TPT framework has many interesting relations to other topics in the Markov chain and network literature; we have briefly discussed the relation to electric resistor network theory and data segmentation tools such as Laplacian eigenmaps and diffusion maps. Future investigations should work out these and other relations in more detail.

8. Summary and Conclusion

A. Appendix

In the Appendix we will derive in detail the numerical discretization scheme for the committor equation associated with the Smoluchowski and Langevin dynamics, respectively. The main challenge will be to devise a stable finite difference scheme for the hypoelliptic committor equation. In Section A.3, we will proof the existence and uniqueness of a weak solution of the elliptic mixed-boundary value problem associated with the elliptic committor equation. Moreover, we will explain the link between the derived discretization schemes and the approximation of diffusion processes via Markov jump processes. We will end the Appendix by giving definitions and the technical proofs for the probability current of reactive trajectories and the expression for their rate.

A.1. Discretization of the Committor Equation

For the sake of a compact notation, we will write the (forward) committor equation (3.6) in the following form

$$\begin{cases} \mathcal{L}_{bw} q = 0 & \text{in } \mathbb{R}^d \setminus \mathcal{S} \\ q = g_D & \text{on } \partial \mathcal{S} \end{cases}$$

where $\mathcal{L}_{bw}$ is the generator of the considered Markov diffusion process, the set $\mathcal{S} = A \cup B$ is the union of two disjoint closed sets $A, B \subset \mathbb{R}^d$ and the Dirichlet condition on the boundary $\partial \mathcal{S}$ is given by the function $g_D : \partial \mathcal{S} \to \mathbb{R}$, defined according to

$$g_D(x) = \begin{cases} 0, & \text{if } x \in \partial A \\ 1, & \text{if } x \in \partial B. \end{cases} \tag{A.1}$$

The numerical treatment of the committor equation requires the choice of a bounded discretization domain $\Omega \subset \mathbb{R}^d$ such that the probability to find the equilibrated diffusion process in Ω is almost one. As explained in Section 2.1.9, the restriction of the diffusion process on Ω leads to additional conditions for the committor function $q(x)$ on the boundary $\partial \Omega$, that are

$$0 = a \nabla q \cdot \hat{n} = \nabla q \cdot a \hat{n}, \tag{A.2}$$

where $a(x)$ is the diffusion matrix and $\hat{n}$ is the unit normal on $\partial \Omega$ pointing outward Ω. Hence, the committor function $q(x)$ considered on a domain Ω has to satisfy the *mixed-boundary value problem*

$$\begin{cases} \mathcal{L}_{bw} q = 0 & \text{in } \Omega_{\mathcal{S}} \\ q = g_D & \text{on } \partial \mathcal{S} \\ \nabla q \cdot a \hat{n} = 0 & \text{on } \partial \Omega. \end{cases} \tag{A.3}$$
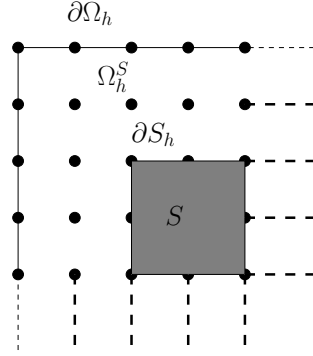
Figure A.1.: Schematic representation of the mesh $\overline{\Omega_h^S}$ and its disjoint boundaries $\partial\Omega_h$ and $\partial\mathcal{S}_h$.

A.1.1. Discretization via Finite Differences

In this section we will introduce the framework for the finite difference discretization of the mixed-boundary value problem (A.3) on a two dimensional domain $\Omega \subset \mathbb{R}^2$.

Remark A.1.1. *We will consider only rectangular domains with boundaries which are piecewise parallel to the axis of the coordinate system. Furthermore, we assume that the shape of the sets A and B are such that their boundaries ∂A and ∂B can be discretized by an appropriate discretization of the domain. The reasons for that restrictions are:*

- *The results of TPT for diffusion processes on rectangular domains already demonstrate the ability of TPT to capture different dynamical scenarios.*

- *The schemes are straightforward to derive and are easy to implement.*

- *The treatment of general domains and sets A and B would go beyond the scope of this thesis.*

Discretization of the Domain

Let $\Omega = (a,b) \times (c,d) \subset \mathbb{R}^2, a < b, c < d$. be a rectangular domain. We discretize Ω by a uniform mesh which is defined by

$$\Omega_h \stackrel{def}{=} \{\mathbf{x} = (a + ih_x, b + jh_y) : 1 < i < N - 1, 1 < j < M - 1\},$$

$$\partial\Omega_h \stackrel{def}{=} \{\mathbf{x} = (a + ih_x, b + jh_y) : 0 \le i \le N, 0 \le j \le M\} \setminus \Omega_h,$$

where $h = (h_x, h_y)$ and, e.g., $h_x = (b - a)/(N + 1)$ is the mesh width in x-direction and $N + 1$ is the number of mesh points in x-direction. Next, we assume that the boundary $\partial\mathcal{S}$ of the set $\mathcal{S}$ can be represented as a closed polygon which is piecewise parallel with respect to the axes of the coordinate system. We discretize the set $\mathcal{S}$ by

$$\mathcal{S}_h \stackrel{def}{=} \Omega_h \cap \mathcal{S}$$

and denote its complement with respect to the mesh Ω_h by

$$\Omega_h^{\mathcal{S}} \stackrel{def}{=} \Omega_h \setminus \mathcal{S}_h.$$

Moreover, the boundary $\partial \mathcal{S}_h$ of $\mathcal{S}_h$ is defined by (cf. A.1.1)

$$\partial \mathcal{S}_h \stackrel{def}{=} \Omega_h \cap \partial \mathcal{S}.$$

The boundary conditions on the disjoint boundaries $\partial \Omega$ and $\partial \mathcal{S}$ requires the incorporation of their respective discretizations $\partial \Omega_h$ and $\partial \mathcal{S}_h$ into the mesh $\Omega_h^{\mathcal{S}}$. We define

$$\overline{\Omega}_h^{\mathcal{S}} \stackrel{def}{=} \Omega_h^{\mathcal{S}} \cup \partial \Omega_h,$$

$$\overline{\Omega_h^{\mathcal{S}}} \stackrel{def}{=} \Omega_h^{\mathcal{S}} \cup \partial \Omega_h \cup \partial \mathcal{S}_h.$$

In Figure A.1 we give a schematic representation of the mesh $\overline{\Omega_h^{\mathcal{S}}}$ and its disjoint boundaries $\partial \Omega_h$ and $\partial \mathcal{S}_h$.

Restrictions

For the proof of consistency and stability it is convenient to introduce an operator which restricts a continuous function onto the mesh $\Omega_h^{\mathcal{S}}$. Let $u : \mathbb{R}^2 \to \mathbb{R}$ then we define the restriction $R_h^{\mathcal{S}} : u \mapsto \mathbb{R}^{|\Omega_h^{\mathcal{S}}|}$ by

$$(R_h^{\mathcal{S}} u)(\mathbf{x}) \stackrel{def}{=} u(\mathbf{x}) \quad \forall \mathbf{x} \in \Omega_h^{\mathcal{S}}.$$

The restriction $\overline{R}_h^{\mathcal{S}}$ with respect to the mesh $\overline{\Omega}_h^{\mathcal{S}}$ and $\overline{R_h^{\mathcal{S}}}$ with respect to the mesh $\overline{\Omega_h^{\mathcal{S}}}$ is defined analogously. We call a function u_h a *mesh function* if u_h is only defined on a mesh.

Discretization Matrix and Elimination of Boundary Conditions

In the following, $D_h \in \mathbb{R}^{|\Omega_h^{\mathcal{S}}| \times |\overline{\Omega_h^{\mathcal{S}}}|}$ denotes the matrix which results from the discretization of the operator $\mathcal{L}_{bw}$ on the mesh $\Omega_h^{\mathcal{S}}$ under consideration of the mesh points in $\overline{\Omega_h^{\mathcal{S}}}$ where, e.g. $|\Omega_h^{\mathcal{S}}|$ is the number of mesh points in $\Omega_h^{\mathcal{S}}$. One option to deal with the Neumann boundary conditions on $\partial \Omega$ is their incorporation into the discretization stencils of the operator $\mathcal{L}_{bw}$ for mesh points in the direct vicinity of the boundary $\partial \Omega_h$. Since we deal here with homogeneous Neumann boundary conditions, we chose an alternative option. Here we discretize the Neumann conditions on $\partial \Omega_h$ explicitly and denote the resulting matrix by $N_h \in \mathbb{R}^{|\partial \Omega_h| \times |\overline{\Omega_h^{\mathcal{S}}}|}$. Combining both matrices in one matrix, we end up with

$$\overline{D}_h \stackrel{def}{=} \begin{pmatrix} D_h \\ N_h \end{pmatrix} \in \mathbb{R}^{|\overline{\Omega}_h^{\mathcal{S}}| \times |\overline{\Omega_h^{\mathcal{S}}}|}. \tag{A.4}$$

Let u_h be a mesh function on $\overline{\Omega_h^{\mathcal{S}}}$. If we apply the vector u_h on the matrix D_h, then the entry $(D_h u_h)(\mathbf{x})$ corresponding to a mesh point $\mathbf{x} \in \Omega_h^{\mathcal{S}}$ can be written as

$$(D_h u_h)(\mathbf{x}) = \sum_{\mathbf{y} \in \Omega_h^{\mathcal{S}}} D_h(\mathbf{x}, \mathbf{y}) u_h(\mathbf{y}) + \sum_{\mathbf{z} \in \partial \mathcal{S}_h} D_h(\mathbf{x}, \mathbf{z}) u(\mathbf{z}). \tag{A.5}$$

If we assume that $u_h(\mathbf{z}) = g_D(\mathbf{z})$ for all $\mathbf{z} \in \partial\Omega_h$, then (A.5) reduces to

$$(D_h u_h)(\mathbf{x}) = (L_h u_h)(\mathbf{x}) + \sum_{\mathbf{z} \in \partial\mathcal{S}_h} D_h(\mathbf{x}, \mathbf{z}) g_D(\mathbf{z}),$$

where $(L_h u_h)(x)$ is a compact notation for the first sum in (A.5). Finally, we can write the finite difference discretization of the mixed-boundary value problem (A.3) *after* elimination of the Dirichlet boundary conditions as the following linear system

$$\overline{L}_h u_h = \overline{F}_h,$$

where the matrix on the left hand side is defined by

$$\overline{L}_h \overset{def}{=} \begin{pmatrix} L_h \\ N_h \end{pmatrix} \in \mathbb{R}^{|\overline{\Omega}_h^{\mathcal{S}}| \times |\overline{\Omega}_h^{\mathcal{S}}|} \tag{A.6}$$

and for $\mathbf{x} \in \overline{\Omega}_h^{\mathcal{S}}$ the right hand side is given by

$$\overline{F}_h(\mathbf{x}) = \begin{cases} -\sum_{\mathbf{z} \in \partial\mathcal{S}_h} D_h(\mathbf{x}, \mathbf{z}) g_D(\mathbf{z}), & \text{if } \mathbf{x} \in \Omega_h^{\mathcal{S}} \\ 0, & \text{if } \mathbf{x} \in \partial\Omega_h. \end{cases}$$

A.1.2. Finite Difference Discretization of the Smoluchowski Committor Equation

In this section, we state a stable finite difference scheme of the committor equation for the Smoluchowski dynamics (2.37) on a two dimensional domain $\Omega \subset \mathbb{R}^2$. The associated mixed-boundary value problem (A.3) reduces to the problem

$$\begin{cases} \mathcal{L}_{bw} q = 0 & \text{in } \Omega_{\mathcal{S}} \\ q = g_D & \text{on } \partial\mathcal{S} \\ \dfrac{\partial q}{\partial \hat{n}} = 0 & \text{on } \partial\Omega, \end{cases} \tag{A.7}$$

where the operator $\mathcal{L}_{bw}$, given by

$$\mathcal{L}_{bw} q = \beta^{-1} \Delta q - \nabla V \cdot \nabla q$$

is an *elliptic* linear second order partial differential operator. Notice, that for the sake of simplicity, we set the friction matrix $\Gamma = \text{diag}(1,1) \in \mathbb{R}^{2 \times 2}$.

There is a long list of literature on stable finite difference discretization schemes of elliptic partial differential operators, e.g. [44, 42]. The discretization schemes we use here are standard schemes which are found in, e.g. [44].

Finite Difference Scheme

For notational simplicity, we henceforth assume that the mesh Ω_h is *total uniform*, i.e. $h_x = h_y$. Let $\mathbf{x} \in \Omega_h^{\mathcal{S}}$ then we discretize the elliptic operator $\mathcal{L}_{bw}$ in $\mathbf{x}$ by the 5-point stencil

$$\beta^{-1} h^{-2} \begin{bmatrix} 0 & 1 & 0 \\ 1 & -4 & 1 \\ 0 & 1 & 0 \end{bmatrix} + (2h)^{-1} \begin{bmatrix} 0 & v_2 & 0 \\ -v_1 & 0 & v_1 \\ 0 & -v_2 & 0 \end{bmatrix}, \tag{A.8}$$

where we set $(v_1, v_2) = -\nabla V(\mathbf{x})$ and $h = h_x = h_y$. The stencil (A.8) leads to a consistent scheme of second order, i.e. for a function $u \in C^2(\Omega)$ we have

$$\left\| D_h \overline{R_h^\mathcal{S}} u - R_h^\mathcal{S} \mathcal{L}_{bw} u \right\|_\infty = \mathcal{O}(h^2). \tag{A.9}$$

For reasons of stability, we have to ensure that all off-diagonal entries in the resulting discretization matrix L_h are non-negative. This leads to a condition on the mesh width h, namely

$$h < 2\beta^{-1} \left(\max_{\mathbf{x} \in \Omega_h^\mathcal{S}} \{ |v_1|, |v_2| : (v_1, v_2) = -\nabla V(\mathbf{x}) \} \right)^{-1}. \tag{A.10}$$

We discretize the Neumann conditions on $\partial\Omega$ explicitly by a single sided difference scheme. For example, consider a mesh point $\mathbf{x} = (x, y) \in \partial\Omega_h$ on the left boundary, i.e. the piece of the boundary $\partial\Omega$ which confines the rectangular domain Ω from the left and let $\hat{n}(x, y) \equiv (-1, 0)$ be the corresponding unit normal vector pointing outward Ω. To ensure the M-matrix property and without lack of generality, we discretize the Neumann conditions in the boundary mesh point $\mathbf{x} = (x, y)$ by

$$\frac{\partial}{\partial \hat{n}(x, y)} q(x, y) = 0 \rightsquigarrow h^{-1}(q(x - h, y) - q(x, y)) = 0$$

which is represented by the stencil

$$h^{-1} \begin{bmatrix} 0 & 0 & 0 \\ 1 & -1 & 0 \\ 0 & 0 & 0 \end{bmatrix}. \tag{A.11}$$

The stencils for the right, upper and lower boundaries are derived analogously. Notice that the stencils in the corners result from the combination of the stencils of the two adjacent boundaries. For example, for the upper-right corner the stencil takes the form

$$h^{-1} \begin{bmatrix} 0 & 0 & 0 \\ 1 & -2 & 0 \\ 0 & 1 & 0 \end{bmatrix}. \tag{A.12}$$

Properties of the Discretization Matrix

As a preparation for the proof of stability, we show that the discretization matrix $\overline{L}_h$ (after elimination of the Dirichlet boundary conditions) is up to its sign an M-matrix. To be more precise, the following properties hold for the matrix $-\overline{L}_h$:

1. For a mesh point $\mathbf{x} \in \Omega_h^\mathcal{S}$ in the direct vicinity of the boundary $\partial\mathcal{S}_h$ the following strict inequality holds

$$|\overline{L}_h(\mathbf{x}, \mathbf{x})| > \sum_{\substack{\mathbf{y} \in \Omega_h^\mathcal{S} \\ \mathbf{y} \neq \mathbf{x}}} |\overline{L}_h(\mathbf{x}, \mathbf{y})|.$$

A. Appendix

2. The entries of the matrix $-\overline{L}_h$ satisfy the following sign conditions

$$-\overline{L}_h(\mathbf{x}, \mathbf{x}) > 0, \quad \forall \mathbf{x} \in \Omega_h^{\mathcal{S}},$$
$$-\overline{L}_h(\mathbf{x}, \mathbf{y}) \leq 0, \quad \forall \mathbf{x}, \mathbf{y} \in \Omega_h^{\mathcal{S}}, \mathbf{x} \neq \mathbf{y}. \tag{A.13}$$

   which immediately follow from the discretization schemes (A.8) and (A.11).

3. Under the assumption that $\Omega \setminus (A \cup B)$ is connected, the matrix $-\overline{L}_h$ is essentially diagonally dominant.

Finally, from Theorem (A.6.6) it follows that the matrix $-\overline{L}_h$ is an M-matrix and in particular invertible.

Proof of Stability

To prove that our scheme is stable, we have to show

$$\sup_{h>0} \left\| \overline{L}_h^{-1} \right\|_\infty < \infty.$$

To be more precise, we have to show that there exists a constant $C > 0$ and a sufficiently small $h_0 > 0$ such that

$$\left\| L_h^{-1} \right\|_\infty \leq C, \quad \forall h \in (0, h_0). \tag{A.14}$$

The idea of the proof is to find a function $s \in C^2(\Omega) \cap C^1(\overline{\Omega})$ and a sufficiently small $h_0 > 0$ such that we have

$$(-\overline{L}_h \overline{R}_h^{\mathcal{S}} s)(\mathbf{x}) \geq 1, \quad \forall \mathbf{x} \in \overline{\Omega}_h^{\mathcal{S}}, \forall h \in (0, h_0). \tag{A.15}$$

Then by virtue of Theorem A.6.7 we deduce the desired result (A.14).

In the case of a pure elliptic Dirichlet boundary value problem, one can state explicitly a function $s(x)$ which leads to (A.15) (see [44], Theorem 5.1.9.). Unfortunately, in our case of the mixed-boundary value problem (A.7) we cannot state such a function explicitly. Instead, we consider the following auxiliary mixed-boundary value problem

$$\begin{cases} \mathcal{L}_{bw} s = -1 & \text{in } \Omega_{\mathcal{S}} \\ s = 0 & \text{on } \partial\mathcal{S} \\ \dfrac{\partial s}{\partial \hat{n}} = -1 & \text{on } \partial\Omega, \end{cases} \tag{A.16}$$

where the operator $\mathcal{L}_{bw}$ is again the generator of the Smoluchowski dynamics and we show that a solution $s(x) \in C^2(\Omega) \cap C^1(\overline{\Omega})$ of (A.16) is the right candidate to deduce (A.15). For an interpretation of the solution of (A.16) see Remark A.1.2.

Theorem A.1.1. *The discretization scheme (A.8) and (A.11) is stable. The stability constant is given by*

$$C = 2 \max_{x \in \overline{\Omega} \setminus \mathcal{S}} \{|s(x)|\},$$

where the function $s(x)$ is the solution of the problem (A.16).

Proof. Let $s(x) \in C^2(\Omega) \cap C^1(\overline{\Omega})$ be the solution of the stability equation (A.16). We define the auxiliary mesh function $u_h = 2\overline{R_h^{\mathcal{S}}}s$ and we deduce

$$-D_h u_h = -2(D_h \overline{R_h^{\mathcal{S}}}s - R_h^{\mathcal{S}}\mathcal{L}_{bw}s) - 2R_h^{\mathcal{S}}\mathcal{L}_{bw}s$$
$$= 2 - 2(D_h \overline{R_h^{\mathcal{S}}}s - R_h^{\mathcal{S}}\mathcal{L}_{bw}s)$$

From the consistency of our scheme follows that there exists an $h_0 > 0$ such that

$$\left\| D_h \overline{R_h^{\mathcal{S}}}s - R_h^{\mathcal{S}}\mathcal{L}_{bw}s \right\|_\infty < \frac{1}{2}, \quad \forall h \in (0, h_0)$$

and we deduce

$$(-D_h u_h)(\mathbf{x}) \geq 1, \quad \forall \mathbf{x} \in \Omega_h^{\mathcal{S}}, \quad \forall h \in (0, h_0).$$

But this immediately implies

$$(-\overline{L}_h u_h)(\mathbf{x}) \geq 1, \quad \forall h \in (0, h_0)$$

for any mesh point $\mathbf{x} \in \Omega_h^{\mathcal{S}}$ which is not in the direct vicinity of the boundary $\partial A_h \cup \partial B_h$. Next, consider a mesh point $\mathbf{x} \in \Omega_h^{\mathcal{S}}$ which is in the direct vicinity of the boundary $\partial A_h \cup \partial B_h$. But since the function $s(\mathbf{x})$ is equal to zero on the boundary of the set $\mathcal{S}$ we have

$$\sum_{\mathbf{y} \in (\partial S_h)} D_h(\mathbf{x}, \mathbf{y}) u_h(\mathbf{y}) = 0$$

and, thus, we finally obtain

$$(-\overline{L}_h u_h)(\mathbf{x}) = (-L_h u_h)(\mathbf{x}) \geq 1 \quad \forall \mathbf{x} \in \Omega_h^{\mathcal{S}}, \forall h \in (0, h_0). \qquad (A.17)$$

It remains to show that $(A.17)$ also holds true for mesh points on the boundary $\partial\Omega_h$. But since the matrix N_h results from the consistent discretization of the Neumann condition, the same reasoning as above yields that there exists an $\tilde{h}_0 > 0$ such that

$$(-\overline{L}_h u_h)(\mathbf{x}) = -(N_h u_h)(\mathbf{x}) \geq 1 \quad \forall \mathbf{x} \in \partial\Omega_h, \forall h \in (0, \tilde{h}_0).$$

All together we have shown that

$$(-\overline{L}_h u_h)(\mathbf{x}) \geq 1 \quad \forall \mathbf{x} \in \overline{\Omega}_h^{\mathcal{S}}, 0 < h < \min\{h_0, \tilde{h}_0\}$$

and by Theorem (A.6.7) we obtain

$$\left\| \overline{L}_h^{-1} \right\|_\infty \leq \|u_h\|_\infty \leq 2 \max_{x \in \overline{\Omega}\backslash\mathcal{S}} \{|s(x)|\} < \infty, \quad 0 < h < \min\{h_0, \tilde{h}_0\}.$$

$\square$

Remark A.1.2. *The stability equation (A.16) admits a partial interpretation if one realizes that its solution $s(x)$ can be decomposed such that*

$$s(x) = s_1(x) + s_2(x),$$
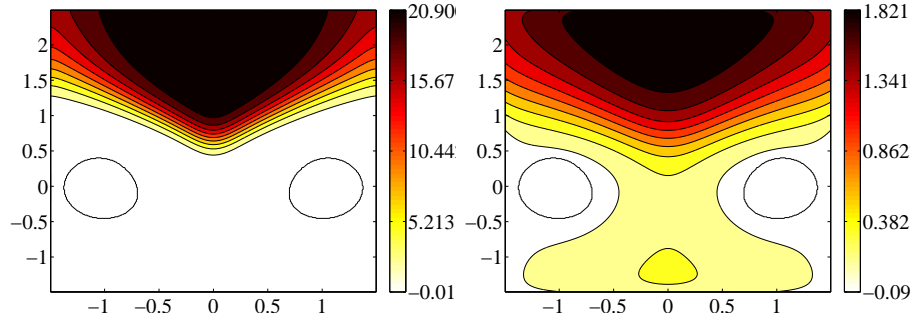
Figure A.2.: Contour plot of the numerical solution $|s(x)|$ of the mixed-boundary value problem (A.16) for the Smoluchowski dynamics in the three-hole potential (given in (3.45)) for a low temperature $\beta = 6.67$ (left panel) and for a high temperature $\beta = 1.67$ (right panel).

where the function s_1 is the solution of the problem

$$\begin{cases} \mathcal{L}_{bw} s_1 = -1 & in\ \Omega_\mathcal{S} \\ s_1 = 0 & on\ \partial\mathcal{S} \\ \dfrac{\partial s_1}{\partial \hat{n}} = 0 & on\ \partial\Omega \end{cases} \tag{A.18}$$

and the function $s_2(x)$ satisfies

$$\begin{cases} \mathcal{L}_{bw} s_2 = 0 & in\ \Omega_\mathcal{S} \\ s_2 = 0 & on\ \partial\mathcal{S} \\ \dfrac{\partial s_2}{\partial \hat{n}} = -1 & on\ \partial\Omega. \end{cases} \tag{A.19}$$

*As shown in Remark (3.1.2), the function $s_1(x)$ is the **mean first passage time** of the Smoluchowski dynamics (2.37) with respect to the set $A \cup B$. In Figure A.2 we show the contour plot of the numerical solution $s(x)$ of the equation in (A.16) for the Smoluchowski dynamics in the three-hole potential (3.45) (see section (3.7.1)) for two different temperatures.*

Proof of Convergence

For the convenience of the reader, we state the proof that our scheme converges which, as usual, follows from the consistency and stability.

Theorem A.1.2. *Let u be the exact solution of the mixed-boundary value problem (A.7) and let $\overline{u}_h$ denote the approximated solution computed via $\overline{u}_h = \overline{L}_h^{-1}\overline{F}_h$. Then we have*

$$\lim_{h \to 0} \left\| \overline{u}_h - \overline{R}_h^\mathcal{S} u \right\|_\infty = 0$$

Proof. Let $\tilde{u}_h$ be the extension of the mesh function $\overline{u}_h$ on the boundary of $\mathcal{S}$, that is

$$\tilde{u}_h(\mathbf{x}) \stackrel{def}{=} \begin{cases} \overline{u}_h(\mathbf{x}), & \text{if } \mathbf{x} \in \overline{\Omega}_h^\mathcal{S} \\ g_D(\mathbf{x}), & \text{if } \mathbf{x} \in \partial\mathcal{S}_h \end{cases}$$

Next, we define the auxiliary mesh function $w_h = \tilde{u}_h - \overline{R_h^{\mathcal{S}}}u$ and deduce

$$\overline{D}_h w_h = \overline{L}_h(\overline{u}_h - \overline{R}_h^{\mathcal{S}}u)$$

because of $w_h(\mathbf{x}) = 0$ on the boundary of $\mathcal{S}$. Now we can estimate the cut-off error by

$$
\begin{aligned}
\left\|\overline{u}_h - \overline{R}_h^{\mathcal{S}}u\right\|_\infty &= \left\|\overline{L}_h^{-1}\overline{D}_h w_h\right\|_\infty \\
&\leq \left\|\overline{L}_h^{-1}\right\|_\infty \cdot \left\|\overline{D}_h(\tilde{u}_h - \overline{R_h^{\mathcal{S}}}u)\right\|_\infty \\
&\leq C \cdot \max\{\left\|D_h\tilde{u}_h - D_h\overline{R_h^{\mathcal{S}}}u\right\|_\infty, \left\|N_h\tilde{u}_h - N_h\overline{R_h^{\mathcal{S}}}u\right\|_\infty\},
\end{aligned}
$$

where the last inequality follows from the stability of the scheme and the definition of the matrix $\overline{D}_h$ (cf. (A.4)). Now observe that

$$(D_h\tilde{u}_h)(\mathbf{x}) = (R_h^{\mathcal{S}}\mathcal{L}_{bw}u)(\mathbf{x}) \qquad \forall \mathbf{x} \in \Omega_h^{\mathcal{S}},$$

$$(N_h\tilde{u}_h)(\mathbf{x}) = (\overline{R}_h^{\mathcal{S}}\frac{\partial u}{\partial \hat{n}})(\mathbf{x}) \qquad \forall \mathbf{x} \in \partial\Omega_h,$$

and, hence, since the schemes are consistent, we finally get

$$\left\|\overline{u}_h - \overline{R}_h^{\mathcal{S}}u\right\|_\infty \longrightarrow 0 \text{ as } h \to 0$$

which completes the proof. □

A.1.3. Finite Difference Discretization of the Langevin Committor Equation

In this section we derive a stable finite difference scheme of the forward committor equation for the Langevin dynamics (2.33) on a two dimensional domain $\Omega \subset \mathbb{R}^2$. For the sake of simplicity, we set the mass equal to one ($m_1 = 1$) and consider the velocity instead of the momentum. The mixed-boundary value problem (A.3) reduces to the problem

$$
\begin{cases}
\mathfrak{L}_{bw}q = 0 & \text{in } \Omega^{\mathcal{S}} = \Omega \setminus \mathcal{S} \\
q = g_D & \text{on } \partial\mathcal{S} \\
\nabla q \cdot a\hat{n} = 0 & \text{on } \partial\Omega,
\end{cases}
\qquad (A.20)
$$

where the operator $\mathfrak{L}_{bw}$, given by

$$\mathfrak{L}_{bw}q = \gamma\beta^{-1}\Delta_v q + v \cdot \nabla_x q - \nabla_x V \cdot \nabla_v q - \gamma v \cdot \nabla_v q, \qquad (A.21)$$

is a degenerate elliptic linear second order partial differential operator.

In contrast to the Smoluchowski dynamics where the involved operator is elliptic, here the degenerate ellipticity of $\mathfrak{L}_{bw}$ imposes geometric restrictions of the domain Ω. Recalling that the diffusion matrix for the Langevin dynamics on a two-dimensional phase space is given by

$$a = \beta^{-1}\gamma \begin{pmatrix} 0 & 0 \\ 0 & 1 \end{pmatrix} \in \mathbb{R}^{2\times 2},$$

A. Appendix

the Neumann conditions for the forward committor function $q(x, v)$ in a boundary point $(x, v) \in \partial\Omega$ reduces to

$$0 = \nabla q(x, v) \cdot a\hat{n} = \frac{dq(x, v)}{dv}\hat{n}_v,$$

where $\hat{n} = (\hat{n}_x, \hat{n}_v)^T$ is the unit normal in $(x, v) \in \partial\Omega$ pointing outward Ω. But this immediately implies that if the shape of boundary in the (x, v) was such that $\hat{n}_v = 0$ then this would lead to an empty boundary condition in that point and the resulting linear system would be under-determined. Consequently, any domain Ω whose boundary consists of pieces which are parallel to the v-axis is inappropriate for the finite difference discretization. Furthermore, in order to be able to impose the Dirichlet boundary conditions on ∂A and ∂B, the unit normal to these sets at (x, v) must span the velocity degrees of freedom everywhere except maybe on a set of zero measure on ∂A and ∂B. One option could be to change the shape the domain and the sets A and B such that their boundaries are not piecewise parallel to the v-axis. But this option would lead to complicated finite difference schemes for the boundary conditions and, hence, it seems not practical.

As a remedy, we introduce a coordinate transformation such that

1. the transformed Langevin dynamics exhibits diffusion in *all* new coordinates,

2. the Neumann boundary conditions for a rectangular domain in the new coordinate system lead to non-empty conditions on the committor function.

To this end, we rotate the coordinate system by $\pi/4$ which can formally be done by introducing the transformation $T : (x, v) \mapsto (\eta(x, v), \xi(x, v))$ with

$$\begin{cases} \eta(x, v) = c(x - v), \\ \xi(x, v) = c(x + v), \quad c = \sqrt{2}/2. \end{cases} \tag{A.22}$$

Then the Langevin dynamics in the new coordinates (η, ξ) takes the form

$$\begin{cases} d\eta = \quad c^2(\xi - \eta)(1 + \gamma) + c\nabla_x V\left(c(\eta + \xi)\right) - c\sqrt{2\gamma\beta^{-1}}\ dW_t \\ d\xi = \quad c^2(\xi - \eta)(1 - \gamma) - c\nabla_x V\left(c(\eta + \xi)\right) + c\sqrt{2\gamma\beta^{-1}}\ dW_t \end{cases} \tag{A.23}$$

where W_t is a 1-dimensional Wiener process and affects both coordinates simultaneously. Now notice that the transformed dynamics (A.23) can be written in the shape of (2.8) by setting

$$\mathbf{b}(\eta, \xi) \quad = \begin{pmatrix} c^2(\xi - \eta)(1 + \gamma) + c\nabla_x V(c(\eta + \xi)) \\ c^2(\xi - \eta)(1 - \gamma) - c\nabla_x V(c(\eta + \xi)) \end{pmatrix}, \quad c = \sqrt{2}/2 \tag{A.24}$$

and

$$\sigma \quad = c\sqrt{2\gamma\beta^{-1}} \begin{pmatrix} 0 & -1 \\ 0 & 1 \end{pmatrix}.$$

The generator $\mathfrak{L}_{bw}$ of the transformed Langevin dynamics (A.23) is given by

$$\mathfrak{L}_{bw} u(\eta, \xi) = \mathbf{a} : \nabla\nabla u(\eta, \xi) + \mathbf{b}(\eta, \xi) \cdot \nabla u(\eta, \xi) \tag{A.25}$$

with the diffusion matrix

$$\mathbf{a} \;=\; c^2\gamma\beta^{-1}\begin{pmatrix} 1 & -1 \\ -1 & 1 \end{pmatrix}.$$

Notice that here $\nabla = (\nabla_\eta, \nabla_\xi)$. Finally, we end up with the mixed-boundary value problem in the new coordinates, that is

$$\begin{cases} \mathfrak{L}_{bw}q = 0 & \text{in } T(\Omega)\setminus T(\mathcal{S}) \\ q = \tilde{g}_D & \text{on } \partial T(\mathcal{S}) \\ \nabla q \cdot \mathbf{a}\hat{n} = 0 & \text{on } \partial T(\Omega) \end{cases} \qquad (A.26)$$

where $\tilde{g}_D(x) = g_D(T^{-1}(x))$.

The same reasoning as above leads to the mixed-boundary value problem associated with the backward committor equation

$$\begin{cases} \mathfrak{L}^R_{bw}q_b = \mathbf{a} : \nabla\nabla q_b + \mathbf{b}^R \cdot \nabla q_b = 0 & \text{in } T(\Omega)\setminus T(\mathcal{S}) \\ q_b = 1 - \tilde{g}_D & \text{on } \partial T(\mathcal{S}) \\ \nabla q_b \cdot \mathbf{a}\hat{n} = 0 & \text{on } \partial T(\Omega), \end{cases} \qquad (A.27)$$

where the reversed drift field $\mathbf{b}^R(\eta,\xi)$ is given by

$$\mathbf{b}^R(\eta,\xi) \;=\; -\begin{pmatrix} c^2(\xi-\eta)(1-\gamma) + c\nabla_x V(c(\eta+\xi)) \\ c^2(\xi-\eta)(1+\gamma) - c\nabla_x V(c(\eta+\xi)) \end{pmatrix}, \quad c = \sqrt{2}/2. \quad (A.28)$$

Remark A.1.3. *In order to keep the notation simple, we do not introduce a new symbol for the transformed domain $T(\Omega)$ as well as for $T(S)$. In what follows, Ω and $\mathcal{S}$ are sets with respect to the new coordinate system. Moreover, instead of solving the problem (A.26) on the transformed domain, we choose a rectangular domain in the new coordinate system and after solving the problem we transform back the resulting solution into the original coordinate system.*

Discretization Scheme

In this section we derive a stable 7-point discretization scheme for the transformed forward committor equation (A.26). The scheme for the transformed backward committor equation follows analogously. Again, the transformed principle part as well as the transformed drift field are discretized by standard schemes which are found in [44]. The key observation in the derivation of the scheme is that we can decompose the transformed drift field such that the M-matrix property of the resulting discretization matrix is achieved.

Discretization of the principle part Without loss of generality, the principle part of (A.25) can be written as

$$\mathbf{a} : \nabla\nabla q = c^2\gamma\beta^{-1}\left(\Delta q - 2\frac{\partial^2 q}{\partial\eta\partial\xi}\right). \qquad (A.29)$$

In contrast to the elliptic case, here we additionally have to deal with a mixed-derivative part. The discretization is done by utilizing again a standard scheme (see

A. Appendix

[44], page 91). Unlike to the elliptic case, here it is necessary that the mesh Ω_h is total uniform, i.e.

$$h_\eta = h_\xi \overset{def}{=} h, \tag{A.30}$$

where h_η is the mesh width of Ω_h in η-direction and h_ξ the mesh width in η-direction. Doing so, we have

$$\frac{\partial^2}{\partial\eta\partial\xi} \rightsquigarrow \frac{1}{2}h^{-2}\begin{pmatrix} 1 & -1 & 0 \\ -1 & 2 & -1 \\ 0 & -1 & 1 \end{pmatrix}.$$

Together with the 5-point stencil for the Laplace operator (cf. (A.8)) we end up with a 3-point stencil for the principle part:

$$c^2\gamma\beta^{-1}(\Delta - 2\frac{\partial^2}{\partial\eta\partial\xi}) \rightsquigarrow c^2\gamma\beta^{-1}h^{-2}\begin{pmatrix} 1 & 0 & 0 \\ 0 & -2 & 0 \\ 0 & 0 & 1 \end{pmatrix}. \tag{A.31}$$

Discretization of the drift part   In order to ensure invertibility of the final discretization matrix $\mathbf{L_h}$ we decompose the transformed drift field $\mathbf{b}(\eta,\xi) = \mathbf{b}^1(\eta,\xi) + \mathbf{b}^2(\eta,\xi) + \mathbf{b}^3(\eta,\xi)$ according to

$$\mathbf{b}(\eta,\xi) = \underbrace{\frac{\xi-\eta}{2}\begin{pmatrix} 0 \\ 1 \end{pmatrix}}_{=\mathbf{b}^1(\eta,\xi)} + \underbrace{\frac{\xi-\eta}{2}\begin{pmatrix} 1+\gamma \\ -\gamma \end{pmatrix}}_{=\mathbf{b}^2(\eta,\xi)} + \underbrace{c\begin{pmatrix} \nabla_x V(c(\eta+\xi)) \\ -\nabla_x V(c(\eta+\xi)) \end{pmatrix}}_{=\mathbf{b}^3(\eta,\xi)} \tag{A.32}$$

and separately discretize the vector fields $\mathbf{b}^1, \mathbf{b}^2$ and $\mathbf{b}^3$ by means of the first-order standard stencil

$$h^{-1}\begin{bmatrix} 0 & b_{i2}^+ & 0 \\ -b_{i1}^- & -|b_1^i| - |b_2^i| & b_{i1}^+ \\ 0 & -b_{i2}^- & 0 \end{bmatrix},$$

where we set $b_{ij}^+ = max\{\mathbf{b}_j^i, 0\}$, $b_{ij}^- = min\{\mathbf{b}_j^i, 0\}$ and $\mathbf{b}_j^i$ is the jth component of the drift field $\mathbf{b}^i = (\mathbf{b}_1^i, \mathbf{b}_2^i)^T$ evaluated in a mesh point. Combining the resulting three stencils in one, we end up with a 5-point stencil for the drift part

$$h^{-1}\begin{pmatrix} 0 & b_{12}^+ + b_{22}^+ + b_{32}^+ & 0 \\ -b_{11}^- - b_{21}^- - b_{31}^- & -[\sum_{i=1}^3\sum_{j=1}^2 |\mathbf{b}_j^i|] & b_{11}^+ + b_{21}^+ + b_{31}^+ \\ 0 & -b_{12}^- - b_{22}^- - b_{32}^- & 0 \end{pmatrix}. \tag{A.33}$$

Discretization of the Neumann-like boundary conditions   We exemplify the derivation of the Neumann-like boundary condition (A.2) in a mesh point on the right boundary. Let $\mathbf{x} = (\eta,\xi) \in \partial\Omega_h$ be a mesh point on the right boundary and $\hat{n} = (1,0)^T$ the corresponding unit normal vector. The boundary condition (A.2) reduces to

$$0 = \nabla u(\mathbf{x}) \cdot \mathbf{a}\hat{n} = \frac{\partial u(\mathbf{x})}{\partial\eta} - \frac{\partial u(\mathbf{x})}{\partial\xi}$$

which is consistently discretized by the scheme

$$0 = h^{-1}[u(\eta-h,\xi) - u(\eta,\xi)] + h^{-1}[u(\eta,\xi) - u(\eta,\xi+h)].$$

The derivation of the schemes for the left, upper and lower boundary are analogously. Eventually, we end up with the following stencils for the right and left boundary

$$
h^{-1}\begin{bmatrix} 0 & 1 & 0 \\ 1 & -2 & 0 \\ 0 & 0 & 0 \end{bmatrix}, h^{-1}\begin{bmatrix} 0 & 0 & 0 \\ 0 & -2 & 1 \\ 0 & 1 & 0 \end{bmatrix} \tag{A.34}
$$

and for the lower and upper boundary

$$
h^{-1}\begin{bmatrix} 0 & 1 & 0 \\ 1 & -2 & 0 \\ 0 & 0 & 0 \end{bmatrix}, h^{-1}\begin{bmatrix} 0 & 0 & 0 \\ 0 & -2 & 1 \\ 0 & 1 & 0 \end{bmatrix}. \tag{A.35}
$$

Finally, we state the discretization stencils for the corners. Since the mesh is total uniform, we can simply use the following stencils for the top-left and the bottom-right corner:

$$
h^{-1}\begin{bmatrix} 0 & 0 & 0 \\ 0 & -1 & 0 \\ 0 & 0 & 1 \end{bmatrix}, h^{-1}\begin{bmatrix} 1 & 0 & 0 \\ 0 & -1 & 0 \\ 0 & 0 & 0 \end{bmatrix}. \tag{A.36}
$$

Unfortunately, we cannot simply apply one of the above schemes in the bottom-left and top right corner of the rectangular mesh Ω_h but the boundary condition (A.2) in a corner $\mathbf{x}_c \in \Omega_h$ is in particular satisfied if

$$
0 = \frac{\partial u(\mathbf{x}_c)}{\partial \eta} = \frac{\partial u(\mathbf{x}_c)}{\partial \xi}.
$$

The stencils for these relaxed boundary conditions in the bottom-left and top-right corner then take the form

$$
h^{-1}\begin{bmatrix} 0 & 1 & 0 \\ 0 & -2 & 1 \\ 0 & 0 & 0 \end{bmatrix}, h^{-1}\begin{bmatrix} 0 & 0 & 0 \\ 1 & -2 & 0 \\ 0 & 1 & 0 \end{bmatrix}. \tag{A.37}
$$

Discretization matrix   Like in the elliptic case, we discretize the operator $\mathfrak{L}_{\mathbf{bw}}$ *on* $\overline{\Omega}_h^{\mathcal{S}}$ *in* $\overline{\Omega}_h^{\mathcal{S}}$ (cf. Sect. A.1.1) and denote the resulting discretization matrix by D_h. The combination of D_h with the matrix N_h which results from the explicit discretization of Neumann conditions is denoted by $\overline{D}_h$. Finally, the elimination of the Dirichlet condition leads to the matrix $\overline{L}_h$.

M-matrix property   In this section it is convenient to use the notation introduced in Section A.6. In the elliptic case, the irreducibility of the matrix $\overline{L}_h$ is a direct consequence of the symmetry of the discretization stencils (cf. (A.8)). Here, the irreducibility of $\overline{L}_h$ follows from the special decomposition of the transformed vector field in (A.32).

For the sake of a compact notation, we define for a mesh point $\mathbf{z} = (z_1, z_2) \in \Omega_h$ a *diagonal* by

$$
\mathcal{D}_{\mathbf{z}} = \overline{\Omega}_h \cap \{\mathbf{z} + \alpha \begin{pmatrix} -1 \\ 1 \end{pmatrix} : \alpha \in \mathbb{R}\}.
$$
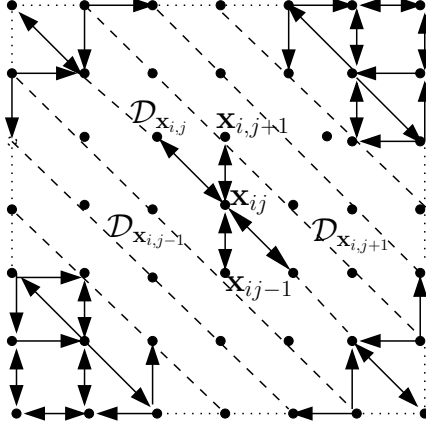
Figure A.3.: Schematic representation of the graph induced by the discretization stencils in (A.31), (A.33) and in (A.34)-(A.37). The diffusion stencil (A.31) ensures the connection of all mesh points lying on the same diagonal whereas the connection among diagonals in the direct vicinity is guaranteed by the stencil in (A.33) via Lemma A.1.4.

A first observation is that the diffusion stencil (A.31) guarantees the mutually connection of all mesh points lying on the same diagonal.

Furthermore, we can prove that diagonals in the direct vicinity to each other are connected too.

Lemma A.1.4. *Let* $\mathbf{x}_{i,j} = (\eta_0 + ih, \xi_0 + jh) \in \overline{\Omega}_h^{\mathcal{S}}$ *be a mesh point. Then the diagonal* $\mathcal{D}_{\mathbf{x}_{i,j}}$ *is connected at least with one of the diagonals* $\mathcal{D}_{\mathbf{x}_{i,j+1}}$ *and* $\mathcal{D}_{\mathbf{x}_{i,j-1}}$. *If* $\mathbf{x}_{i,j} \in \Omega_h^{\mathcal{S}}$ *then* $\mathcal{D}_{\mathbf{x}_{i,j}}$ *is connected with both.*

Proof. Let $\mathbf{x}_{i,j} \in \Omega_h$ and, firstly, assume that neither $\mathbf{x}_{i,j+1}$ nor $\mathbf{x}_{i,j-1}$ lies on the boundary $\partial\Omega_h$ and that $\eta_i \neq \xi_j$. Consider the vector field decomposition in (A.32) and the stencil given in (A.33); provided that $\gamma > 0$ we deduce

$$\mathbf{b}_{12} \neq 0 \Leftrightarrow -\gamma \frac{\eta_i - \xi_j}{2} \neq 0 \Leftrightarrow \mathbf{b}_{22} \neq 0.$$

But this immediately implies that either

$$\mathbf{b}_{12}^+ \neq 0 \text{ and } \mathbf{b}_{22}^- \neq 0 \quad \text{or} \quad \mathbf{b}_{12}^- \neq 0 \text{ and } \mathbf{b}_{22}^+ \neq 0$$

holds true and, hence, $\mathbf{x}_{i,j}$ is directly connected with $\mathbf{x}_{i,j-1}$ and $\mathbf{x}_{i,j+1}$, respectively.

Next, let $\mathbf{x}_{i,j} \in \partial\Omega_h$. The stencils in (A.34) and (A.34) for the discretization of the Neumann-like condition show that $\mathbf{x}_{i,j}$ is directly connected to a mesh point in Ω_h and hence $\mathcal{D}_{\mathbf{x}_{i,j}}$ is connected at least with one of the diagonals $\mathcal{D}_{\mathbf{x}_{i,j+1}}$ and $\mathcal{D}_{\mathbf{x}_{i,j-1}}$. The same reasoning holds true for the corners. $\qquad\square$

For a schematic representation of the connectivity of diagonals induced by the discretization matrix $\overline{L}_h$ see Figure A.3. Now we are prepared to prove

Lemma A.1.5. *The matrix* $-\overline{L}_h$ *is an M-matrix.*

Proof. The matrix $-\overline{L}_h$ satisfies the sign conditions (A.60) and (A.61) and for every mesh point in the direct vicinity of $\partial A_h \cup \partial B_h$ we have

$$|\overline{L}_h(\mathbf{x}, \mathbf{x})| > \sum_{\mathbf{y} \neq \mathbf{x}} |\overline{L}_h(\mathbf{x}, \mathbf{y})|. \tag{A.38}$$

But from the connectivity within the diagonals, by Lemma A.1.4 and the discretization of the Neumann-like boundary conditions it immediately follows that for every mesh point $\mathbf{z} \in \overline{\Omega}_h^{\mathcal{S}}$ we can find a directed path $p = (\mathbf{z} = \mathbf{x}_0, \ldots, \mathbf{x}_n)$, $\mathbf{x}_0, \ldots, \mathbf{x}_n \in \overline{\Omega}_h^{\mathcal{S}}$ in the graph associated with $\overline{L}_h$ to an $\mathbf{x}_n$ which satisfies the inequality in (A.38). For schematic presentation of the associated graph see Figure A.3. This proves that $-\overline{L}_h$ is essentially diagonally dominant and, finally, by virtue of Theorem A.6.6 we are done. □

Stability and Convergence

The proof that the discretization scheme for the Langevin committor equation is stable as well as the proof of convergence is analogously to the proof for the Smoluchowski case, given in Section A.1.2 and Section A.1.2 because we only exploited the M-matrix property of the discretization matrix and the consistency of the schemes.
   We summarize both results in

Theorem A.1.3. *The discretization scheme resulting from (A.31),(A.33) together with the stencils in (A.34)-(A.37) is stable. The stability constant is given by*

$$C = 2 \max_{\mathbf{x} \in \overline{\Omega} \setminus \mathcal{S}} \{|s(\mathbf{x})|\},$$

where the function $s(x) \in C^2(\Omega) \cap C^1(\overline{\Omega})$ is the solution of the auxiliary mixed-boundary value problem

$$\begin{cases} \mathfrak{L}_{bw}s = -1 & \text{in } \Omega \setminus \mathcal{S} \\ s = 0 & \text{on } \partial\mathcal{S} \\ \nabla s \cdot \mathbf{a}\hat{n} = -1 & \text{on } \partial\Omega. \end{cases} \tag{A.39}$$

Let u be the analytical solution of the mixed-boundary value problem (A.26) and let $\overline{u}_h = \overline{L}_h^{-1}\overline{F}_h$ denote the approximated solution with respect to the total uniform mesh width h. Then we have

$$\lim_{h \to 0} \left\| \overline{u}_h - \overline{R}_h^{\mathcal{S}} u \right\|_{\infty} = 0.$$

A.2. Weak Formulation for the Elliptic Mixed-Boundary Value Problem

In this section we will derive a weak formulation of the elliptic mixed-boundary value problem

$$\begin{cases} \beta^{-1}\Delta u + \nabla V \cdot \nabla u = f & \text{in } \Omega_{\mathcal{S}} \stackrel{def}{=} \Omega \setminus \mathcal{S} \\ u = g_D & \text{on } \partial\mathcal{S} \\ \dfrac{\partial u}{\partial \hat{n}} = g_N & \text{on } \partial\Omega \end{cases} \tag{A.40}$$
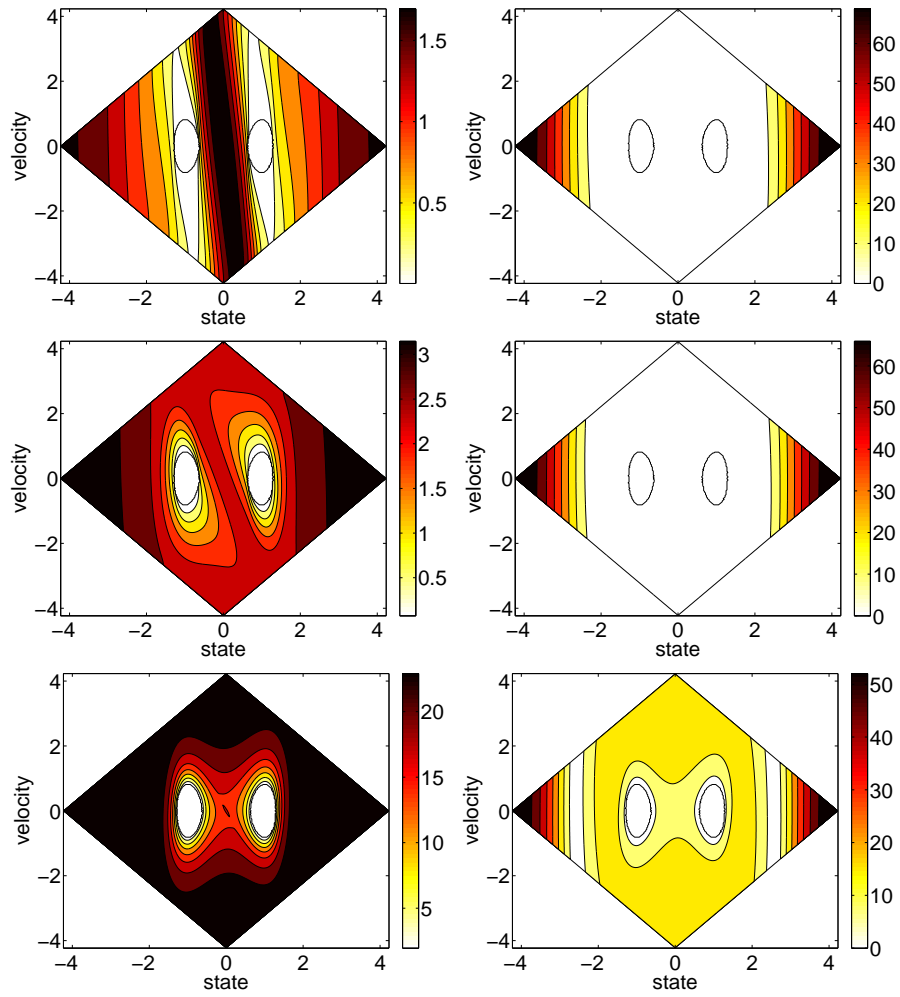
Figure A.4.: Contour plots of solutions of the mean first passage times equation (3.10) with respect to the set $\mathcal{S} = A \cup B$ (first column) and solutions $|s(x)|$ of the auxiliary problem in (A.39) (second column). Results for constant temperature $\beta = 1$ and for three different friction constants: from top to bottom: $\gamma = 10$, $\gamma = 1$ and $\gamma = 0.001$.

where $\Omega \subset \mathbb{R}^d$ is a domain (open and connected) and $\mathcal{S} \subset \Omega$ is a close subset. In particular, we show the existence of a weak solution of the problem (A.7) and (A.16). For the derivation we follow the usual steps, except that we introduce a suitable weight function which simplifies the resulting bilinear form in the weak formulation.

As the weight function, we choose the equilibrium probability density function of the Smoluchowski dynamics (2.37), that is

$$\alpha(x) \stackrel{def}{=} \exp\left(-\beta V(x)\right),$$

where $\beta > 0$ is usually referred to as the inverse temperature. Provided that the potential $V(x)$ is sufficiently smooth, we have

$$0 < \alpha_0 \leq \alpha(x) \leq \alpha_1 < \infty, \quad \forall x \in \overline{\Omega_{\mathcal{S}}},$$

where we set $\alpha_0 = \min_{x \in \overline{\Omega_{\mathcal{S}}}}\{\alpha(x)\}$ and $\alpha_1 = \max_{x \in \overline{\Omega_{\mathcal{S}}}}\{\alpha(x)\}$. For a compact notation we abbreviate the inner product on $L^2(\Omega_{\mathcal{S}})$ by

$$(u, v) \stackrel{def}{=} \int_{\Omega_{\mathcal{S}}} u(x)v(x)\,\mathrm{d}x.$$

In the first step of the derivation of the weak formulation we multiply the equation in (A.40) with a test function $\phi \in C^\infty(\Omega_{\mathcal{S}})$ and with the weight function $\alpha(x)$. Integrating over the domain $\Omega_{\mathcal{S}}$ yields

$$\beta^{-1}(\Delta u, \phi\alpha) - (\nabla V, \nabla u \ \phi\alpha) = (f, \phi\alpha). \tag{A.41}$$

By Green's first integral identity and $\nabla\alpha = -\beta\nabla V\alpha$ we expand the first integral in the equation (A.41)

$$\begin{aligned}
\beta^{-1}(\Delta u, \phi\alpha) = &(\nabla V, \nabla u \ \phi\alpha) - \beta^{-1}(\nabla u, \nabla\phi \ \alpha) \\
&+ \beta^{-1}\int_{\partial\mathcal{S}} \frac{\partial u}{\partial\hat{n}} \ \phi\alpha \,\mathrm{d}\sigma_{\partial\mathcal{S}}(x) + \beta^{-1}\int_{\partial\Omega} \frac{\partial u}{\partial\hat{n}} \ \phi\alpha \,\mathrm{d}\sigma_{\partial\Omega}(x).
\end{aligned} \tag{A.42}$$

Substituting the left hand side of (A.42) in (A.41) and recalling that the normal derivative is prescribed on $\partial\Omega$ we end up with

$$(\nabla u, \nabla\phi \ \alpha) - \int_{\partial\mathcal{S}} \frac{\partial u}{\partial\hat{n}} \ \phi\alpha \,\mathrm{d}\sigma_{\partial\mathcal{S}}(x) - \int_{\partial\Omega} g_N \ \phi\alpha \,\mathrm{d}\sigma_{\partial\Omega}(x) = -\beta(f, \phi\alpha).$$

The last equation motivates the following weak formulation

$$\text{Find } u \in H^1(\Omega_{\mathcal{S}}) \text{ such that}$$
$$\begin{cases} a(u, \phi) &= l_{f,g_N}(\phi), \quad \forall\phi \in H^1(\Omega_{\mathcal{S}}) \\ u &= g_D \text{ on } \partial\mathcal{S} \end{cases} \tag{A.43}$$

where we define

$$a(u, \phi) \stackrel{def}{=} (\nabla u, \nabla\phi \ \alpha), \tag{A.44}$$

$$l_{f,g_N}(\phi) \stackrel{def}{=} -\beta(f, \phi\alpha) + \int_{\partial\Omega} g_N\phi\alpha \,\mathrm{d}\sigma_{\partial\Omega}(x). \tag{A.45}$$

A. Appendix

Notice that the function $a(\cdot, \cdot)$ is a symmetric bilinear form and the function $l_{f,g_N}(\cdot)$ is linear. Provided that the function $g_D \in H^{\frac{1}{2}}(\partial S)$ we can use its continuation $\overline{g}_D(x)$ to decompose the unknown function $u(x)$ by $u(x) = w(x) + \overline{g}_D(x)$, where the new unknown function $w(x)$ has to vanish on ∂S. This leads to an equivalent weak formulation

$$
\begin{array}{l}
\text{Find } w \in \mathcal{H} \text{ such that} \\
\quad a(w, \phi) = l_{f,g_N}(\phi) - a(\overline{g}_D, \phi), \quad \forall \phi \in H^1(\Omega_S)
\end{array} \tag{A.46}
$$

where the Sobolev space $\mathcal{H}$ is defined by

$$
\mathcal{H} \overset{def}{=} \{ v \in H^1(\Omega_S) : tr_{\partial S} v = 0 \}. \tag{A.47}
$$

A.2.1. Existence of a Weak Solution

The existence of a unique solution of the weak problem (A.46) is usually proved by showing that the prerequisites of the Lemma of Lax-Milgram are satisfied. In doing so, we have to show that the bilinear form (A.44) is $\mathcal{H}$-elliptic, i.e,

$$
\begin{array}{llll}
\exists c_1 > 0 : & a(v, v) & \geq c_1 \|v\|_{H^1}^2 & \forall v \in \mathcal{H} & (A.48) \\
\exists c_2 > 0 : & |a(v, w)| & \leq c_2 \|v\|_{H^1} \|w\|_{H^1} & \forall v, w \in \mathcal{H} & (A.49)
\end{array}
$$

and that the linear function defined on the right hand side of (A.46) is an element in the dual space $(H^1(\Omega_S))' = \{ l : H^1(\Omega_S) \to \mathbb{R} : l \text{ is linear and continuous} \}$.

We first prove that our bilinear form (A.44) satisfies the condition (A.48). Let $v \in C^\infty(\overline{\Omega_S})$ such that $v|_{\partial S} = 0$. Then we deduce

$$
a(v, v) = \int_{\Omega_S} \nabla v \cdot \nabla v \, \alpha \, \mathrm{d}x \geq \alpha_0 \| \, |\nabla v| \, \|_{L^2}^2 .
$$

In the last step we estimate the H^1-norm of v by

$$
\begin{aligned}
\alpha_0 \|v\|_{H^1}^2 &= \alpha_0 \left(\|v\|_{L^2}^2 + \| \, |\nabla v| \, \|_{L^2}^2 \right) \\
&\leq \alpha_0 \left(C \| \, |\nabla v| \, \|_{L^2}^2 + \| \, |\nabla v| \, \|_{L^2}^2 \right) \\
&\leq (1 + C) a(v, v),
\end{aligned}
$$

where the first inequality follows from the Poincaré-inequality for functions vanishing only on a part of the boundary (see Theorem A.6.3 in Appendix). Since $C^\infty(\overline{\Omega_S})$ is dense in $H^1(\Omega_S)$ we get for $0 < c_1 = (1 + C)/\alpha_0$ the desired result. The second condition (A.49) is a simple consequence of the Cauchy-Schwartz-inequality in $\mathbb{R}^2$ and in L^2. We deduce

$$
\begin{aligned}
|a(v, w)| &\leq \alpha_1 \int_{\Omega_S} |\nabla v \cdot \nabla w| \, \mathrm{d}x \\
&\leq \alpha_1 \int_{\Omega_S} |\nabla v| \cdot |\nabla w| \, \mathrm{d}x \\
&\leq \alpha_1 \left(\int_{\Omega_S} |\nabla v|^2 \right)^{\frac{1}{2}} \cdot \left(\int_{\Omega_S} |\nabla w|^2 \right)^{\frac{1}{2}} \\
&\leq \alpha_1 \|v\|_{H^1} \|w\|_{H^1}
\end{aligned}
$$

In the last step we have to show that the right hand side in (A.46)

$$l_{f,g_N,g_D}(v) \stackrel{def}{=} -\beta^{-1}(f,\alpha v) + \int_{\partial\Omega} g_N \; \alpha v \, \mathrm{d}\sigma_{\partial\Omega}(x) - a(\overline{g}_D, v)$$

belongs to $(H^1(\Omega_{\mathcal{S}}))'$. Hence, we have to show that

$$\exists K > 0 : \|l_{f,g_N,g_D}\|_{(H^1)'} = \sup_{\|v\|_{H^1}=1} |l_{f,g_N,g_D}(v)| \leq K.$$

which immediately follows from

1.) $|(f, \alpha v)| \leq \|f\alpha\|_{L^2} \cdot \|v\|_{H^1}$,

2.) $|a(\overline{g}_D, v)| \leq \alpha_1 \|\overline{g}_D\|_{H^1} \|v\|_{H^1}$,

3.) $|\int_{\partial\Omega} g_N \; \alpha v \, \mathrm{d}\sigma_{\partial\Omega}(x)| \leq \|g_N \alpha\|_{L^2(\partial\Omega)} \cdot \|v\|_{H^1}$.

A.2.2. Classical Solution vs. Weak Solution

The following theorem gives an answer to the question under which conditions a weak solution is also a classical solution.

Theorem A.2.1. *Let $u \in C^2(\overline{\Omega_{\mathcal{S}}}) \cap H^1(\Omega_{\mathcal{S}})$ be a solution of the weak problem (A.43). Then u is a classical solution, i.e. $u \in C^2(\Omega_{\mathcal{S}}) \cap C^1(\overline{\Omega_{\mathcal{S}}})$, of the mixed-boundary value problem (A.3).*

Proof. First notice that we have the following sequence of inclusions

$$H_0^1(\Omega_{\mathcal{S}}) \subset \mathcal{H} \subset H^1(\Omega_{\mathcal{S}}),$$

where $\mathcal{H}$ is the Sobolev space defined in (A.47). Since u is a solution of the weak problem (A.43),

$$-\beta^{-1}(\nabla u, \nabla \phi \; \alpha) + \beta^{-1} \int_{\partial\Omega} g_N \phi \alpha \, \mathrm{d}\sigma_{\partial\Omega}(x) = (f, \phi\alpha) \quad \forall \phi \in \mathcal{H},$$

we get by applying Green's integral identity

$$(\beta^{-1}\Delta u - \nabla V \nabla u, \phi\alpha) + \beta^{-1} \int_{\partial\Omega} (g_N - \frac{\partial u}{\partial \hat{n}})\phi\alpha \, \mathrm{d}\sigma_{\partial\Omega}(x) = (f, \phi\alpha) \quad \forall \phi \in \mathcal{H}$$

and in particular

$$((\beta^{-1}\Delta u - \nabla V \nabla u - f)\alpha, \phi) = 0 \quad \forall \phi \in H_0^1(\Omega_{\mathcal{S}}).$$

Because of the strict positivity of the weight function $\alpha(x)$ we conclude

$$\beta^{-1}\Delta u - \nabla V \nabla u = f \quad \text{in } \Omega_{\mathcal{S}}.$$

Moreover, we obtain

$$\int_{\partial\Omega} (g_N - \frac{\partial u}{\partial \hat{n}})\phi\alpha \, \mathrm{d}\sigma_{\partial\Omega}(x) = 0 \quad \forall \phi \in H^1(\Omega_{\mathcal{S}})$$

which shows that the Neumann boundary conditions are also satisfied,

$$\frac{\partial}{\partial \hat{n}} u = g_N \quad \text{on } \partial\Omega.$$

By assumption, the function u satisfies the Dirichlet boundary conditions on $\partial\mathcal{S}$ which completes the proof. $\qquad\square$

A.3. Approximation of Diffusion Processes via Markov Jump Processes

In this section we will show that the Birth-Death process in Section 4.3.1, given by its generator (4.44), is indeed an approximation of the considered Smoluchowski dynamics.

It is a well-known fact that every diffusion process of the form (2.8) can be approximated under weak conditions on the diffusion matrix by a Birth-Death process. In general, the opposite implication does not hold. According to Gardiner [41], Sect. 7.2, the basic idea of the proof that a family of Birth-Death processes, parameterized by a scaling parameter ϵ, approximates a diffusion process is to show that in the limit $\epsilon \to 0$ the associated Master-equations passes to the Fokker-Planck equation associated with the diffusion process. In order to explain that idea in more detail and to motivate our alternative approach, we present the construction given in [41], page 248. Consider a 1-dimensional diffusion process $X_t \in \mathbb{R}$ of the form

$$\mathrm{d}X_t = A(X_t)\mathrm{d}t + \sqrt{B(X_t)}\mathrm{d}W_t \tag{A.50}$$

with sufficiently smooth coefficients $A : \mathbb{R} \to \mathbb{R}$ and $B : \mathbb{R} \to \mathbb{R}^+$. The jump rates of the approximating Birth-Death process on the state space $S = \epsilon\mathbb{Z}$ are defined according to

$$W_\epsilon(x, x') \stackrel{def}{=} \left(\frac{A(x)}{2\epsilon} + \frac{B(x)}{2\epsilon^2} \right) \delta_{x', x+\epsilon} + \left(-\frac{A(x)}{2\epsilon} + \frac{B(x)}{2\epsilon^2} \right) \delta_{x', x-\epsilon} \tag{A.51}$$

such that for a sufficiently small $\epsilon > 0$, (A.51) is positive for all $x \in S$. Next it is shown, that in the limit $\epsilon \to 0$, the Master-equation

$$\begin{aligned}
\frac{\partial p_\epsilon(x, t)}{\partial t} &= \int_\mathbb{R} \left[W_\epsilon(x', x)p_\epsilon(x', t) - W_\epsilon(x, x')p_\epsilon(x, t) \right] \mathrm{d}x' \\
&= W_\epsilon(x - \epsilon, x)p(x - \epsilon, t) + W_\epsilon(x + \epsilon, x)p_\epsilon(x + \epsilon, t) \\
&\quad - (W_\epsilon(x, x + \epsilon) + W_\epsilon(x, x - \epsilon))p_\epsilon(x, t)
\end{aligned} \tag{A.52}$$

becomes the Fokker-Planck equation

$$\frac{\partial p(x, t)}{\partial t} = \mathcal{L}_{fw}p(x, t) = \frac{1}{2}\frac{\partial^2}{\partial x^2}(B(x)p(x, t)) - \frac{\partial}{\partial x}(A(x)p(x, t)). \tag{A.53}$$

An alternative way to see that the Master-equation passes in the limit $\epsilon \to 0$ to (A.53) bases on the observation that from the view point of finite differences, the right hand side in (A.51) results from a second order finite differences discretization of the operator

$$\mathcal{L}_{bw} = \frac{1}{2}B(x)\frac{\partial^2}{\partial x^2} + A(x)\frac{\partial}{\partial x},$$

which is the generator associated with the diffusion process in (A.50). For the sake of simplicity we consider the diffusion process of a finite interval $[a, b] \subset \mathbb{R}$ and assume periodic boundary conditions. Let $W_\epsilon \in \mathbb{R}^{|S| \times |S|}$ denote the matrix resulting from the jump rates in (A.51) where $S = \epsilon\mathbb{Z} \cap [a, b]$ and we additionally set

$$W_\epsilon(x, x) \stackrel{def}{=} -(W_\epsilon(x, x + \epsilon) + W_\epsilon(x, x - \epsilon)).$$

Notice that the Master equation in (A.52) can now be written in a compact form,

$$\frac{\partial p_\epsilon}{\partial t} = W_\epsilon^T p_\epsilon,$$

where $p_\epsilon = (p_\epsilon(x))_{x \in S}$. Encouraged by a Remark in [44], page 94, we next show that the transposed matrix W_ϵ^T is a consistent discretization of the operator $\mathcal{L}_{fw}$ on the right hand side in the Fokker-Planck equation (A.53). With the notation introduced in Section A.1, we have for any $p \in C^2$

Lemma A.3.1.

$$\left\| W_\epsilon^T R_\epsilon p - R_\epsilon \mathcal{L}_{fw} p \right\|_\infty \to 0 \ \ as \ \epsilon \to 0.$$

Proof. Let $x \in S$ be a mesh point. We deduce

$$
\begin{aligned}
(W_\epsilon^T R_\epsilon p)(x) = & W_\epsilon(x - \epsilon, x)p(x - \epsilon) + W_\epsilon(x + \epsilon, x)p(x + \epsilon) \\
& - (W_\epsilon(x, x + \epsilon) + W_\epsilon(x, x - \epsilon))p(x) \\
= & \frac{1}{2\epsilon^2} \left[B(x - \epsilon)p(x - \epsilon) - B(x)p(x) + 2B(x + \epsilon)p(x + \epsilon) \right] \\
& - \frac{1}{2\epsilon} \left[A(x + \epsilon)p(x + \epsilon) - A(x - \epsilon)p(x - \epsilon) \right] \\
= & \frac{1}{2} \frac{\partial^2}{\partial x^2}(B(x)p(x)) + \mathcal{O}(\epsilon^2) - \frac{\partial}{\partial x}(A(x)p(x)) + \mathcal{O}(\epsilon^2),
\end{aligned}
$$

which proves the assertion. $\qquad \square$

The view point that the construction of the jump rates of an approximating Birth-Death process can also be obtained via finite difference discretization of the generator $\mathcal{L}_{bw}$ allows a straightforward generalization for the approximation of diffusion processes in higher dimension. For example, the generator of the Birth-Death process considered in Section 4.3.1, results from the discretization of the generator

$$\mathcal{L}_{bw} = \beta^{-1}\Delta - \nabla V \nabla$$

via the second order scheme in (A.8) where we additionally included reflecting boundary conditions.

A.4. Proofs

A.4.1. Proof for the Representation of the Probability Current of Reactive Trajectories

To derive (3.15), we take first the limit as $T \to \infty$ in (3.14) using ergodicity to obtain

$$
\begin{aligned}
\lim_{s \to 0^+} \frac{1}{s} \Big(& \int_{\mathcal{S}} \rho(x)q_b(x)\mathbb{E}_x\big(q(X(s))\mathbf{1}_{\mathbb{R}^d \setminus \mathcal{S}}(X(s)))\big)\mathrm{d}x \\
& - \int_{\mathbb{R}^d \setminus \mathcal{S}} \rho(x)q_b(x)\mathbb{E}_x\big(q(X(s))\mathbf{1}_{\mathcal{S}}(X(s)))\big)\mathrm{d}x \Big) \qquad \text{(A.54)} \\
= & \int_{\partial \mathcal{S}} \hat{n}_{\partial \mathcal{S}}(x) \cdot J_{AB}(x)\mathrm{d}\sigma_{\partial \mathcal{S}}(x),
\end{aligned}
$$

A. Appendix

where $\mathbb{E}_x$ denotes expectation conditional on $X(0) = x$. Taking the limit as $s \to 0^+$ can now be done using

$$\lim_{t \to 0^+} \frac{1}{t}\big(\mathbb{E}_x\phi(X(t)) - \phi(x)\big)$$

$$= \sum_{i,j=1}^{d} a_{ij}(x)\frac{\partial^2\phi(x)}{\partial x_i \partial x_j} + \sum_{i=1}^{d} b_i(x)\frac{\partial\phi(x)}{\partial x_i} \equiv (\mathcal{L}_{bw}\phi)(x),$$

where $\phi(x)$ is any suitable observable. However, taking the limit on (A.54) is somewhat tricky because of the presence of the discontinuous functions $\mathbf{1}_{\mathcal{S}}(x)$ and $\mathbf{1}_{\mathbb{R}^d \setminus \mathcal{S}}(x)$. The proper way to avoid ambiguities on how to interpret the derivatives of $\mathbf{1}_{\mathcal{S}}(x)$ and $\mathbf{1}_{\mathbb{R}^d \setminus \mathcal{S}}(x)$ is to mollify these functions, that is, replace them by functions varying rapidly on $\partial\mathcal{S}$ but smooth, then let $s \to 0^+$ and finally remove the mollification. Let then $f_\delta(x)$ be a smooth function which is 1 in $\mathcal{S}$ at a distance δ from $\partial\mathcal{S}$, 0 out of $\mathcal{S}$ at a distance δ from $\partial\mathcal{S}$ and varies rapidly but smoothly from 0 to 1 in the strip of size 2δ around $\partial\mathcal{S}$. Thus (A.54) is the limit as $\delta \to 0$ of

$$I_\delta = \lim_{s \to 0^+} \frac{1}{s}\int_{\mathbb{R}^d} \rho(x)q_b(x)$$

$$\times \Big(f_\delta(x)\mathbb{E}_x\big(q(X(s))(1 - f_\delta(X(s)))\big) -$$

$$(1 - f_\delta(x))\mathbb{E}_x\big(q(X(s))f_\delta(X(s)))\big)\Big)\mathrm{d}x.$$

Inserting

$$0 = -\rho(x)q_b(x)f_\delta(x)\big(q(x)(1 - f_\delta(x))\big)$$
$$+ \rho(x)q_b(x)(1 - f_\delta(x))\big(q(x)f_\delta(x)\big)$$

under the integral then letting $s \to 0^+$, we obtain

$$I_\delta = \int_{\mathbb{R}^d} \rho(x)q_b(x)\Big(f_\delta(x)\big(\mathcal{L}_{bw}(q(1 - f_\delta))\big)(x)$$

$$- (1 - f_\delta(x))\big(\mathcal{L}_{bw}(qf_\delta)\big)(x)\Big)\mathrm{d}x.$$

Expanding the integrand, several terms cancel and we are simply left with

$$I_\delta = -\int_{\mathbb{R}^d} \rho(x)q_b(x)\big(\mathcal{L}_{bw}(qf_\delta))\big)(x)\mathrm{d}x.$$

Using the explicit form for L and expanding, this is

$$I_\delta = -\int_{\mathbb{R}^d} \rho(x)q_b(x)\Big(f_\delta(x)\mathcal{L}_{bw}q(x)$$

$$+ \sum_{i,j=1}^{d} a_{ij}(x)\frac{\partial}{\partial x_i}\Big(q(x)\frac{\partial f_\delta(x)}{\partial x_j}\Big)$$

$$+ \sum_{i=1}^{d} \frac{\partial f_\delta(x)}{\partial x_i}\Big(b_i(x)q(x) + \sum_{j=1}^{d} a_{ij}(x)\frac{\partial q(x)}{\partial x_j}\Big)\Big)\mathrm{d}x.$$

By (3.6), $\mathcal{L}_{bw}q(x) = 0$ and integrating by parts the second term in the parenthesis under the integral, we arrive at

$$I_\delta = -\int_{\mathbb{R}^d} \sum_{i=1}^d \frac{\partial f_\delta(x)}{\partial x_i}\Big(q(x)q_b(x)J_i(x)$$

$$+ q_b(x)\rho(x)\sum_{j=1}^d a_{ij}(x)\frac{\partial q(x)}{\partial x_j}$$

$$- q(x)\rho(x)\sum_{j=1}^d a_{ij}(x)\frac{\partial q_b(x)}{\partial x_j}\Big)\mathrm{d}x.$$

Now let $\delta \to 0$ and recall that for any suitable $F(x) = (F_1(x), \ldots, F_d(x))^T$

$$\lim_{\delta\to 0}\int_{\mathbb{R}^d} \sum_{i=1}^d \frac{\partial f_\delta(x)}{\partial x_i}F_i(x)\mathrm{d}x$$

$$= -\lim_{\delta\to 0}\int_{\mathbb{R}^d} f_\delta(x)\sum_{i=1}^d \frac{\partial F_i(x)}{\partial x_i}\mathrm{d}x$$

$$= -\int_{\mathcal{S}} \sum_{i=1}^d \frac{\partial F_i(x)}{\partial x_i}\mathrm{d}x$$

$$= -\int_{\partial\mathcal{S}} \sum_{i=1}^d \hat{n}_{S,i}(x)F_i(x)\mathrm{d}\sigma_{\partial\mathcal{S}}(x),$$

where the first equality follows by integration by parts, the second by definition of $f_\delta(x)$, and the third by the divergence theorem. Using this result, we conclude that the limit of the expression above for I_δ as $\delta \to 0$ is the surface integral of the current $J_{AB}(x)$ given in (3.15), as claimed.

A.4.2. Proof for the Representation of the Transition Rate via a Volume Integral

To check that (3.19) gives the rate, let $\partial\mathcal{S}(\zeta) = \{x : q(x) = \zeta\}$ be the (forward) isocommittor surface with committor value $\zeta \in [0, 1]$, and consider the integral

$$A(\zeta) = \int_{\partial\mathcal{S}(\zeta)} \rho(x)\sum_{i,j=1}^d \hat{n}_{\partial\mathcal{S}(\zeta),i}(x)a_{ij}(x)\frac{\partial q(x)}{\partial x_j}\mathrm{d}\sigma_{\partial\mathcal{S}(\zeta)}(x).$$

Since $\partial\mathcal{S}(0) \equiv \partial A$, is easy to see from (3.17) and (3.18) with $\partial\mathcal{S} = \partial A$ that:

$$A(0) = \int_{\partial A} \rho(x)\sum_{i,j=1}^d \hat{n}_{\partial A,i}(x)a_{ij}(x)\frac{\partial q(x)}{\partial x_j}\mathrm{d}\sigma_{\partial A}(x)$$

$$\equiv k_{AB},$$

where we used $q(x) = 0$ and $q_b(x) = 1$ on ∂A. Next, we show that $A(\zeta) = A(0) = k_{AB}$ for all $\zeta \in [0, 1]$. Using the Dirac delta function we can express $A(\zeta)$ as

$$A(\zeta) = \int_{\mathbb{R}^d} \rho(x)\sum_{i,j=1}^d \frac{\partial q(x)}{\partial x_i}a_{ij}(x)\frac{\partial q(x)}{\partial x_j}\delta(q(x) - \zeta)\mathrm{d}x$$

and hence

$$\frac{\mathrm{d}A(\zeta)}{\mathrm{d}\zeta}$$

$$= -\int_{\mathbb{R}^d} \rho(x) \sum_{i,j=1}^d \frac{\partial q(x)}{\partial x_i} a_{ij}(x) \frac{\partial q(x)}{\partial x_j} \delta'(q(x) - \zeta) \mathrm{d}x$$

$$= -\int_{\mathbb{R}^d} \rho(x) \sum_{i,j=1}^d \frac{\partial q(x)}{\partial x_i} a_{ij}(x) \frac{\partial}{\partial x_j} \delta(q(x) - \zeta) \mathrm{d}x.$$

Integrating by parts, this gives

$$\frac{dA(\zeta)}{d\zeta} = \int_{\mathbb{R}^d} \rho(x) \sum_{i,j=1}^d a_{ij}(x) \frac{\partial^2 q(x)}{\partial x_i \partial x_j} \delta(q(x) - \zeta) \mathrm{d}x$$

$$+ \int_{\mathbb{R}^d} \sum_{i,j=1}^d \frac{\partial q(x)}{\partial x_i} \frac{\partial}{\partial x_j} (a_{ij}(x)\rho(x)) \delta(q(x) - \zeta) \mathrm{d}x$$

$$= -\int_{\mathbb{R}^d} \rho(x) \sum_{i=1}^d b_i(x) \frac{\partial q(x)}{\partial x_i} \delta(q(x) - \zeta) \mathrm{d}x$$

$$+ \int_{\mathbb{R}^d} \sum_{i,j=1}^d \frac{\partial q(x)}{\partial x_i} \frac{\partial}{\partial x_j} (a_{ij}(x)\rho(x)) \delta(q(x) - \zeta) \mathrm{d}x,$$

where in the second step we used (3.6). Using the definition (3.16) for the equilibrium current $J(x)$, the two integrals in the last equality can be recombined into

$$\frac{\mathrm{d}A(\zeta)}{\mathrm{d}\zeta} = -\int_{\mathbb{R}^d} \sum_{i=1}^d \frac{\partial q(x)}{\partial x_i} J_i(x) \delta(q(x) - \zeta) \mathrm{d}x$$

$$= -\int_{\partial \mathcal{S}(\zeta)} \sum_{i=1}^d n_{\partial \mathcal{S}(\zeta),i}(x) J_i(x) \mathrm{d}\sigma_{\partial \mathcal{S}(\zeta)}(x) = 0, \tag{A.55}$$

where in the last equality we use the fact that the probability flux of the regular (by opposition to reactive) trajectories through any surface is zero at equilibrium. (A.55) implies that $A(\zeta) = A(0) = k_{AB}$ for all $\zeta \in [0,1]$ as claimed. Hence, $\int_0^1 A(\zeta)d\zeta = k_{AB}$ which gives

$$\int_0^1 \int_{\mathbb{R}^d} \rho(x) \sum_{i,j=1}^d \frac{\partial q(x)}{\partial x_j} a_{ij}(x) \frac{\partial q(x)}{\partial x_j} \delta(q(x) - \zeta) \mathrm{d}x \mathrm{d}\zeta$$

$$= \int_{\Omega_{AB}} \rho(x) \sum_{i,j=1}^d \frac{\partial q(x)}{\partial x_j} a_{ij}(x) \frac{\partial q(x)}{\partial x_j} \mathrm{d}x = k_{AB}.$$

This is (3.19).

A.5. Short Account to Free Energy

An important quantity to characterize the transition behavior of a diffusion process in a (non-trivial) potential landscape is the *free energy* with respect to a reaction

coordinate. A reaction coordinate can be seen as an observable providing information on the progress of a reaction between a reactant state and a product state. Formally, a reaction coordinate is a continuous and smooth function $\xi : \mathbb{R}^d \mapsto \mathbb{R}^n$ whose level sets $\xi^{-1}(c) = \{x \in \mathbb{R}^d : \xi(x) = c\}$, $c \in \mathbb{R}^n$ foliate the state space and comprise all states which are indistinguishable with respect to the reaction, respectively. In the traditional way, the free energy is defined by means of the marginal distribution of the equilibrated process with respect to a given reaction coordinate. Here we give only a short introduction to the free energy. For details see, e.g. [45, 46]. To formalize things, consider the Smoluchowski dynamics in a potential landscape

$$\mathrm{d}X_t = -\nabla V(X_t)\mathrm{d}t + \sqrt{2\beta^{-1}}\mathrm{d}W_t,$$

where $X_t \in \mathbb{R}^d$ and the remaining parameters are as in (2.37). The probability to find the equilibrated system in a certain region, say $D \subset \mathbb{R}^d$, is given in terms of the equilibrium density function $\exp(-\beta V(x))$, that is

$$\mathbb{P}(X_t \in D) = Z^{-1} \int_D \exp(-\beta V(x))\mathrm{d}x,$$

where Z is the normalization factor.

In order to define the free energy, consider the marginal probability density function with respect to the reaction coordinate ξ, that is

$$Z(c) = \int_{\mathbb{R}^d} \exp(-\beta V(x))\delta(\xi(x) - c)\mathrm{d}x,$$

where $\delta(x)$ is the famous delta-function. The standard free energy is defined as the logarithm of the marginal probability density function $Z(c)$,

$$V_{free} : \mathbb{R}^n \to \mathbb{R}$$
$$V_{free}(c) \stackrel{def}{=} -\beta^{-1} \log Z(c).$$

A.6. Definitions and Theorems

Wiener process   The Wiener process W_t is a mathematical model of the Brownian motion of a free particle in the absence of friction.

Definition A.6.1 (Wiener process and white noise). *The standard d-dimensional **Wiener process** W_t is a d-dimensional, time-homogeneous Markov process on $\mathbb{R}^d$ with independent and stationary $\mathcal{N}(0, (t-s)I)$-distributed increments $W_t - W_s$, with initial value $W_0 = 0$, and with almost certainly continuous sample functions.*

*A d-dimensional stochastic process η is said to be a **white noise** if it is a Gaussian process with mean zero and covariance $\langle \eta_i(t)\eta_j(s) \rangle = \delta_{ij}\delta(t - s)$.*

Existence and Uniqueness of Solution

Theorem A.6.1. *([3], page 105) Suppose that we have a stochastic differential equation*

$$dX_t = b(t, X_t)dt + \sigma(t, X_t)dW_t, X_0 = c, \quad 0 \le t \le T < \infty, \tag{A.56}$$

A. Appendix

where W_t is standard d-dimensional standard Wiener process and c is a random variable independent of $W_t - W_0$ for $t \geq 0$. Suppose that the $\mathbb{R}^d$-valued function $b(t, x)$ and the $(d \times d)$-valued function $\sigma(t, x)$ are measurable on $[0, T] \times \mathbb{R}^d$ and have the following properties: There exists a constant $K > 0$ such that

a) (Lipschitz condition) for all $t \in [0, T], x, y \in \mathbb{R}^d$,

$$\|b(t, x) - b(t, y)\| + \|\sigma(t, x) - \sigma(t, y)\| \leq K\|x - y\|.$$

b) (Restriction of growth) For all $t \in [0, T], x \in \mathbb{R}^d$,

$$\|b(t, x)\|^2 + \|\sigma(t, x)\|^2 \leq K^2 \left\|1 + \|x\|^2\right\|.$$

Then, equation (A.56) has on $[0, T]$ a unique $\mathbb{R}^d$-valued solution $\{X_t, 0 \leq t \leq T\}$, continuous with probability 1, that satisfies the initial condition $X_0 = c$.

Time reversal of diffusion The following theorem on time reversal of a diffusion process $\{X_t, 0 \leq t \leq T\}$, $T > 0$ satisfying the stochastic differential equation

$$\mathrm{d}X_t = b(t, X_t)\mathrm{d}t + \sigma(t, X_t)\mathrm{d}W_t,$$

where $b : [0, T] \times \to \mathbb{R}^d, \sigma : [0, T] \times \mathbb{R}^d \to \mathbb{R}^{d \times d}$, is found in [47] which generalizes results in [14].

Define the reversed time process by $X_t^R \overset{def}{=} X_{T-t}$, then

Theorem A.6.2. *If for almost all $t > 0$, the law of X_t has a probability density $v(t, x)$ such that for all $s > 0$ and any open bounded set $C \subset \mathbb{R}^d$*

$$\int_s^T \int_C \|v(t, x)\|^2 + \sum_{i=1}^d \|\sum_{j=1}^d \sigma_{ij}(t, x)v(t, x)_{x_j}\|^2 dx\, dt < \infty,$$

where $v(t, x)_{x_j}$ denotes the partial derivative of $v(t, x)$ in the distribution sense, then the reversed time process X_t^R is a Markov diffusion process satisfying the SDE

$$dX_t^R = b^R(t, X_t^R)dt + \sigma^R(t, X_t^R)dW_t,$$

where

$$b_i^R(t, x) = -b_i(T - t, x) + 2\frac{\sum_{j=1}^d \frac{d}{dx_j}\left[a_{ij}(T - t, x)v(T - t, x)\right]}{v(T - t, x)},\ 1 \leq i \leq d,$$

$$\sigma_{ij}^R(x, t) = \sigma_{ij}(x, T - t),\quad 1 \leq i, j \leq d,$$

$$a(x, t) = \frac{1}{2}\sigma(x, t)\sigma^T(x, t).$$

Poincaré Lemma The proof of the existence of a unique weak solution of the elliptic mixed-value boundary problem (A.40) bases on the general version of the Poincaré-Lemma.

Theorem A.6.3. *([20], page 127-130)Assume that the Lipschitz domain $\Omega \subset \mathbb{R}^d$ is bounded, connected and open and the subset $\Sigma \subset \partial\Omega$ is Lipschitz continuous and has a positive Hausdorff measure. Then there exists an $C_\Omega > 0$ such that*

$$\int_\Omega |\nabla v|^2 \, dx \geq C_\Omega \int_\Omega v^2 \, dx, \quad \forall v \in H^1_\Sigma(\Omega)$$

where the Sobolev space $H^1_\Sigma(\Omega)$ is defined by

$$H^1_\Sigma(\Omega) = \{u \in H^1(\Omega) : tr_\Sigma u = 0\}.$$

Hypoelliptic operators

Definition A.6.2. *([71], page 139) A linear second order operator G with infinitely often differentiable coefficients defined in a domain $\Omega \subset \mathbb{R}^d$ is called **hypoelliptic** in Ω if for any distribution u in $D(\Omega)$ and any domain $\Omega_1 \subset \Omega$ the condition that $Gu \in C^\infty$ implies that u is infinitely often differentiable in Ω_1.*

Theorem A.6.4. *([71],page 139) If the second order operator*

$$Gu = a : \nabla\nabla u + b \cdot \nabla u + cu$$

with real coefficients $a_{ij}(x), b_i(x), c(x)$ in the class $C^\infty(\Omega)$ is hypoelliptic in the domain Ω, then for any point $x \in \Omega$

$$either \ \sum_{i,j=1}^d a_{ij}\xi_i\xi_j \geq 0 \ or \ \sum_{i,j=1}^d a_{ij}\xi_i\xi_j \leq 0$$

for all $\xi \in \mathbb{R}^d$.

Theorem A.6.5. *([96],page 9) If the operator $(-\frac{d}{dt} + \mathcal{L}_{fw})$ is hypoelliptic, then the law of X_t has a smooth density $p(t,x)$ on $(0,\infty) \times \mathbb{R}^d$, i.e.,*

$$\mathbb{P}(X_t \in dy) = p(t,y)dy,$$

and $p(t,x)$ satisfies the Fokker-Planck equation

$$\frac{dp}{dt} = \mathcal{L}_{fw}p.$$

M-matrix The following definitions and Lemmata are found in [44]. The elements of a matrix A are denoted by a_{ij}, $i,j \in I$. Here A and the index set I assume the places of $\overline{L}_h$ and $\overline{\Omega}_h^\mathcal{S}$. The index $i \in I$ is said to be *directly connected* with $j \in I$ if $a_{ij} \neq 0$. We say that $i \in I$ is *connected* with $j \in I$, denoted by $i \rightarrow j$, if there exists a *connection*

$$i = i_0, i_1, \ldots, i_n = j \text{ with } a_{i_{k-1}i_k} \neq 0, \ (1 \leq k \leq n).$$

A. Appendix

Definition A.6.3. *A matrix $A \in \mathbb{R}^{I \times I}$ is called* irreducible *if every $i \in I$ is connected to every $j \in I$.*

Definition A.6.4. *A matrix $A \in \mathbb{R}^{I \times I}$ is called* strictly diagonally dominant *if*

$$|a_{ii}| > \sum_{j \neq i} |a_{ij}|, \quad \forall i \in I, \tag{A.57}$$

weakly diagonally dominant *if*

$$|a_{ii}| \geq \sum_{j \neq i} |a_{ij}|, \quad \forall i \in I, \tag{A.58}$$

irreducible diagonally dominant *if A is irreducible and weakly diagonally dominant and if, furthermore,*

$$|a_{kk}| > \sum_{j \neq k} |a_{kj}| \quad \text{for at least one } k \in I \tag{A.59}$$

and essentially diagonally dominant *if A is weakly diagonally dominant and every $i \in I$ is connected to a $k \in I$ for which the inequality in (A.59) holds true.*

Now we turn our attention to special subclass of positive matrices.

Definition A.6.5. *A matrix $A \in \mathbb{R}^{I \times I}$ is said to be an M-matrix if A satisfies*

$$a_{ii} > 0, \text{for all } i \in I, \tag{A.60}$$
$$a_{ij} \leq 0, \text{for all } i \neq j, \tag{A.61}$$
$$A \text{ is regular and } A^{-1} \geq 0 \text{ componentwise.}$$

Theorem A.6.6. *Let $A \in \mathbb{R}^{I \times I}$ be strictly or essentially or irreducibly diagonally dominant. If the sign conditions (A.60),(A.61) are satisfied then A is an M-matrix.*

The proofs for stability of the discretization schemes derived in Section A.1.2 and Section A.1.3 are based on the following theorem.

Theorem A.6.7. *Let $A \in \mathbb{R}^{d \times d}$ be an M-matrix. If a vector $w \in \mathbb{R}^d$ exists with $Aw \geq \mathbb{1}$ then*
$$\left\| A^{-1} \right\|_\infty \leq \|w\|_\infty,$$
where $\left\| A^{-1} \right\|_\infty = \sup_{\|w\|_\infty = 1} \left\| A^{-1} w \right\|_\infty$ is the matrix-norm with respect to the maximum norm $\|\cdot\|_\infty$.

Two theorems on the existence of generators The following Theorems are found in [53]. They give sufficient conditions for the existence of a generator of a given transition matrix.

Theorem A.6.8. *Let P be a transition matrix and suppose that*

(a) $\det(P) \leq 0$, or

(b) $\det(P) > \prod_i p_{ii}$, or

(c) there are states i and j such that j is accessible from i, but $p_{ij} = 0$.

Then, there is no generator $L \in \mathfrak{G}$ such that $P = \exp(L)$.

Theorem A.6.9. *Let P be a transition matrix.*

(a) If $\det(P) > \frac{1}{2}$, then P has at most one generator.

(b) If $\det(P) > \frac{1}{2}$ and $\|P - I\| < \frac{1}{2}$ (using any operator norm), then the only possible generator for P is the principal branch of the logarithm of P.

(c) If P has distinct eigenvalues and $\det(P) > e^{-\pi}$, then the only possible generator for P is the principal branch of the logarithm of P.

Zusammenfassung

Übergangsereignisse in komplexen Systemen zwischen langlebigen Zuständen treten in vielen Bereichen der Naturwissenschaft auf, wie zum Beispiel in der Physik, Chemie, Biologie, etc. . Charakteristisch für Übergangsereignisse sind deren seltenes Auftreten verglichen mit der Zeitskala der Fluktuationen innerhalb langlebiger (metastabiler) Zustände des Systems. Aus der Sicht von Computersimulationen komplexer Systeme verursacht die Zeitskalentrennung einen enormen numerischen Aufwand zur Bestimmung von makroskopischen Grö ßen, wie zum Beispiel die Übergangsrate zwischen Konformationen eines (Bio-)Moleküle. Zu den bekanntesten Ansätzen in der Literatur zur Lösung dieses Problems gehören "Transition State Theory" (TST) und "Transition Path Sampling" (TPS). Die Idee von TST ist es, die Reaktionsrate (Übergangsrate) zwischen zwei Zuständen durch die mittlere Anzahl von Durchgängen in einem geeigneten Übergangsbereich zu approximieren. Ohne genaue Kenntnis der Reaktionskoordinaten aber ist es sehr schwierig einen geeigneten Übergangsbereich zu identifizieren und somit zuverlässige Ergebnisse zu erhalten. TPS hingegen erlaubt es, ohne Annahmen über Übergangsbereiche und Reaktionskoordinaten ein Ensemble von Übergangspfaden zu erzeugen. Die Schwierigkeit hier besteht aber in der weiteren Auswertung des erzeugten Ensembles hinsichtlich zum Beispiel der Berechnung der Übergangsrate oder der Identfizierung unterschiedlicher Übergangsmechanismen.

Gegenstand der vorliegenden Dissertation ist die Präsentation eines neuen Ansatzes, genannt "Transition Path Theory" (TPT), der ein vollständiges Verständnis von Übergangsprozessen für zeitkontinuierliche Markovprozesse ermöglicht. TPT beschreibt die statistischen Eigenschaften des *Ensembles aller Reaktionspfade* (Übergangspfade) zwischen zwei nicht notwendigerweise metastabilen Zuständen durch die Committor-Funktion, die Verteilungsfunktion der reaktiven Pfade, der durch die reaktiven Pfade induzierte Wahrscheinlichkeitsfluss und die Übergangsrate. Wir illustrieren TPT für Markovprozesse auf kontinuierlichen Zustandsräumen anhand von verschiedenen niedrig dimensionalen Beispielen und zeigen, dass mit TPT präzise Voraussagen über Übergänge in unschiedlichen dynamischen Szenarien (z.B. entropische Barrieren, temperaturabhängige Übergangsbereiche, schnelle und langsame Freiheitsgrade) gemacht werden können.

Der zweite Schwerpunkt dieser Arbeit liegt in der Anwendung von TPT auf höher dimensionale komplexe Systeme. Zunächst leiten wir TPT für Markovprozesse mit diskreten Zustandsräumen (Markov Sprungprozesse) her und zeigen, dass Übergangsereignisse im diskreten Zustandsraum vollständig durch TPT beschrieben werden können. Aufbauend auf dem diskreten Wahrscheinlichkeitsfluss beweisen wir eine hierarchische Zerlegung des Ensembles aller (diskreten) Übergangspfade und entwickeln effiziente graphen-basierte Algorithmen zur numerischen Bestimmung dieser Zerlegung. Als Anwendung von TPT analysieren wir die Konformationsdynamik des Glyzin-Moleküls gelöst in Wasser auf der Datenbasis einer Molekülsimulation. Dazu bestimmen wir den der diskretisierten Zeitreihe zugrunde liegenden Markovprozess durch eine verbesserte Maximum-Likelihood Methode zur Rekonstruktion von Markov Sprungprozessen aus unvollständigen Beobachtungen und bestimmen dann die dominanten Übergangspfade zwischen zwei Konformationen.

Curriculum vitae

Philipp Metzner
Pflügerstr. 11
12047 Berlin

04.02.1975	geboren in Berlin
1987 – 1991	Gymnasium St. Marien Oberschule (Berlin)
1991 – 1994	Gymnasium Leonardo-da-Vinci Oberschule (Berlin)
1994 – 1995	Zivildienst auf dem "Ökohof Kuhhorst" (Brandenburg)
1995 – 2002	Mathematikstudium an der Freien Universitt Berlin Abschluss: Diplom-Mathematiker, Prädikat "Sehr gut"
2002 – heute	Wissenschaftlicher Mitarbeiter, Biocomputing Group am Institut für Mathematik II der FU Berlin und MATHEON

A. Appendix

Bibliography

[1] R. K. Ahuja, T. L. Magnanti, and J. B. Orlin. *Network Flows*. Prentice Hall, Englewood Cliffs, New Jersey, 1993.

[2] R. Albert and A.-L. Barabási. Statistical mechanics of complex networks. *Rev. Mod. Phys.*, 74(1):48–97, 2002.

[3] L. Arnold. *Stochastic differential equations : theory and applications*. Wiley, New York, 1974.

[4] G. Ben Arous, A. Bovier, and V. Gayrard. Aging in the random energy model under glauber dynamics. *Phys. Rev. Lett.*, 88:87201, 2002.

[5] S. Asmussen, M. Olsson, and O. Nerman. Fitting phase-type distributions via the em algorithm. *Scand. J. Statist.*, 23(4):419–441, 1996.

[6] M. Belkin and P. Niyogi. Laplacian eigenmaps for dimensionality reduction and data representation. *Neural Computation*, 15(6):1373–1396, 2003.

[7] C. H. Bennett. Molecular dynamics and transition state theory: the simulation of infrequent events. In A. S. Nowick and J. J. Burton, editors, *Algorithms for Chemical Computation*, 46, pages 63–97. ACS Symposium Series, 1977.

[8] H. J. C. Berendsen, D. van der Spoel, and R. van Drunen. Gromacs: A message-passing parallel molecular dynamics implementation. *Comp. Phys. Comm.*, 91(1-3):43–56, 1995.

[9] M. Bladt and M. Sörensen. Statistical inference for discretely observed markov jump processes. *J. R. Statist. Soc. B*, 67(3):395–410, 2005.

[10] A. Bovier. Metastability: Lecture notes given at the 5th pragues summer school on mathematical statistical physics, 2006.

[11] A. Bovier, M. Eckhoff, V. Gayrard, and M. Klein. Metastability in stochastic dynamics of disordered mean-field models. *Probab. Theor. Rel. Fields*, 119(1):99–161, 2001.

[12] A. Bovier, M. Eckhoff, V. Gayrard, and M. Klein. Metastability and low lying spectra in reversible markov chains. *Comm. Math. Phys.*, 228(2):219–255, 2002.

[13] P. Br'emaud. *Markov Chains: Gibbs Fields, Monte Carlo Simulation and Queues*. Springer Verlag, 1999.

[14] D. A. Castanon. Reverse-time diffusion processes. *IEEE Trans. Inform. Theory*, 28(6):953–956, 1982.

Bibliography

[15] D. Chandler. Statistical mechanics of isomerization dynamics in liquids and the transition state approximation. *J. Chem. Phys.*, 68(6), 1978.

[16] R. C. Coifman and S. Lafon. Diffusion maps. *Appl. Comput. Harmon. Anal.*, 21:5–30, 2006.

[17] F. Cordes, M. Weber, and J. Schmidt-Ehrenberg. Metastable conformations via successive perron-cluster cluster analysis of dihedrals. *ZIB-Report 02-40*, 7, 2002.

[18] T. Cormen, C. Leiserson, and R. Rivest. *Introduction to Algorithms*. MIT Press, 1990.

[19] D.T. Crommelin and E. Vanden-Eijnden. Fitting timeseries by continuous-time markov chains: A quadratic programming approach. *J. Comp. Phys.*, 217(2):782–805, 2006.

[20] R. Dautray and J.-L. Lions. *Mathematical Analysis and Numerical Methods for Science and Technology*, volume 2, Functional and Variational Methods. Springer Verlag, 2000.

[21] C. Dellago, P. G. Bolhuis, and P. L. Geissler. Transition path sampling. *Advances in Chemical Physics*, 123, 2002.

[22] M. Dellnitz, M. Hessel von Molo, P. Metzner, R. Preis, and Ch. Schütte. Graph algorithms for dynamical systems. In A. Mielke, editor, *Analysis, Modeling and Simulation of Multiscale Problems*. Springer Verlag, 2006.

[23] A. P. Dempster, N. M. Laird, and D.B. Rubin. Maximum likelihood from incomplete data via the em-algorithm. *J. R. Statist. Soc. B*, 39(1):1–38, 1977.

[24] P. Deuflhard, W. Huisinga, A. Fischer, and Ch. Schütte. Identification of almost invariant aggregates in reversible nearly uncoupled markov chains. *Lin. Alg. Appl.*, 315(1–3):39–59, 2000.

[25] P. Deuflhard and Ch. Schütte. Molecular conformational dynamics and computational drug design. In J. M. Hill and R. Moore, editors, *Applied Mathematics Entering the 21st Century*, volume 116, pages 91–119. SIAM, 2004.

[26] D.L. Donoho and C. Grimes. Hessian eigenmaps: New locally linear embedding techniques for high-dimensional data. *Proc. Nat. Acad. Sci. USA*, 100(10):5591–5596, 2003.

[27] P.G. Doyle and J. L. Snell. Random walks and electric networks, 2000.

[28] P. DuChateau and D. W. Zachmann. *Schaum's Outline of Partial Differential Equations*. MacGraw-Hill, 1986.

[29] R. Durrett. *Stochastic Calculus*. CRC Press, 1996.

[30] W. E, W. Ren, and E. Vanden-Eijnden. String method for the study of rare events. *Phys. Rev. B*, 66, 2002.

[31] W. E, W. Ren, and E. Vanden-Eijnden. Energy landscape and thermally activated switching of submicron-sized ferromagnetic elements. *J. App. Phys.*, 93, 2003.

[32] W. E, W. Ren, and E. Vanden-Eijnden. Finite-temperature string method for the study of rare events. *J. Phys. Chem. B*, 109, 2005.

[33] W. E, W. Ren, and E. Vanden-Eijnden. Transition pathways in complex systems: Reaction coordinates, isocommittor surfaces, and transition tubes. *Chem. Phys. Lett.*, 413, 2005.

[34] W. E and E. Vanden-Eijnden. Towards a theory of transition paths. *J. Statist. Phys.*, 123(3):503–523, 2006.

[35] R. Elber, A. Ghosh, and A. Cárdenas. Long time dynamics of complex systems. *Account of Chemical Research*, 35, 2002.

[36] R. Elber, A. Ghosh, A. Cárdenas, and H. Stern. Bridging the gap between reaction pathways, long time dynamics and calculation of rates. *Advances in Chemical Physics*, 126, 2003.

[37] H. Eyring. The activated complex in chemical reactions. *J. Chem. Phys.*, 3(2), 1935.

[38] M. I. Freidlin and A. D. Wentzell. *Random Perturbations of Dynamical Systems.* Springer Verlag, 1984.

[39] D. Frenkel and B. Smit. *Understanding molecular simulation: From Algorithms to applications.* Academic Press, 1996.

[40] A. Friedman. *Stochastic differential equations and applications*, volume 1. Academic Press,Inc., 1975.

[41] C. W. Gardiner. *Handbook of stochastic methods : for physics, chemistry and the natural sciences.* Springer Verlag, 2004.

[42] Ch. Großmann and H.-G. Roos. *Numerik partieller Differentialgleichungen.* Teubner, 1992.

[43] A. Gupta, M. Zangril, A. Sundararaj, P. A. Dinda, and B. B. Lowekamp. Free Network Measurements for Adaptive Virtualized Distributed Computing. Technical report, College of William&Mary, Computer Science Department, 2005.

[44] W. Hackbusch. *Elliptic differential Equations: Theroy and numerical treatment.* Springer, 1992.

[45] C. Hartmann. *Model reduction in classical molecular dynamics.* PhD thesis, Free University Berlin, 2007.

[46] C. Hartmann and Ch. Schütte. Comment on two distinct notions of free energy. *Physica D*, 228(1), 2007.

[47] U. G. Haussmann and E. Pardoux. Time reversal of diffusions. *The Annals of Probability*, 14(4):1188–1205, 1986.

Bibliography

[48] A. Hobolth and J. L. Jensen. Statistical inference in evolutionary models of dna sequences via em-algorithm. *Statist. Applications in Genetics and Molecular Biology*, 4(1):Article 18, 2005.

[49] I. Holmes and G. M. Rubin. An expectation maximization algorithm for training hidden substitution models. *J. Mol. Biol.*, 317(5):753–764, 2002.

[50] J. Horiuti. On the statistical mechanical treatment of the absolute rate of chemical reaction. *Bull. Chem. Soc. Jpn.*, 13(1), 1938.

[51] W. Huisinga. *Metastability of Markovian Systems: A transfer operator approach in application to molecular dynamics*. PhD thesis, Free University Berlin, 2001.

[52] G. Hummer. From transition paths to transition states and rate coefficients. *J. Chem. Phys.*, 120(2), 2004.

[53] R. B. Israel, J. S. Rosenthal, and J. Z. Wei. Finding generators for markov chains via empirical transition matrices with applications to credit ranking. *Mathematical finance*, 11(2), 2001.

[54] B. Korte and J. Vygen. *Combinatorial Optimization: Theory and Algorithms*. Springer Verlag, second edition, 2001.

[55] S. Lafon and A. B. Lee. Diffusion maps and coarse-graining: A unified framework for dimensionality reduction, graph partitioning, and data set parameterization. *IEEE Transactions on Pattern Analysis and Machine Intelligence*, 28(9):1393–1403, 2006.

[56] D. P. Landau and K. Binder. *A guide to monte carlo simulation in statistical physics*. Cambridge University Press, 2000.

[57] A. Lasota and M. C. Mackey. *Chaos, Fractals, and Noise: Stochastic Aspects of Dynamics*, volume 97. Springer Verlag, 1994.

[58] A. Levine. *Theory of Probability*. Addison-Wesley Publishing Company, 1971.

[59] E. Lindahl, B. Hess, and D. van der Spoel. Gromacs 3.0: A package for molecular simulation and trajectory analysis. *J. Mol. Mod.*, 7(8):306–317, 2001.

[60] L. Maragliano, A. Fischer, E. Vanden-Eijnden, and G. Ciccotti. String method in collective variables: Minimum free energy paths and committor surfaces. *J. Chem. Phys*, 125, 2006.

[61] E. Meerbach, Ch. Schütte, I. Horenko, and B. Schmidt. Metastable conformational structure and dynamics: Peptides between gas phase and aqueous solution. In O. Kühn and L. Wöste, editors, *Analysis and Control of Ultrafast Photoinduced Reactions*, Series in Chemical Physics 87, pages 796–806. Springer, 2007.

[62] M. Meila and J. Shi. A random walk's view of spectral segmentation. *AI and Statistics (AISTATS)*, 2001.

[63] P. Metzner, E. Dittmer, T. Jahnke, and Ch. Schütte. Generator estimation for markov jump processes. *J. Comp. Phys., in press*, 2007.

[64] P. Metzner and Ch. Schütte. Generator estimation for markov jump processes based on incomplete observations non-equidistante in time. *submitted to Physical Review E*, 2007.

[65] P. Metzner, Ch. Schütte, and E. Vanden-Eijnden. Illustration of transition path theory on a collection of simple examples. *J. Chem. Phys.*, 125(8):084110, 2006.

[66] P. Metzner, Ch. Schütte, and E. Vanden-Eijnden. Transition path theory for Markov jump processes. *submitted to Multiscale Modeling and Simulation*, 2007.

[67] M. F. Neuts. *Algorithmic Probability: a Collection of Problems.* Chapman and Hall, 1995.

[68] M. E. J. Newman. The structure and function of complex networks. *SIAM Re.*, 45(2):167–256, 2003.

[69] J. R. Norris. *Markov chains.* Cambridge University Press, 1998.

[70] B. Oksendal. *Stochastic Differential Equations: An Introduction with Applications.* Springer, 6 edition, 2003.

[71] O. A. Oleinik and E. V. Radkevic. *Second Order Equations with Nonnegative Characteristic Form.* American Mathematical Society, Providence, Rhode Island and Plenum Press, New York, 1973.

[72] C. Dellago P. G. Bolhuis, D. Chandler and P. Geissler. Transition path sampling: throwing ropes over dark mountain passes. *Ann. Rev. Phys. Chem.*, 53, 2002.

[73] S. Park, M. K. Sener, D. Lu, and K. Schulten. Reaction paths based on mean first-passage times. *J. Chem. Phys.*, 119(3):1313–1319, 2003.

[74] Y. Pokern, A. M. Stuart, and P. Wiberg. Parameter estimation for partially observed hypoelliptic diffusions. *submitted to J. R. Stat. Soc.*

[75] W. Ren, E. Vanden-Eijnden, P. Maragakis, and W. E. Transition pathways in complex systems: Application of the finite-temperature string method to the alanine dipeptide. *J. Chem. Phys.*, 123, 2005.

[76] H. Risken. *The Fokker-Planck equation : methods of solution and applications.* Springer, Berlin, 1996.

[77] D. M. Roma, R. O'Flanagan, A. Ruckenstein, A. M. Sengupta, and R. Mukhopadhyay. Optimal path in epigenetic switching. *Phys. Review E*, 71:011902, 2005.

[78] S. T. Roweis and L.K. Saul. Nonlinear dimensionality reduction by locally linear embedding. *Science*, 290(5500):2323–2326, 2000.

[79] K. Schulten and I. Kosztin. Lecture notes in theoretical biophysics, 2000.

[80] Ch. Schütte. *Conformational Dynamics: Modelling, Theory, Algorithm, and Application to Biomolecules*. Habilitation Thesis, Fachbereich Mathematik und Informatik, Freie Universität Berlin, 1998.

[81] Ch. Schütte, A. Fischer, W. Huisinga, and P. Deuflhard. A direct approach to conformational dynamics based on hybrid monte carlo. *J. Comp. Phys*, 151(1):146–168, 1999.

[82] Ch. Schütte, W. Huisinga, and P. Deuflhard. Transfer operator approach to conformational dynamics in biomolecular systems. In B. Fiedler, editor, *Ergodic Theory, Analysis, and Efficient Simulation of Dynamical Systems*, pages 191–223. Springer Verlag, 2001.

[83] Ch. Schütte, J. Walter, C. Hartmann, and W. Huisinga. An averaging principle for fast degrees of freedom exhibiting long term relations. *Multiscale Model. Simul.*, 2(3):501–526, 2004.

[84] J. Shi and J. Malik. Normalized cuts and image segmentation. *IEEE Trans. Pattern Analysis and Machine Intelligence*, 22(8):888–905, 2000.

[85] N. Singhal and V. S. Pande. Error analysis and efficient sampling in markovian state models for molecular dynamics. *J. Chem. Phys.*, 123(20):204909, 2005.

[86] S.Meyn and R. Tweedie. *Markov Chains and Stochastic Stability*. Springer Verlag, 1993.

[87] M. V. Smoluchowski. Zur kinetischen theorie der brownschen molekularbewegung und der suspensionen. *Ann. Phys. (Leipzig)*, 4(21), 1906.

[88] E. Süli. Finite element approximation of high-dimensional transport-dominated diffusion problems. *NA Group Research NA-05/19*, 2005.

[89] R. Syski. *Passage Times for Markov Chains*. IOS Press, 1992.

[90] K. Taira. *Diffusion Processes and Partial Differential Equations*. Academic Press,Inc., 1988.

[91] F. Tal and E. Vanden-Eijnden. Transition state theory and dynamical corrections in ergodic systems. *Nonlinearity*, 19(2), 2006.

[92] E. Vanden-Eijnden. Transition path theory. In M. Ferrario, G. Ciccotti, and K. Binder, editors, *Computer Simulations in Condensed Matter: from Materials to Chemical Biology*, volume 2 of *703*. Springer Verlag, 2006.

[93] E. Vanden-Eijnden and G. Ciccotti. Second-order integrator for langevin equation with holonomic constrains. *Chem. Phys. Lett.*, 429, 2006.

[94] E. Vanden-Eijnden and F. Tal. Transition state theory: Variational formulation, dynamical corrections, and error estimates. *J. Chem. Phys.*, 123(18), 2005.

[95] E. Wigner. The transition state method. *Trans. Faraday Soc.*, 34, 1938.

[96] D. Williams. To Begin at the Beginning. In A. Dold and B. Eckmann, editors, *Lecture Notes in Mathematics: Stochastic Integrals, Proceedings, LMS Durham Symposium.* Springer Verlag, 1980.

[97] T. Yamamoto. Quantum statistical mechanical theory of the rate of exchange chemical reactions in the gas phase. *J. Chem. Phys.*, 33(1), 1960.